CRANFIELD UNIVERSITY

DAVID JAMES BENTLEY

REVERSE THRUST AERODYNAMICS OF ULTRA-HIGH BYPASS VARIABLE-PITCH TURBOFANS

SCHOOL OF AEROSPACE, TRANSPORT & MANUFACTUING
(SATM)

PhD THESIS
Academic Year: 2018

Supervisor: Professor Vassilios Pachidis
April 2018

CRANFIELD UNIVERSITY

SCHOOL OF AEROSPACE, TRANSPORT & MANUFACTUING
(SATM)
Gas Turbine Performance Engineering Group

PhD THESIS

Academic Year 2018

DAVID JAMES BENTLEY

REVERSE THRUST AERODYNAMICS OF ULTRA-HIGH BYPASS VARIABLE-PITCH TURBOFANS

Supervisor: Professor Vassilios Pachidis
April 2018

ABSTRACT

This thesis constitutes the first research project into reverse thrust aerodynamics of variable-pitch turbofans within the Cranfield Rolls-Royce UTC in Aero System Design, Integration & Performance. The study focussed on development and validation of a steady-state (RANS) CFD research model, including the presentation of initial results.

The engine model was developed primarily around NASA's publicly available 22" Advanced Ducted Propulsor (ADP) variable-pitch fan. The 3D fan & OGV models were modified and scaled to suit the correct engine size for the study. An annular engine model was then developed, which consisted of an optimised 0D thermodynamic model, a 2D preliminary gas-path & component sizing model, and a 2D preliminary aero-line design for the nacelle & engine exhaust systems. These 2D models were extruded to provide 3D axisymmetric definitions. The resulting engine design was considered to represent a near-future ultra-high bypass ratio turbofan, of conventional geared architecture. Furthermore, in accordance with the project requirements, the engine satisfied the 'middle-of-the-market' thrust class (40,000 lbf/178 kN). A 3D pylon model was created, to mount the engine under the wing of NASA's DLR F11 airframe, in accordance with the outcomes of previous turbofan installation aerodynamics studies conducted at Cranfield. The airframe was scaled to the approximate size & weight characteristics of a Boeing 757 aircraft.

The research model was tested with the VPF at a single speed/pitch setting for reverse thrust, where it was found that flow within and around the engine was highly influenced by the fan's rotational speed. The outer radius of the fan produced a reverse stream exiting the nacelle inlet at all tested landing speeds, which remained attached to the nacelle outer surface until re-ingestion through the bypass nozzle. Engine core distortion was measured during reverse thrust operation, which was most prominent at higher landing speeds (with peak DC60 = 0.21). The study concluded with new understandings of the challenges associated with a real-world (installed on airframe) VPF-reverse-thrust capable engine. More research is recommended to quantify the overall aerodynamic drag on the aircraft, and to test alternative fan pitch /RPM configurations.

Keywords: *UltraFan, UHBR, VPF, Reverser, DLR F11, Advanced Ducted Propulsor, ADP*

ACKNOWLEDGEMENTS

The author would like to thank Professor Vassilios Pachidis, both for providing the opportunity to undertake this doctorate program, and for his continued support, patience & trust throughout the project, and especially during the teething problems with the model development.

I would also like to express my gratitude to Richard Tunstall, John Whurr & John Mason; the industrial supervisors to the project for their guidance, advice & knowledge. Additionally, I am extremely grateful to Rolls-Royce Holdings for sponsoring this study.

I would also like to thank the following individuals for their contributions during the project:

- ***Dr Christos Mourouzidis*** *(UltraFan™ team, Turbomatch & ATLAS)*
- ***Dr Bjorn Cleton*** *(UltraFan™ team, Turbomatch)*
- ***Dr Hasani Azamar-Aguirre*** *(SOCRATES)*
- ***David John Rajendran*** *(Cranfield UTC VPF)*
- ***Tim Williams*** *(Cambridge UTC VPF)*
- ***Dr Ioannis Goulos*** *(GEMINI)*
- ***Alvise Pellegrini*** *(Turbomatch Optimiser)*
- ***Dr Lucas Pawsey***
- ***Maria Negus*** *(UTC Administrator)*
- ***Francesco Mastropierro***
- ***Daniel Cuenca-Blasco***
- ***Marco Moretti***
- ***Meropi Siatara***
- ***Thomas Mourouzidis***

Finally, I wish to express my gratitude to my family; my mother for her support and encouragement, and to my late father, for providing me with the determination and discipline required to undertake this doctoral study.

TABLE OF CONTENTS

LIST OF FIGURES

LIST OF TABLES

LIST OF EQUATIONS

ABBREVIATIONS & ACRONYMS

ACARE	Advisory Council for Aviation Research and innovation in Europe
ADP	Advanced Ducted Propulsor
AIAA	American Institute of Aeronautics and Astronautics
BPR	Bypass ratio
CAA	Civil Aviation Authority (UK)
CAD	Computer aided design
CFD	Computational fluid dynamics
CIGV	Core inlet guide vanes
CPU	Central processing unit
CRM	Common research model
DPW	Drag prediction workshop
ECU	Engine control unit
EoR	End-of-runway
ESS	Engine stator section
ETOPS	Extended-range Twin-engine Operational Performance Standards
FAA	Federal Aviation Administration (USA)
FEGV	Fan exit guide vane
FOD	Foreign object debris
FPR	Fan pressure ratio
FTR	Fan temperature ratio
HLPW	High-lift prediction workshop
HPC	High pressure compressor, *or* high-performance computer
HPT	High pressure turbine
GEMINI	Geometric Engine Modeller Including Nozzle Installation
GDP	Gross domestic product
GUI	Graphical user interface
ICAO	International Civil Aviation Organization
ISA	International Standard Atmosphere
IPC	Intermediate pressure compressor
IPT	Intermediate pressure turbine
JAA	Joint Aviation Authorities (EU)
LPT	Low pressure turbine
MLW	Maximum landing weight
MTOW	Maximum take-off weight
NACA	National Advisory Committee for Aeronautics
NASA	National Aeronautics & Space Administration
OGV	Outlet guide vane
OPR	Overall pressure ratio
PGB	Power transmission gearbox
PR	Pressure ratio
QCSEE	Quiet, clean, short-haul experimental engine
RANS	Reynolds-averaged Navier-Stokes
RPM	Revolutions per minute
RTO	Rejected take-off
SFC	Specific fuel consumption
SLS	Sea-level static
SLTO	Sea-level take-off
SST	Shear-stress transport
T30	High pressure compressor exit temperature
T40	Combustion chamber exit temperature

TE	Trailing edge
TET	Turbine entry temperature
ToC	Top-of-climb
TRB	Thrust ratio barcode
TRU	Thrust-reverser unit
VAFN	Variable-area Fan nozzle
VIGV	Variable-inlet guide vane
VHBR	Very-high bypass ratio
VPF	Variable-pitch fan
VSV	Variable-stator vane
UHBR	Ultra-high bypass ratio
UTC	University Technology Centre

NONMENCLATURE

α	Inlet flow angle
γ	Ratio of specific heats
Δ	Change in quantity
η_{rev}	Thrust reverser effectiveness
η_{isen}	Isentropic (adiabatic) efficiency
η_{prop}	Propulsive efficiency
$\eta_{prop,rev}$	Reverser propulsive efficiency
ρ_∞	Freestream density
ρ	Density
$\varkappa$	Blade stagger angle
v	Kinematic fluid viscosity
A	Area
AoA	Angle of attack
C_{DF}	Drag factor (pod drag)
$C_{D.noz}$	Nozzle discharge coefficient
C_D	Drag coefficient
C_V	Nozzle exit velocity coefficient
C_L	Lift coefficient
C_p	Pressure coefficient
CDI	Circumferential distortion index
DC_{60}	Distortion coefficient (60˚ sectors)
F_{ax}	Axial thrust
F_{core}	Core-stream thrust
F_{nom}	Nominal thrust
F_{rev}	Reverse thrust
H	Enthalpy
L	Lift force
N_1	Non-dimensional low-pressure system shaft speed
N_2	Non-dimensional high-pressure system shaft speed
PAV	Area-weighted averaged total pressure
PAV_{60}	Area-weighted average of the total pressure in lowest 60˚ sector
P	Total pressure
P_∞	Freestream total pressure
P_{inlet}	Inlet total pressure
P_o	Average total pressure
$P_{o,avg}$	Average total pressure for entire inlet
$P_{o,min}$	Minimum total pressure
q	Dynamic pressure
R	Ideal gas constant
RDI	Radial distortion index
S_s/S	Spoiler/wing surface area ratio
t	Static temperature
T, T_{Total}	Total temperature
U	Blade rotational speed
U_{tip}	Blade tip rotational speed
U_τ	Friction velocity next to wall
V	Velocity
V_∞	Freestream velocity
V_1	Commit-to-fly speed
V_2	Safe-to-climb speed

$\boldsymbol{Va}$	Axial velocity
$\boldsymbol{V_{ideal}}$	Ideal nozzle exit velocity
$\boldsymbol{V_{noz.exit}}$	Actual nozzle exit velocity
$\boldsymbol{V_{rj}}$	Reverse jet velocity
$\boldsymbol{V_R}$	Nose-up/rotate speed
$\boldsymbol{W}$	Mass-flow
$\boldsymbol{Y^+}$	Dimensionless wall distance
$\boldsymbol{y}$	First node offset height
$\%\boldsymbol{T_{max}}$	Maximum blade profile thickness as % of chord length
$\%\boldsymbol{T_{max}P}$	Location of blade profile maximum thickness as % along chord

1 Introduction

1.1 Background

Gas turbines have become the dominant propulsion system in the aviation. It is estimated that the industry directly supports 9.9 million jobs globally, which according to Oxford Economics, are, on average, 3.6 times more productive than average jobs around the world. The aviation industry's current worth is $2.7 trillion GDP globally, accounting for over 3.7 billion passengers and 1/3 of the world's freight (by value) annually. Furthermore, the most recent estimates suggest that demand for air transport will increase by an average of 4.3% per annum over the next 20 years, visualised in *Figure 1-1*. [1]

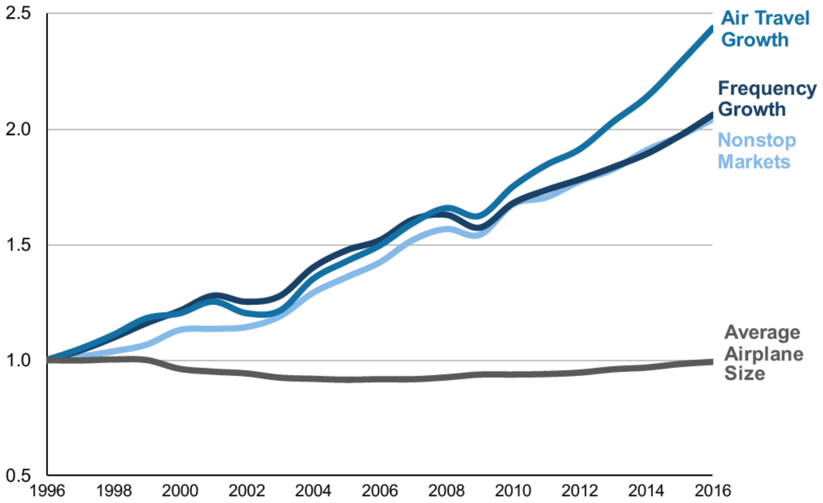

Figure 1-1: Aviation growth, published by Boeing [2]

In an attempt to control & reduce environmental concerns, aviation bodies such as ICAO and ACARE have set targets for the industry, as far ahead as 2050. These targets can be presented below, and are relative to an aircraft entering service in 2000 [3]:

- 75% reduction in CO_2 emissions (per passenger kilometre)
- 90% reduction in NO_X emissions (per passenger kilometre)
- 65% reduction in noise pollution

When looking at previous generations of aero gas turbines, a prominent trend is the increase in bypass-ratio (BPR) & fan diameter, and reduction in fan pressure-ratio (FPR). The result is an improvement in propulsive efficiency by moving to lower specific-thrust designs (described in more detail in *Ch 2.1 & 2.2*). Current engines are designed with BPRs as high as 10:1. [4] If bypass ratios are to continue to rise, the propulsive benefits are expected to soon become offset by increases in engine weight & drag. Other issues, such as fan operability, become more problematic with lower FPR designs. To overcome these concerns, manufacturers such as Rolls-Royce are assessing the viability of new engine technologies & alternative architectures for the future generations of Ultra-High Bypass Ratio (UHBR) engines.

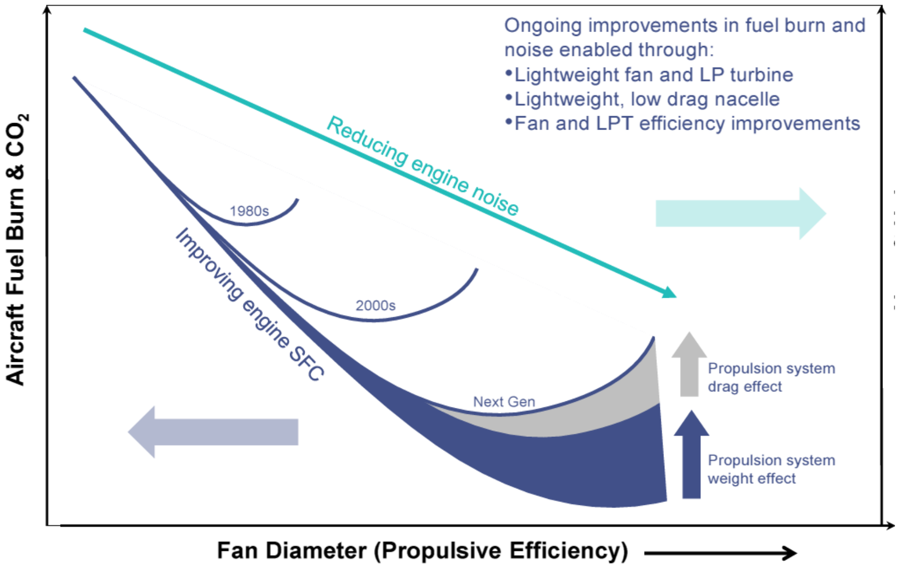

Figure 1-2: The trend of improvement in engine specific-fuel consumption (SFC) [5]

The primary driver for new engine designs is to improve the overall efficiency, and thus reducing the quantity of fuel used. However, there are two fundamental challenges to the improvement of gas turbines. The first is the improvements in technology and engine design required to achieve greater thermal and propulsive efficiencies.

The second is the enhancement of knowledge to enable architectural and technological changes to take place. Rapid change in engine designs without fully appreciating the challenges often results in financial collapse, as the engineering investment required for gas turbines is enormous. One area of concern that falls under this category, is the inherent fan instability that occurs when moving towards very low specific-thrust turbofans. *Figure 1-3* illustrates this, comparing three fan maps of varying specific thrust, using cores with an overall pressure ratio (OPR) of 30. Under the low-specific thrust case, the fan operating point is pushed to the far left of the map, well outside the normal operating region, and towards a state of stall/surge.

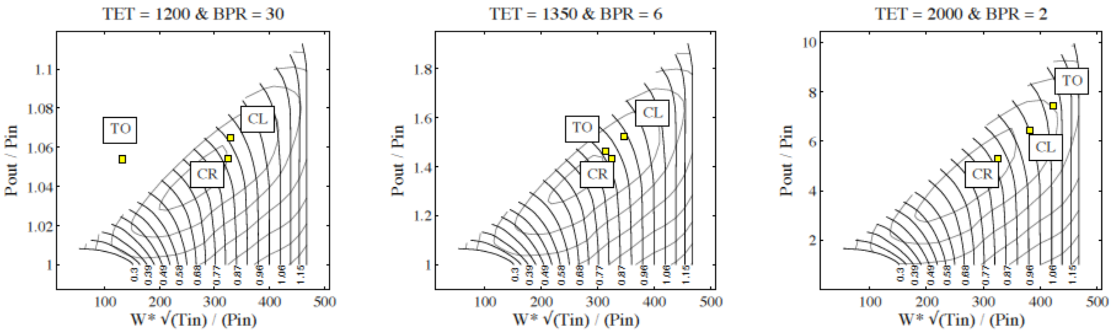

(a) Low ST (b) Medium ST (c) High ST

Figure 1-3: Effect of varying specific-thrust on fan performance characteristics [6]

This is due to the bypass nozzle of a civil turbofan which is usually designed for cruise flow capacity, to maximise efficiency for the longest phase of flight. This is discussed in more detail in *Chapter 2.2*. Two design solutions have been proposed which could address these issues; variable-area fan nozzles (VAFNs) & variable-pitch fans (VPFs), shown in *Figure 1-4*. [7]

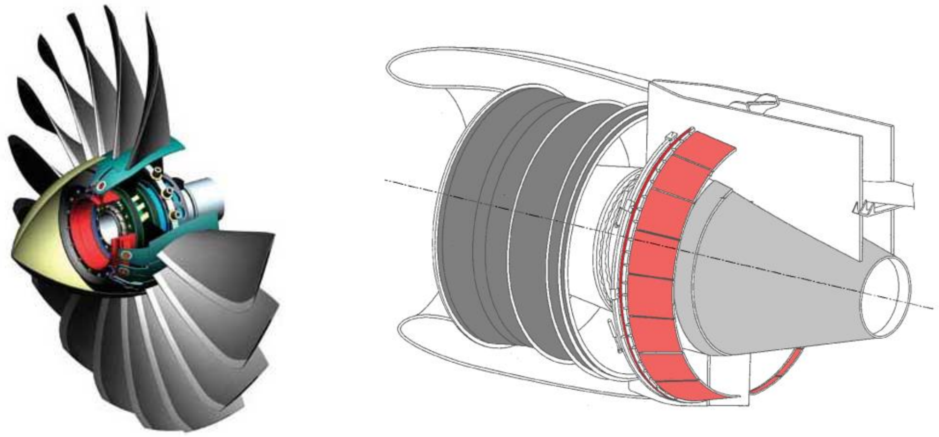

Figure 1-4: Left: Variable-pitch fan [8]***, Right: Variable-area Fan Nozzle*** [9]

Both technologies introduce variable geometry systems, where the fan-nozzle-area or fan-blade-pitch can be changed to modify the fan performance characteristics & overcome operability issues. Whilst these devices are not new to the industry, the cost and complexity involved in development for large turbofan applications has so far prohibited them from featuring on any production models. Instead, manufacturers have favoured the less-risky approach of small incremental improvements on existing engine architectures. This slow-but-steady refinement can be seen in the rising trends in component efficiency, overall pressure ratio (OPR), and turbine-entry-temperature (TET), only capable due to advances in technology. The traditional method of progressing engine designs is, however, approaching a plateau. To continue reducing mission fuel-burn, manufacturers are being left with little choice but to consider alternative architectures.

These new architectures will require enormous effort and capital investment before viable designs is engineered. To mitigate the development risks, engineers need to establish a better field of knowledge on any new gaps which appear. One of these gaps that has been identified by the industry is the aerodynamic performance of a variable-pitch turbofan, when the fan pitch is set to pump air in reverse. If the capabilities of a reversed VPF are adequate, they could replace conventional thrust reversers.

As such, a request was made to Cranfield Rolls-Royce University Technology Centre (UTC) by the industrial partner to conduct research into this largely undiscovered field, for potential application on the UltraFan™ engine concept. The research request was to entail development of a large-scale 3D model, for generating flow predictions both inside and outside of the engine nacelle. This doctoral project represents the first undertaking into the topic of VPF reverse thrust in the department, and therefore focusses on the methodology, validation, and initial flow simulation results of the developed research model.

1.2 Aims & Objectives

The main aim of the study was to develop a CFD-based research model, to investigate the flow-phenomena associated with reverse thrust operation, of an engine fitted with a variable-pitch fan. These are presented below:

- Under reverse thrust operation the bypass nozzle becomes the engine inlet. Aggressive turning of the flow around the nozzle lip is expected to result in significant total pressure loss. This directly affects the FPR that can be achieved.
- As airflow through the bypass duct is reversed, core flow is required to turn sharply into the compressor inlet, which is expected to induce distortion, pressure losses, and possibly restrict the mass-flow onto the intermediate-pressure compressor (IPC) face through blockage. The presence of both the outlet guide vane (OGV) and engine section stator (ESS) stages may also contribute to flow instability/blockage.
- It is considered possible (depending on engine design), that the core exhaust stream could be partially re-ingested during reverse-thrust, due to shearing against the opposing flow entering into the bypass nozzle.
- Reverse thrust operation only makes up a fraction of a typical mission profile, as such fan blades are not designed specifically to operate under these conditions. This, coupled with the unpredictable flow conditions either side of the fan, make it difficult to anticipate exactly how the stage will operate aerodynamically. The fan numerical (CFD) model needs to therefore be robust enough to accommodate unexpected aerodynamics.
- The presence of the airframe and nearby ground was expected to influence the flow-field during reverse-thrust operation, which could induce additional circumferential flow distortion through the nacelle.

The list of project objectives consists mainly of model development criteria, and is presented below:

- Develop a preliminary engine model to satisfy a ‘middle-of-the-market’ thrust class turbofan (40,000 lbf/178 kN nominal sea-level static thrust), with technology limitations reflecting an expected entry into service of 2025-2030.
- Engine to feature a low pressure-ratio (FPR>1.45) variable-pitch fan, based on an existing design.
- The engine CFD model should include fluid domains for the splitter/core inlet duct, OGV stage & bypass duct/nozzle. The domains should be fully annular where required, to capture circumferential distortion into the engine core.
- An airframe (wing & fuselage) should be included in the CFD model to assess the engine aerodynamics in an installed environment. The airframe should represent a conventional twin-engine aircraft during landing, sized to suit the engine thrust class. This required the inclusion of deployed high-lift devices (slats & flaps), spoilers. Additionally, a ground-plane was also required beneath the engine to ascertain any engine-ground aero-interactions.
- Develop a preliminary pylon model to mount the engine/nacelle onto the aircraft wing in an appropriate position. The dimensions should be in accordance with engine-installations guidelines previously established by studies into the topic conducted within the UTC.
- Establish an approach to modelling the aerodynamics using steady state, Reynolds-averaged Navier-Stokes CFD numerical solutions. This method also needed to be assessed for errors, which could have credibility implications for the results.

1.3 Research Scope

The topic of VPF reverse thrust has many aspects, and given the broad knowledge required for developing an engine & airframe model, it is important to establish what is and is not considered within scope of the project.

Reverse-thrust is normally only engaged for a very short duration relative to the length of a typical flight – as such, civil engines don’t typically compromise on designs for improved reverse-thrust performance. Instead, they are optimised for minimum mission fuel-burn across the normal operating profile (forward thrust) to reduce operating costs. This approach was taken when developing and testing the various model components, such as the engine thermodynamic cycle model & engine exhaust system. Regarding the VPF CFD model, the main requirement was for a robust fan representation that was not excessively computationally expensive. As a result, the CFD model created under this project is considered a preliminary representation of a modern engine suitable for investigating systems-level reverse-thrust aerodynamics. The model also sets a baseline for future improvement, and more in-depth analysis of the subject on subsequent project(s).

Additionally, the expected flow regime during reverse-thrust using a VPF is so unconventional and far from the normal operating regime, it was deemed that the components of the model needed to function aerodynamically under normal operation without significant concern, but that optimised designs were not necessary.

Areas considered not in scope of the project are listed below:

- Mechanical integrity
- Core modelling during reverse-thrust operation
- Transient performance
- Foreign object debris (FOD) ingestion risks
- Engine noise
- Structural design
- Control systems

1.4 Contribution to Knowledge

Variable-pitch turbofans have been conceptualised and researched since at least the 1960s, from which several experimental engines have been developed. However, there is a distinct lack of knowledge on the subject in the public domain, with only a handful of previous reverse-thrust studies documented. [10, 11, 12] Many of the reports were commercially sponsored by aero-engine manufacturers. It is therefore fair to draw the conclusion that the topic has been studied, but much of the knowledge gained has remained commercially sensitive to its proprietors.

Whilst historically variable-pitch fans have not seen commercial success, the technology is being seriously considered again by engine-manufacturers for near-future designs. Therefore, this project aims to help establish a foundation of knowledge on the topic, upon which the viability & operation of such a device may be better understood.

Areas of understanding that are expected to be improved from this research are summarised in the points below:

- Total pressure loss in the bypass duct due to flow separation on bypass nozzle lip for a large-scale integrated engine.
- Total pressure loss and distortion at the ESS inlet, due to sharp turning around the splitter, and circumferential variations in flow field.
- The mode of operation for the fan – an overview of its aerodynamic performance & observed characteristics at the tested reverse-thrust pitch, in an installed-engine environment.
- Estimation of the net deceleration force associated with the reverse-thrust engine operation, across the full landing speed spectrum (from 140 to 5 knots).
- Summary of the external flow-field characteristics, including noticeable interactions with the airframe & ground, and stream-tubes leading in/out of the engine.
- Computational performance of the large-scale high fidelity numerical/CFD model.

1.5 Thesis Outline

The main chapters of the thesis have been organised in the following order:

Chapter 2 covers the literature review undertaken for the project. The chapter first discusses the rising interest in VPF technology for near-future turbofan engines. A summary of conventional thrust-reverser systems for current and near-future turbofans is then presented, going into more depth on the variable-pitch thrust reverser system. Additionally, some basic elements on compressor inlet distortion metrics, and public domain airframe models is provided, in support of the results & methodology chapters respectively.

Chapter 3 initially contains the methodology relating to development of the various components which make up the CFD model. These are presented in three parts; the 2D annular engine, 3D turbomachinery, & airframe related components. Following this, the chapter presents the approach adopted to meshing the 3D geometries, and the solver settings for the CFD numerical flow predictions.

Chapter 4 supports the methodology, by providing a brief overview of the validation and verification work undertaken during component development. Whilst this is not essential to understanding the area of research or the results, it is crucial for verifying the credibility & accuracy of the reverse-thrust CFD solutions.

Chapter 5 presents the results of the project, focussing first on the numerical solver performance, before discussing the flow metrics & observations taken from the initial set of CFD results.

Finally, *Chapter 6* summarises the results and outcomes from the research, and draws attention to the most significant findings. The chapter concludes with recommendations for future work.

2 Literature Review

This chapter presents the existing knowledge relevant to the research topic that has been found in the public domain. The following sub-chapters aim to provide the reader with a fundamental understanding of variable-pitch fan reverse-thrust. Additional areas such as engine architecture, compressor distortion analysis & airframe modelling are also covered, to support the methodology rationale described in *Chapter 3*.

2.1 Current Turbofan Designs

The modern turbofan is one of the most complex pieces of engineering hardware in existence. Since the first-generation turbofan engines entered service, the overall architectural design has remained more-or-less unchanged. Manufacturers have chosen to optimise and refine existing designs, evolving them to incorporate the latest technologies available. *Figure 2-1* demonstrates how some notable historic technological advances have improved the efficiency and performance of civil fans until 1985. A lower FPR results in a lower energy transfer to the flow. One parameter used to assess the work limit of the fan is the stage loading ($\Delta H/U^2$). [13] As such, if FPR is reduced, the RPM can also be reduced, without exceeding the aerodynamic capabilities of blades – reducing shock losses etc.

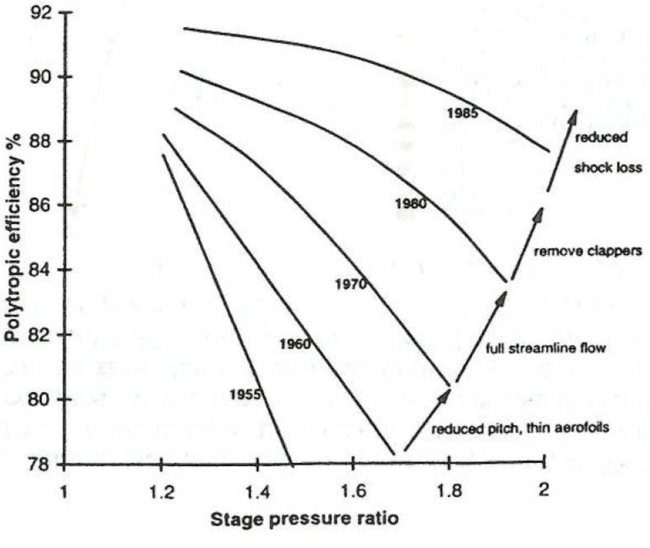

Figure 2-1: Improvements in Civil Fan Performance [14]

Improvements have continued since 1985, and fan polytropic efficiency lies typically around 95% by modern standards. This can be attributed to both a move to lower specific-thrust engines, and improvements in manufacturing & aerodynamic design capabilities. *Figure 2-2* shows how specific fuel consumption (SFC) reduction is achievable by using a lower specific-thrust arrangement (higher BPR, lower FPR), on a fixed core engine size. [15]

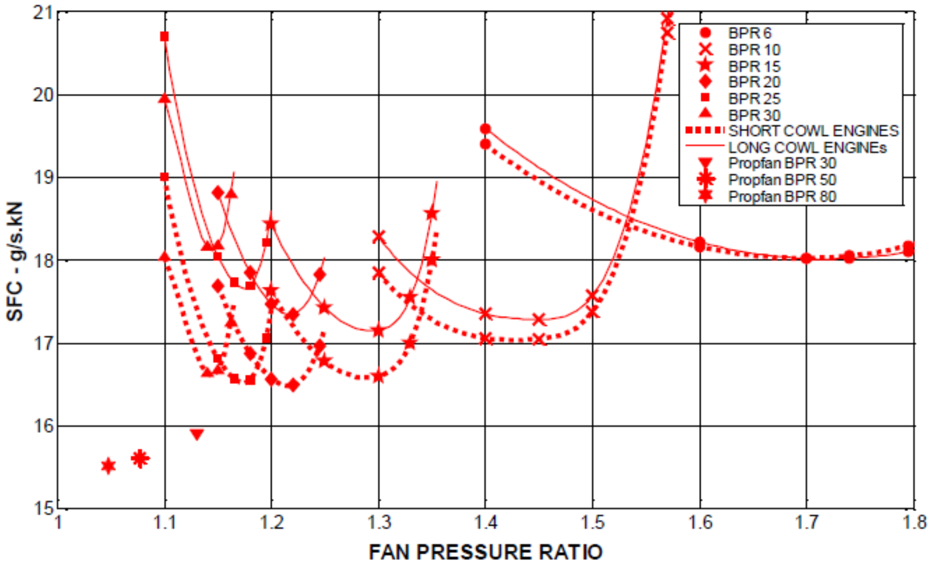

Figure 2-2: SFC & FPR comparison for a fixed core size operating at cruise [15]

One of the drawbacks of having a low-speed fan, is that the low-pressure turbines (LPT) which power it, also must reduce RPM, as they lie on the same shaft. If a turbine stage rotational speed is lowered, its ability to harvest energy from the working fluid is reduced, as they follow the same stage-loading characteristic. The low speed and lower pressure working fluid across current turbofan low-pressure turbines (LPTs) has led to multi-stage systems with large weight penalties, as can be seen in *Figure 2-3.*

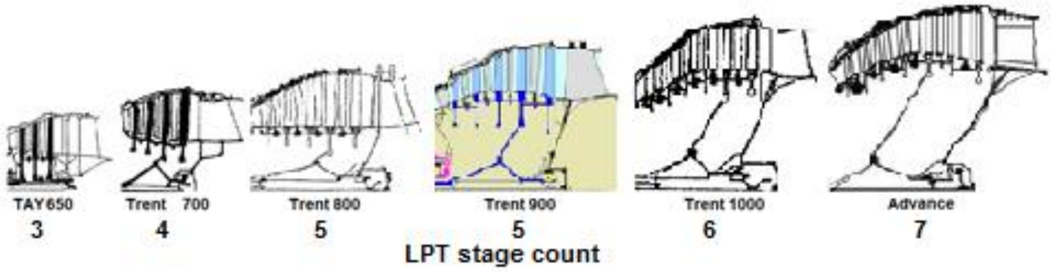

Figure 2-3: Historic increase in number of LPT stages in Rolls-Royce engines [16]

2.2 Future Expected Engine Architecture

It is unclear exactly what the future generations of aero-engines will look like, but there is a clear trend towards engines with larger fan diameters, OPRs & peak temperatures to achieve better thermal and propulsive efficiencies. The most significant recent development has been the intention for manufacturers to integrate a power transmission gearbox (PGB) into the engine; to decouple the fan & LPT stages. The first of these new generation engines to enter service was Pratt & Whitney's PW1000G family in 2016 *(*shown in *Figure 2-4)*. [17] Rolls-Royce has also shown serious intentions to utilized geared architecture, investing in a new gearbox test facility in Dalchewitz, Germany. [18]

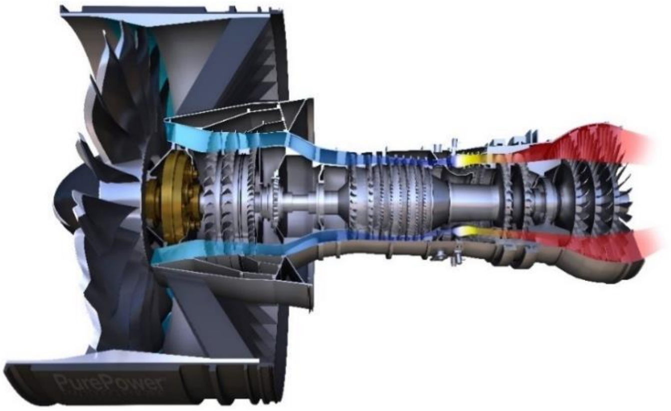

Figure 2-4: Pratt & Whitney's geared PW1000G architecture [19]

On a turbofan engine, the gearbox allows the low-speed fan to be powered by a high-speed LPT. The higher work-coefficient of the LPTs would require less stages, resulting in a significant reduction in turbine weight & shaft length. [16] *Figure 2-5* illustrates this change in architecture, from the modern Trent XWB to the envisaged UltraFan™.

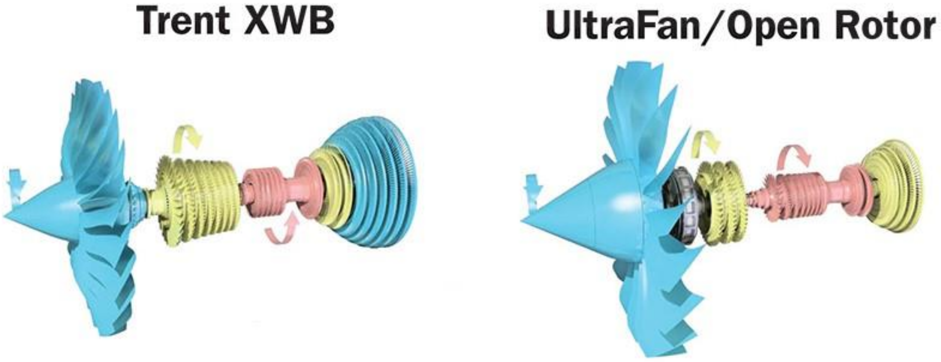

Figure 2-5: Comparison between Trent XWB & UltraFan turbomachinery [20]

In a 3-spool engine, such as the Trent XWB, the third shaft turbines only power the fan stage. This isn't necessary when the PGB is fitted, and a 2-spool architecture can be used instead, with the fan powered by the second shaft turbines (which also drives the IPC). The PGB does bring with it some additional complications. Weight contributions from the gearbox are estimated to be approximately 10% of bare-engine weight. The gearbox efficiency is also critical, as this has a direct effect on the transmission efficiency. Studies into geared engine optimisation conducted within Cranfield UTC, concluded that a gearbox would need a transmission efficiency in the region of 99.2 - 99.6% to achieve SFC reduction. Additional secondary systems are required, such as gearbox lubrication & cooling systems. These should not be underestimated given the magnitude of energy transfer the gearbox undertakes. [16]

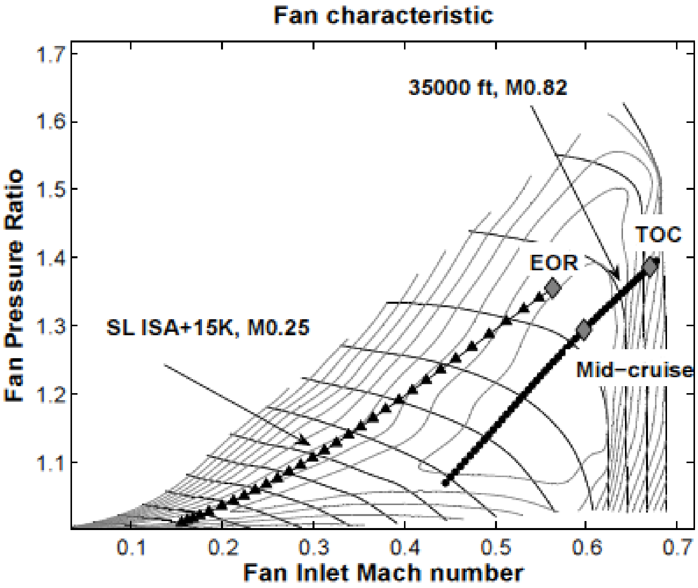

Figure 2-6: Effect of flight conditions on a high BPR fan's operating line [21]

There are additional aerodynamic concerns which need addressing for lower-specific thrust turbofans. Civil aircraft operate under a wide-range of conditions, but spend most of their time at cruise. Therefore, turbofans need to operate close to peak efficiency when travelling at approximately 35,000 ft, and 0.8 Mach. However, they also need to be capable of operating at sea-level static conditions for starting, idling/taxing, and take-off. For engines with very low pressure-ratio (PR) fans, inherent aerodynamic problems arise at off-design conditions. When operating at lower airspeed, the momentum drag drops, and the bypass nozzle static pressure increases. This results in a reduction in the nozzle PR, and a restriction in the bypass nozzle's flow capacity. [16] This reduction in flow capacity pushes the operating line to the left on the performance map; as the axial velocity reduces through the fan, disrupting the velocity triangles and pushing the blades closer to aerodynamic stall. This can be seen in *Figure 2-6*, when comparing the end-of-runway (EoR) and top-of-climb (ToC) operating lines. By moving to higher BPR configurations, this effect becomes more pronounced, as can be seen from *Figure 1-3*; at low specific-thrust configuration the take-off operating point is well into the region of fan flutter stall.

Figure 2-7: VAFN Demonstrators (Left: CFM56-7B, Right: PW1000G) [16]

To address this, two devices have been proposed to allow modulation of the flow capacity across the engine's operating spectrum. [7] The first is the variable-area fan nozzle (VAFN), shown in *Figure 2-7*. This device can change the throat area of the bypass nozzle, such that when normal flow capacity is reached, the nozzle can compensate by opening up, providing a larger throat area. Such devices already exist on small diameter, high specific-thrust military engines, but the application for a large diameter civil turbofan is more challenging. The second is the variable-pitch fan, which allows blade angle changes to be made during engine operation, to adjust the fan's flow capacity & velocity triangles.

Interest has been shown in both technologies, and it is unclear whether one will become a dominant feature on future engines. This project focusses around the VPF concept, and its potential to make redundant current thrust-reverser units (TRUs).

2.3 Conventional Reverse-Thrust Systems

To appreciate the lack of knowledge on the topic of VPF-based thrust reversal, one must first establish how the system is different from a conventional one. To do this, a study of existing thrust reverser units (TRUs) has been conducted and summarised on the following pages.

Thrust reversers are typically used to decelerate an aircraft during a landing or rejected take-off (RTO). They have also been known to be used for self-propelled pushback, but this is often not the case for underwing mounted engines, due to the risk of foreign object debris (FOD) ingestion, and contamination of the air conditioning system if de-icing chemicals are present. [22] Reversers have also seen in-flight application for both civil & military aircraft, to allow rapid deceleration or descent. However, due to safety concerns and the inefficient nature of operation, in a civil turbofan setting this is generally prohibited by the engine control unit (ECU). [23]

TRUs are usually complex, maintenance-critical components with significant weight penalties to the overall engine design. General Electric indicate that TRUs contribute to approximately 30% of nacelle weight (excluding engine) [24], and this added weight can increase fuel consumption by up to 2%. [25] Leakage and pressure drops around the TRU seals, typically contribute to an additional 0.5-1% reduction in SFC. [23] Historically, failures of thrust reversal systems have also contributed to numerous accidents in the past, where axisymmetric reverse thrust, or unintended in-flight deployment has resulted in loss of control.

One may wonder why airlines chose to operate aircraft with these expensive & heavy devices fitted to their engines, which don’t benefit the normal engine operation, given the ever-rising cost of fuel. Furthermore, there is no requirement for TRUs when it comes to engine certification. To understand why they are so widely used on civil jet aircraft, NASA’s *‘Langley Aircraft Deceleration Study Group’* put forward a questionnaire to 65 of the world’s largest airlines at the time, in 1995. [23] It concluded that the primary need was due to the additional stopping force on wet or slippery runways, where wheel brake traction is degraded. This can be seen in *Figure 2-8*, where in dry conditions reversers provide a minor improvement to landing distance, but under icy conditions, they play a vital role in avoiding runway overshoot.

Aircraft Landing on a Dry Runway

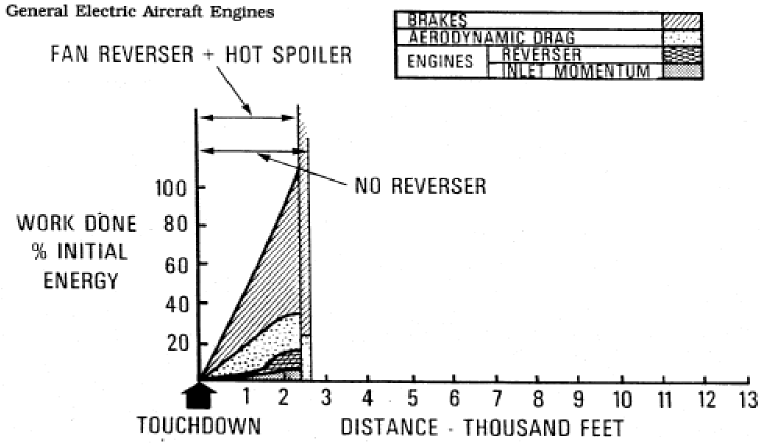
Source: General Electric Aircraft Engines

Aircraft Landing on a Icy Runway

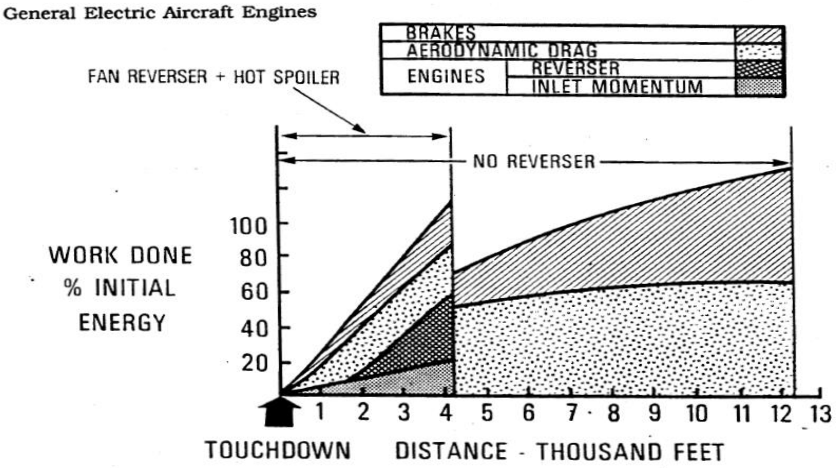
Source: General Electric Aircraft Engines

Figure 2-8: Aircraft landing distances on dry & icy runways [23]

The study group also concluded that, whilst they add significant costs to the maintenance and operation of the aircraft, the additional safety margin of having 3 braking systems provided operational benefits. Thrust reversers are also used to decelerate during an aborted take-off. The guarantee of a shorter stopping distance allows airlines to maximise payload weight, especially from airports where aircraft are restricted by runway length. As well as increasing safety margin, they also reduce wear on the wheel brakes, extending the maintenance/servicing interval.

2.3.1 Landing Conditions

Before each commercial flight, legislation dictates that a flight plan is filed and approved. Within it, estimates for required runway distances on take-off and landing are calculated to ensure safety margins are maintained. Runway overruns have long been one of the major causes of aviation accidents & serious incidents, accounting for 12% worldwide through 1984 to 1997. [26]

The Flight Safety Foundation's 'Approach & Landing Accident Reduction' (ALAR) Task Force provides aircraft operators with a prescribed method for calculating required runway length (*Figure 2-9*).

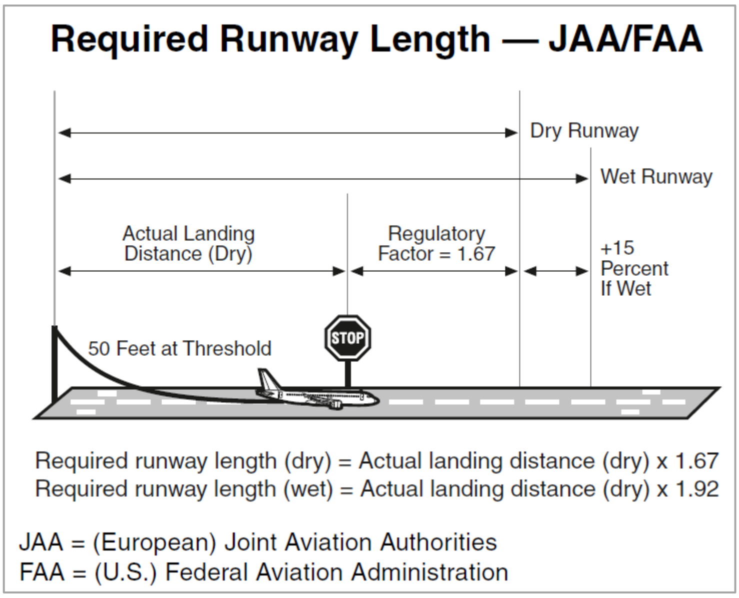

Figure 2-9: Definition of required runway length for landing (JAA/FAA standards) [26]

The method uses a baseline value for actual landing distance, as quoted by the airframe manufacturer. A range of actual landing distances are quoted for each aircraft, based upon its expected landing mass. The distances are determined from test flights, and a regulatory factor is applied to provide a safety margin, in case any braking systems fail to perform nominally. For JAA/FAA there are separate dry and wet conditions factors; 1.67 and 1.92 respectively. However, under CAA (UK) requirements, the wet factor (1.92) is used regardless.

Additional factors are used to account for variables & safety margins specific to each planned landing. A similar calculation is performed for each take-off, to determine the commit-to-fly speed (V_1), the pitch-rotation-speed (V_R), and safe-climb-speed (V_2), should an emergency occur. The V_1 speed takes the same factors into account to determine at which point the aircraft would run out of runway, if an aborted take-off was initiated given expected braking conditions.

Variables integrated into the calculations are listed following, with some of the relevant factors visualised in *Figure 2-10*. These are primarily from the viewpoint of turbine-powered airplanes with underwing-mounted engines, but can be adapted to aircraft fitted with turboprop, piston, or fuselage-mounted turbine engines. [26]

- High airport elevation which results in increased groundspeed on landing due to the wing's coefficient of lift (C_L) reducing with the ambient air density;
- Runway gradient;
- Runway surface conditions (concrete or tarmac, dry, wet or contaminated by standing water, slush, snow or ice);
- Wind conditions (head or tail-wind);
- Braking systems available (pedal brakes, autobrakes, thrust reversers, lift-dumping spoilers);
- Safety margin for anti-skid system failure;
- Standard operating procedure deviations (e.g. failure to arm spoilers on landing);
- Minimum equipment list/dispatch deviation guide conditions (where a braking system is known to be inoperable before the flight); and,
- System malfunctions (either resulting in reducing braking capability, or increased final approach speed).

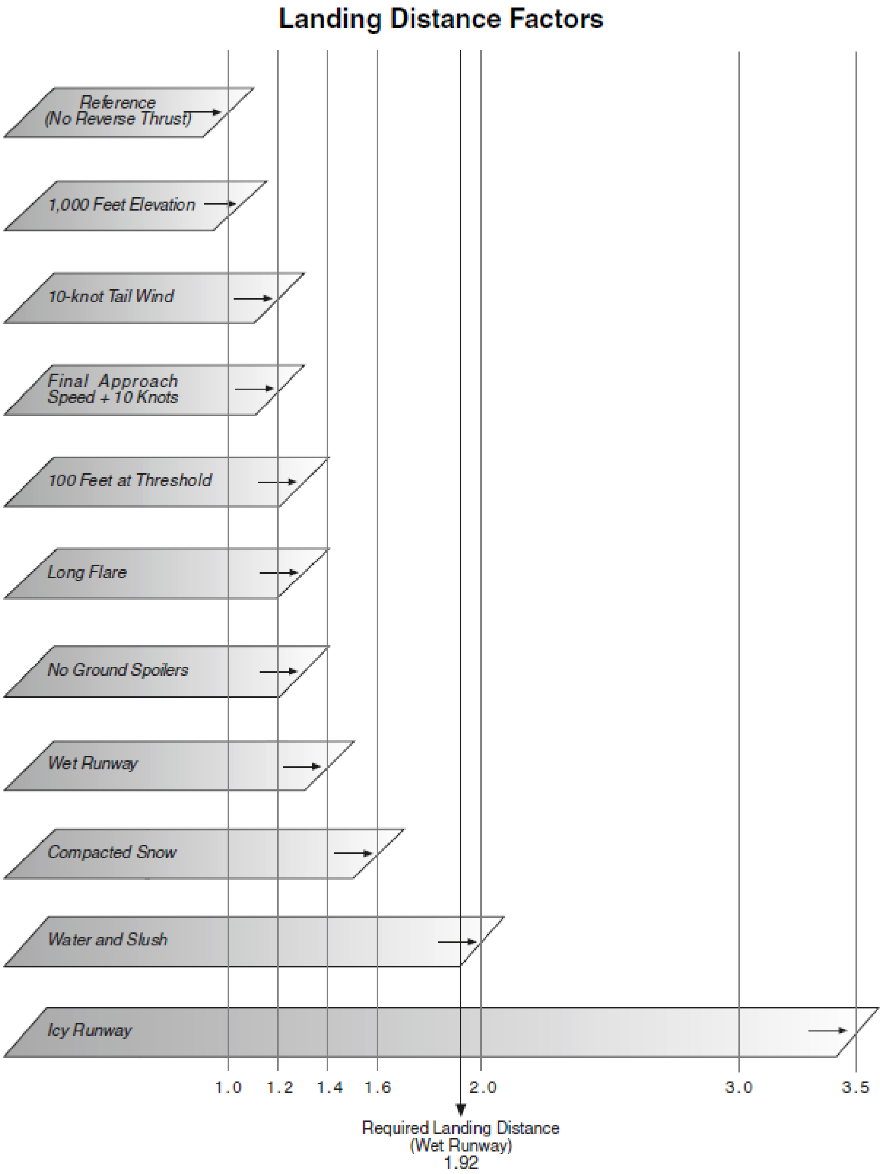

Figure 2-10: Factors affecting landing & their impact on required stopping distance [26]

Most of the factors remain below 1.6, which whilst increasing the runway distance required, is marginal compared with the impact of runway ice. The ALAR tool kit indicates that standing water/slush contaminated runways required a factor of about 2.0 – 2.3, and icy runways 3.5-4.5.

It can be concluded then, that the 4 most detrimental factors to landing distance required involve contamination of the runway, which primarily effects wheel brake performance only. When cross-referencing *Figures 2-8* & *2-10*, it becomes clear why there is a wide-spread demand for thrust reversers on civil aircraft, and that the requirement for such systems is unlikely to change in the foreseeable future.

It can also be determined that the availability of a thrust-reverser system, has a disproportionate impact on safety for flights operating to/from mid-latitude and polar climates. In fact, airlines consider thrust reverser systems essential to achieving the maximum level of operating safety & therefore capacity. [23]

2.3.2 Thrust Reverser Deployment

Thrust reversers are usually designed to operate when the aircraft is landing, immediately after touchdown. The typical landing speed for civil jet aircraft is between 120 and 145 knots. They are deployed by the pilot, first by closing the throttle levers to idle. Reverser levers are then moved backwards, which are also mounted to the throttle quadrant. However, the engine control unit (ECU) will only activate the system once a weight-on-wheels sensor is triggered, and no conflicting commands are detected (such as reverse thrust selected on engine #1, and above-idle power on engine #2). Additionally, the engine needs to have reached idle RPM before the system engages. Once the aircraft has decelerated to a speed between 80-60 knots, the reversers are stowed. This is primarily to avoid (FOD) ingestion, and is done manually by the pilot, by returning the reverser levers to their default position. The engine then remains at idle power, and aircraft deceleration continues via the wheel brakes down to a safe taxi speed. This method is the most efficient in terms of fuel consumption and brake wear. [23, 27]

2.3.3 Engine Performance

This section aims to provide an overview of the engine operation during reverse-thrust. The typical operating regime is shown in *Figure 2-11*, where it can be see that a surge region is present in the RPM range <55 knots airspeed. Whilst reversers are normally stowed before this speed, this imposes an operating limit whereby the N1 (low pressure shaft) speed would need to be reduced to maintain surge margin – reducing reverse thrust achievable. This is because as the aircraft slows down, the ability for the fan to ingest air is reduced. The surge-margin can also be narrowed if there is an exhaust outlet area mismatch when the reversers are deployed.

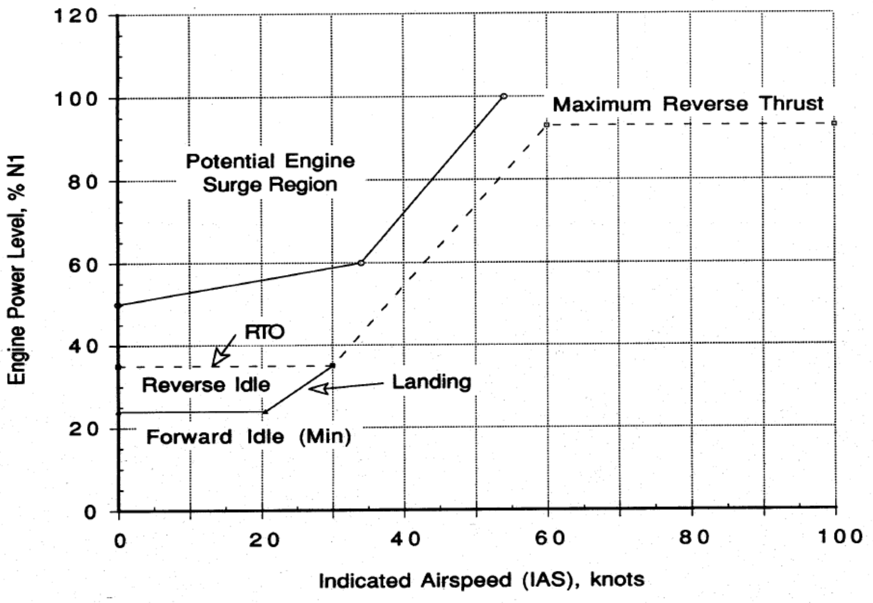

Figure 2-11: Influence of surge margin on N1 during reverse thrust [23]

Regarding the magnitude of reverse thrust from current systems, published data indicates narrow-body aircraft capabilities lie around 30-40% of nominal static forward thrust (*Table 2-1*).

Category	Aircraft	# of Operations	Percent of Max Rated Thrust (%)	Weighted Thrust Value	Weighted Thrust Average (%)
Narrowbody	A320	10,066	32.0	14	36.5
	B737-400	11,721	41.3	21	
	B767-200ER	1,270	28.0	1.5	

Table 2-1: Comparison between reverse thrust quoted for different aircraft [28]

Studies at Cranfield have been conducted into the engine operability during reverse-thrust operation, using a conventional multi-door system. Fan, IPC & HPC compressor maps from a 0D cycle performance code, modelling a Trent 722 (A330) 3-spool turbofan engine, are presented in *Figure 2-12* to *2-14*. The engine features variable inlet guide vanes (VIGVs) and variable stator vanes (VSVs) for the first 2 stages of the IPC.

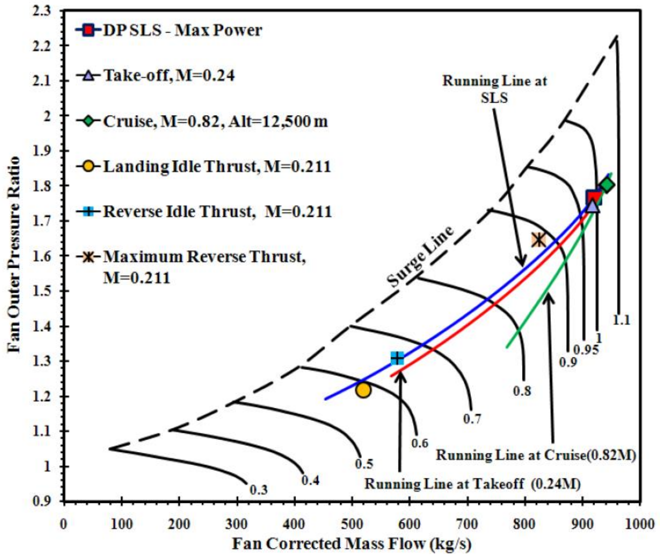

Figure 2-12: Fan working line comparison between forward & reverse operation [29]

It should be noted that during ‘reverse idle’ condition, the engine is at a higher power setting than at ‘landing idle’. This ensures that should the need arise; engine response is faster (e.g. the pilot needs to perform an emergency take-off at the start of the landing deceleration phase). For the fan, the deployment of the TRUs reduces slightly the surge margin, even when idle thrust is being produced, due to the change in fan exhaust outlet area. As reverse thrust increases, this becomes more apparent, but does not impinge on operability, and the margin is still acceptable. [29] The maximum reverse thrust was achieved at N1 speeds between 70% and 85%. No benefit was found in utilizing higher power, as no braking force was generated.

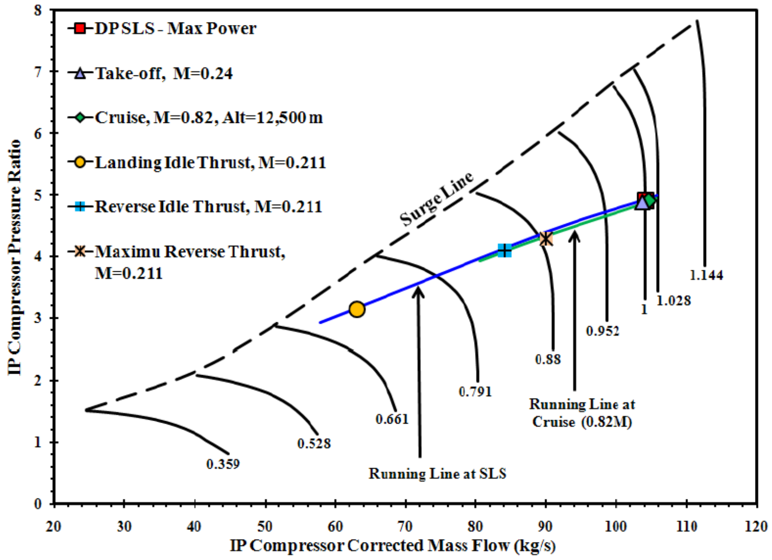

Figure 2-13: IPC working line comparison between forward & reverse operation [29]

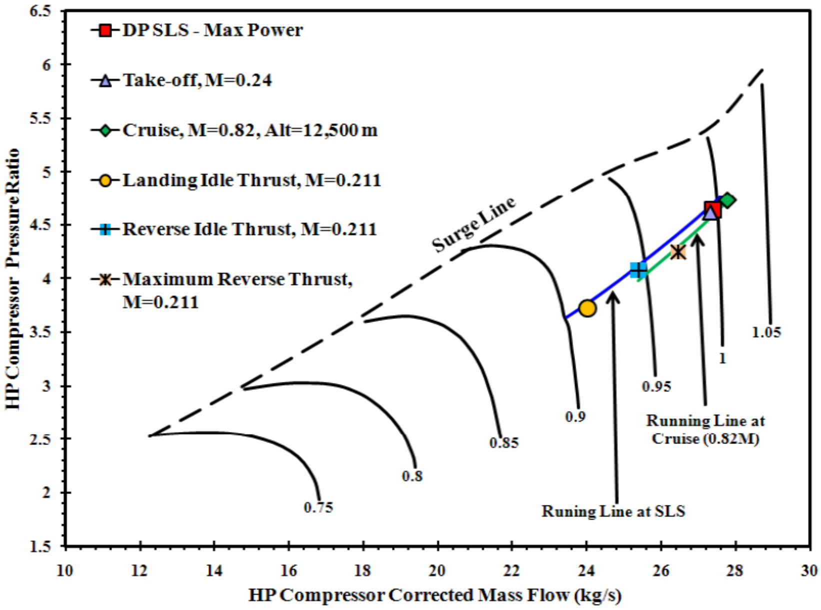

Figure 2-14: HPC working line comparison between forward & reverse operation [22]

Regarding the core compressor stages (IPC & HPC), it can be seen that the operating regimes under reverse thust are relatively unaffected. The IPC is more transient across the landing cycle, with N2 (intermediate pressure shaft) dropping to approxiamately 70% at landing idle. Upon thrust reverser deployment, the IPC accelerates faster than the fan, upto 85-90%, reducing the bypass ratio. The running line & surge margin remain unaffected. This is no-doubt due to the presence of the VIGVs and VSVs on the IPC, which allows the compressor's flow capacity to be varied in reponse to changes in fan operation (as the core inlet is located directly downstream of the fan).

The HPC has an inherently narrower speed range for normal operation compared with the other compressor stages, due to the different stage loading charactersitics associated with a much higher RPM.

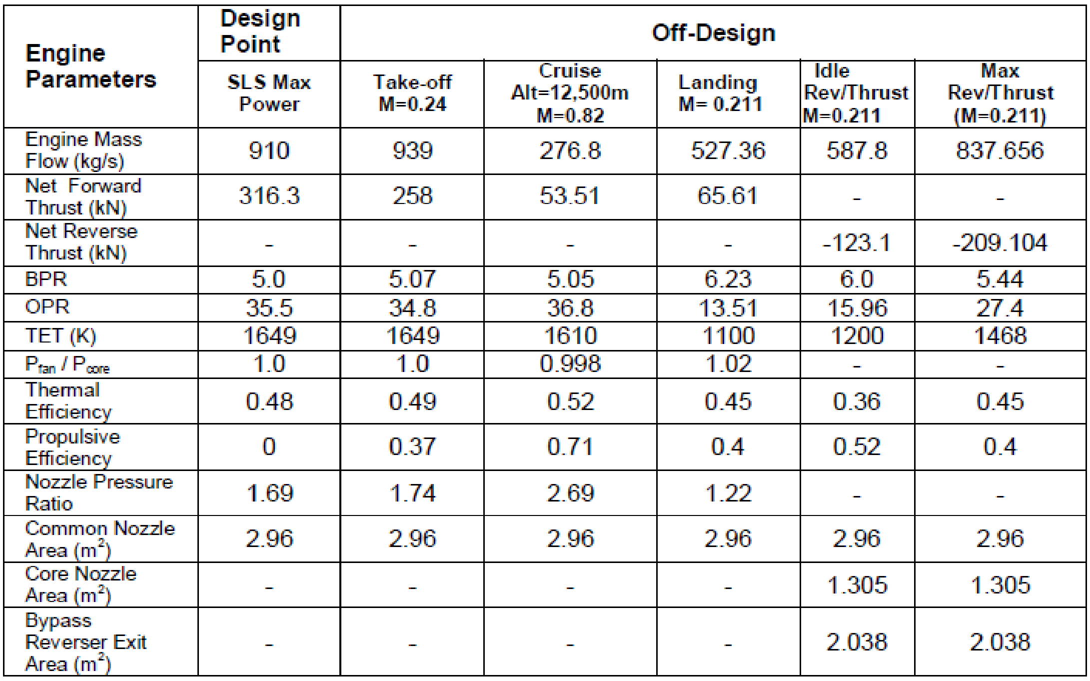

Engine Parameters	Design Point	Off-Design				
	SLS Max Power	Take-off M=0.24	Cruise Alt=12,500m M=0.82	Landing M= 0.211	Idle Rev/Thrust M=0.211	Max Rev/Thrust (M=0.211)
Engine Mass Flow (kg/s)	910	939	276.8	527.36	587.8	837.656
Net Forward Thrust (kN)	316.3	258	53.51	65.61	-	-
Net Reverse Thrust (kN)	-	-	-	-	-123.1	-209.104
BPR	5.0	5.07	5.05	6.23	6.0	5.44
OPR	35.5	34.8	36.8	13.51	15.96	27.4
TET (K)	1649	1649	1610	1100	1200	1468
P_{fan} / P_{core}	1.0	1.0	0.998	1.02	-	-
Thermal Efficiency	0.48	0.49	0.52	0.45	0.36	0.45
Propulsive Efficiency	0	0.37	0.71	0.4	0.52	0.4
Nozzle Pressure Ratio	1.69	1.74	2.69	1.22	-	-
Common Nozzle Area (m^2)	2.96	2.96	2.96	2.96	2.96	2.96
Core Nozzle Area (m^2)	-	-	-	-	1.305	1.305
Bypass Reverser Exit Area (m^2)	-	-	-	-	2.038	2.038

Table 2-2: Performance parameters for the Cranfield study engine [29]

The engine TET during maximum reverse thrust lies in the middle of the operating range, as can be seen in *Table 2-2*. When the core exhaust flow expands from the core nozzle area to the common nozzle, the forward thrust diminishes, caused by the lack of bypass flow in the relevant nozzle exhaust, and the associated pressure losses. This reduction in outlet pressure to the core, coupled with a max power N1 figure of 85%, explains why the TET is relatively low. The core becomes effectively more powerful, at the cost of a large increased momentum drag and nozzle pressure losses. For braking/reverse thrust use, this is exactly what is intended. However, the core nozzle pressure drop can also result in an increase in low pressure turbine (LPT) shaft speed as the PR across the stage increases. Therefore, a limit of 75-85% RPM during reverse operation is implemented via the control system. It should be noted that this is also present on a separate-exhaust type engine, as the momentum drag increase caused by diverting the bypass stream still exists.

Furthermore, thrust-reversers are most effective at high airspeed, due to the larger difference in velocity, ΔV, between the freestream and the reversed-jet. Using the equation for gross thrust (assuming a fully-expanded exhaust), and ignoring polarity, the forward (freestream) airspeed V_∞, is added to the reversed-jet forward velocity, V_{rj}, to calculate the gross thrust.

$$F_{rev} = W(V_{rj} + V_\infty) \tag{2-1}$$

The propulsive efficiency is calculated in the same manner, taking the opposing directions of the two streams into account, as shown in the formula below:

$$\eta_{prop,rev} = \frac{2}{1 + \frac{V_{rj} + V_\infty}{V_\infty}} \tag{2-2}$$

From the propulsive efficiency plot (*Figure 2-15*), it can be seen why the reverse-thrust achievable diminishes with airspeed. The change in velocity, ΔV, of the bypass flow during reversal is greatest when the aircraft is at highest forward velocity. As the airspeed and thus ΔV reduce, the reaction force diminishes linearly, according to the thrust equation.

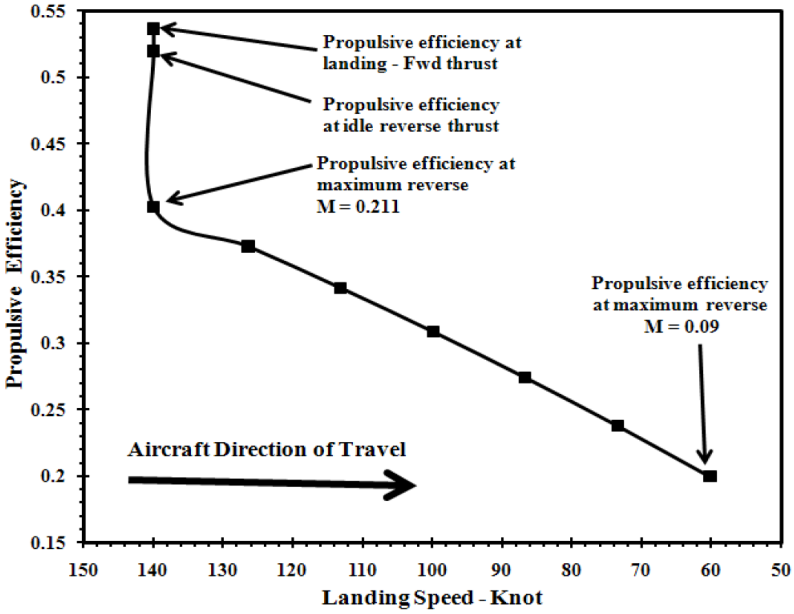

Figure 2-15: Effect on propulsive efficiency of reducing landing speed [27]

From the studies it can be concluded then, that from an engine-operability perspective, the core operates notably below design point. Performance is well within limits regarding TET, shaft speeds, surge margin, and pressure ratios. [27] [29] With a properly designed reverser system, this should be the case, as the fundamental operation of the fan & engine core remain the same. This is not the case, however, for the reversing VPF.

The standard metric for measuring reverser/airbrake effectiveness is to normalise it against the nominal forward thrust at SLS. This parameter can then be used to compare the effectiveness of different system architectures, regardless of thrust-class or units of measurement. The equation for thrust reverser effectiveness is provided below.

$$\eta_{rev} = \frac{F_{rev}}{F_{nom}} \tag{2-3}$$

For a turbofan with a bypass-only reverser, F_{rev} is calculated as the net figure when the core & bypass axial thrust components (F_{core} & F_{ax}) are added together. This accounts for the forward thrust still being produced by the core exhaust, whilst the bypass stream is being reversed. This is equated below, where F_{ax} is the axial force of the reversed flow.

$$F_{rev} = F_{core} + F_{ax} \tag{2-4}$$

2.4 Existing Thrust Reverser Designs

Current designs of thrust reversal systems will now be discussed, starting with those most relevant to the modern high bypass ratio turbofans. Additionally, some more novel concepts that haven't yet seen commercial success will also be mentioned.

2.4.1 Cascade Reversers

The cascade or type thrust reverser is the most commonly found TRU system today's large turbofan engines, and operates exclusively on the cold stream. This is sufficient for high bypass ratio engines, where the majority of the engine thrust is derived from the cold stream. [30] *Figure 2-16* below illustrates how the system operates.

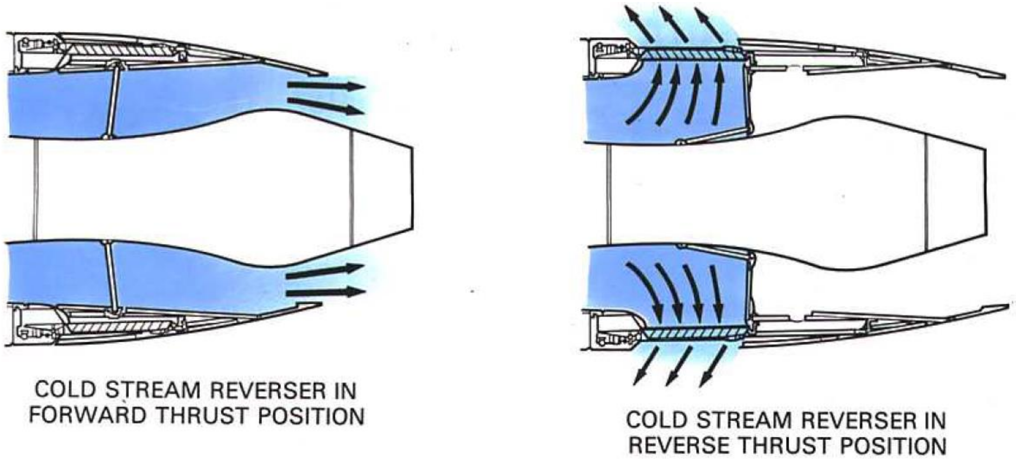

Figure 2-16: Cascade type reverser operation [30]

During forward thrust operation, the nacelle & bypass duct take on a conventional shape. When the thrust reversers are deployed, the aft-body of the nacelle is traversed rearward on screw-jacks, actuated by either hydraulic rams or air motors. Panels which normally form part of the bypass duct outer wall, are pivoted on the inner bypass duct casing, approximately 90˚, to block of the flow from entering the bypass nozzle. Instead, the flow is redirected out of the new openings exposed in the side of the nacelle. To maximise reverse-thrust, ideally the flow should be ejected completely in the forward direction. It is not possible to achieve this, mainly for aerodynamic reasons, and therefore a discharge angle of approximately 45˚ is used, implemented by louvres/vanes in the openings.

Additionally, the expelled flow adds to the disturbance caused by the aircraft as it passes through the air, increasing aerodynamic drag. Therefore, the system has both first and second order effects on the overall braking performance.

2.4.2 Multi-Door Reversers

Another type of reverser currently in service on large-turbofans, is the multi-door type. They currently feature on both CFM56-5 Series engines (powering the Airbus A320 & A330), and the Trent 700 (A340). [20] Their operation is similar to the cascade system, operating exclusively on the cold bypass stream flow. The design carries additional complexities, such as the need for multiple actuators; one for each door. Additionally, the deployment angle and position of the doors may be restricted by factors such as ground clearance beneath the engine. An illustration of the design architecture with an image of the CFM56-5 reversers in use is featured in *Figures 2-17 & 2-18*.

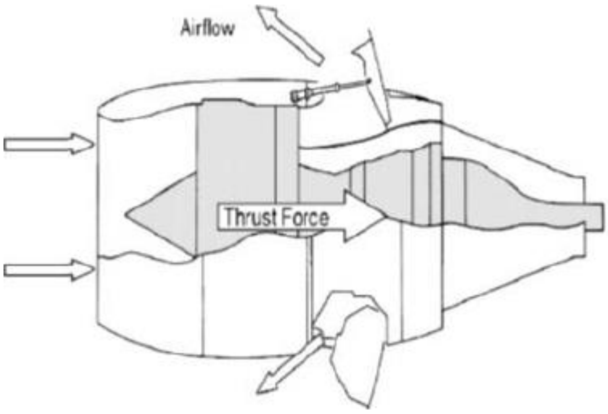

Figure 2-17: Multi-door type thrust reverse schematic [31]

Figure 2-18: CFM-56-5 turbofan with deployed reversers [32]

The similarities to cascade reversers is obvious. The main differences are that instead of dislocating the nacelle aft-body, it remains in place. Instead, multiple doors located around the nacelle mid-aft-body annulus perform the same task as the panels in the cascade; blocking & redirecting the cold stream. The size of these doors needs to be sufficiently block off the bypass nozzle when actuated, even though the system is not fully annular. The deployment angle of the doors varies with engine, but for the CFM56-5B is quoted as approximately 120˚. [27]

2.4.3 Bucket Type

The third reverser system in wide use today is the bucket or target type. The design uses two bucket-shaped doors which block and redirect the exhaust flow forward. The doors are actuated by a single hydraulic ram, connected via two conventional pushrods (one for each door), illustrated in *Figure 2-19*. The single actuator guarantees door synchronisation, which isn't necessarily the case with alternative designs (such as the multi-door). Under conventional operation, the doors form the nacelle aft-body/nozzle outer-wall. [30] *Figure 2-20* shows the deployed bucket reversers on a Fokker 70 regional jet.

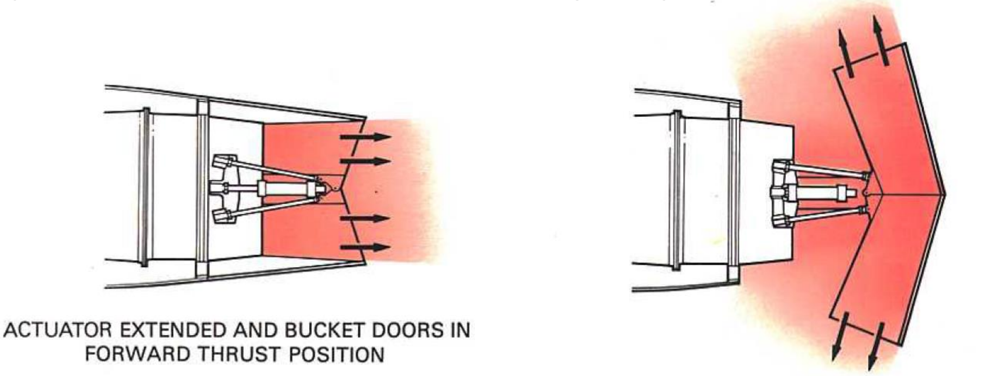

ACTUATOR EXTENDED AND BUCKET DOORS IN FORWARD THRUST POSITION

ACTUATOR AND BUCKET DOORS IN REVERSE THRUST POSITION

Figure 2-19: Bucket type reverser operation [30]

The size of the bucket panels increases exponentially with nozzle diameter. As such, their application has been limited to physically smaller engines, such as those used on regional or business jets, and some military fighters.

Figure 2-20: Bucket reversers deployed on a Fokker 70 [33]

Because of the nature of the systems architecture, it is only really suited to low BPR mixed-exhaust turbofans, or pure-turbojets. A form of the system could in theory be developed for separate-exhaust turbofans, working either on the core nozzle, bypass nozzle, or both. However, this has not been necessary, due to the success of the cascade and multi-door architectures. Another point of interest is that the system's working fluid is composed at least partially of the high temperature core exhaust gases. The thermal cycle mode induced on the buckets & pushrods reduces their mechanical life, and adds additional thermal resistance requirements to the component material, not present on cold-stream systems. The result is an increase in the maintenance and production costs, which mitigates some of the benefits of the design's relatively simple nature.

2.4.4 Clamshell Type

The Clamshell door system contains features of the previous three systems. On selection of reverse thrust, the doors rotate via pneumatic rams to uncover the exhaust ducts, and close the normal gas stream exit. Cascade vanes in the new openings then redirect the flow stream in the forward direction, producing reverse thrust. In terms of operation principle & application suitability, the clamshell reverser is very similar to the bucket type, working with low BPR mixed turbofans. As such, the doors & actuation mechanisms likewise need to be suitable for operating in the hot gas stream.

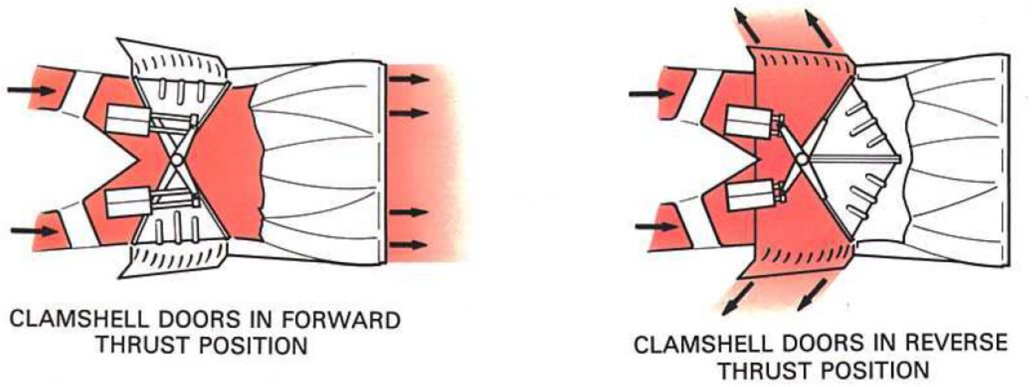

CLAMSHELL DOORS IN FORWARD THRUST POSITION

CLAMSHELL DOORS IN REVERSE THRUST POSITION

Figure 2-21: Clamshell type reverser operation [30]

The system architecture can be seen in *Figure 2-21*. Note that, unlike the bucket type, the flow redirection occurs internally and the exit angle is determined by the vanes rather than the doors.

2.4.5 Turboprop Reversers

Propeller driven aircraft can also achieve reverse thrust by changing the pitch of the propeller blades through a hydro-mechanical pitch control system. When reverse thrust is selected, the blade angle is reduced to zero, then a negative (reverse) pitch. This is very similar to how a VPF reverse system would operate; discussed in *Ch 2.7.3*. However, turboprops have a radically different architecture from high BPR turbofans, such as lack of a nacelle, simple round core intakes (rather than ring-shaped ones), and very low PR, low solidity propellors. As such, the existing knowledge surrounding turboprop reverse-thrust operation does not suffice to satisfy the concerns outlined in the project Aims & Objectives.

2.5 Alternative Reverser Concepts

Whilst searching the public domain for current TRU designs, the author has discovered several novel alternatives, some of which are still being research. A summary of these is provided across the following sub-chapters.

2.5.1 NASA/ATA Engine Air-Brake (EAB)

In 2016, NASA published a report into the performance of a new engine braking concept. The Engine Air-Brake (EAB) (*Figure 2-22*) is a deployable swirl vane mechanism for a turbofan exhaust. The EAB generates a swirling outflow from the exhaust nozzle when deployed, producing significant drag behind the engine during approach and/or descent phases of flight. As can be seen in the streamline visual in *Figure 2-23*, the core stream remains relatively unaffected, without swirl. When stowed, the movable vanes close,to form a conventional convergent nozzle. The vanes are controlled by an actuator ring, similar in fashion to those used on VIGVs & VSVs.


(b) EAB stowed (a) EAB fully deployed

Figure 2-22: NASA's Engine Air Brake (EAB) Demonstrator [34]

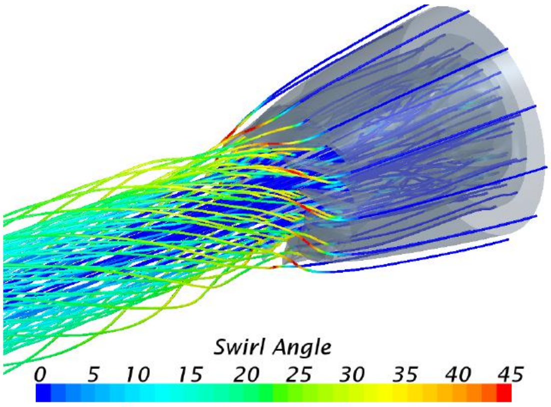

(b) Streamlines colored by swirl angle

Figure 2-23: Exhaust streamlines through NASA's EAB whilst deployed [34]

It has achieved NASA's Technology Readiness Level 6; i.e. fully functional prototype, and has been demonstrated on a medium BPR business jet turbofan (Williams FJ44-4A). CFD simulations have also been conducted. The purpose of the device is for small civil jets, allowing steeper approaches for noise & obstruction restricted airports, such as London City (LCY).

In terms of engine performance, NASA concluded that the system did not compromise on operability during either stowed, transient or deployed operations. The thrust reverser effectiveness was in the order of 15%. When the swirl vanes are opened, the nozzle area increases by approxiamtely 3%, reducing the FPR and increasing the flow beyond stowed conditions. [34]

To conclude, the system looks promising for its application. The flow regime is less intrisically problematic than conventional reversers; as the flow is not reversed, so recirculation into the intake should not be a concern. However, whether there is a requirements such a system at the larger end of the turbofan market is unclear. Current systems perform adequately, and given the limited braking force obtainable by the device, it is likely to remain a niche application.

2.5.2 NASA's 6 Innovative Reverse Thrust Concepts

In 1998/2000, NASA published results from an investigation into the static aerodynamic performance of 6 novel thrust reverse concepts in partnership with several aerospace companies, including Boeing, General Electric, Pratt & Whitney & Rolls-Royce. [24, 35] The study was conducted on a 7.9% scale test rig of a turbofan exhaust system of BPR ~9, mounted via a scaled pylon and wing. The overall target of the research was to establish the performance metrics for these alternative designs offer, which offer reductions in nacelle weight, drag, cost and maintenance access, by utilising a simpler system. These new designs could be of great value to future engine manufacturers, especially if the trend in engine fan diameters continues to increase. It is important to note, that these tests were conducted under static conditions, and as such, the aerodynamic drag added by the systems is not measured. Additionally, the study used fixed geometries, and didn't incorporate development of the mechanisms which would be required to operate such systems.

The concepts are outlined in Figure 2-24, and summarised following.

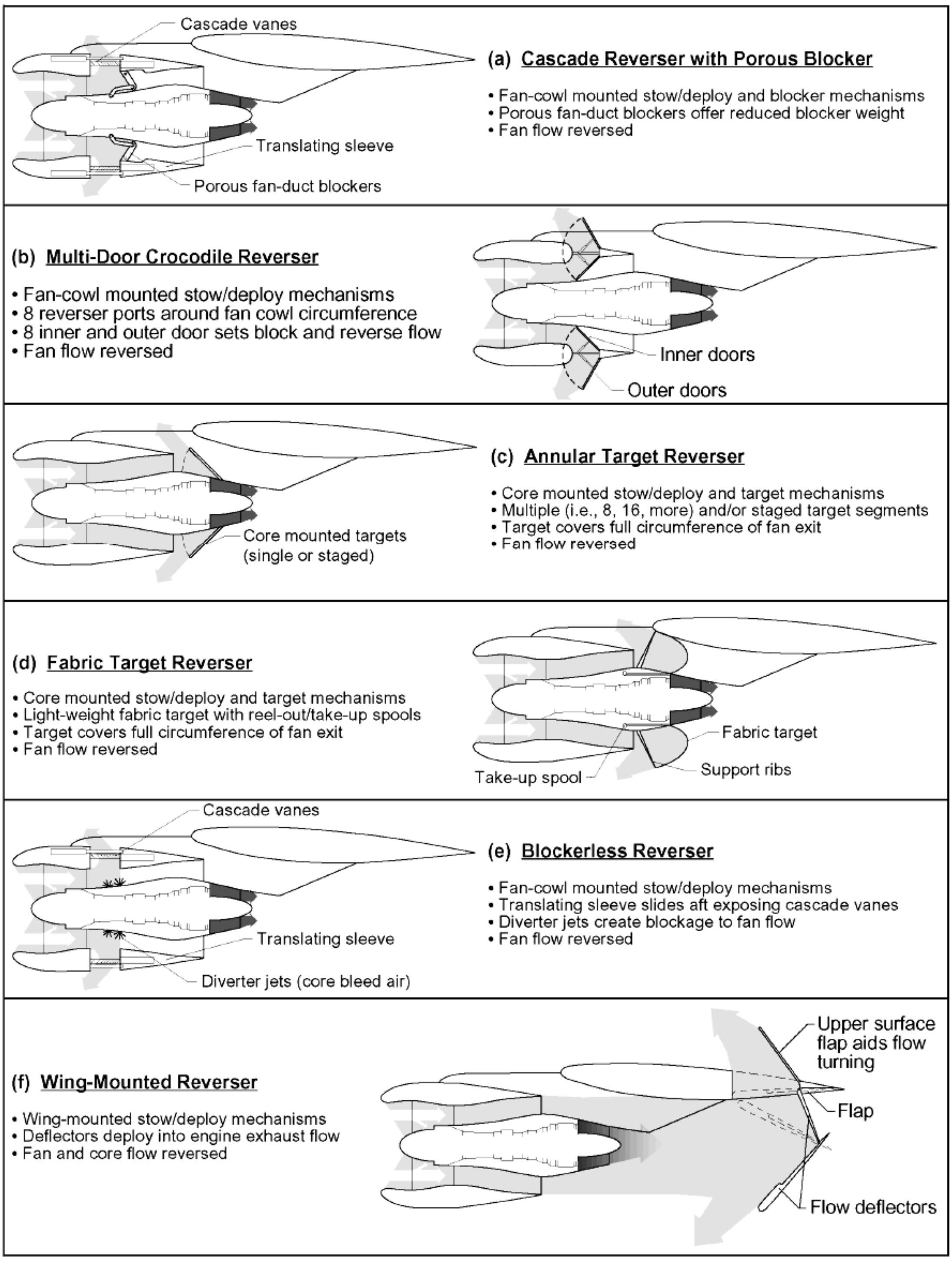

Figure 2-24: NASA's 6 innovative thrust reverser concepts [24]

Concept (a) offers reduced TRU weight by tolerating a degree of porosity in the blocker doors, primarily as a retrofit or improvement on the conventional cascade type reverse. To conclude, the system offers marginal weight savings to existing systems, but beyond 12-25% porosity, the loss in effectiveness due to the flow leakage through the pores, makes the system increasingly impractical.

Concept (b); a variation on the common multi-door reverser, offers a potentially simpler actuation system, and reduced manufacturing costs versus the cascade type. The outer door deployment angle was also an effective way to control the bypass flow exist area during reversal. Overall, the system delivered a consistent nominal effectiveness of approximately 0.2 across the tested configurations.

The type target-type thrust-reversers (c & d), achieved the worst performance metrics out of the 6 tested designs, achieving up to only 10% reverse thrust. This was found to be an inherent problem with the designs, where the target doors tend to block the bypass flow exit area, rather than redirecting the flow direction. Additionally, the location and size of the target buckets, and their actuators, is restricted by the nacelle and engine-aft body architecture.

The blockerless thrust reverser concept (e), eliminates blocker doors from the conventional cascade system, and uses jets powered by high pressure core bleed to block the bypass duct. It offers a significant weight reduction, whilst allowing more freedom in nacelle design, and potentially a simpler sealing when stowed. Multiple configurations of different bleed-air-injector positions were tested. The performance metrics varied greatly between the different nozzle arrangements, but the nominal performance was comparable with cascade reversers. The system is particularly suitable for low FPR turbofans, as it was found the effectiveness of the bleed air to redirect the bypass flow depends on the momentum ratio between the two streams. However, the system is also heavily dependent on injector weighted-flow, which essentially is underpinned by the BPR. Therefore, there is a practical limit to the concept which may make it unfeasible for UHBR engines.

The final and most radical of the tested concepts was the wing-mounted thrust reverser, (f). By relocating the TRU hardware to the wing, both cold and hot exhaust streams can be redirected, regardless of nozzle design & BPR. When deployed, these deflectors can create openings in the wing, dumping any additional lift the system may generate by retaining high pressure fluid underneath the wing's lifting surface. The practicality of the design is uncertain, and there maybe unquantified structural or thermal complications, which make reversers of this nature unfeasible. Nevertheless, the tests indicated thrust reverser effectiveness of 0.3 – 0.4 was easily achievable, and values up to 0.58 were possible under certain configurations – a significant improvement over conventional cascade/multi-door architectures.

To conclude, 4 of the concepts showed promise, with the two target-type reversers deemed uncompetitive. The wing-mounted reverser concept proved capable of exceeding by a notable degree the current performance of TRU types. However, the study was published nearly two decades ago, and none of these designs have yet manifested in a production engine.

2.5.3 SNECMA Hot-Stream Deflector Patent

In 2008 SNECMA filed US patents for a new thrust reversal concept, which uses redirected core flow to deflect the bypass stream, alike to NASA's blockerless reverser concept (e). The patent drawings below demonstrate how the system is intended to work aerodynamically. Two versions were described. [36]

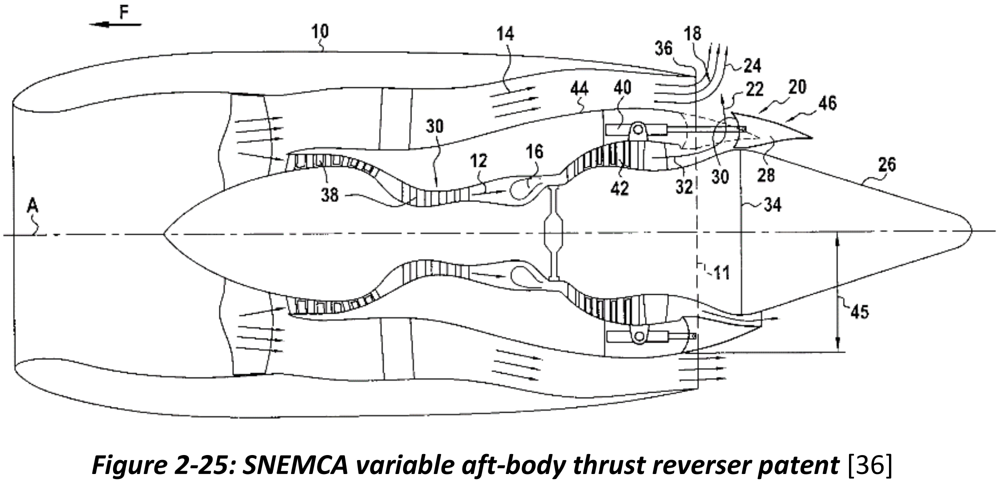

Figure 2-25: SNEMCA variable aft-body thrust reverser patent [36]

The first (*Figure 2-25*) operates using a variable geometry aft-body, which can shut off the core nozzle, and redirect the flow to eject radially behind the bypass nozzle plane. The high-pressure core exhaust would exchange kinetic energy by accelerating the bypass radially, significantly increasing momentum drag.

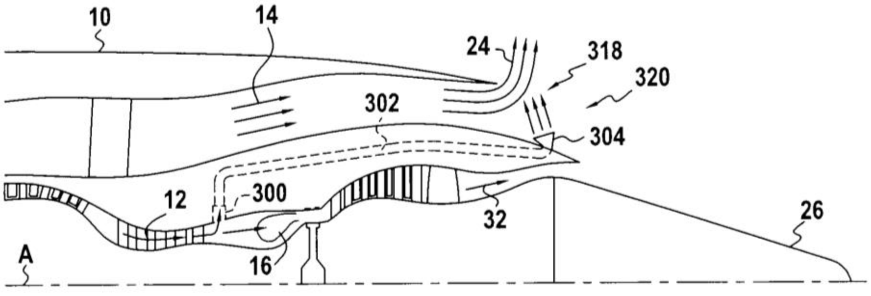

Figure 2-26: SNECMA bleed deflector jet thrust reverser patent [36]

The second design (*Figure 2-26*), is slightly less controversial and does not require variable geometry. Instead it takes bleed air from downstream of the HPC final stage, and ejects it radially at the same location as the variable aft-body design. Such a thrust reverser would be simple in design, inexpensive, and makes it possible to avoid having moving parts present on the outside portion of the nacelle. This would reduce weight and drag penalties associated with the nacelle and conventional TRUs, but the effectiveness, ease of design, and core operability are unclear. Unlike the NASA proposed blockerless reverser, this design does not feature cascade vanes.

2.6 Variable-Pitch Fans

As mentioned in *Chapter 2.2*, when using FPR values below 1.45, fan instability and surge issues begin to intrude on the normal operating region of the fan performance map. When inlet momentum is low (and thus ram compression), the bypass nozzle's flow capacity drops, pushing the operating point towards the stall/surge line. The variable-pitch fan concept offers a way round these problems, by being able to modulate the fan's operating characteristics, by changing the stagger angle of the blades. Extensive research has been published on the potential operability and fuel-burn gains by utilising VPFs. [7, 37, 38, 39, 40] The following sub-chapters provide the reader with an explanation of some of the fundamental characteristics which have been identified.

2.6.1 Fan Stability/Operability

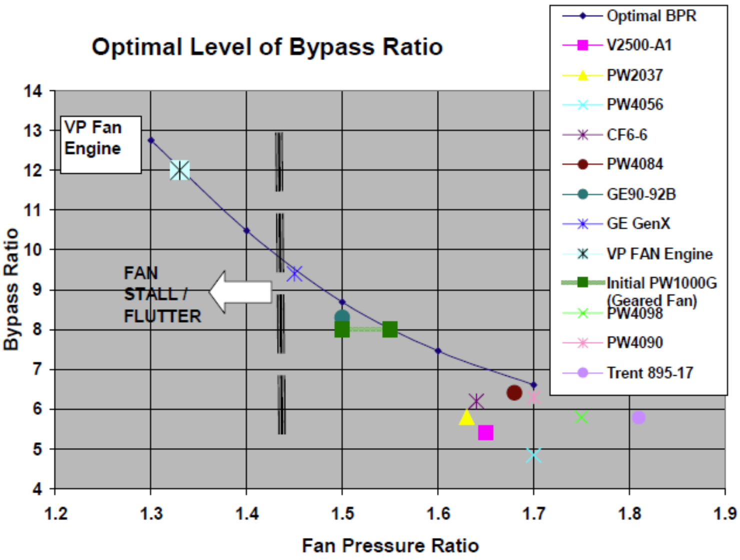

Figure 2-27: Optimum FPR versus BPR trend [39]

By altering the blade stagger, the fan's flow capacity is changed, and variations in flow rate can be better accommodated. This added degree of flexibility provides an effective way of enabling very low PR fans to avoid encountering aerodynamic stall/surge. *Figure 2-27* indicates that fixed pitch turbofans are limited to FPRs greater than 1.45. The change in fan compressor map characteristics associated with pitch change during forward flight can be seen in *Figure 2.28*.

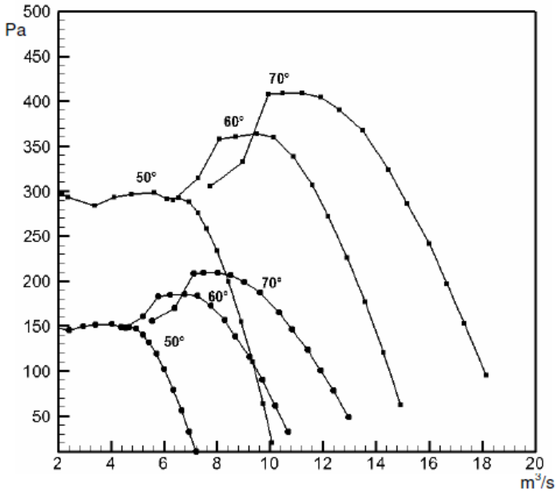

Figure 2-28: Variable-pitch fan performance at 3 pitch angle settings & 2 fan speeds [41]

From the perspective of the blade velocities, a flow reduction manifests in the form of a drop in axial velocity, Va. This drop in Va increases the incidence angle, i, on the blade inlet, eventually leading to flow separation on the suction-surface. The VPF mechanism allows the blade stagger (and thus blade inlet angle) to react to this change of incidence. As a result, this moves the speed lines across the fan performance map (*see Figure 2-28*), and can be used to maintain a suitable stall/surge margin, by changing the stage flow capacity.

2.6.2 Performance Improvements

When the flow capacity is not of concern, the VPF can use its pitch-adjusting mechanism to augment the thrust, without necessarily needing to change fan RPM. This operating regime is already utilized on most turboprop and turboshaft engines, where a variable-pitch mechanism is used to control the thrust/lift/power generation, and a constant RPM is maintained by varying the fuel/torque. As such, a VPF-fitted turbofan is capable of generating up to 20% more thrust at sea-level static (SLS), versus a fixed-pitch equivalent. [39, 42] It also brings potential benefits of reduced reaction time for changes in engine power, and the ability to run the engine closer to its optimum speed throughout a larger proportion of its operating regime. If the engine design is properly optimised with this new performance variable considered, a reduction in SFC may also be achieved. Its estimated this could be in the order of a 10-18% fuel saving over current fixed-pitch turbofans. [39, 42]

Finally, if the variable-pitch fan in question is capable of changing pitch to the extent that flow reversal is possible, it may be a suitable replacement for conventional TRUs. [43] This would eliminate many of the performance losses that are associated with TRUs, and allow the use of very short or ‘slimline’ nacelles (*Figure 2-29*).

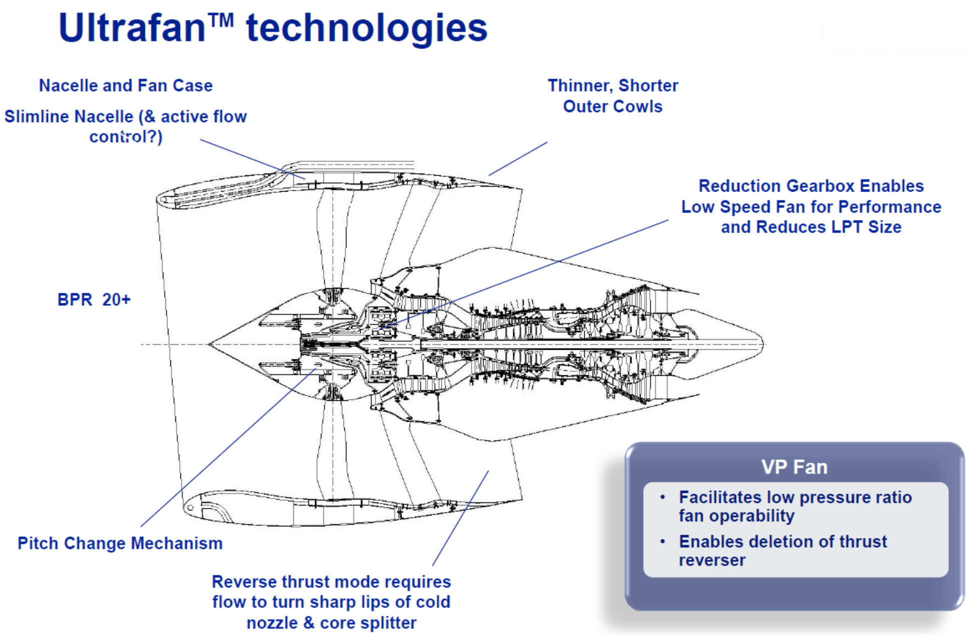

Figure 2-29: Rolls-Royce RB282/UltraFan™ engine concept with slimline nacelle [5]

2.6.3 VPF Engines

Variable-pitch fan fitted engines have remained a novel concept for turbofan applications, although several demonstrators and prototype engines have been documented in the public domain. A brief summary of each is presented following.

2.6.3.1 NASA’s Advanced Ducted Propulsor (ADP)

In the 1990 a joint venture was started between NASA and Pratt & Whitney to assess the current feasibility of a geared high-bypass variable-pitch turbofan. A series of scaled-down test rig engines, as-well as a full-sized (2.5 m fan diameter) demonstrator were assembled, shown in *Figure 2-30*. The testing took into consideration mechanical/structural, aero-mechanical, acoustic, and aerodynamic elements, with focus on the fan itself. The ADP’s design philosophy included the requirement to produce reverse thrust, which was achieved via the ‘through-feather’ method (*ref. Ch 2.7.3*). ADP cruise BPR ranged from approximately 13-15 depending on variant, with a FPR of approximately 1.3. [44, 45]

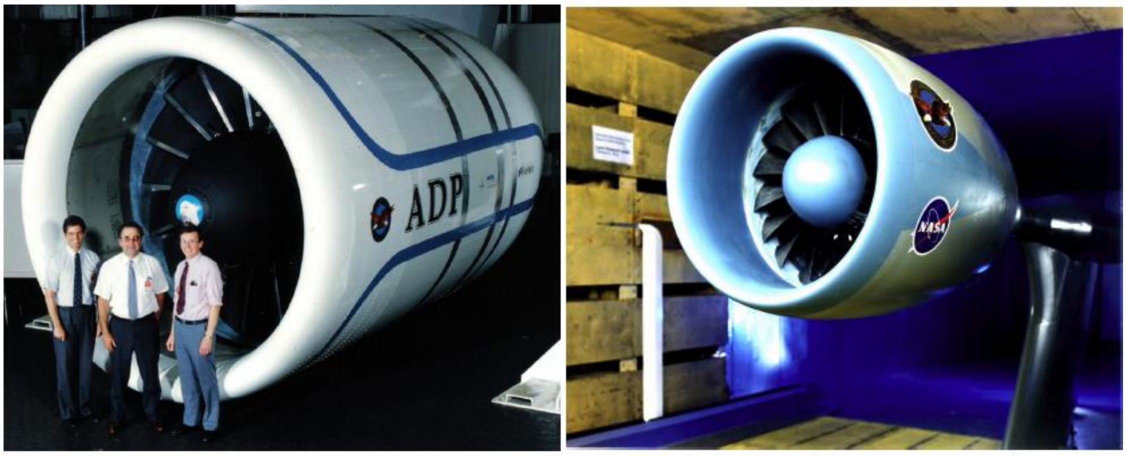

Figure 2-30: Left: ADP 118” demonstrator, *[35]* ***Right: ADP 22” wind-tunnel test-rig*** [45]

Overall, the design was deemed quiet and efficient, but the engine design too long & heavy, rendering it uncompetitive. Studies on the ADP designs have continued well into the 2010s, including CFD analysis and validation. [45, 46, 47] As such, this is the most modern and well documented VPF design currently in the public domain. Reverse-thrust was tested on at least one of the small-scale rigs, [47] however the performance data relating to the fan and engine has not been found – and assumed to be held confidential by Pratt & Whitney.

2.6.3.2 NASA’s Quiet, Clean Short-haul Experimental Engine (QCSEE)

The NASA QCSEE project studied the design, manufacturing and testing of two experimental gear-driven turbofans, intended for public transport aircraft. The first engine featured a fixed-pitch fan, mounted ‘over-the-wing’ (OTW), whilst the second featured a variable-pitch fan engine, mounted ‘under-the-wing’ (UTW). [48] This VPF engine was designed to test reverse-thrust operation, using both blade reversing techniques; through-feather & through-flat pitch (*ref. Ch 2.7.3*). A schematic of the UTW engine is shown in *Figure 2-31*.

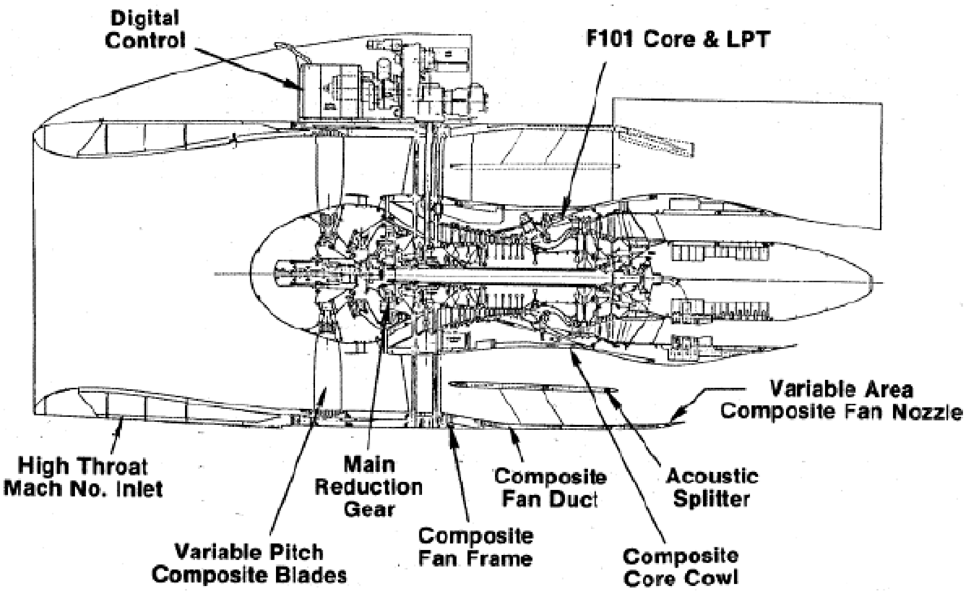

Figure 2-31: Schematic of the QCSEE UTW turbofan engine featuring VPF [40]

The QCSEE study provides the only comprehensive experimental data for engine transient & reverse-thrust performance. However, the engine was predominately tested at static conditions, with one report mentioning effects at up to 60 knots airspeed on a test bed. [11]

2.6.3.3 IAE SuperFan

In the 1980s International Aero Engines (IAE) (initially a consortium comprised of Rolls-Royce, Pratt & Whitney, Japanese Aero Engine Corporation & MTU) proposed a new engine known as the SuperFan, to power the in-development Airbus A340. Rated at 27,500 lbf (122 kN), the engine featured a V2500 based core, with a Rolls-Royce Tyne derived gearbox & variable-pitch fan. It was hoped that the engine would dominate its category by providing up to 15% reduction in SFC against the competition. [49] It is also believed the engine was intended to utilise a slimline nacelle, and generate reverse thrust using the VPF. However, the SuperFan project was abandoned before any demonstrator was ever built due to the risk, funding and time constraints associated with its design. [50]

2.6.3.4 Rolls-Royce/SNECMA RB410/M45S

In the early 1970s Rolls-Royce & SNECMA began jointly exploring the use of geared variable-pitch fans for low-thrust class turbofan applications. A demonstrator was planned, which would feature an M45H derived core, with 1 additional turbine stage, a BPR of ~9, and thrust rating of 10,000 lbf (44 kN). [51] The engine architecture is illustrated in *Figure 2-32*.

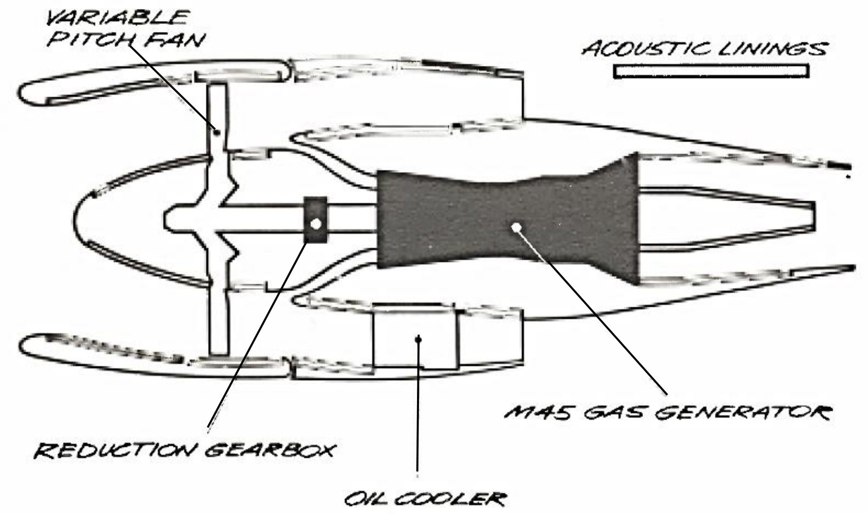

Figure 2-32: M45H engine arrangement [52]

The engine would have been capable of VPF reverse-thrust, potentially using auxiliary inlet systems; mentioned later in this chapter. The pitch-actuation mechanism would be of the gear-driven type. [52] Unfortunately, the engine never made it into production.

2.6.3.5 Kutzenov NK-93

In 1986 the Russian aero-engine manufacturer began development of a very high BPR variable-pitch ducted-fan engine. The architecture was derived largely from the company's previous experimental propfan engines. Static engine tests began in 1991, and reports of the first flight tests onboard an Ilyushin 76LL aircraft were published in 2007. The fan is a two-stage configuration, gear-driven, with a BPR of 16.6 and fan diameter of 2.9 m (114"). The core is of three-spool architecture, with a cruise OPR of about 37. [53] A cross-sectional drawing of the engine is provided in *Figure 2-33*.

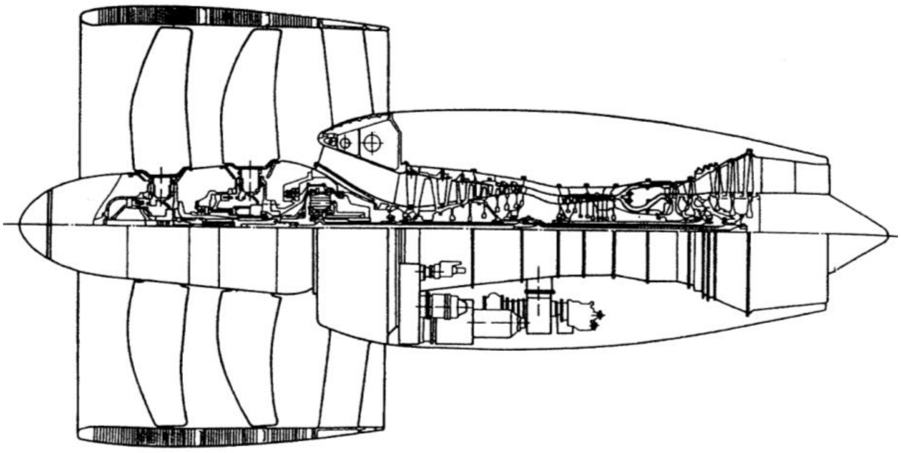

Figure 2-33: Kutzenov NK-93 engine annular arrangement [53]

Static thrust tests have demonstrated thrust achievable exceeds 45,000 lbf (200 kN) in forward, and under reverse, 31,000 lbf (138 kN). [53] It is unsubstantiated, but the very high reverse thrust achieved (69% effectiveness) maybe due in-part to the two-stage fan and ultra-short nacelle configuration. There is no indication at this moment in time of when or if the engine will enter service.

2.6.3.6 Turbomeca Astafan

The Astafan (*Figure 2-34*) was a geared variable-pitch turbofan demonstrator, derived in the early 1970s by French engine-manufacturer Turbomeca, from their existing Astazou turboshaft engine. The engine was flight tested aboard a Turbo Commander 680T in 1971, and the final variant achieved a thrust rating of ~2,500 lbf (11 kN) – aimed for use on light regional aircraft operating in short take-off and landing (STOL) contexts. [54]

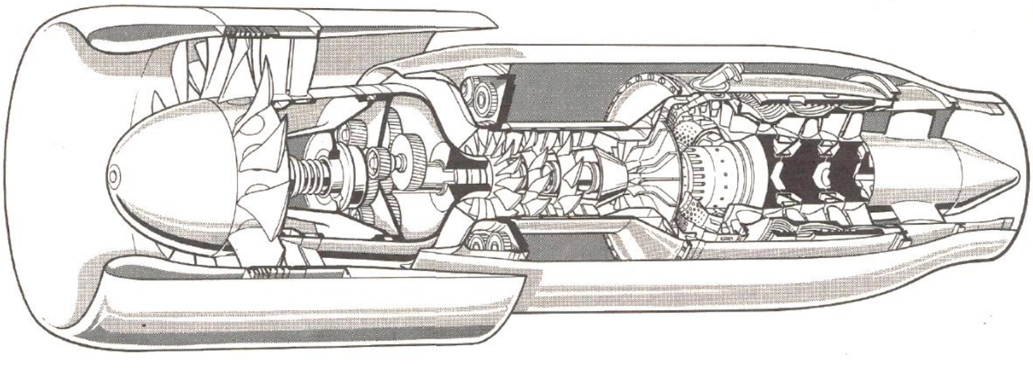

Figure 2-34: Cutaway of Turbomeca's Astafan engine [54]

It featured a single shaft with reduction gearbox to the fan, operating with a cruise OPR of approximately 10. The engine was designed for constant speed operation, (much like its Astazou counterpart), and augmented thrust by varying the fan blade pitch angle. Whilst the design proved promising, the engine never went into production.

2.7 VPF Reverse Thrust Performance

Whilst bringing potential benefits in the form of improved operability and efficiency to the turbofan, the VPF concept also offers a novel solution to generating reverse thrust. By utilizing the existing variable-pitch mechanism, it may be possible to rotate the fan blades to such a degree that the flow direction reverses. Instead of acting to propel the aircraft forward, the force from the bypass stream would now be acting to decelerate the aircraft in the same manner as a conventional TRU. However, the mode of operation of a VPF reversing engine compared to a normal reverser system is very different. The reported reverse-thrust flow regime for a VPF engine, taken from one of NASA's QCSEE publications, is shown below (*Figure 2.35*).

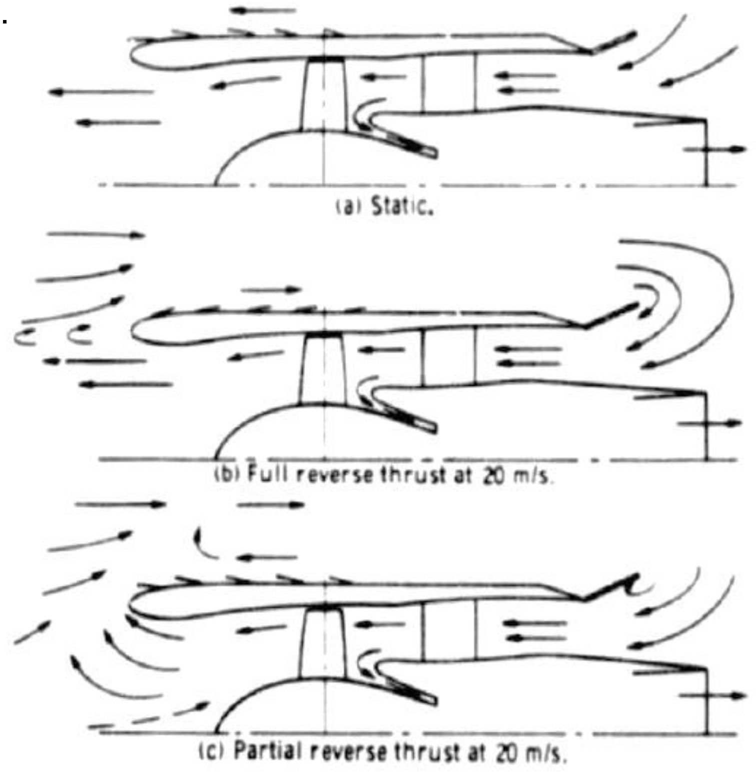

Figure 2-35: QCSEE VPF reverse-thrust bypass stream flow variation with airspeed [11]

The report indicates two fundamental operating modes were found to exist during VPF reverse-thrust testing, using a 55-inch (1.4 m) diameter fan engine rig. During static and low airspeed conditions, when the inlet momentum is low, the fan reverses the flow effectively out of the nacelle intake. As the airspeed increases, the dynamic head becomes too great for the lowest PR section of the fan (the hub) to overcome. Therefore, some flow does begin to enter through the conventional inlet, although the fan is still producing effective reverse thrust. [11] The partial reverse mode could be favourable from an engine operability perspective, as it may allow easier ingestion of flow into the core engine inlet duct, as the fan hub region is blocked. Whilst not documented in literature, it would seem apparent that, should airspeed rise to a point where the dynamic head is too great for the fan to overcome, even towards the blade tip flow reversal would cease. This becomes even more problematic when dealing with a very low PR fan design.

2.7.1 Bypass Nozzle ‘Inlet’ Performance

Additionally, the fan’s ability to overcome the dynamic head is determined not just by its ability to generate a pressure rise, but also by the pressure of its inlet flow. Reversal of the bypass stream means that bypass nozzle and nacelle inlet have exchanged roles. This can be detrimental, as the nozzle area is significantly less than the inlet throat. The result is that the fan will be throttled from upstream, and the unfavourable geometry of the bypass nozzle for reverse flow (namely the sharp trailing edge lip of the nacelle), induces a total pressure loss. This total pressure loss limits the fan’s ability to generate a higher delivery total pressure than the dynamic head pushing against it. This restricts the magnitude and operating range of reverse thrust that the fan can deliver. As a result, most historic studies conducted into VPF thrust reversal have featured ‘exlets’.[55, 56, 57, 58]

These are essentially variable geometry nozzles, which open the bypass nozzle throat by flaring the rear-nacelle assembly (*Figure 2-36*). When stowed the exlet doors align with the nacelle, to form a conventional nozzle shape.

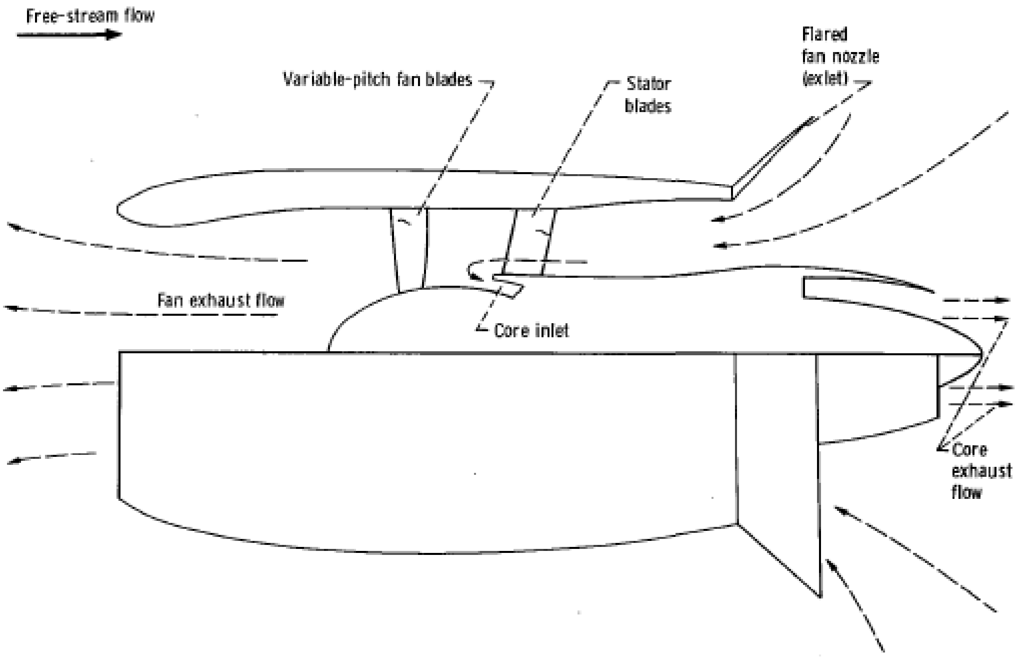

Figure 2-36: Bypass nozzle 'exlets' as tested on the UTW QCSEE engine [59]

An experimental comparison between different exlet configurations was compiled and reported by NASA. [59] A summary of the findings with regards to total pressure recovery (a commonly used inlet performance metric), is provided in *Figure 2-37*. The formula for total pressure recovery, is provided in Equation 2-6.

$$P_{recovery} = \frac{P_{inlet}}{P_{\infty}} \qquad \textbf{(2-5)}$$

Where
$\boldsymbol{P_{inlet}}$ *= inlet total pressure*
$\boldsymbol{P_{\infty}}$ *= freestream (ambient) total pressure*

The baseline (no exlet) configuration has been highlighted. Note that restriction from the baseline provides a significant degradation in total pressure recovery, of about 0.86. Whereas all other configurations exceed 0.96. This highlights the magnitude of this concern, which again, is most significant when using low PR fans.

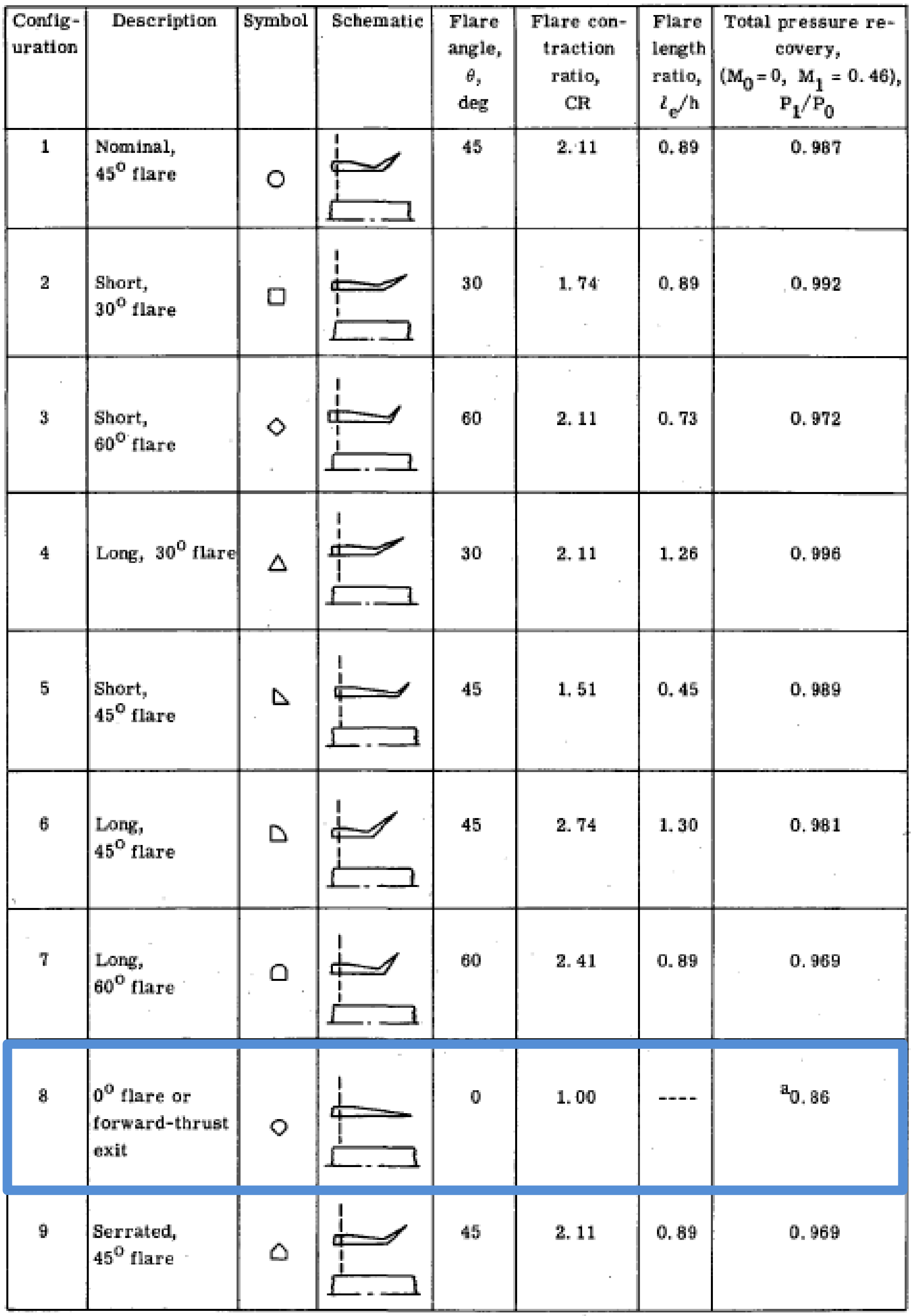

Configuration	Description	Symbol	Schematic	Flare angle, θ, deg	Flare contraction ratio, CR	Flare length ratio, l_e/h	Total pressure recovery, $(M_0 = 0,\ M_1 = 0.46)$, P_1/P_0
1	Nominal, 45° flare	○		45	2.11	0.89	0.987
2	Short, 30° flare	□		30	1.74	0.89	0.992
3	Short, 60° flare	◇		60	2.11	0.73	0.972
4	Long, 30° flare	△		30	2.11	1.26	0.996
5	Short, 45° flare	◺		45	1.51	0.45	0.989
6	Long, 45° flare	◗		45	2.74	1.30	0.981
7	Long, 60° flare	⌓		60	2.41	0.89	0.969
8	0° flare or forward-thrust exit	○		0	1.00	----	[a]0.86
9	Serrated, 45° flare	⌂		45	2.11	0.89	0.969

Figure 2-37: Tested exlet configurations & their respective total pressure recoveries [59]

An alternative to the exlet is to fit auxiliary intakes on the side of the bypass duct, much like a cascade reverser, as published by Rolls Royce in 1972 (*Figure 2-38*). This potentially eliminates the upstream throttle issues, whilst ignoring the aerodynamic losses around the bypass nozzle lip (which could increase momentum drag/braking effectiveness).

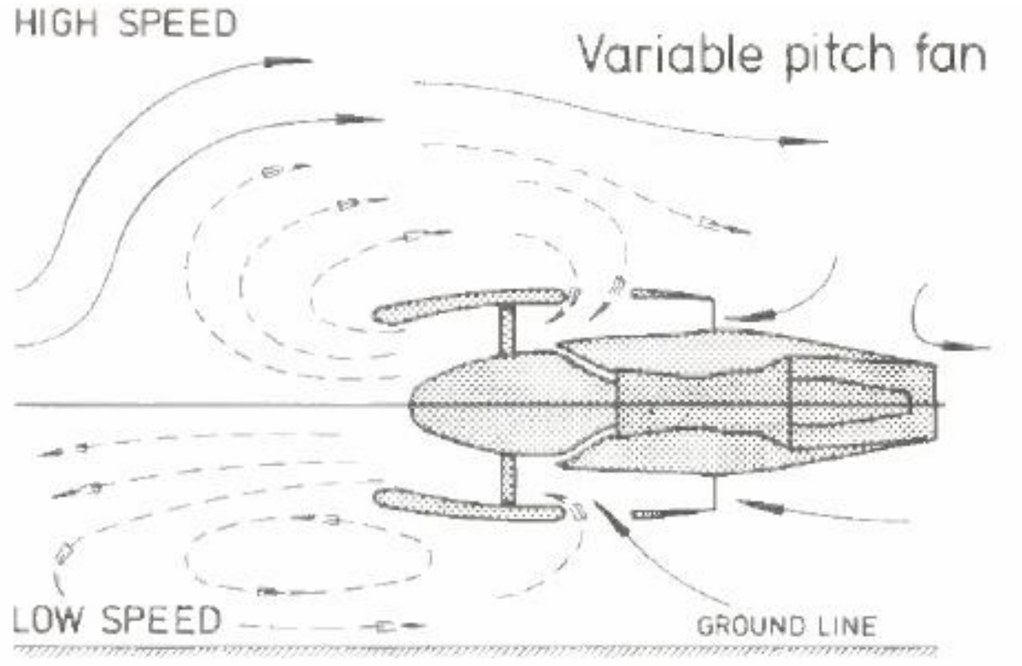

Figure 2-38: Rolls-Royce/SNECMA RB.410/M45H auxiliary bypass duct intakes [52]

However, from the perspective of the engine designer, given the added weight & complexity of the variable-pitch mechanism and its associated architecture, supplementary devices for reverse thrust operation would be unfavourable. The use of a variable area nozzle in conjunction with a VPF has widely been dismissed, as for forward operation, they serve the same function – to adjust fan flow capacity. The added weight and drag of any supplementary system for flow reversal will erode the benefits expected from removing the conventional TRUs. Furthermore, the use of an ultra-short or ‘slimline’ nacelle, may play a role in improving the bypass nozzle pressure recovery.

Following similar logic, SNECMA recently patented an idea for a two-part nacelle, whereby the rear section may translate longitudinally forward during reverser operation. This design could offer to retract the thin trailing edge of the bypass nozzle, providing a thicker edge for the flow to turn around, resulting in a lower degree of total pressure loss due to separation. [60]

2.7.2 Core Inlet Performance

It is expected that similar aerodynamic phenomena to those at the bypass nozzle lip are also present in the core duct. As the bypass stream is now reversed, to enter the engine core the relevant flow needs to turn around the splitter. This could induce separation as the boundary layer is unable to remain attached around the sharp splitter leading edge. The total pressure loss and radial distortion generated by this could compromise engine core operability. Furthermore, under normal operating conditions, the core inlet flow first passes through the fan hub, where it is supercharged. Under thrust-reversal however, this is no longer the case, reducing the overall delivery pressure which can be obtained. Rolls-Royce identified these as potentially serious issues when developing their RB.410 VPF prototype engine in 1971. They proposed additional auxiliary slot intakes in the splitter walls (*see Figure 2-39*), to improve the total pressure recovery & reduce radial distortion during reverse-thrust operation. [61]

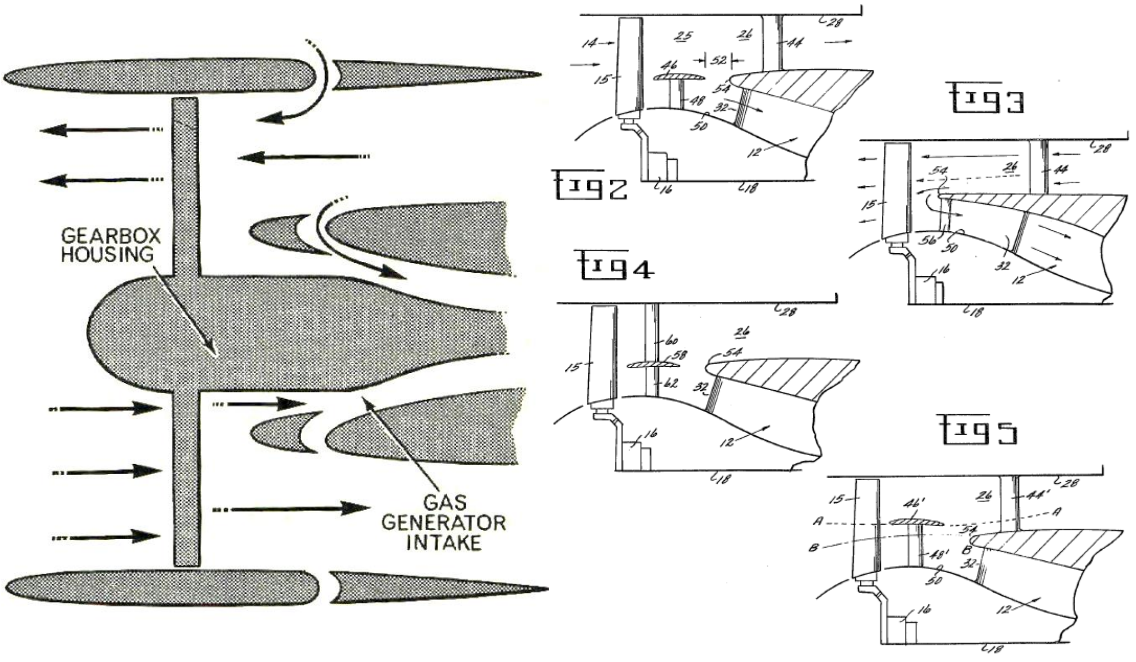

Figure 2-39: Left; RB410 auxiliary slot doors, Right; NASA two-part splitter patent [61, 62]

NASA also patented a similar design, whereby a two-part splitter was used to address the same core-duct problems under thrust reversal (*see Figure 2-39*). [62] There is also a concern regarding the swirl induced on the flow entering the core, as it passes through the OGVs beforehand in the bypass duct. Within the core-duct there are normally located the entry section stators (ESS), which are a set of fixed geometry blades, and act as structural members to the engine. The inlet angle of these is set such that under normal operation they accommodate the swirl induced by the fan upstream. However, under reverse, the swirl induced by the OGVs turns the flow in the wrong direction for the ESS blades, once it has turned around the splitter. Being able to bypass the OGVs by strategically locating auxiliary inlets, or relocating the OGV upstream of the splitter may solve this.

2.7.3 Fan Reversing Techniques

When reversing a variable-pitch fan, the blades can be rotated in either direction to achieve a reversed flow. The two methods are commonly known as ‘through-feather’ and ‘through-flat’ pitch operation. These two methods are differentiated in *Figure 2-40*.

2.7.3.1 Through-flat pitch operation

In the ‘through-flat’ mode, the blades angle of attack is reduced until the fan is effective 'closed', blocking the passage, and substantially reducing the axial flow either side of the fan. The blades then turn past this position, effectively reversing the direction of the fan. As the blades pass through the 'zero-lift' angle rather than feathering, the fan does not aerodynamically stall. [63] However, this operation requires solidity to be <1 along the whole span of the fan, in order for the blades to pass each other when reversing pitch. [55] The other penalty for this design is that when the blades are reversed, the camber is now unfavourable, as the rotational direction does not change. This reverses the aero-loading on the blades, causing bending in the opposite direction - something which would introduce additional mechanical requirements to fan designs. [64]

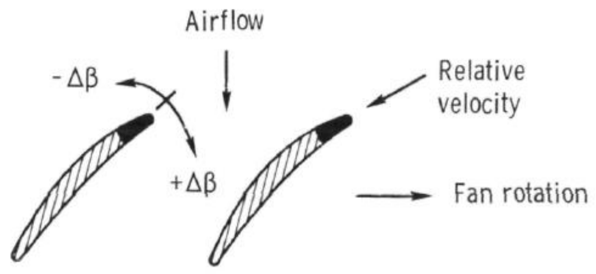

(a) Forward thrust.

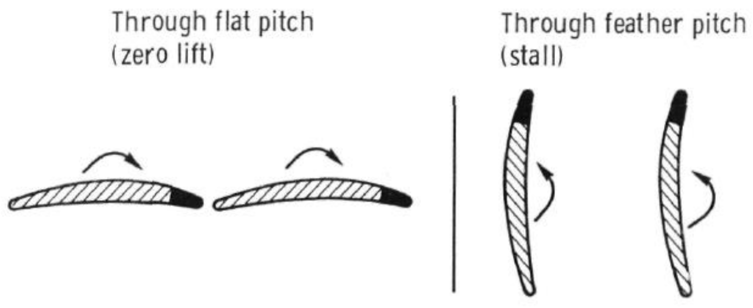

(b) Transition.

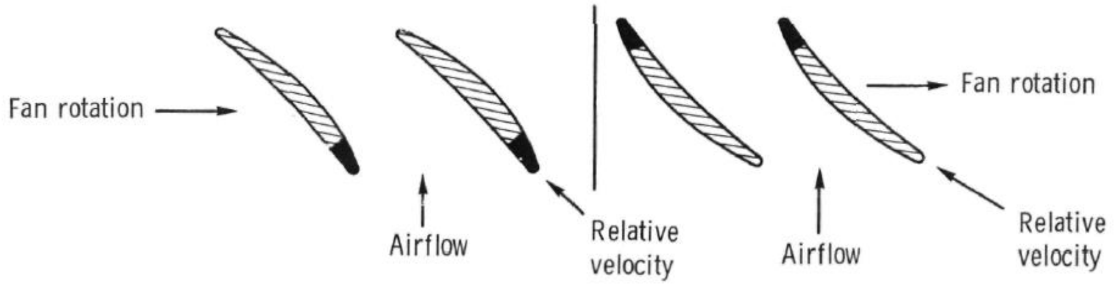

(c) Reverse thrust.

Figure 2-40: Comparison between through-feather & through-flat reversal [56]

2.7.3.2 Through-feather pitch operation

During through-feather operation, the fan blades are turned into the flow. As this happens the blade angle of attack becomes too high for the flow to remain attached to the suction surface of the blade, resulting in stall. As a result, the flow absolute velocity in the fan passage becomes mostly circumferential, rotating with the fan. In order to quickly re-establish flow attachment once the blade has passed through feather, an overshoot technique was required. [55] This involved turning the blades past the desired pitch angle for reverse thrust, to overcome the static pressure at the inlet, as the rotor is effectively creating a blockage in the duct whilst stalled. Once the flow reattaches, the blade pitch is moved back towards feather, until the desired pitch is achieved. This requires a thorough investigation of the blade aerodynamics whilst operating in this region to optimise/reduce the time required to generate reverse thrust. The blade cambers remain favourable even when reversed, which is not the case for the 'through-flat' mode. This also means that the bending on the blades due to aero-loading remains in the same direction. Solidity along the blade can also exceed values of 1, which offer more flexibility to the fan designer, and a greater retention of blade overlap through the pitch setting regime.

2.7.4 Summary of Previous Studies

Most of the knowledge on VPF reverse-thrust performance in the public domain can be attributed to the work published from the NASA's QCSEE studies. A comparison between the transient operating regimes for the two fan reversing methods (flat & feather) is provided on the following pages.

When reviewing the transient graphs (*Figures 2-41 & 2-42*), engine thrust, torque and fan speed should be viewed collectively. When the fan pitch is actuated through-flat, the blades begin to close, reducing the fan work, and therefore torque. This accelerates the fan when the aerodynamic loading plummets. To accommodate this, the transient starts with a low enough speed such that this acceleration doesn't result in the fan RPM exceeding 100%. When the blades pass through flat-pitch, the loading starts to increase as the flow begins to reverse through the fan, and some of the torque is recovered. The total transition time is approximately 1 second. The compressor inlet recovery drops to about 0.95 (fitted with exlets) as the flow regime reverses in the bypass duct. Compressor speed and discharge pressure remained more-or-less constant, as there was no change in power setting/fuel flow. The maximum attained level of thrust reverser effectiveness however, was only about 20%. [56]

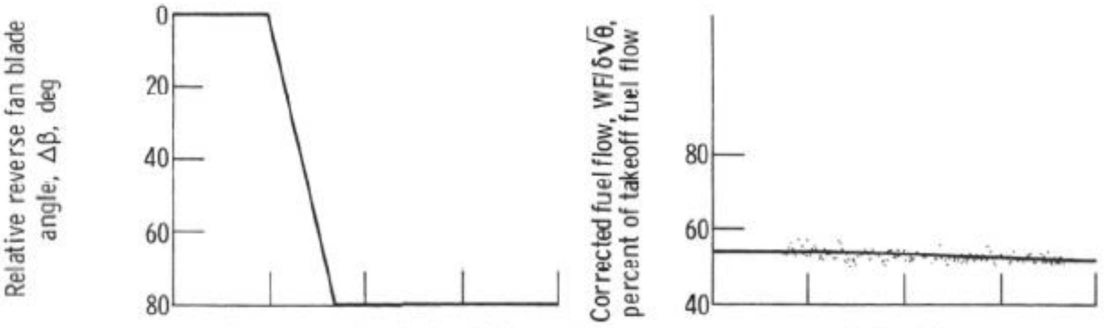

(a) Relative reverse fan blade setting angle.

(b) Fuel flow.

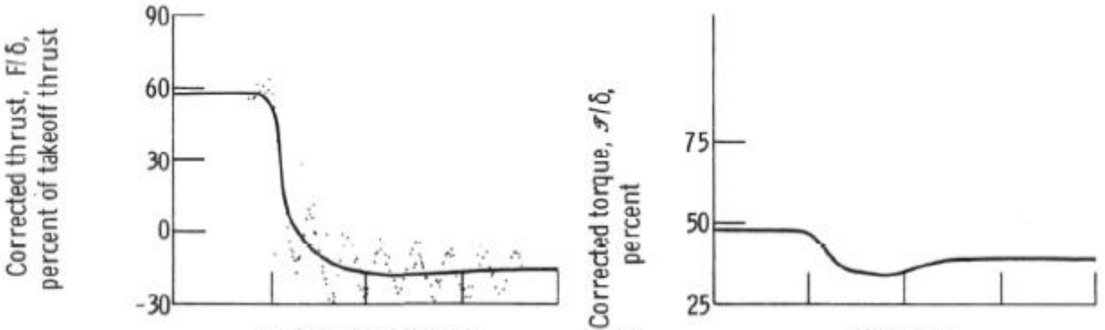

(c) Corrected thrust.

(d) Torque.

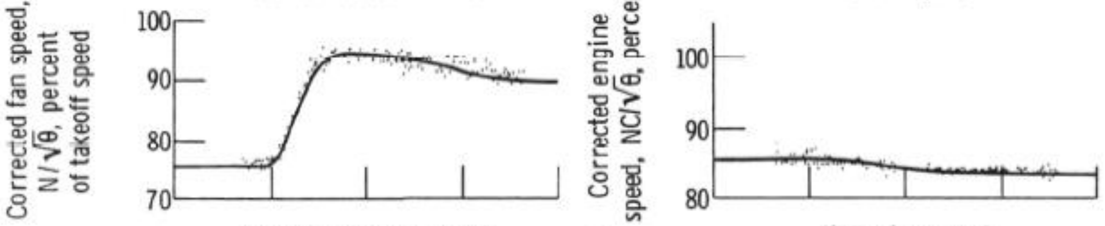

(e) Corrected fan speed.

(f) Engine speed.

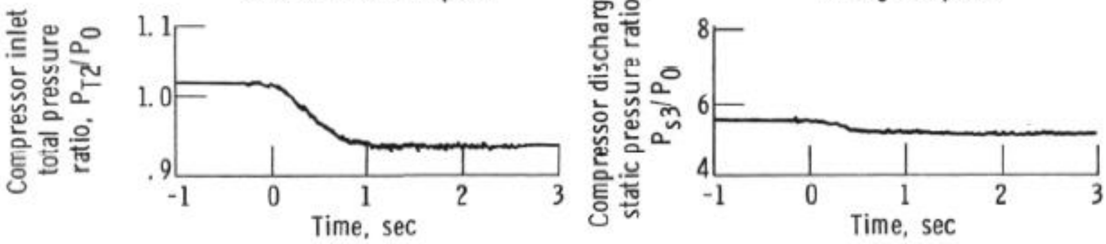

(g) Compressor inlet total pressure ratio.

(h) Compressor discharge static pressure ratio.

Figure 2-41: Real time traces of QCSEE engine parameters for flat-pitch transient [56]

Reviewing the graphs for through-feather, it can be witnessed that the transient effects are much more pronounced compared with the through-flat method. As the pitch transition begins, the blades open, increasing the thrust temporarily, which results in torque and fuel flow spikes. The fan then stalls as it approaches feather, and continues to travel until its final pitch setting - no blade overshoot was used in the documented run, as it was a static test. The total transition time is also approximately 1 second. Regarding the core, the transition results in a smooth acceleration in core speed, but peaks/oscillations in the fuel schedule, compressor discharge pressure, and compressor inlet pressure are present, due to the sudden change in fan work.

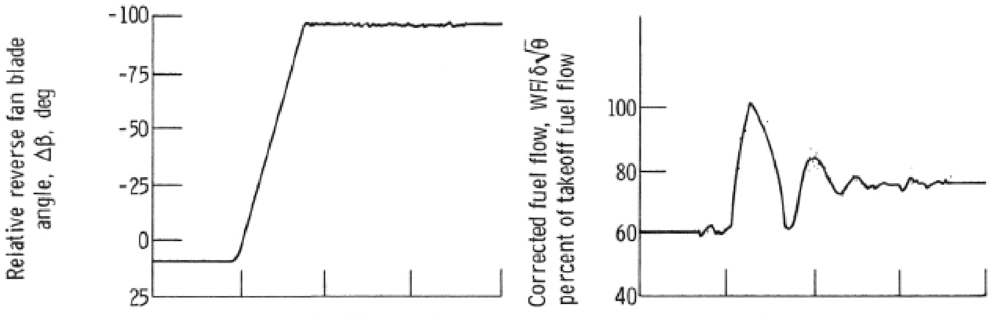

(a) Relative reverse fan blade setting angle.

(b) Fuel flow.

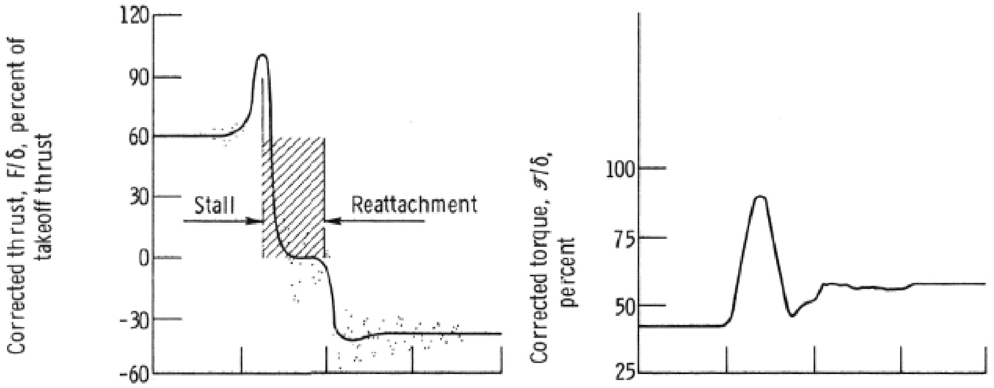

(c) Corrected thrust.

(d) Torque.

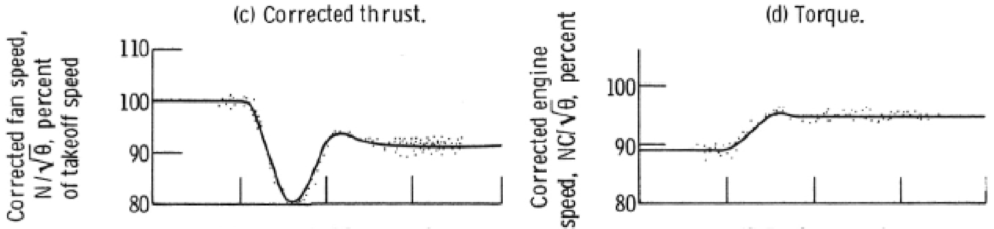

(e) Corrected fan speed.

(f) Engine speed.

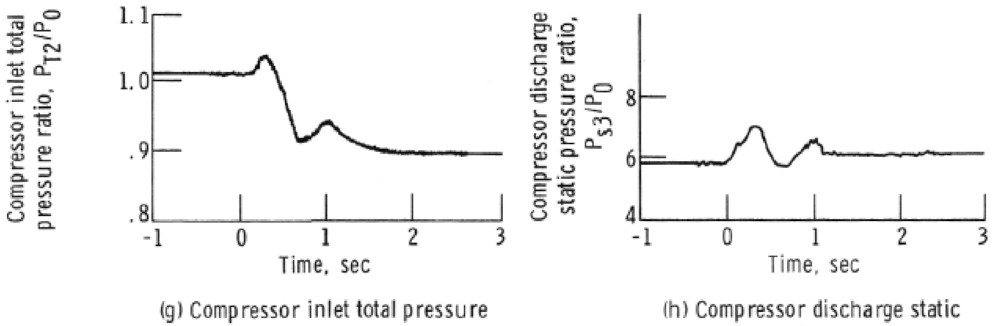

(g) Compressor inlet total pressure ratio.

(h) Compressor discharge static pressure ratio.

Figure 2-42: Real time traces of QCSEE engine parameters for feather-pitch transient [56]

In terms of reverse thrust achieved, experimental results have been published from two sources, shown below in *Figure 2-43* (NASA QCSEE & Kutzenov NK-93 tests). Note that the NK-93 graph, m represents bypass ratio, approximately proportional to fan mass-flow.

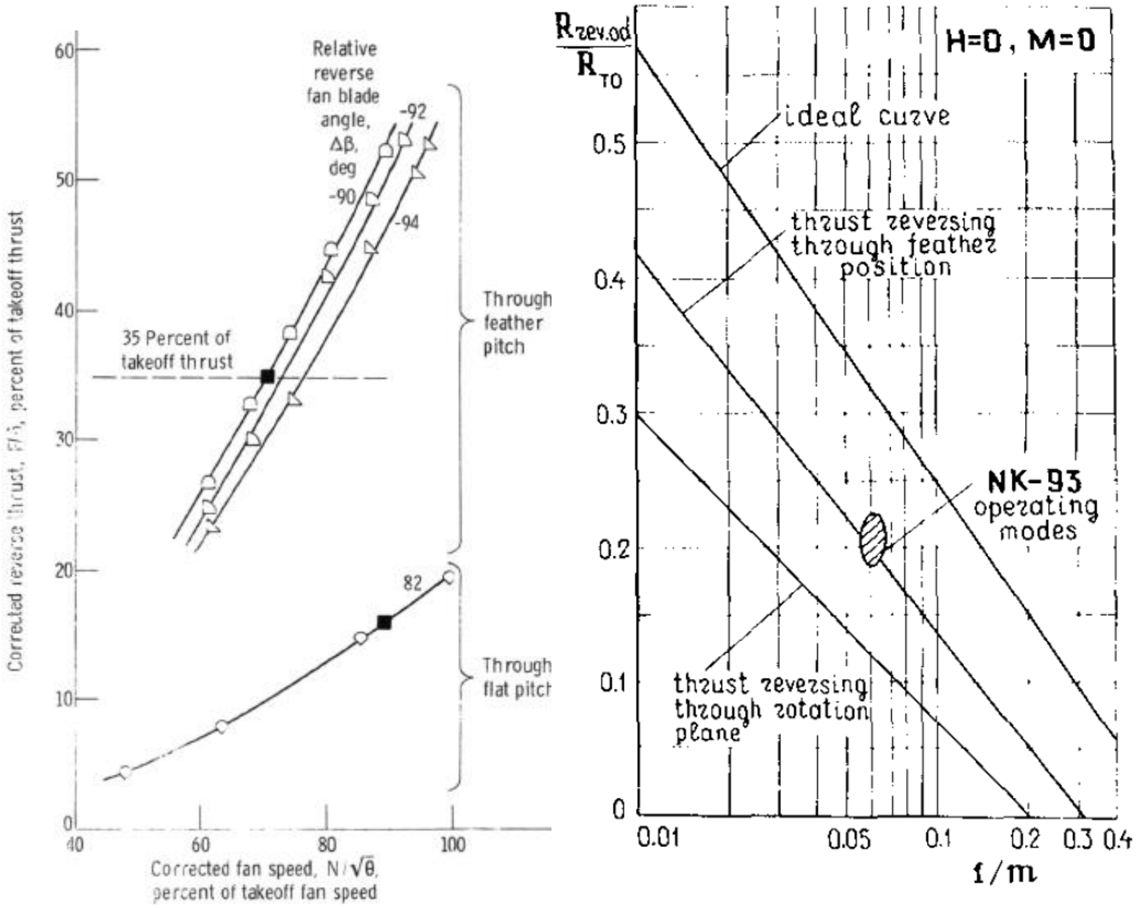

Figure 2-43: Comparison of VPF thrust reverse force attained
Left: NASA's UTW QCSEE [56] ***Right; Kutzenov NK-93*** [10]

The same performance comparison can be drawn from both sets experimental data; in terms of thrust reverser effectiveness, the through-feather operation is far superior, achieving up to 35-40%. By comparison, the through-flat mode produces a peak of 20-30% nominal thrust. This can be attributed to the single main difference between the two regimes; the curvature of the fan blades. Under feather, the curvature is favourable, so the aerodynamic profile of the blades allows for reasonably efficient performance. With the through-flat mode however, the camber is reversed, which limits the FPR that can be delivered. The main benefit to the flat mode is that its operating regime is relatively straight forward utilizing a constant power setting, and exerts lower peak stresses on the blades. Whereas the through-feather regime requires a much more tailored fuel schedule to accommodate the fluctuations in fan loading, and higher structural requirements for fan blades. The QCSEE studies concluded that either operation was sustainable, with issues regarding pressure-loss and component stress not detrimental to engine stability or mechanical life, for engine designs at the time. [55, 56]

2.8 Distortion Effects & Analysis

Inlet distortion is the spatial variation of inlet pressure and/or temperature, and can significantly affect the overall compressor map. Numerous studies have established a firm grasp of the aerodynamic response, and mechanical modes, such as high-cycle-fatigue associated with distorted flow. [65, 66, 67, 68, 69, 70, 71, 72, 73] Under reverse-thrust, a VPF engine is expected to experience distorted flow caused by separation from the bypass nozzle TE lip, and also as the flow turns around the splitter into the engine core. These areas of distortion maybe exasperated by circumferential flow variations induced by the external flow field. For the purposes of this study, distortion metrics were used to assess flow variations in the core inlet duct immediately downstream of the bypass splitter.

The total pressure distortion in the context of turbomachinery compressors, is usually quantified in terms of sectional distortion coefficient (DC60), circumferential distortion index (CDI), and radial distortion index (RDI). [66, 68] These are collectively known as ‘parallel compressor’ methods of assessing distortion.

DC60 is defined by the difference between the area-weighted average total pressure, PAV, and the area-weighted average the 60˚ sector with lowest average total pressure, PAV_{60}. [13, 74]

$$DC_{60} = \frac{(PAV) - (PAV_{60})}{q} \qquad \textbf{(2-6)}$$

Where

$$q = \frac{1}{2}\,\rho V^2 \tag{2-7}$$

Walsh & Fletcher indicate that subsonic aircraft compressors can typically tolerate up to a DC60 distortion of 0.2. [74] Whilst the DC60 method alone does not fully encompass all concerns with distortion, it is one of the most common low-order approaches for assessing total pressure flux. Variations on the method exist which use larger different sector angles (i.e. DC90, DC120). The same approach can also be used to give rise to a temperature distortion coefficient, such as TC120, by replacing total pressure values with those of total temperature. [74]

CDI assesses the uniformity of the circumferential total pressure distribution, at specific radial positions, as visualised in *Figure 2-44*, and defined in *Eq. 2-8*.

$$CDI = Max_{i=1}^{n_{radius}-1}\left(0.5\left[\frac{P_{o,i} - P_{o,min_i}}{P_{o,avg}} + \frac{pP_{o,i+1} - P_{o,min_{i+1}}}{P_{o,avg}}\right]\right) \tag{2-8}$$

Where
$\boldsymbol{P_{o,i}}$ = *the average total pressure on the* i*-th ring*
$\boldsymbol{P_{0,min_i}}$ = *the minimum total pressure along the same ring*
$\boldsymbol{P_{0,avg}}$ = *the average total pressure for the whole inlet*

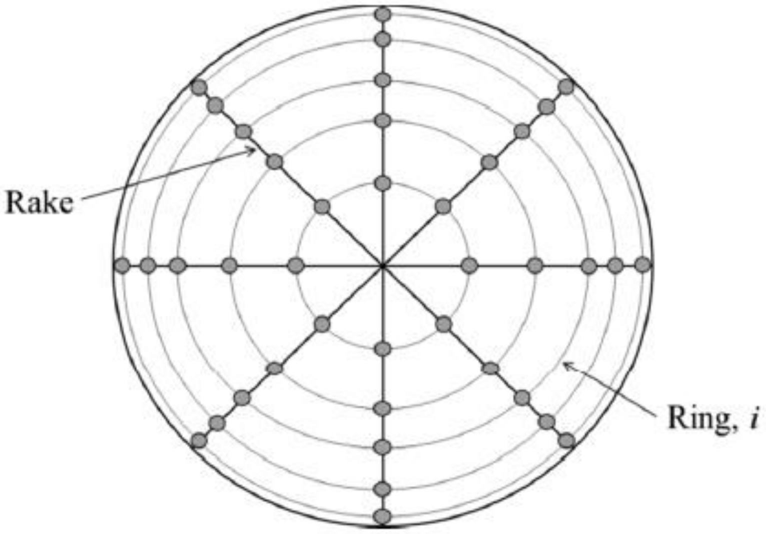

Figure 2-44: 8x5 inlet flow distortion measurement stations for CDI & RDI [68]

The radial distortion index is calculated following the same logic as CDI, and is defined as follow [66, 68]:

$$RDI = Max\left(\frac{P_{o\,,avg} - P_{o,inner\ ring}}{P_{o,avg}} + \frac{P_{o\,,avg} - P_{o,outer\ ring}}{P_{o,avg}}\right) \qquad \textbf{(2-9)}$$

Where
$P_{0,inner\ ring}$ = *average total pressure of the inner ring*
$P_{o,outer\ ring}$ = *average total pressure of the outer ring*

Figure 2-45 shows the difference in working line for the distorted and undistorted sectors, as would be measured with the DC60 metric. As the distortion implies a drop-in pressure/temperature, it pushes the compressor working line left on the performance map; towards the surge margin. This is because the distortion reduces the local total pressure for the compressor, which increases susceptibility to delaminate the blade boundary layer flow, due to the increase in relative static-back-pressure on the rotor. Should flow stalling occur in a compressor, it can quickly spread from a localised issue to a fully annular one.

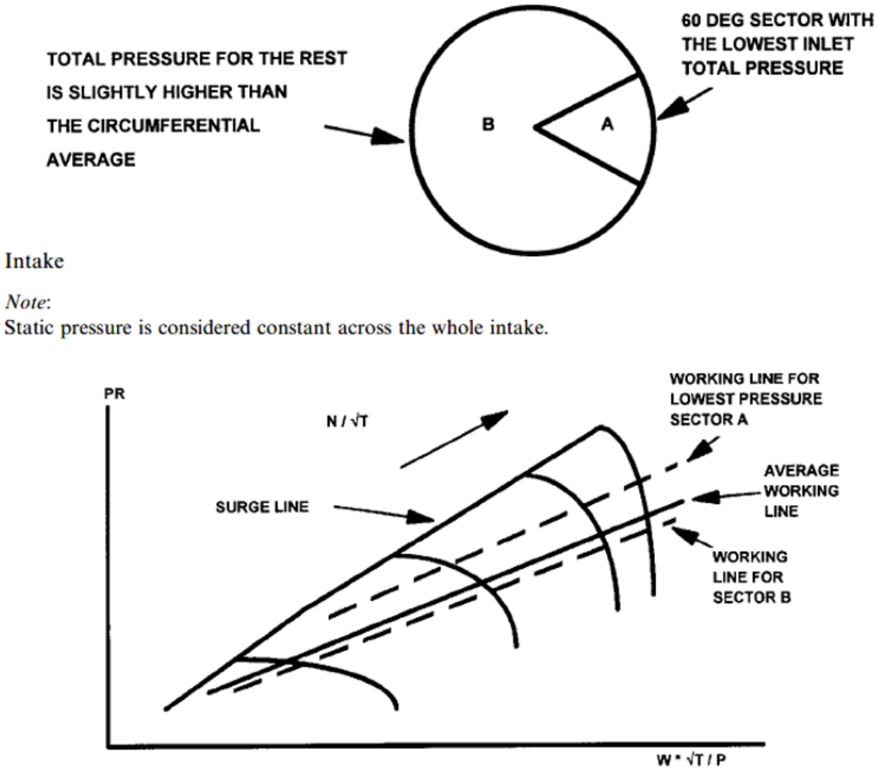

Figure 2-45: Measuring method for calculating DC60, and the effect of distortion on the compressor working line [74]

The effect on surge margin degradation has been quantified based on the distortion 'area of spoiling', and is presented in *Figure 2-46*. The charts are taken from a study into axial flow compressor distortion, published by Rolls-Royce in 1969. [69]

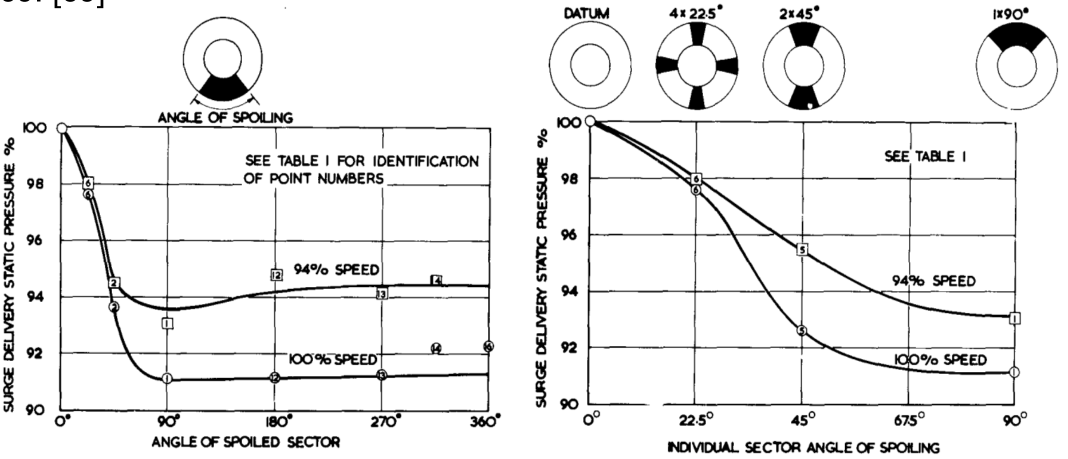

Figure 2-46: Effect of varying circumferential distortion spoiling profile on surge margin [69]

Figure 2.47 shows that surge delivery pressure is related to the size of the individual sector of distortion. The critical size whereby surge/stall margin degrades occurs between 30-90˚. Furthermore, whether the distortion occurs in a single large sector, or multiple smaller elements also affects the extent of surge margin reduction. By comparison, radial distortion is much less detrimental to compressor stability, with only one-fifth the loss in surge pressure compared to the 90˚ sector (when equal areas of distortion are used).

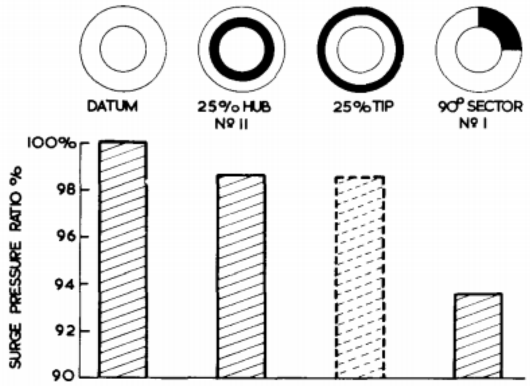

Figure 2-47: Comparative effects of radial & circum. distortion on compressor surge[69]

Additionally, the extent to which distortion can affect modern high-tip speed compressors, measured using the parallel compressor method is well documented by several publications.[66, 73, 71]

2.9 Aircraft Research Models

Under the project objectives, it has been stated that the model that has been developed needed to include both engine and airframe geometries for a fully integrated scenario. As such, a brief review of the existing aircraft models in the public domain was undertaken.

2.9.1 DLR-ALVAST

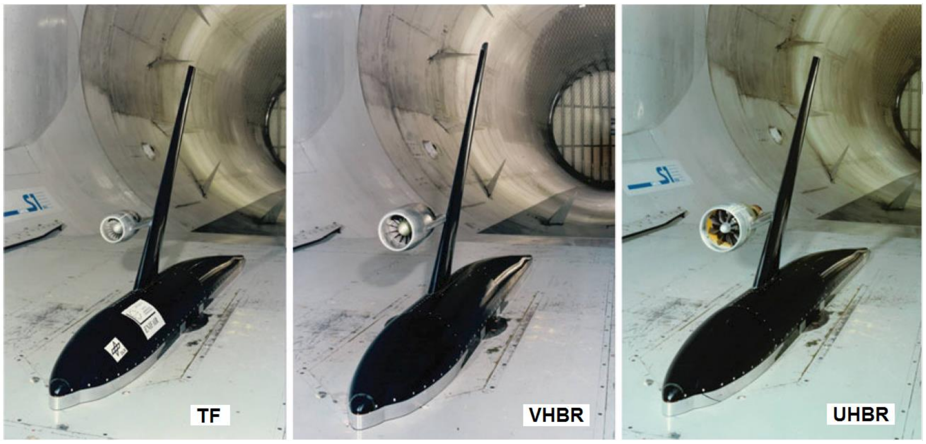

Figure 2-48: View of the three engine simulators mounted to the DLR-ALAVAST airframe [75]

The DLR-ALVAST is a wind tunnel airframe model, that represents a wide-body twin engine aircraft. The design Mach number is 0.75 at a coefficient of lift $C_L = 0.5$. Its main purpose was to investigate engine-airframe installation aerodynamics, and could be fitted with 1 of 3 turbo-powered ‘engine simulators’, as pictured in *Figure 2-48*. These engines were the turbofan simulator (TF), very-high-bypass-ratio (VHBR) and ultra-high bypass ratio (UBHR), representing cruise BPRs of 5, 9.2 and 15.7 respectively. The corresponding cruise FPRs were 1.58, 1.44, and 1.25. Tests were conducted to assess aerodynamic performance at Mach numbers ranging from 0.3 to 0.75, at two different facilities. [75] Whilst the data has been published, the geometry itself is not publicly available. [76]

2.9.2 DLR F6

Another wind tunnel model used for the study of engine-airframe installation aerodynamics, is the DLR F6. The model represents a subsonic civil transport aircraft, which was tested across 4 wind tunnel campaigns. The model was tested with and without engines - represented as through-flow nacelles. An engine fitted version of the wind tunnel model is shown in *Figure 2-49*.

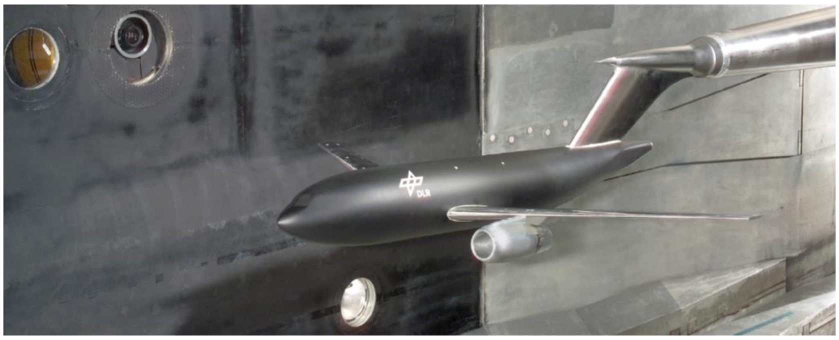

Figure 2-49: A DLR-F6 model in NASA's NTF wind-tunnel with CFM-56 engine model [77]

The aircraft was designed for a cruise Mach number = 0.75, and $C_L = 0.5$. The model became a benchmark case for the validation of numerical methods as part of the 2nd & 3rd Drag Prediction Workshops (DPWs) [78, 79]. The test configurations all measured cruise performance (Mach 0.75), but varied the aircraft angle of attack (AoA), to establish the C_L variation. The geometry is publicly available online.

2.9.3 Common Research Model

The Common Research Model (CRM) (*see Figure 2-50*) was developed by NASA, with the aim of interested third parties [80], much alike the DLR F6. It answered the arising need for a more contemporary subsonic transport aircraft model than had been used in the previous DPWs. The geometry was designed for a vehicle cruise of Mach 0.85, with $C_L = 0.5$. The model again came in clean-wing and installed-engine variants, and was used extensively to establish meshing guidelines for future comparable CFD studies. It has since been used in the 4th, 5th & 6th DPWs, and the geometry is publicly available. [81, 82, 83]

Figure 2-50: Clean-wing CRM in NASA's Ames Research Center Unitary Plan Wind-tunnel [82]

2.9.4 DLR F11

The DLR F11 is a derivative of the CRM airframe model, only with added high-lift devices (wing flap and slats) in a fully deployed configuration. It was utilized as the study model for the 2nd High-Lift Prediction Workshop (HLPW). [84] The high-lift workshops were conducted very much alike the drag prediction workshops; instead studying aerodynamics of high-lift configuration wings. The complexities of high-lift flows were deemed to present significant degrees of uncertainty with respect to validation of modern numerical methods, such as CFD, and the HLPWs aimed to establish a guideline for meshing and solver configurations of this type. The flow complexities include wakes in pressure gradients, wake-boundary-layer merging, separated & possible unsteady flow, and laminar/turbulent transition regions on each wing element (slat, main wing, flap). [84] Two wind-tunnel models including the high lift devices were tested and used as validation for the numerical models, and both geometry and data is publicly available. [85] One of the DLR F11 wind tunnel models is shown in *Figure 2-51*.

Figure 2-51: DLR F11 in the Airbus-Deutschland low-speed wind tunnel (B-LSWT) [84]

Testing was conducted primarily at Mach 0.175, and varied the AoA onto the model, to measure variation in C_L. The peak $C_{L,max}$ was identified at approximately 20˚ AoA, which was matched in the numerical solutions. [84]

2.10 Identified Knowledge Gaps

Having reviewed what is currently available in the public domain on the topic, there is clearly more knowledge required before the operation of variable-pitch fans under reverse-thrust conditions is fully understood.

Whilst much work has been done to quantify the potential of VPFs for turbofan applications, little has been published regarding reverser-operation. The key contributor to the field was the QCSEE study conducted by NASA in the 1970s. [55, 56] Whilst the study established the fundamental principles behind VPF thrust reversal, the published data revealed only static performance, with an indication of flow regimes at 60 knots. [11] It was deemed at the time, that a full understanding of the operation could only be obtained from flight testing. [86, 87]

As conventional thrust reversers are typically disengaged at 80-60 knots, and still provide enough benefit to justify their existence, VPF reverse thrust performance needs to be better understood at higher landing speeds.

Furthermore, previous studies have primarily focussed around static test rig modelling. The variation in aerodynamic performance with the aircrafts airspeed, particularly when installed on the airframe has not been studied. Whilst NASA’s ADP studies did encompass an integrated engine/airframe model, data was published only for the changes to airframe performance; no reverse-thrust operational data was provided on the engine. [12]

Engineering capabilities have advanced since in the QCSEE studies, including the introduction of high-powered numerical simulation tools, only made capable by the decades of development in computational technology. Using tools such as CFD, aerodynamic research can now be conducted into areas which were previously cost-prohibited; traditionally requiring experimental testing. CFD capabilities have now reached levels where large-scale simulations into subjects such as airframe-integrated VPF thrust-reversal have become viable undertakings. The author's work hereafter, is a contribution to these identified gaps in knowledge, with the intention to provide a better understanding on the topic, to the sponsor & universal aerospace community alike. Improving on the aerodynamic operation of the system, researchers and engine-manufacturers should be able to better assess the feasibility and design concerns regarding future thrust-revering VPF engines. *Figure 2.52* illustrates one of the main differentials between this work and previous studies with respect to the landing speed spectrum. Previous work has largely relied on static tests.

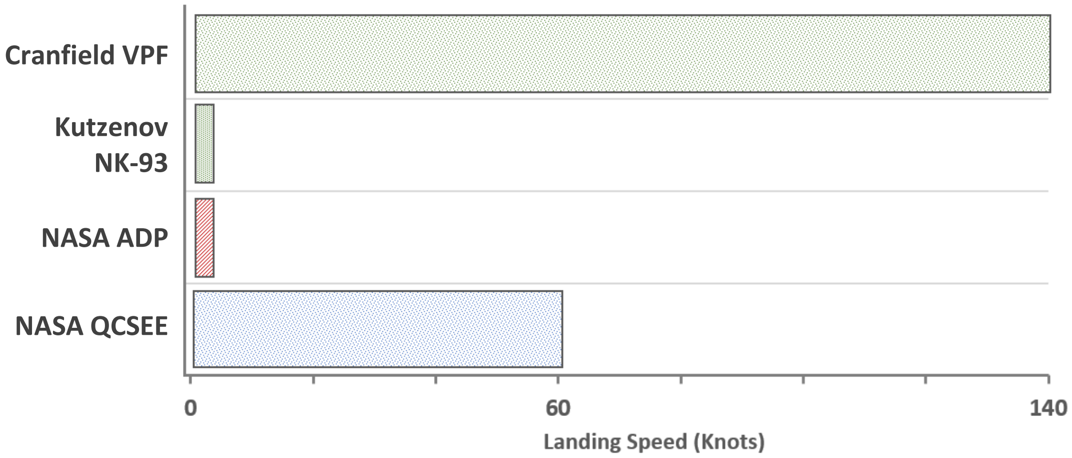

Figure 2-52: Comparison with previous studies based on landing speed range

3 Methodology

To investigate the aerodynamics of variable-pitch fan thrust-reversal, this project utilises the current capabilities of computational fluid dynamics (CFD) software. In accordance with the 'scope-of-work' provided by the project's industrial sponsor, it was determined that a full-scale 3D aircraft/engine model should be produced, to fully capture cold-stream flow dynamics, in an integrated engine environment. The model needed to represent a conventional modern civil transport aircraft, satisfying the 'middle-of-the-market' weight and thrust class, during landing. This required high lift devices on the wing (flaps & slats), spoilers/airbrakes, engine pylon, and a ground-plane to be featured in the model. Additionally, the bypass stream inside the nacelle was also required in the fluid simulation, including high fidelity OGV & fan blades, and the splitter/core inlet; to capture the full annular flow feeding the fan and engine core. *Figure 3-1* shows an overview of the developed model.

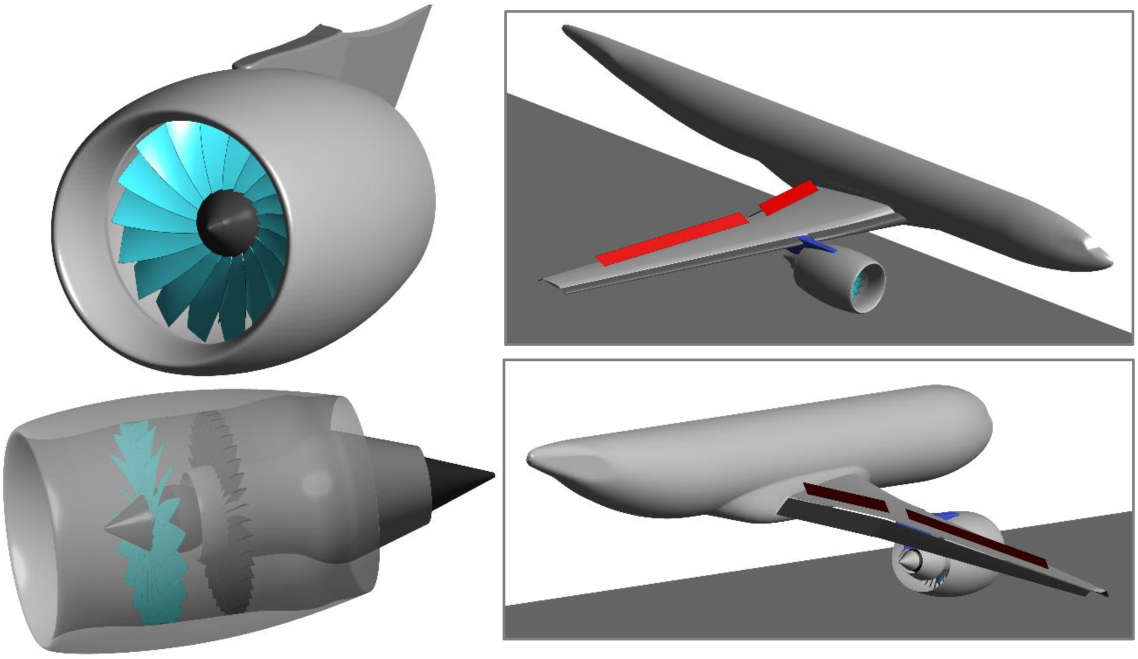

Figure 3-1: Developed engine & airframe models

Most of the work undertaken during this study has been the development and integration of the components which make up the research models. This chapter provides an account of the methodology developed during these stages of work, such that the results may be reproduced if required by another party – in accordance with the scientific method. This chapter also details the specifications of the model, some of which should be considered when reviewing the results in *Chapter 5*. Each component has at least one degree of integration with another, therefore there is a logical order which must be adhered to during development. However, the contents of this chapter are instead arranged according to the component type (engine annulus, turbomachine, or airframe), so that development of the 3 main modules is presented together. Only details directly relevant to the final assembled model are presented in this Chapter. Supporting content covering the component validation/verification procedures is provided in *Chapter 4*, although this is not necessary to understand the project outcomes and conclusions.

3.1 Methodology Overview

Before discussing individual components in more detail, one should first establish an understanding of what these components are. The complete model can be broken down into three modules – each approaching a different system or part. These are; the engine annulus, the turbomachinery, and the aircraft. The components which make up these modules are shown in *Figure 3.2*.

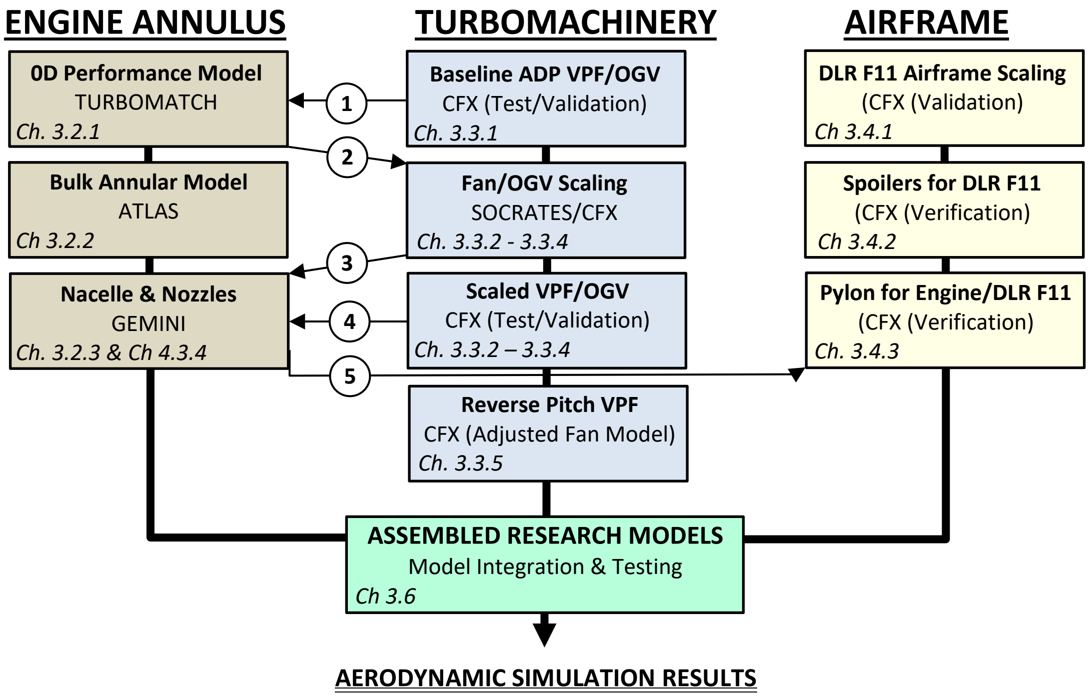

① *ADP fan design point characteristic imposed on TURBOMATCH model*
② *Fan diameter & design point mass-flow data transferred to VPF scaling work*
③ *Nacelle profile based on a scaled ADP design*
④ *Axial/radial coordinates of OGV duct outlet transferred to GEMINI for bypass nozzle design*
⑤ *GEMINI annular engine model used for design of the pylon 3D model*

Figure 3-2: Methodology flow-path for research model components

As can be seen, each module contains three/four components. Whilst the airframe module is more-or-less independent of the others, the engine annulus & turbomachinery are closely interlinked, as one would expect.

3.2 Engine Annulus Module

3.2.1 TURBOMATCH 0D Performance Model

It was specified in the scope of work that the project would focus on a ‘middle-of-the-market’ thrust class (~40,000 lbf/178 kN). To realistically simulate an engine, an 0D cycle model was required to set the boundary conditions for the engine compressor intake, and core exhaust. This allows the model to have a feasible core, without the need to represent it in the CFD model. It also provides the input for the bulk annular engine sizing method (*ref. Ch 3.2.2*). As the study was conducted inside the Cranfield UTC, the in-house 0D performance code TURBOMATCH was utilized for this task. The code has recently been improved by other studies within the UTC, and an optimiser has been developed to derive the optimum cycle designs. The code allows the user to specify certain parameters, such as FPR, inlet Mach number, and operating conditions. Constraints and requirements such as thrust, fan size, T30 & T40 limits, and OPR are also defined.

The engine is broken down into ‘blocks’ which model different components or stages within the engine, such as compressors, nozzles, combustors and so on. Each block contains data on the relevant performance parameters, and where necessary component performance maps for turbines & compressors are provided from a database of scalable maps, based on current/modern engines. It should be noted that at the time the study was undertaken, TURBOMATCH did not have any pre-existing variable-pitch fan maps. As such, the 0D model uses a fixed pitch fan map. This was deemed an acceptable simplification given the time restrictions on the project. With these inputs the code generates numerous engine models using a Matlab-based genetic algorithm optimiser, that satisfy the performance requirements at 3 operating conditions; cruise, top-of-climb (ToC) and end-of-runway (EoR). [16, 88] The thrust requirement for these cases is defined by a 'Thrust Ratio Barcode' (TRB), which in this case was provided by the sponsor. This essentially provides a ratio of required thrust between the three operating points. These three operating points & their determined thrust targets are summarised in *Table 3-1*.

Operating Point	Ambient Conditions	Altitude	Flight Mach	Net Thrust
Cruise	ISA	10670 m	0.82	7,530 lbf *(33.5 kN)*
Top of Climb (ToC)	ISA	10670 m	0.82	9,788 lbf *(43.5 kN)*
End of Runway (EoR)	ISA + 15 ºC	0 m	0.25	40,000 lbf *(177.9 kN)*

Table 3-1: Engine operating points

The engine models with the lowest specific thrust/lowest SFC are then selected, and a Pareto front is generated of the optimum engines, as shown in *Figure 3-3*. This procedure is conducted several times to refine the results, producing a new generation of engines each time. Any engines which are not competitive, or which exceed the performance limitations imposed, are discarded and do not progress into future generations.

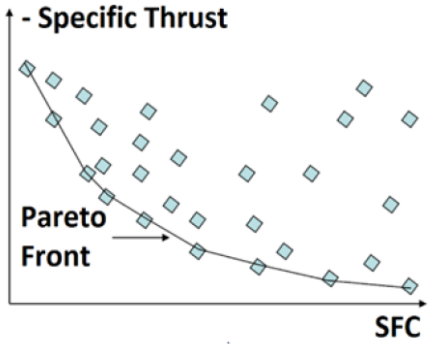

Figure 3-3: Example Pareto front [88]

The engine model architecture was based on that generated within the UltraFan™ team at Cranfield UTC, [16] with fan parameters fixed, using values from the selected fan definition (*ref. Ch 3.3.1*). The engine configuration is shown in *Figure 3-4*, which has a 2-spool core, with a gearbox to decouple the fan from the LP shaft. Additionally, some of the specified parameters are presented in *Table 3-2*.

Parameter	Fixed Value
Fan Inlet Mach No.*	0.6
Fan Bypass Pressure Ratio*	1.295
Fan Hub Pressure Ratio*	1.10
Bypass Ratio*	13.5
Hub/Tip	0.3

**At Design Point (DP) - Cruise*

Table 3-2: Fixed fan parameters

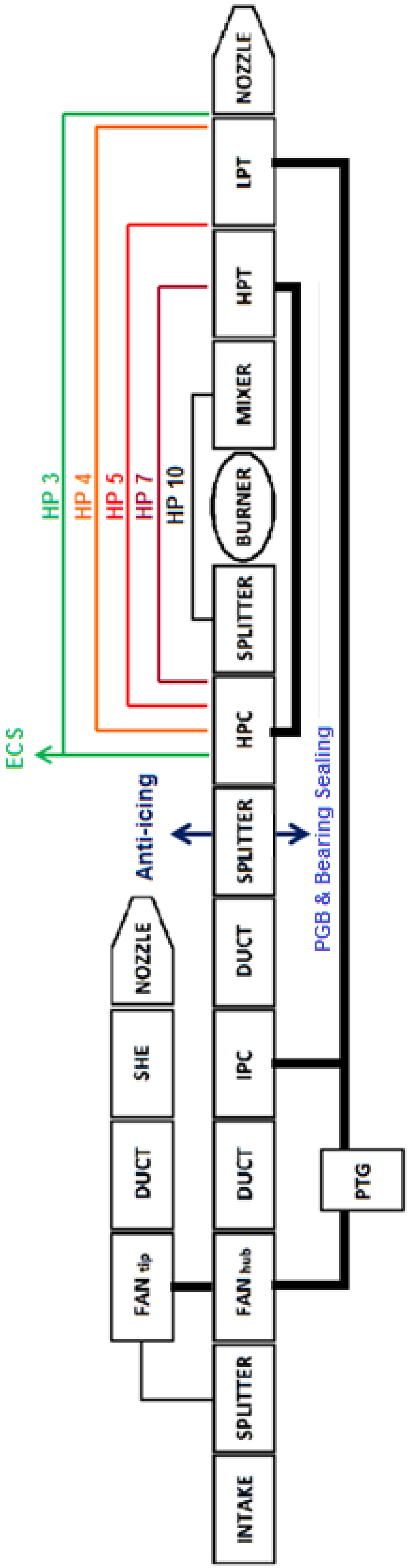

Figure 3-4: 2-Spool geared TURBOMATCH block arrangement [16]

It is important to note that at the time of this study, TURBOMATCH does not feature component maps for variable-pitch fans. As such, the fan remains a fixed-pitch model in the 0D code. However, this is not a significant issue; whilst it may not be considered completely optimised, it still fulfils its purpose for this study; to provide a viable engine core to establish the more important elements of the engine model around. Furthermore, as the parameters which are fixed for the fan are at design point, where the engine cycle is primarily determined, it can still be considered a very close approximation to the optimum configuration, as the fan work should be approximately the same regardless of whether it is a fixed-pitch or variable-pitch fan.

The Pareto front of optimum engines is presented in *Figure 3-5.* From this pool of engines, a single case was selected to be carried forward. From the 663 individual models in the final pool, the engine with the lowest SFC was the one chosen.

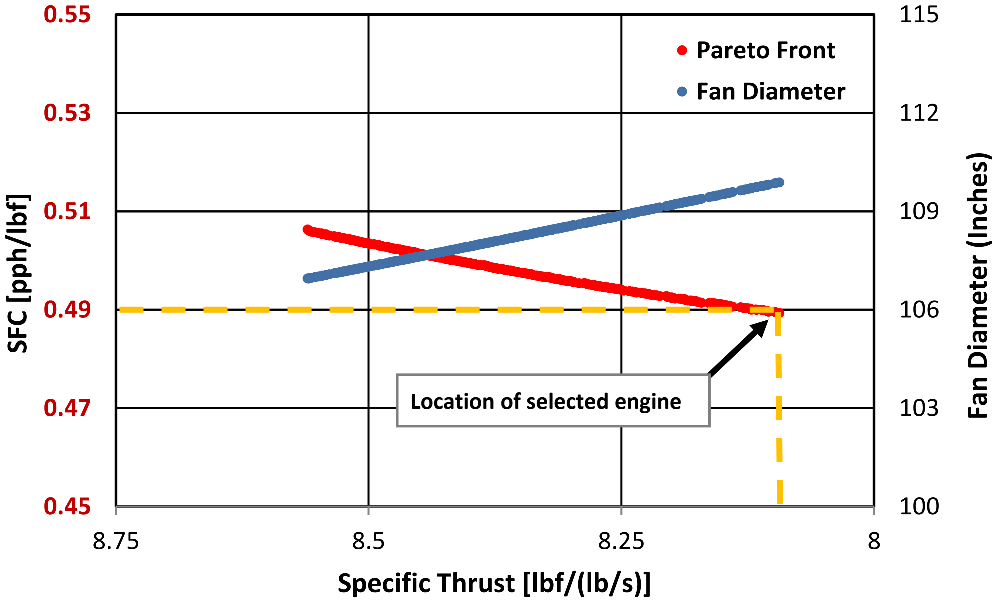

Figure 3-5: Pareto front & fan diameter of optimised engines

Details of the selected engine, as well as the parametric ranges for the final engine pool, are presented in *Table 3-3*. The selected engine model is the top-performing cycle in terms of thermal, propulsive & overall efficiency. This comes at the expense of having the largest fan diameter & thus momentum drag, although the restrictions imposed on the fan have meant that the optimisation process has been conducted in a narrow design space. Therefore, the actual range of fan diameters capable of producing the required thrust is very narrow – with only 2.93” (7.4 cm) variation across the final pool.

Parameter	Selected Engine	Pool Range
OPR (DP)	47.09	46.53 – 47.31
Massflow$_{fan}$ (EoR)	982.2 kg/s	982.2 - 1002.3 kg/s
Massflow$_{fan}$ (ToC)	414.6 kg/s	414.6 - 423.8 kg/s
Massflow$_{fan}$ (Cruise)	402.8 kg/s	402.8 - 412.8 kg/s
Fan Diameter	109.88” 2.79 m	106.95” (2.79 m) – 109.88” (2.72 m)
Thermal Efficiency	0.426	0.402 – 0.426
Propulsive Efficiency	0.838	0.828 – 0.838
Overall Efficiency	0.357	0.333 – 0.357
Bypass Nozzle Area	3.245 m^2	
Core Nozzle Area	0.270 m^2	

Table 3-3: Final engine pool cycle characteristics

3.2.2 ATLAS Bulk Annular Model

The second stage of the engine annulus methodology was the generation of a 2D bulk annulus model, to determine the approximate engine dimensions. For this, Cranfield’s ATLAS tool was utilised; which estimates turbomachinery component size & weight for aero-gas turbines. Based on gas turbine theory fundamentals, it performs flow path designation and preliminary design for each of the main engine components. [89, 90] The process is conducted using the TURBOMATCH output files for the selected engine, which ensures the 2D design is capable of satisfying the desired thermodynamic performance. Stress calculations are also conducted, which determine parameters such as the disc thickness. The user has control of the 2D model design by changing parameters such as:

- Radial position of components (altering RPM/stage loading)
- Compressor/turbine design characteristics (rising/falling/constant mean/hub/shroud line)
- Stage inlet/outlet Mach numbers (determines the passage height/areas)
- Shaft speeds
- Length of inter-stage ducts

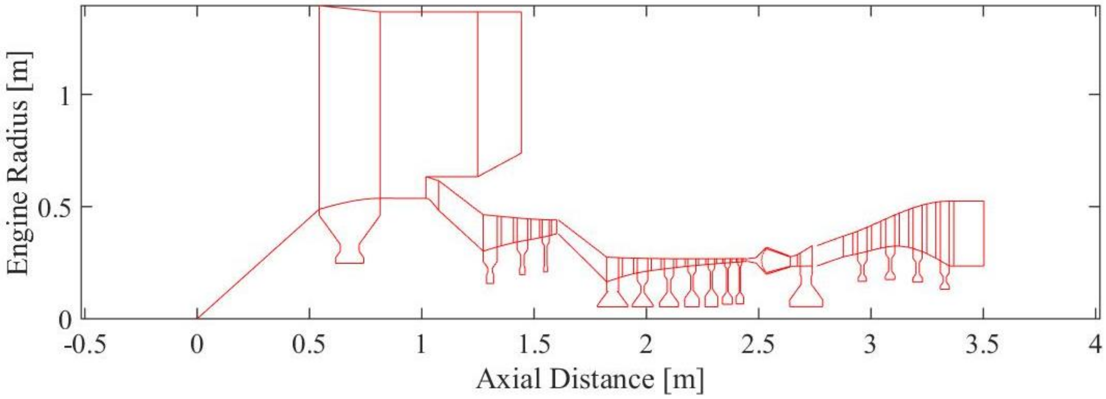

Figure 3-6: ATLAS 2D annular model

The annular dimensions of the ATLAS model are presented in *Figure 3-6*. The model was refined manually by adjusting parameters such as axial velocity where needed, to ensure that the gas-path and number of turbo-stages is sensible. The main contribution the ATLAS model makes to the overall methodology is providing a dimensional skeleton to design the subsequent engine parts around. Of particular importance are; the splitter LE radial position, the core engine length, and the radius and cross-sectional areas of the IPC inlet & LPT outlet. A breakdown of the axial dimensions and weight estimation is provided in *Table 3-4.*

Engine Module	Length (m)	Weight (kg)	% Total Weight
Fan/OGV	1.754	1439	33.3
IPC (3 stage)	0.327	244	5.6
HPC (7 stage)	0.622	374	8.6
Combustor	0.190	30	0.7
HPT (1 stage)	0.098	150	3.4
LPT (4 stage)	0.626	418	9.6
Gearbox	-	706	16.2
HP Shaft	2.926	29	0.7
LP Shaft	0.910	30	0.7
Structural & Ducts	-	501	11.5
Accessories	-	432	9.9
TOTAL	**3.47**	**4353**	

Table 3-4: ATLAS component axial length & weight estimation results

The accuracy of this method had been previously approved by the industrial sponsor, when used to conduct other UltraFan™ studies with Cranfield's UTC. It should be appreciated that, no VPF weight considerations have been made, so this should only be treated as a ball-park estimate, as this lies outside the project scope. A comparison between the engine model developed for this study, and some of the current engines of similar thrust rating is provided in *Table 3-5*.

Parameter	Cranfield VPF Engine Model	Rolls Royce RB211-535	Pratt & Whitney PW2000	Aviadvigatel PS-90
OPR	47.09	25.8 - 28	27.6 – 31.2	35.5
BPR	13.5	4.3	6.0	4.6
Fan Diameter	2.79 m	1.86 m	1.99 m	1.90 m
FPR	1.295	*n/a*	1.63	1.747
Massflow (take-off)	982 kg/s	520 kg/s	608 kg/s	470 kg/s
Bare Weight	4353 kg	~3330 kg	~ 3310 kg	~2950 kg
Entered Service	-	1983	1984	1992

Table 3-5: Comparison of overall engine specifications [17, 53, 91]

There are two key observations to be made from the contents of *Table 3-5*. The engine model developed for this study has a notably larger fan diameter, and greater weight compared with existing engines in service. These two parameters are fundamentally interlinked, as the fan accounts for the highest % weight of any engine module. The move to a lower specific-thrust configuration requires larger a mass-flow of working fluid, and thus fan diameter, to achieve comparable levels of thrust. As fan diameter increases, the weight of the fan module rises exponentially following the scaling laws. The second most significant component regarding engine weight is the gearbox, which neither of the 3 featured production engines possess. Therefore, whilst the weight for the Cranfield engine is significantly higher, it is not without justification. Furthermore, the quoted values are for bare engine weight, not including installation structures, nozzles, or the nacelle. This is an area one would expect a VPF to excel in terms of weight savings, due to the removal of conventional TRUs, and the use of short-bypass-nozzle slimline nacelle.

3.2.3 GEMINI Nacelle & Bypass/Core Nozzle

With the annular dimensions defined, the next step for development of the engine model was to generate aero-lines for the nacelle and both exhaust nozzles. To do this, another of Cranfield's in-house software codes was used, known as

GEMINI (Geometric Engine Modeller Including Nozzle Installation). The code's purpose is to design and assess nacelle and separate-jet nozzle design for turbofans. The core part of the tool comprises software modules for cycle analysis, geometry parametrisation, mesh generation, and a Reynolds-averaged Navier-Stokes (RANS) flow solution (using ANSYS Fluent). [92] The modules can be turned on or off depending on the user's requirements by changing settings within the input files. As the software has been developed in-house, it has been designed to accept TURBOMATCH engine cycle results files as part of the geometric input (such as nozzle areas).

For this study, the requirement from GEMINI was the generation of a reasonable geometric representation of a short-cowl nacelle, with both the bypass and core nozzles. Therefore, the geometric parametrisation module was of most importance. The process splits the geometric design into three fundamental parts; the spinner, the nacelle, and the nozzles. Each of these parts has its own input file to define dimensions. The input parameters are normalised against the fan blade radius. This means that the design becomes independent of the actual engine size, allowing a standardised approach to be adopted. *Figure 3-7* & *Table 3-6* present the method of calculation for some of the key parameters used in the design process for the nacelle. [92, 93]

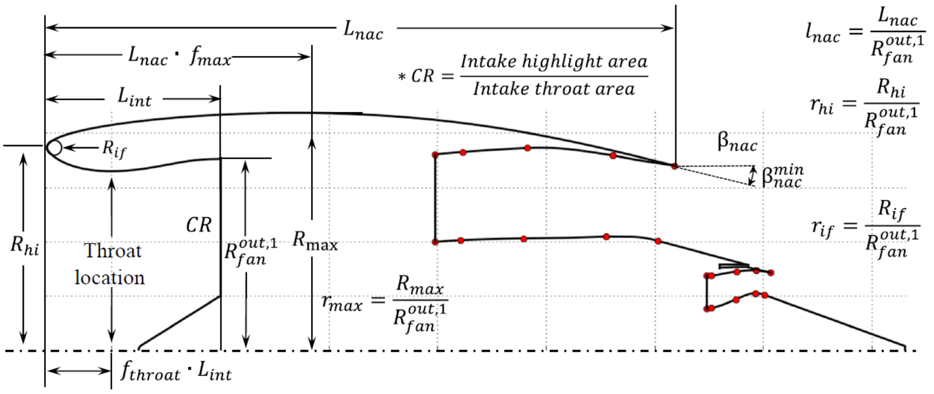

Figure 3-7: Normalised design parameters for the nacelle component of GEMINI [92]

Symbol	GEMINI key	Definition	Unit	Description
l_{nac}	`l_nac_ratio`	$\frac{L_{nac}}{R^{out,1}_{fan}}$	–	Normalised nacelle length
r_{hi}	`r_hi_ratio`	$\frac{R_{hi}}{R^{out,1}_{fan}}$	–	Normalised intake highlight radius
r_{if}	`r_if_ratio`	$\frac{R_{if}}{R^{out,1}_{fan}}$	–	Normalised intake nose curvature radius
r_{max}	`r_max_ratio`	$\frac{R_{max}}{R^{out,1}_{fan}}$	–	Normalised nacelle maximum radial thickness
f_{max}	`f_max`	$\frac{L(R_{max})}{L_{nac}}$	–	Normalised axial location of maximum radial coordinate
β_{nac}	`beta_nac`	–	degrees	Nacelle trailing edge afterbody angle
β^{min}_{nac}	`beta_nac_min`	–	degrees	Nacelle trailing edge wedge angle
f_{throat}	`f_throat`	$\frac{L_{throat}}{L_{int}}$	–	Normalised throat axial location
CR	CR	$\frac{R^2_{throat}}{R^2_{hi}}$	–	Intake contraction ratio
f_{infl}	`f_infl`	–	–	Axial location of intake inflation point (leave to zero)

Table 3-6: Normalised design parameters for the nacelle component of GEMINI [92]

To generate a design with the least difficulty, the model started as the default example provided in GEMINI, to which changes were gradually applied until the desired geometry obtained. The changes include specifying the required fan radius, and axial distance of the engine; from spinner-nose to LPT exit. Additionally, some of the nacelle characteristics were copied from a scaled version of one of the more conventional nacelles utilised in NASA's ADP studies, as this was the origin of the fan geometry, (*ref. Ch 3.2.1*). As such, the nacelle fore-body & inlet geometries should remain compatible with the fan's operating regime, and has been previously demonstrated to perform well, [94] even at high incidence. *Figure 3-8* shows the annular model that was created in GEMINI, overlapped with the ATLAS model. *Figure 3-9* compares the GEMINI model with the relevant ADP nacelle (which has been scaled to the same fan diameter). The region between the fan inlet & OGV outlet is defined as part of the fan/OGV design.

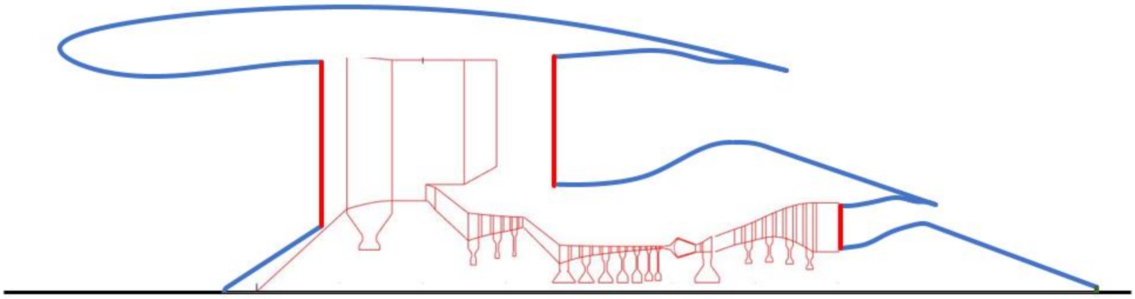

Figure 3-8: GEMINI produced geometry with ATLAS overlay

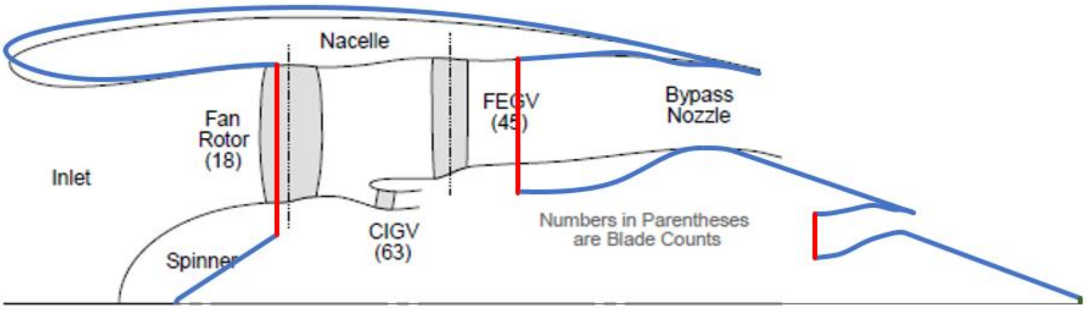

Figure 3-9: Comparison between GEMINI & ADP nacelles [47]

It can be seen in *Figure 3-9* that the nacelle has retained the approximate inlet profile for the nacelle lip. There is some variation due to the change in contraction ratio required to retain the same fan inlet Mach number at cruise, given the difference in spinner design and fan hub/tip ratio. The variation in the bypass hub-line downstream of the nozzle exit plane can also be ignored, as this is how the ADP test-rig was mounted by NASA within the wind tunnel. [47]

There is also considerable difference between the spinners of the two designs in *Figure 3-9*. The ADP features a domed spinner, atypical on modern turbofan engines. It was decided to stick with the more conventional conical spinner, that was defined in the pre-existing GEMINI model. Additionally, the nacelle created was axisymmetric, which is not normally the case for modern turbofans. However, given the nature of the study, it was expected that featuring this in the CFD model would have a marginal-at-best impact on the reverser aerodynamics. Therefore, the model remains axisymmetric throughout this report, which simplified the tasks of meshing, and integrating with other components.

The most valuable contribution from GEMINI to the annular geometry is the design of the bypass and core exhaust nozzles. The requirement of annular lines which provide the correct nozzle exit areas, whilst not imposing excessive aerodynamic losses is not an easy task to conduct manually. The nozzle exit-areas, as mentioned earlier, are defined by the TURBOMATCH engine results file.

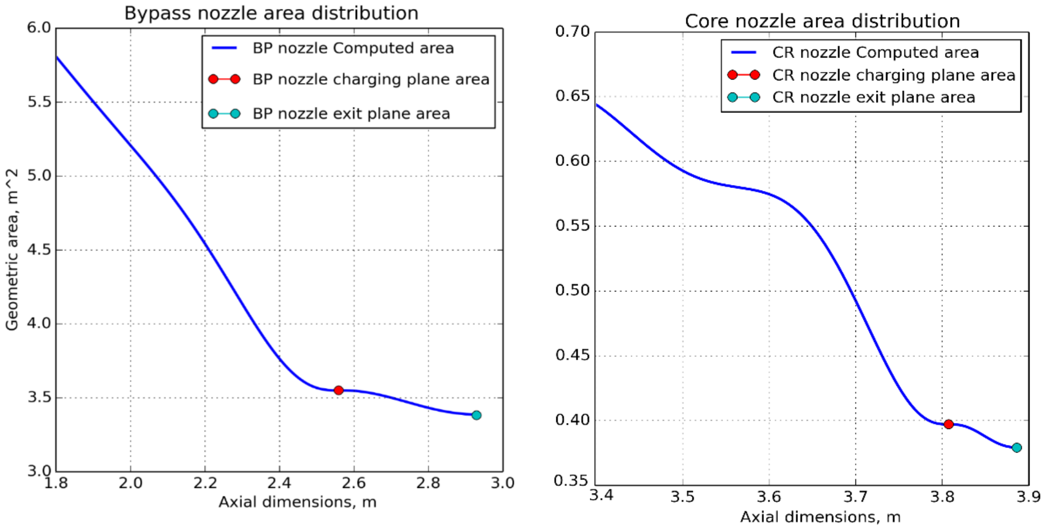

Figure 3-10: Area distributions for bypass & core exhaust nozzles

The nozzles are both convergent, as can be seen from the area distributions plots in *Figure 3-10* above. The 'axial dimensions' on the x-axes refer to the axial distance from the fan spinner leading edge. Furthermore, with reference to *Figure 3-11*, the bypass nozzle is estimated to be near critical Mach number during cruise, which provides additional reassurance that the output geometry is appropriate. The reader can review the geometric parameters for the nacelle design carried forward in *Appendix A*. The GEMINI generated annular model was meshed in ICEM, and a lightweight verification case was tested in CFX, (as this was the solver used throughout this study). The design was eventually integrated with the airframe geometry, to form the external domain of the simulation model. Additionally, the annular lines upstream of the bypass and core exhaust nozzle charging planes were separated, so that the internal regions could be meshed separately.

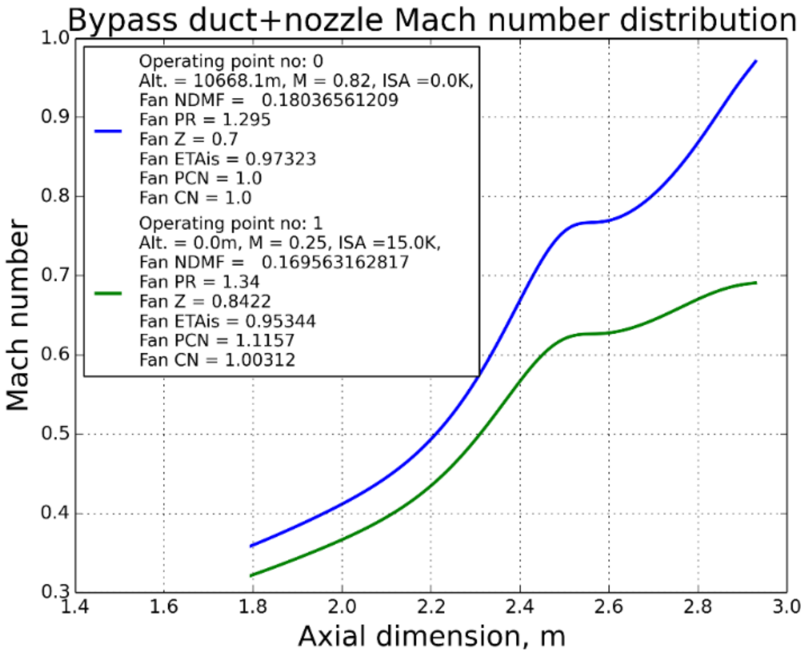

Figure 3-11: Mach number distribution for bypass nozzle

3.3 Turbomachinery

3.3.1 Baseline Fan & OGV

The most critical component to the development of the research model for this project, is arguable the variable-pitch fan itself. Highly efficient fans are difficult to design correctly, given their physical size, wide operating regimes, and the likelihood of encountering difficult to anticipate phenomena, (such as vibration modes) under certain conditions. These challenges are magnified when adding the variability of a VPF. Given the multi-disciplinary aspect of the geometry development undertaken on this project, constructing a VPF fan model from scratch was deemed an unrealistic undertaking, given the already restricting time constraint. Therefore, an alternative needed to be sourced. It came to attention of this project that a similar study was being conducted at the Rolls-Royce UTC based at Cambridge University. The study focusses primarily on CFD predictions and analysis of NASA’s 22” ADP variable-pitch fan under reverse-thrust conditions, from a fan-performance perspective, rather than a systems level approach. After discussions with the Cambridge project, it was decided that the ADP geometry would be adopted for this research program also.

The ADP was chosen for several reasons:

- The FPR and BPR are well suited to an engine with a lower specific-thrust than current hardware. The BPR is not overly ambitious though; 13.3 compared with today's maximum of about 10. [94]
- The FPR is also sufficiently low to necessitate the VPF during normal operation, to avoid fan stall/flutter (*ref. Ch 2.6.1*).
- Extensive CFD and experimental data under forward-thrust pitch has been published by NASA over the last 20 years. [44, 45, 46, 47, 95, 96]
- The design is still considered relatively modern, featuring a conventional wide-chord style fan blade, with diffusion-controlled profiles.
- The ADP was designed to cruise at Mach 0.8, 30,000 ft; very close to the operating conditions of the UltraFan™, which the engine model developed in this study is meant to represent. [88]
- The design is suited for thrust-reversal through feather, having a solidity just above 1 towards the hub.
- The baseline ADP geometry had already been extracted by the Cambridge UTC study from NASA publications, so the geometry was readily available. Utilizing the same fundamental fan definition would also maintain comparability between the studies.
- Additionally, the Cambridge study provided additional insight into 'clean flow' reverse-thrust performance of the baseline ADP numerical results using their in-house CFD code. The Cambridge simulations utilized a two-equation Spalart-Allmaras turbulence model. This was crucial in establishing a degree of certainty regarding the simulated fan performance, and deciding on the reverse-pitch fan configurations to investigate on the integrated research model.

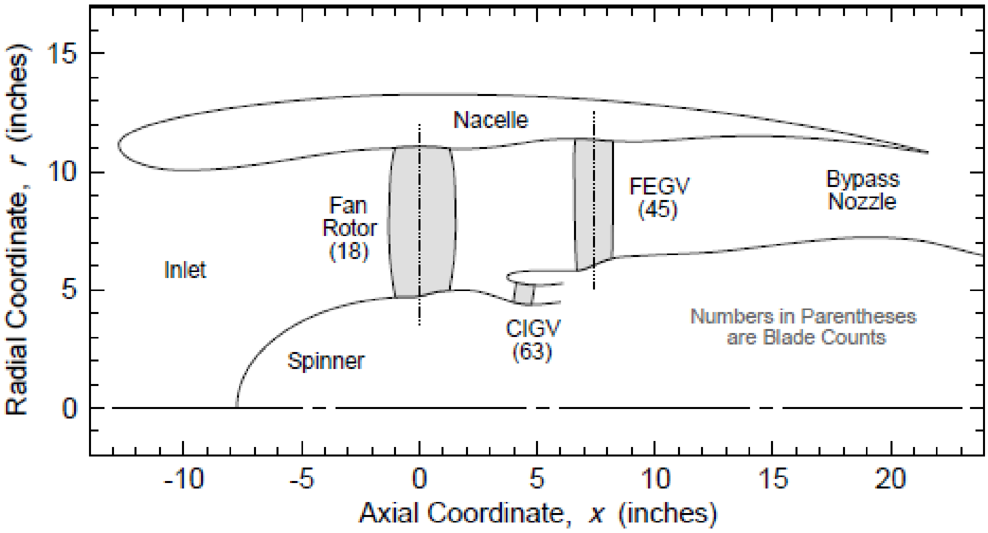

Figure 3-12: Annular schematic of the 22" ADP [96]

Figure 3-12 presents an annular schematic of the ADP, including the specified number of blades for the fan, fan-exit-guide-vanes (FEGVs: same as OGVs), and core-inlet-guide-vanes (CIGVs: same as ESSs). A summary of the 22" ADP performance parameters at the 4 main operating conditions that have been published are presented below in *Table 3-7*. The data was taken for the highest performing variant, as the 22" ADP was operated with two fans (titanium & graphite composite), and two types of fan blade tip seals. [45] The fan's total pressure & temperature radial profiles are provided in *Figure 3-13*.

Parameter	SLTO*	Cruise (DP)	Cutback	Approach
BPR	11.49	13.30	11.73	9.95
FPR_{BYPASS}	1.282	1.294	1.205	1.099
FTR_{BYPASS}	1.078	1.088	1.058	1.029
Adiabatic Efficiency	0.936	0.937	0.9475	0.9412
Fan RPM (%N1)	8,750 (104.2%)	8,400 (100.0%)	7,525 (89.5%)	5,425 (64.6%)
Fan tip speed (U)	256 m/s	246 m/s	220 m/s	159 m/s
Blade pitch setting	-9˚	0˚	-9˚	-9˚
Mass-flow$_{corrected}$	36.11 kg/s	41.65 kg/s	31.23 kg/s	22.73 kg/s

**SLTO refers to sea-level take-off*

Table 3-7: Performance data for the 22" ADP fan [45, 47]

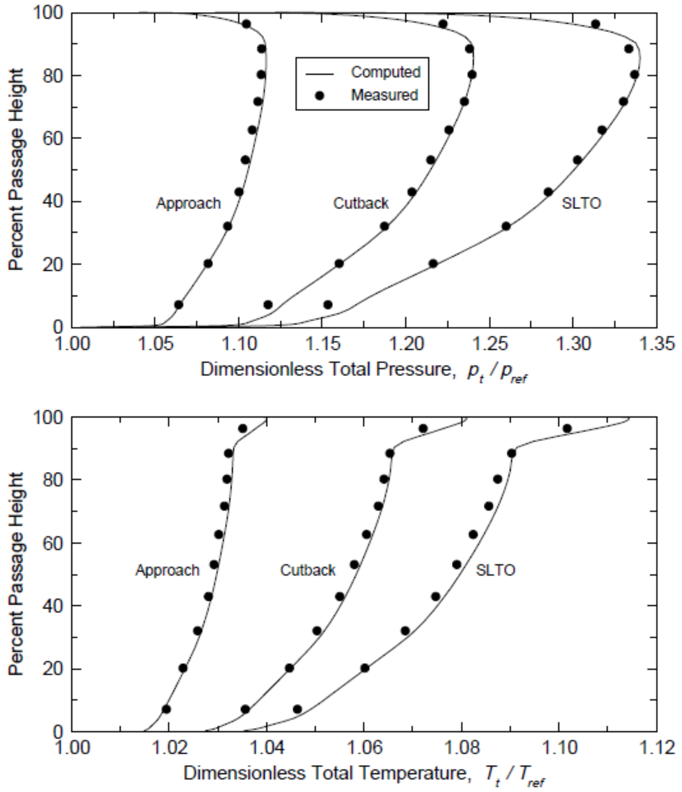

Figure 3-13: ADP fan radial performance profiles for -9˚ pitch setting [47]

The geometry of the turbomachinery components was determined from data available in the public domain by the Cambridge VPF study, rather than provided by NASA itself. The blade has been tested operating at three different pitch settings during forward thrust operation. The blade pitch at design-point cruise is used as the reference, with pitch deviations measured from this. -9˚ & -15˚ were also used, where the blades are closed slightly. These settings are utilized during low flight speed, such as approach & take-off, where volumetric flow capacity through the nozzle is reduced. The blade angles are presented in *Figure 3-14.*

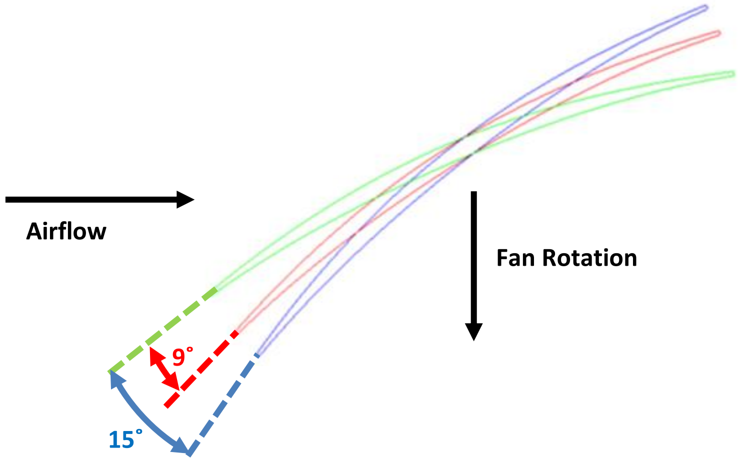

Figure 3-14: 51% span ADP pitch settings as documented for forward thrust operation [97]

The files provided by Cambridge UTC consisted of the following geometry, all defined as point data in .csv format, compatible with most CAD & geometry handling suites. For all future reverse, FEGV and CIGV stages will be referred to as ESS & OGV, following the format convention of this work.

- 2D annular lines for the spinner, fan hub & core inlet/ESS hub
- 2D annular lines for the shroud from nacelle lip to OGV outlet
- 2D annular lines for the bypass splitter, OGV hub, & core inlet/ESS shroud
- 26 radially stacked profiles for a single fan blade
- 27 radially stacked profiles for a single OGV blade
- 3 radially stacked profiles for a single ESS blade

These point-data based models are presented assembled in *Figure 3-15*.

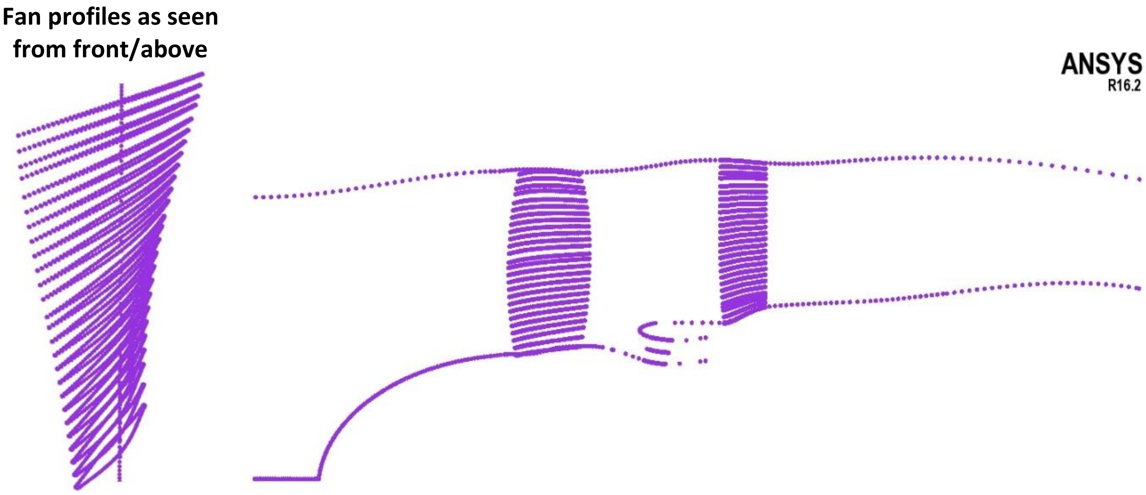

Figure 3-15: ADP raw point-data visualised for the annulus & 3 blades

The geometry was split up into 4 sections, each to be meshed separately; the fan, the OGV, the ESS, and an interconnecting mesh between the fan and OGV/ESS domains, as shown below. This was so that the blade passage domains could be meshed automatically using ANSYS Turbogrid. The interconnecting mesh, known as the ‘middle-passage’ was meshed manually in ANSYS ICEM. A 2D annular mesh was first created, which was extruded rotationally into the third-dimension. Additionally, domain extensions were added upstream of the spinner, and downstream of the OGV & ESS blades to provide adequate flow settling between the domain boundaries, and the areas of interest.

These methods are explained in further detail in *Ch 3.5.2*. *Figure 3-16* provides a cross-sectional overview of the computational model domains.

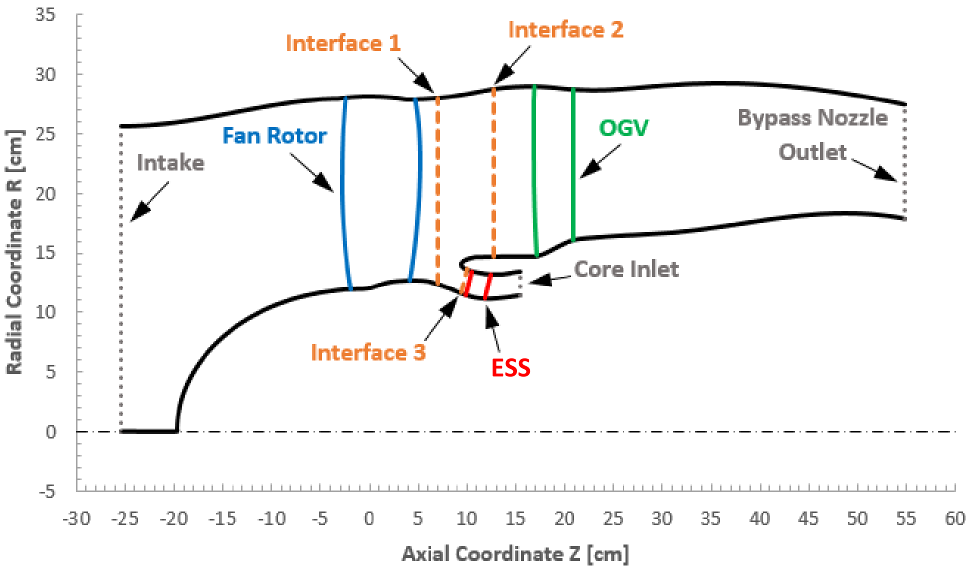

Figure 3-16: ADP geometry split into 4 separate domains for the CFD modelling [97]

Two different fan blade angles were simulated as part of this study, for validation of the geometry definition and the CFD method. The angles chosen were; 0˚ (design-point cruise), and -9˚ (cutback & approach, &sea-level take-off/SLTO). The reasoning behind these choices was; the cruise performance is of most importance, as this is where a turbofan engine normally spends most of its time, and is designed to operate at peak efficiency. However, the published data from NASA documents mainly the SLTO, approach & cutback conditions. Therefore, two fan domains were created; one with the blade at cruise pitch, and one at -9˚. The domains were then assembled in CFX-Pre, and appropriate cases were setup to recreate the 4 published operating conditions for the simulation. Certain adaptations were made to the model, to simplify the meshing process. Rotor tip clearance on the fan blades was not featured in the solver. This adds time & complexity to both meshing and solver processes, and it was not expected that this would have a noticeable impact on the simulation results.

Furthermore, the ADP fan blades sit upon discs on the hub/spinner, which are part of the actuator mechanism. This disc is limited in size due to the presence of adjacent blades. As a result, the ADP fan blade hub leading and trailing edges essentially float, with gaps beneath the blade tips and the hub casing. The clearance gaps are located at 18.5% & 72.5% of the blade chord, which can be seen in *Figure 3-17*. The average clearance gap heights were recorded at about 0.34 and 0.47 mm for the leading & trailing edges respectively. [47] However, these have also been excluded from the CFD modelling; a VPF through-feather design is not mandated to feature this, and the added complexity to the meshing process is not expected to have noticeable difference on the overall flow-regime through the fan – given the very small gap height. Further details of the fan validation work undertaken, is provided in *Ch 4-2*.

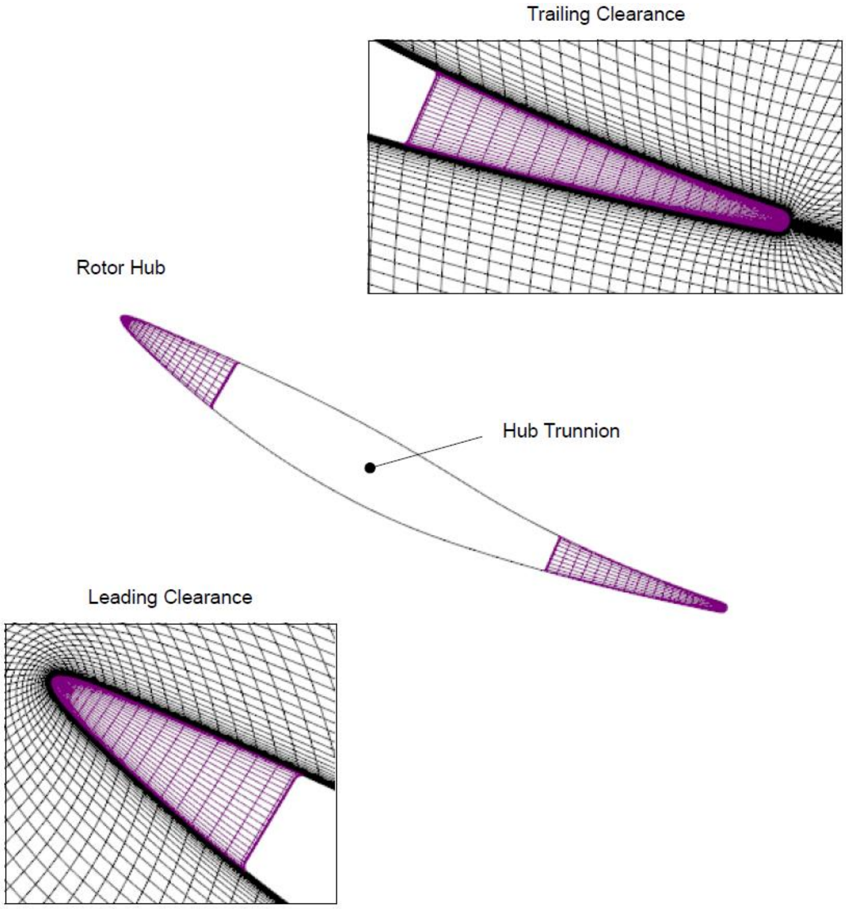

Figure 3-17: Hub LE & TE clearances [47]

3.3.2 Fan Scaling & Adaptation

Having successfully validated the Cranfield ADP geometry against both experimental & CFD data published in open literature (*ref. Ch 4.2.1*), the next step in developing the fan & OGV was to adapt the models to fit the full-sized engine. This required two fundamental tasks; scaling the fan to the appropriate physical size (based on fan diameter), and adapting the geometry to suit a lower hub/tip ratio design. The 22” ADP features a hub/tip ratio of 0.426 for the fan blades. [86] The fan is sized based on the volumetric flow it is designed to operate with. As the hub/tip ratio determines the size of the hub relative to the fan diameter, a high value will result in a larger fan diameter. It is preferable then, to keep the hub/tip ratio under control, to reduce the size of the engine profile, and thus the inherent momentum drag. However, the requirement for a gearbox and VPF actuation mechanism to be housed within the hub imposes additional constraints how low the hub/tip ratio can feasibly be reduced. After discussions with the industrial sponsor, it was believed that a hub/tip ratio of 0.3 could be achievable on a full-scale VPF turbofan – as the fan diameter for a low specific-thrust engine is proportionally greater than the core, compared with modern designs (of higher specific thrust). Therefore, the ADP fan blade geometry needed to be adapted from a hub/tip ratio of 0.426 to 0.3, in-line with the annular engine model components mentioned previous. This task was undertaken in the context of Cranfield’s independently developed turbomachinery throughflow code; SOCRATES. The work itself was conducted with the assistance of another doctoral propulsion-researcher within Cranfield, whose own project focusses primarily on SOCRATES. The fan & OGV geometries were loaded into SOCRATES, and the profile data (camber line, thickness distributions, inlet/outlet angles) were interpolated. The fan adaptation process required four stages of development. The first was to reduce the hub annular walls to suit the new hub/tip ratio, as can be visualised in *Figure 3-18*. The stacked radial profiles which define the fan blade, were then redistributed across the new blade height by scaling the blade, to maintain aspect ratio.

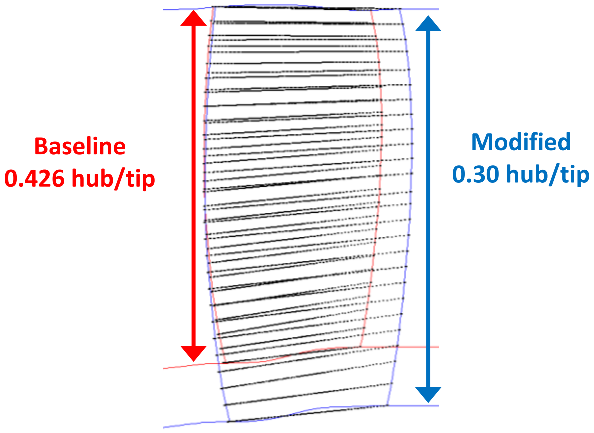

Figure 3-18: Comparison between original and hub/tip modified ADP fan blade

The second step was to realign the blade profiles to correct their respective inlet angles; as changing the radial location of a profile changes its blade speed, and therefore velocity triangles. This was carried out by making small corrections to the blade stagger for each of the 26 profiles, such that there was minimal flow incidence onto the blade inlet. Reducing the hub/tip ratio by lowering the hub, rather than extending the tip, results in the misalignment being concentrated towards the root of the fan. The tip region; aerodynamically most critical to get correct in the design, is left largely undisturbed.

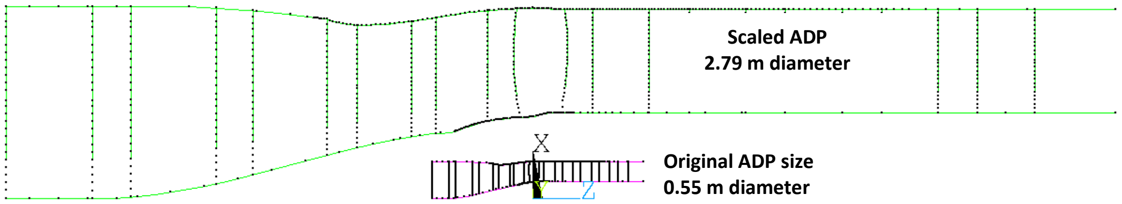

Figure 3-19: ADP original and scaled fan sizes compared

The third step was to scale the ADP model from its baseline size of 0.55 m, to 2.79 m; the fan diameter required to integrate with the annular engine model. This process was straightforward, with a scaling factor of 507% applied to the model in all 3 axes, shown in *Figure 3-19*. At this point the modified & scaled fan was taken out of SOCRATES for reproduction and testing in CFD. Before this was conducted however, the new annular lines for the spinner/fan hub were generated. The spinner was changed from a domed-type to a conical-type, with a sloped angle of 30˚. This is the default value in GEMINI, but also corresponds with measurements taken from Trent 1000 cross-sectional diagrams in the public domain. The shroud was left unchanged during the turbomachinery development models. The resulting fan domain can be seen in *Figure 3-20.*

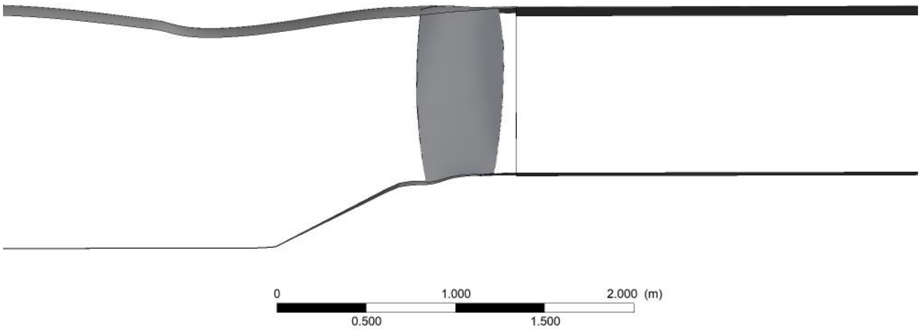

Figure 3-20: Meridional view of single passage scaled ADP-based VPF

The model was then tested in CFD as a ducted single passage fan, with extended inlet and outlet. It was found that the changes made to the blade passage due to the lower hub/tip ratio, even after the staggering process, were causing very poor aerodynamic performance at the hub. A consequence of lower hub/tip ratio is the higher solidity towards the root – as the blades are physically closer together than before. This can be seen by comparison of the two fans shown in *Figure 3-21*. This also has implications in the range of pitch-variability. As such, the maximum reversal pitch-angle that can be obtained before blade tangle was approximately -100 degrees. This is still comparable to the original design, which is quoted to be capable of just over -100 degrees. [42]

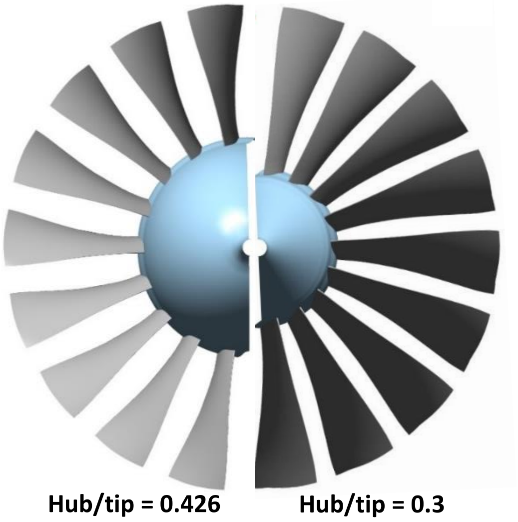

Figure 3-21: Comparison between fan blades with different hub/tip ratios

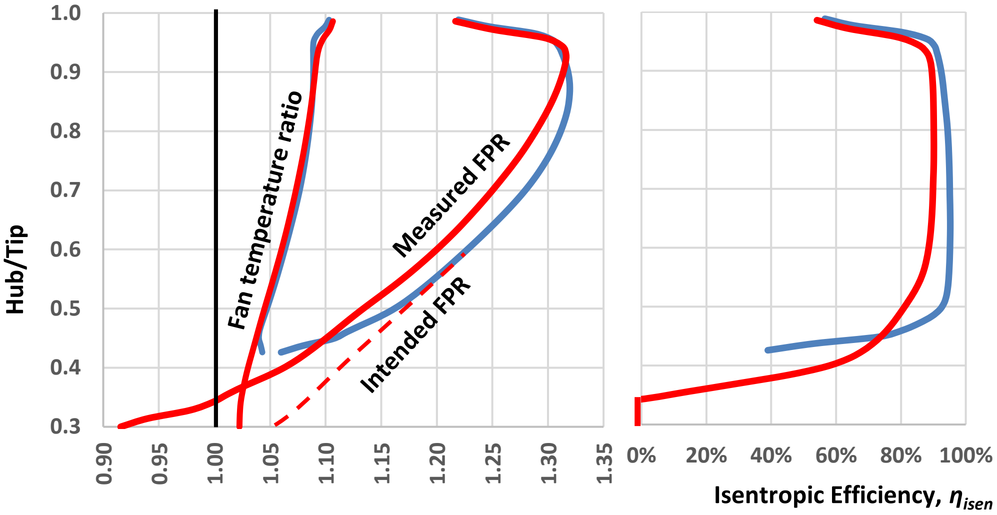

Figure 3-22: Span-wise comparison of FPR, FTR & η_{isen} for original & modified ADP fans

It can be seen from *Figure 3-22* that at the new section of hub on the modified VPF, between a hub/tip ratio of 0.3-0.426 (corresponding with 0-15% span), the efficiency begins to plummet, as the total pressure ratio drops below unity. This needed to be addressed; if the fan could not perform adequately at design point, there was little point in progressing further to explore reverse thrust.

The pressure loss at the hub has a knock-on effect to the blade in general, reducing the overall FPR by about 0.025 along the comparable span sections. This can be better understood by comparing the local blade-to-blade flow fields, as provided in *Figure 3-23.*

Due the narrowing of the blade passages at the hub, the flow capacity is reduced; resulting in a higher peak Mach number across the suction-surface. This change in flow passage dynamics, coupled with the high thickness and curvature of the hub profiles, results in boundary layer separation, or ‘stall’, immediately downstream of throat.

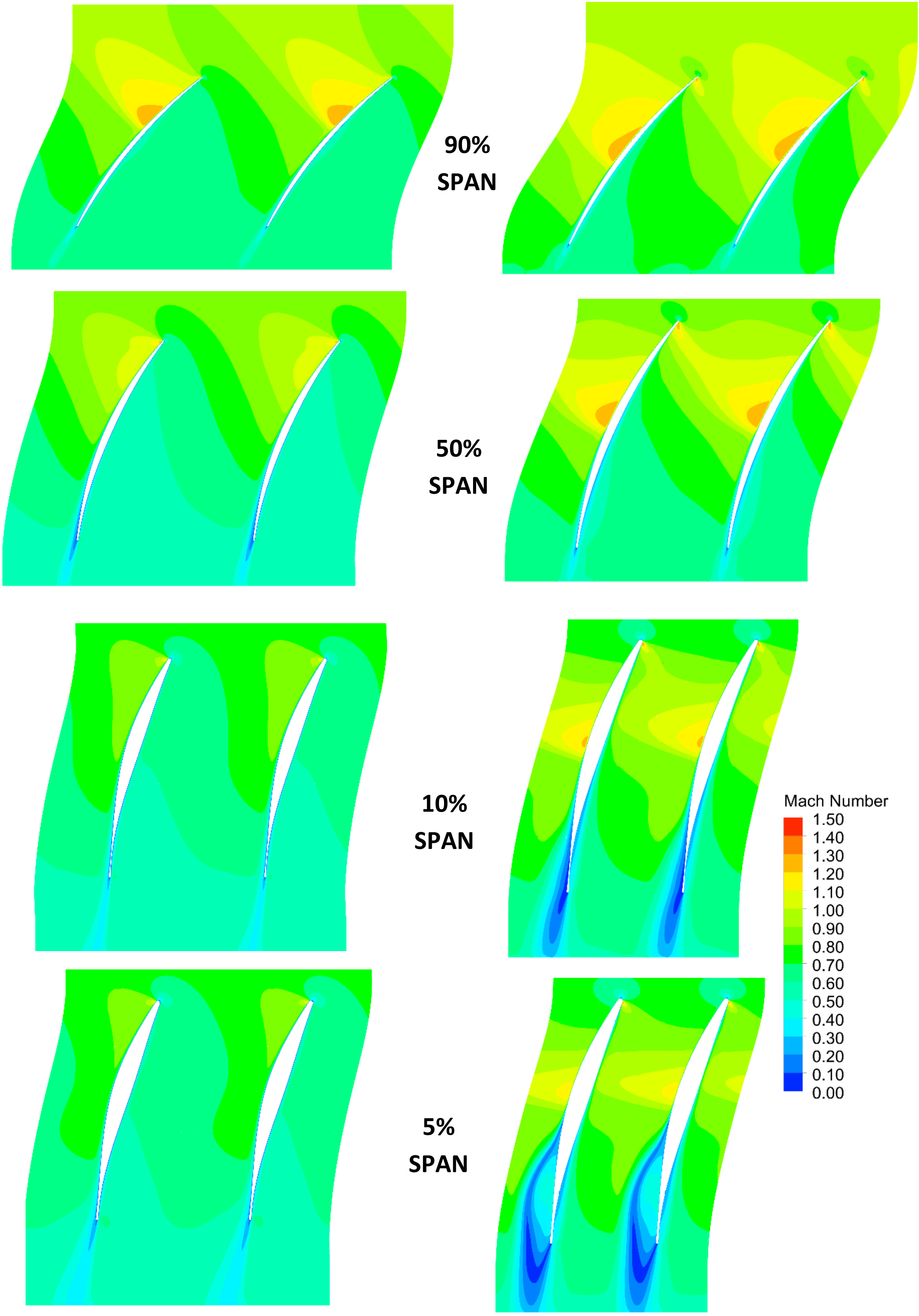

Hub/tip = 0.426 **Hub/tip = 0.3**

Figure 3-23: Mach Number field comparison between original and modified ADP fans

Given the low blade number (18) and the original solidity characteristics, it was hoped that the hub/tip ratio modifications made would not result in performance degradation to this extent. There are however, a number of ways to address these issues without radical changes to the fan geometry. Three parameters were identified, that if minorly adjusted, could potentially address this separation issue, and restore the hub performance, without sacrificing excessive man-hours.

- % Max Thickness, ($\%T_{max}$) – Changing the maximum profile thickness (measured as % of the local blade chord), would reduce the diffusion rate in the passage, and increase the volumetric flow capacity. The thickness for the hub region profiles were reduced, to increase flow capacity, thus decreasing the peak velocities in the blade passage.
- Distance of Max Thickness from LE, ($\%T_{max}P/Z$) – Relocating the location of maximum thickness along the chord of the blade can help reduce choking through the blade passage by changing the throat location, and thus area. The baseline ADP max thickness lies between 35-52% of the chord, depending on span-wise location. For the modified VPF, the max thickness at the hub profiles was moved towards the rear by approximately 5-10% chord length. Additionally, the thickness location along the entire span was the adjusted to allow a smooth distribution, preventing the blade from becoming distorted due to incompatibility between the layers.
- Stagger Angle, (ξ) – Closing the blade profiles at the hub would lower axial velocity, reducing the volumetric flowrate through the passages. This would lead to a reduced Mach number profile. Again, the hub sections were re-staggered, to reduce blade passage peak velocities.

These three parameters are easily changed within the SOCRATES model. Two new version of the blade were created, one with only thickness changes applied, the other with both thickness and stagger angle changes. Only the 6 profiles nearest the hub wall were changed. Details of the modifications are presented in *Table 3-8*. These two modified fan geometries were then exported into Turbogrid, and tested in CFX at cruise, alike the previous models.

Profile # (% Span)	Modified VPF Version 1			Modified Thickness		Re-staggered
	Stagger, ϰ	**TmaxP/Z**	**Tmax**	**%TmaxP/Z**	**%Tmax**	**Stagger, ϰ**
6 (20.0%)	16.5˚	35.0%	5.1%	41.3%	5.1%	16.5˚
5 (16.0%)	15.9˚	34.7%	5.6%	41.3%	5.0%	17.9˚
4 (11.9%)	15.5˚	34.9%	6.2%	41.8%	5.6%	16.0˚
3 (7.9%)	15.4˚	35.5%	7.0%	42.8%	6.3%	18.4˚
2 (3.5%)	15.8˚	37.2%	8.9%	44.8%	7.5%	19.1˚
1 (-0.9%)	16.7˚	40.0%	11.5%	48.0%	8.5%	20.7˚

Stagger, ϰ *refers to the stagger angle of the blade profile,*
%T$_{max}$ *refers to the maximum thickness of the blade profile, as a percentage of the chord length. The blade chord was kept constant, so % thickness is directly proportional to actual thickness.*
%TmaxP/Z *refers to the location of the maximum thickness point for the blade profile, as a % of the blade chord.*

Table 3-8: Changes to stagger and thickness to address poor fan hub performance

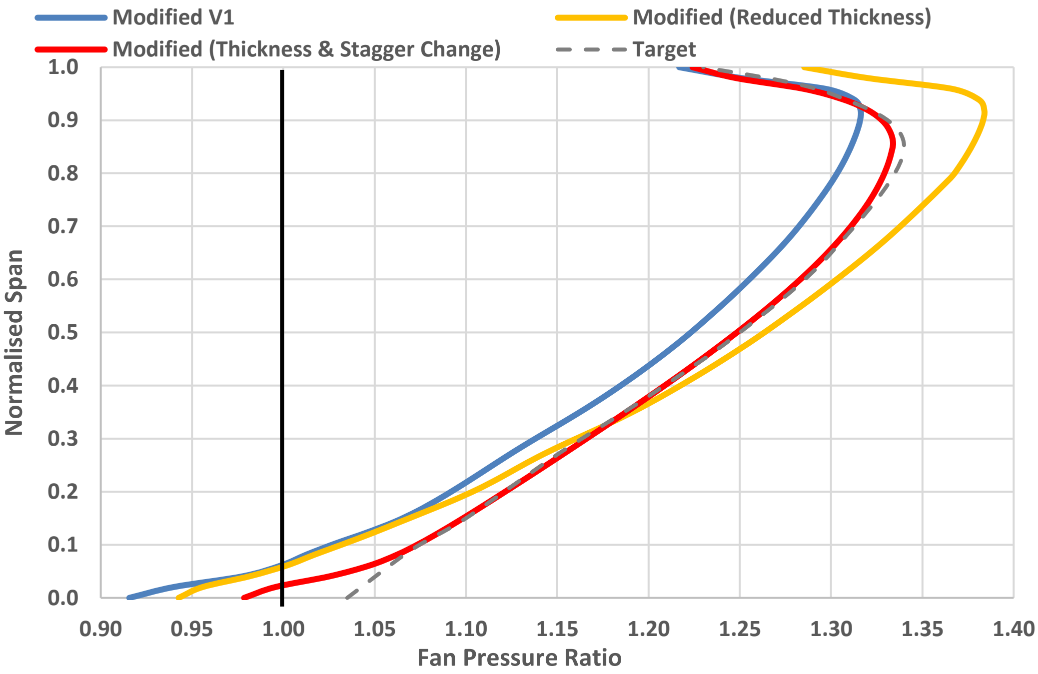

Figure 3-24: Span-wise FPR profiles for modified (0.3 hub/tip) fan at cruise

From the comparison of span-wise FPR in Figure *3-24*, it’s clear that the blade featuring both modifications was most effective at resolving the poor performance, with a hub pressure ratio value of approximately 1.0, rather than a loss. Whilst not achieving the intended profile, analysis of the aerodynamics suggested the separation issues were largely addressed, particularly by the re-staggering of the blade. The isentropic efficiency span-wise profile is also presented, in *Figure 3-25.*

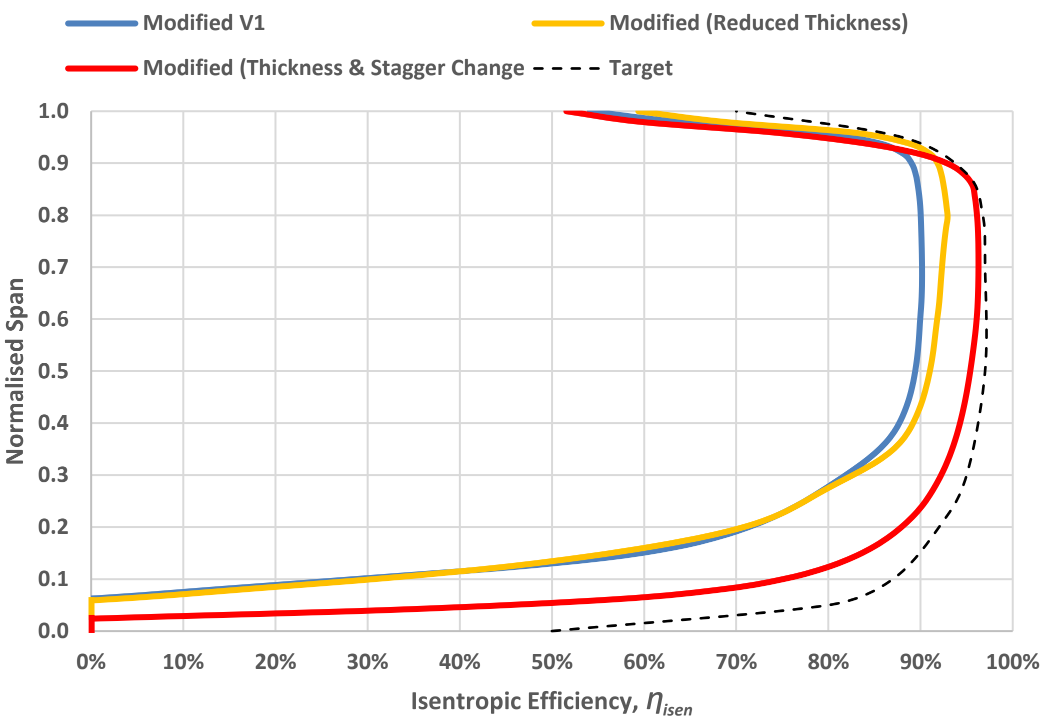

Figure 3-25: Isentropic efficiency profiles for the three modified fans

Figure 3-26 presents a comparison between two of the modified blades, where the re-staggering of the profiles is shown to reduce the extent of trailing edge flow delamination.

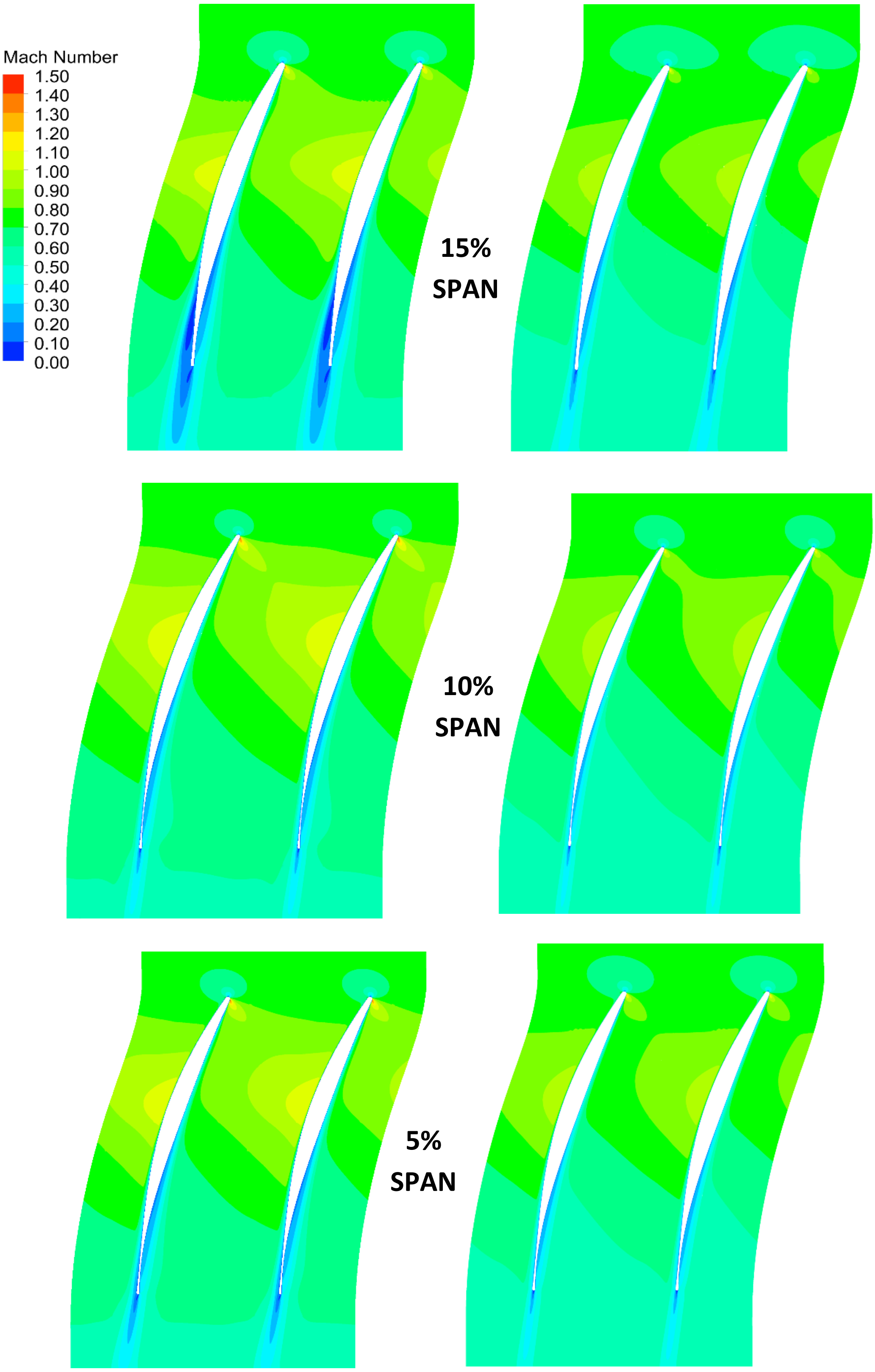

Reduced Thickness **Reduced Thickness & Re-staggered**

Figure 3-26: Hub region Mach number contours for the two improved fan blades

Reducing the hub separation and associated pressure losses restored the efficiency profile for the fan. Whilst not quite achieving the target efficiency, the fan was significantly improved, most notably below 50% span. Some pressure loss is still witnessed below 5% span. This has been deemed tolerable however, given how localised and marginal the losses are. Above 50% span, the fan retains the ADP's inherent high efficiency.

To summarise, as this doctoral project is a systems-level study; the requirement for the fan model was to be of preliminary design quality, focussing on developing a computationally-robust model, rather than achieving nominal forward-thrust efficiency. Furthermore, given the unusual nature of the reverse-thrust operating regime, engine design philosophy dictates that's, for a mission profile where reverse thrust is only used on landing, little to no compromise would be given to a fan design for operating under these conditions. Any such changes in profile geometry to improve reverse-thrust performance, for a fixed or variable-pitch fan, would almost certainly reduce the blade efficiency under normal operation. Therefore, having resolved the hub flow separation down to an acceptable level for the study, the model was progressed forwards, and work on OGV and related geometries began. A summary of the fan model carried forward is provided below in *Table 3-9*.

Baseline 22" ADP	Parameter	Modified VPF
1.281	**FPR**	1.271
1.078	**FTR**	1.081
0.945	η_{isen}	0.875
42.5 kg/s	**Corrected Fan Massflow**	1191 kg/s
0.198 m^2	**Fan Outlet Highlighted Area**	5.434 m^2
214.6 $kg/s/m^2$	**MF/Outlet Area**	219.2 $kg/s/m^2$
8,400	**RPM**	1,680
245 m/s	**Tip Speed, U_{tip}**	245 m/s
0.55 m	**Fan Diameter**	2.79 m

Table 3-9: Cruise comparison between baseline ADP fan & scaled VPF [45, 94]

3.3.3 Splitter & Core Duct

Having established the fan geometry, a ‘middle-passage’ domain needed to be developed for the new hub/tip ratio design. The passage needed to match with both the fan and OGV domains either side, as well as defining both the bypass splitter profile, and the core inlet duct as dictated by the ATLAS dimensions. It was also decided that the original ADP splitter geometry should be replaced with something more conventional, in line with the project scope. It was decided that a Trent 1000 based splitter would be adopted into the model.

The first stage of the process was to establish a 2D annular drawing in ANSYS ICEM using the fan hub & shroud lines. By overlaying the Trent 1000 hub and splitter annular lines onto the fan & hub shrouds in ICEM, an adaptation could easily be developed by manually translating or adjusting the curves. Coordinates from the ATLAS model were used as reference points for both the splitter leading edge radius, and the IPC inlet axial & radial positioning.

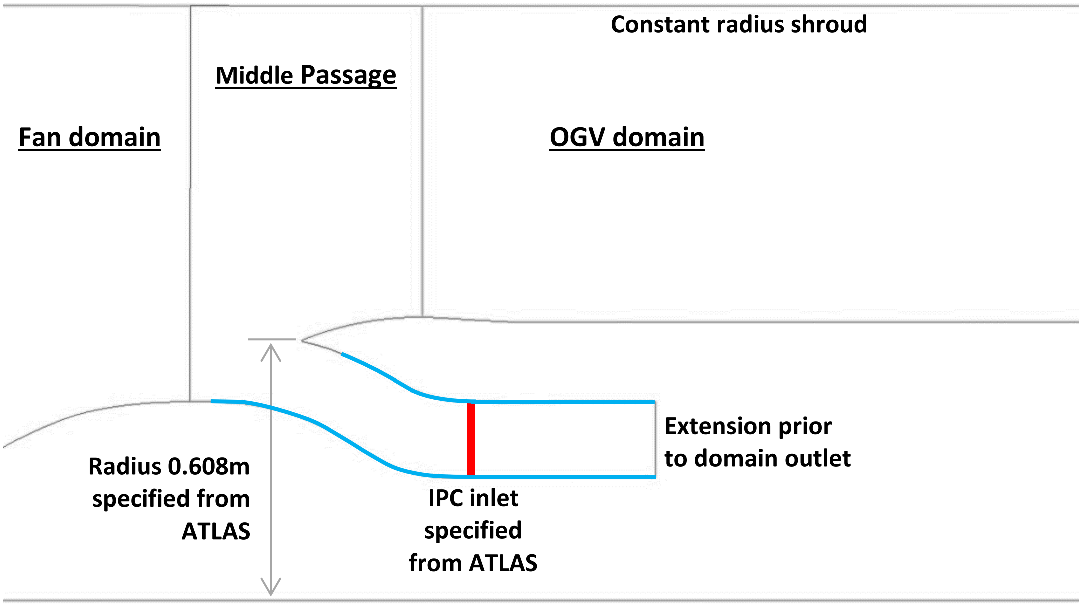

Figure 3-27: Annular view of the developed splitter & core duct geometry

By overlaying the two geometry sets based on fan location, the splitter remains approximately the same position downstream of the fan. The lines marked in blue along the core inlet duct were user-generated, whilst the main splitter profile remains unchanged. The duct was designed such that cross-sectional-area reduction in the swan-neck was controlled with a smooth, approximately linear gradient. As for the splitter location, the default splitter leading edge radius of the Trent 1000 model was only a few centimetres off from the ATLAS model, making integration simple. The shroud was maintained at a constant radius downstream of the fan, for ease of design, and to aid alignment of the meshes during assembly in CFX-Pre. *Figure 3-27* illustrates the new fan, splitter & OGV domains.

Due to a concern with flow dynamics during reverse operation, it was decided the core duct for the large-scale fan model would not feature ESS or IGV geometries. When the engine operates with a reversed-pitch fan, the flow passing up the bypass nozzle gets a swirl induced onto it by the OGV. This includes the flow which was expected to enter the core inlet duct, via turning around the splitter. As the flow is reversed, the swirl is now resulting in an extremely high incidence onto the ESS blades. This can be seen in *Figure 3-28.*

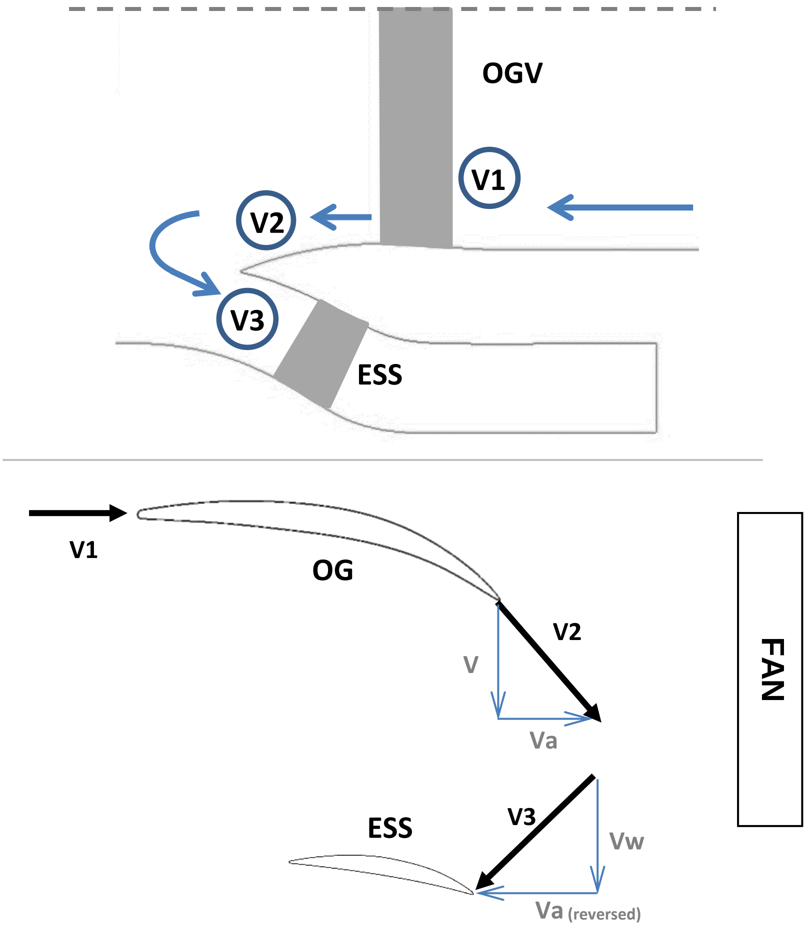

Figure 3-28: Velocity triangles for core intake flow under reverse thrust

With the nearby outlet boundary at the end of the core inlet duct, there were concerns regarding the CFD solver stability. Additionally, if this phenomenon causes significant blockage through the ESS passages, the ability to observe splitter-related flow separation; one of the main project objectives, may be hindered. The splitter was tested together with the scaled OGV, where no issues could be identified; the splitter was properly positioned radially for cruise, with no spillage or flow separation issues with the Trent 1000 based profile.

3.3.4 Scaled OGV

The third requirement within the turbomachinery module was to acquire a suitable OGV geometry. The OGVs main aerodynamic purpose is to negate the bypass flow swirl induced by the fan, such that the nozzle exit flow is wholly axial, maximising thrust. Furthermore, the OGV blades act as forward structural members, connecting the engine core to the nacelle. Having derived the fan from NASA’s 22” ADP, it made sense to first try to adopt the respective OGV models to suit the needs of this study also. This work was also conducted in SOCRATES, alike the fan modifications. The OGV design was ultimately successful, but a second iteration of the model was required, incorporating additional modifications to recover some identified degradation in aerodynamic performance.

The first task was to take the geometry from the baseline ADP OGV model, and scale it to match the correct tip diameter for the VPF engine design. At this point the difference in hub/tip ratio between the original ADP and the newly created bypass annular duct were identified, as was expected. The values of hub/tip ratio for the ADP and VPF engine are 0.5 and 0.46 respectively. Therefore, the blades needed to be enlarged to extend the full height of the new passage.

The geometry was first enlarged following the same technique as the fan; by holding the shroud radius constant, and enlarging the OGV until it fully occupied the new annular passage; maintaining aspect ratio. Redistribution of the radially stacked profiles was then conducted, with the appropriate corrections to inlet angles applied, taken from the already tested modified VPF outlet-flow-angle profile. The new OGV passage featured constant radius annular walls for simplicity & to maintain maximum cross-sectional area; which minimizes velocity associated pressure losses in the duct. The re-appropriation work is visually presented in *Figure 3-29.*

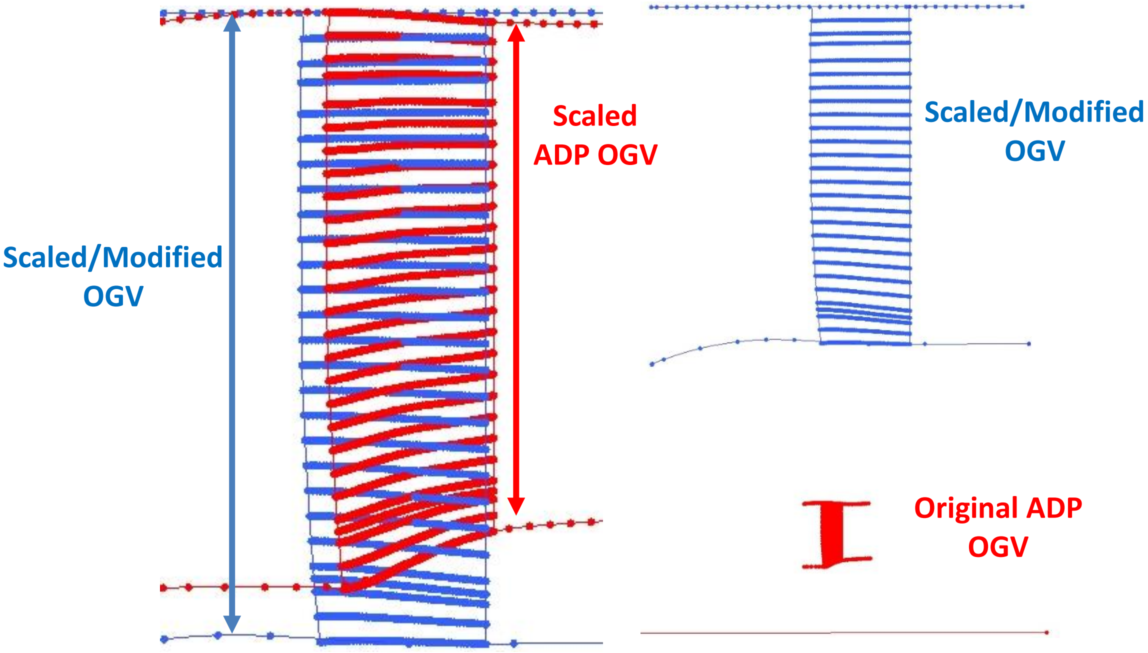

Figure 3-29: Comparison between baseline 22" ADP & scaled/adapted OGV

The final stage involved determining the total number of OGV blades for the VPF engine model that was being developed. The baseline ADP features 45 OGV blades. After initial testing, it was decided that this could be reduced to 40 blades. Reducing the blade number widens the gap between the blades, increasing the throat area through the OGV passages; reducing peak Mach number and the associated total pressure losses with the blade wakes.

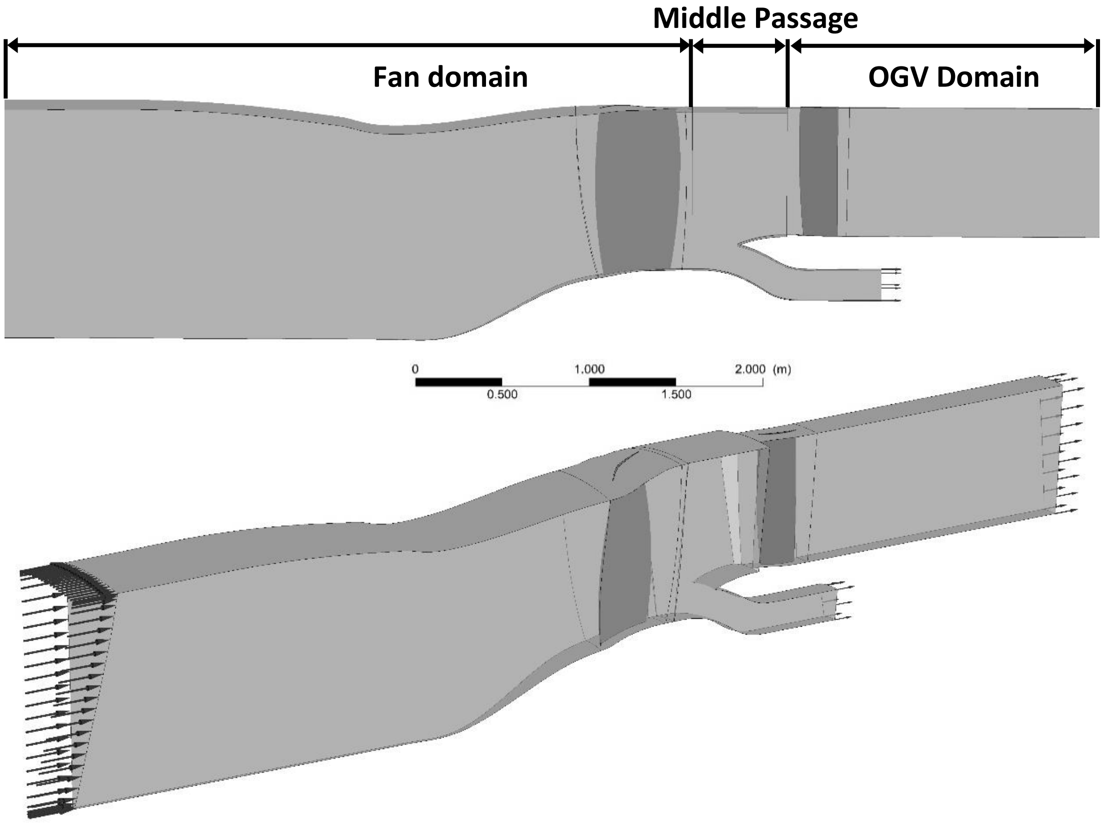

Figure 3-30: Assembled single-passage fan, middle-passage & OGV domains

The newly assembled OGV was exported from SOCRATES, meshed as a single passage, and mounted downstream of the already developed fan & splitter domains. An extension was added to the OGV outlet, such that measurements downstream could be taken, and to ensure no boundary interactions would be experienced in the region of interest, that can be seen in *Figure 3-30*. The 3-domain model was then tested under cruise operating conditions, to ensure the OGVs were correcting the flow swirl as intended. Performance was observed to be adequate, with minimal separation or wake profiles, and calculated mass-flow-averaged exit flow-angle was to within 2 degrees of the axial direction. The design is by no means optimised, and there is room for refinement in the geometry. However, it should provide a perfectly adequate representation of outlet guide vanes for the simulation of VPF reverse-thrust.

3.3.5 Fan Blade Reversal

Having established turbomachinery components which performed adequately at cruise, a decision needed to be made as to which configurations to test the variable-pitch fan for reverse-thrust simulation. At this stage in time, the doctoral study at Cambridge UTC on variable-pitch fan performance had produced some initial CFD results of the 22” ADP in reverse-pitch operation, at three different fan speeds & three different pitch settings. All tested pitch settings were for the through-feather reversal method. The model simulated the engine with ‘clean’ boundaries for the bypass nozzle and nacelle inlet. Nevertheless, it provides the best indication of fan performance characteristics for the ADP, and thus the VPF which has been derived from it under this study.

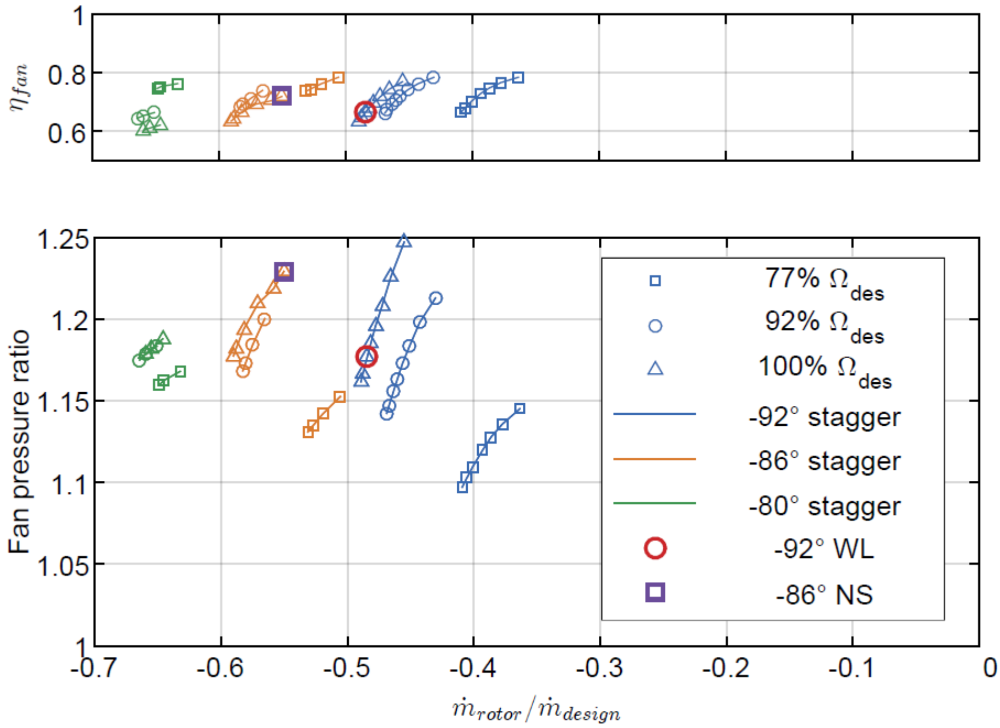

Figure 3-31: Performance map for the 22” ADP in forward & reverse [90]

The compressor map in *Figure 3-31* expresses the two fundamental parameters to producing effective reverse-thrust; the reversed flow FPR & the mass-flow. The FPR must be sufficient to overcome the dynamic head (unless the aircraft is stationary). This is of most concern at the higher-end of the landing speed spectrum, where knowledge on VPF thrust reversal is scarce.

It was decided based on the findings from the Cambridge study to initially test the blade at 92% RPM. From the QCSEE transient performance summary (*ref. Ch 2.7.4*), it was indicated that around 90% RPM was achievable directly after pitch transition, with a starting (forward pitch) RPM of 100%.

Regarding the pitch-setting choice; whilst thrust reverser effectiveness is largely dependent on the reverse-stream mass-flow, there were concerns about the fan's initialisation in the CFD solver. The intention was to conduct a steady-state simulation, the overshoot technique for through-feather pitch reversal (*ref. Ch 2.7.3*), which is a transient operation, cannot be used to establish effective fan performance. It was decided therefore the fan would be tested at -92˚ pitch setting. This is close to the maximum through-feather angle; ~100˚, but from the Cambridge data, still offers a potential of 45% of forward thrust nominal mass-flow. The blade-to-blade passages at 5%, 50%, & 95% span for the -92˚ VPF are illustrated in *Figure 3-32.*

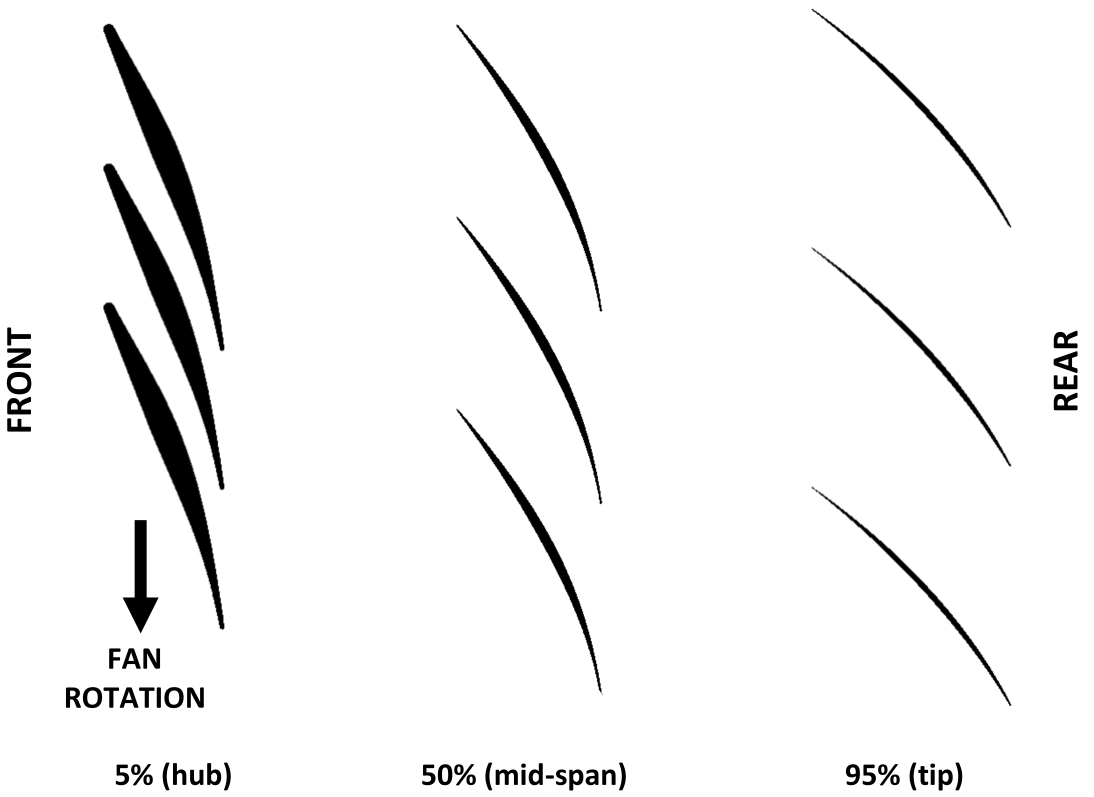

Figure 3-32: Blade-to-blade view at 3 spans for modified blade (-92˚ pitch setting)

3.4 Airframe

3.4.1 Airframe Scaling

The third module which composes the VPF reverse-thrust research model is the airframe. The requirement from the airframe component is to represent conventional architecture of current and near future aircraft, sized for the appropriate thrust/weight class. Most modern medium-sized narrow-body jets currently operate with two podded turbofan engines mounted to pylons under the wings. This is due largely to the achieved standards in engine reliability, enabling twin-engine aircraft to viably operate most routes globally whilst satisfying ETOPS requirements since 1985. [99] The most comparable aircraft in today's current operational fleet is the Boeing 757 series aircraft. It first flew in 1982, and whilst production ceased in 2005, it remains in service to this day, and still represents a modern format medium-sized transonic civil transport jet. The 757 exists in two main formats; the 757-200 series (which includes a freight version), and 757-300 series. The two variants differ only in fuselage length (47.3 – 54.4 m), retaining a common wing (seen in *Figure 3-33*). [100] For this study, the fuselage length is not of importance, but the existence of a common wing across the different variants demonstrates some flexibility in the wing/maximum take-off weight (MTOW) relationship.

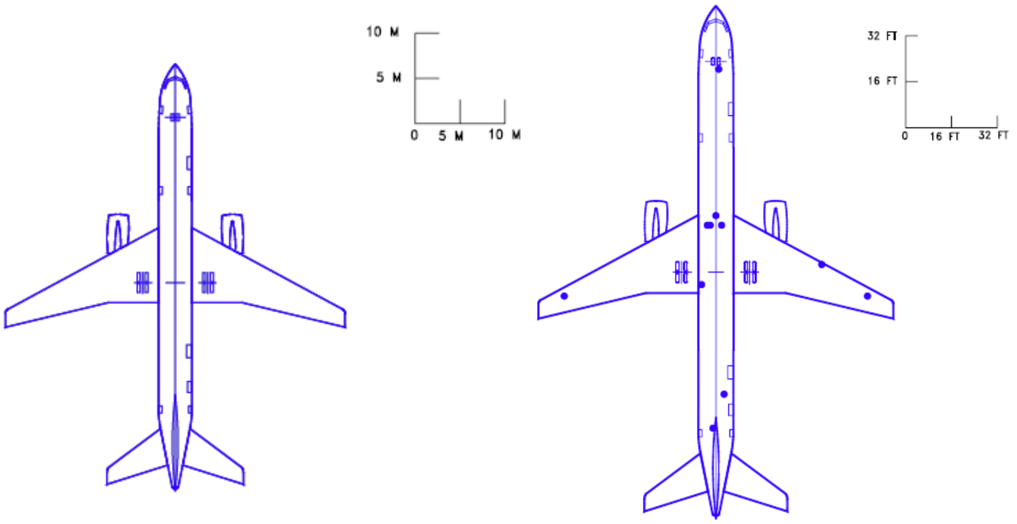

Figure 3-33: Footprint comparison between Boeing 757-200 & 300 variants- same scale [101]

After studying the availability of existing models in open literature, it was decided the most suitable geometry to carry forward was that available from NASA's 2nd high-lift prediction workshop. The geometry used, which is freely available online, is commonly known as the DLR F11, a brief summary of which is provided in *Ch 2.9.4*. The selection of this model was based on two key factors; the availability of published experimental & CFD data, and the suitability of the airframe. The most important reason the DLR F11 was chosen over any of the other CRM variants was the presence of fully-deployed high lift devices on the wing. This includes a single-piece slotted slat on the wing leading edge, deployed to 26.5˚, and a single piece slotted flap on the trailing edge, deployed to 32˚. [85] A version also exists which features the flap & slat linkages and actuator housing pods, although this study makes use of the simpler model for computational ease (seen in *Figure 3-34*).

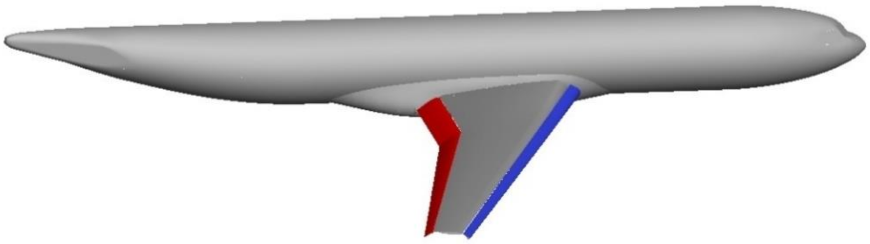

Figure 3-34: DLR F11 geometry, with flaps and slats highlighted in red & blue respectively

The DLR scaling was conducted based on the wingspan measurements of the Boeing 757 series aircraft. The wingspan quoted by Boeing for the 757 wing is 38.05 m. [100, 101] The DLR F11 wind-tunnel model, which the CAD geometry represents has a wingspan of 2.80 m. [85] Therefore, a scaling factor of 13.57 was applied, for a comparison between the two models. The result of which showed that the DLR F11 was surprisingly similar proportionally to the B757, with approximately the same cabin cross-section diameter, and wing area. *Table 3-10* presents a comparison between the scaled DLR F11 and B757 main airframe/fuselage dimensions, visualised in *Figure 3-35.*

Boeing 757-200	Parameter	CU DLR F11
38.05 m	**Wingspan**	38.05 m
47.3 m	**Fuselage Length**	41.77 m
3.76 m	**Fuselage Diameter**	4.0 m
185.25 m^2	**Wing Area**	184.14 m^2

Table 3-10: Dimensional comparison between B757 & scaled DLR F11 [100, 101]

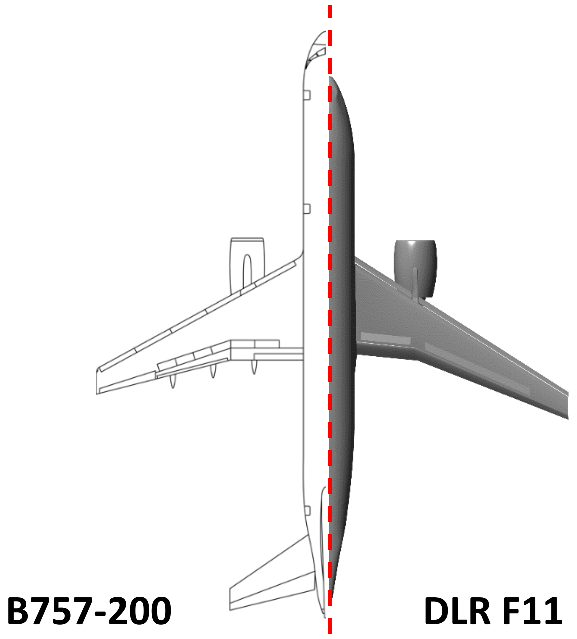

Figure 3-35: Comparison between B757 & scaled DLR F11 footprint [101]

The scaled DLR F11 model was then meshed using ANSYS ICEM. Given the detailed geometry of the wing with flaps & slats, an unstructured meshing approach was adopted. The model was validated against both experimental and numerical results, alongside a mesh independency study. The independency study also established a guideline size for an efficient, but robust unstructured airframe mesh. A suitability check was then conducted, to measure the lift produced by both wings, and compare against published weight data for the Boeing 757-300. *Figure 3-36* presents the measured lifting force for the scaled DLR F11 model. The measured lift was found suitable to support an airframe weight comparable to a 757-300 with a flight AoA of around 0˚

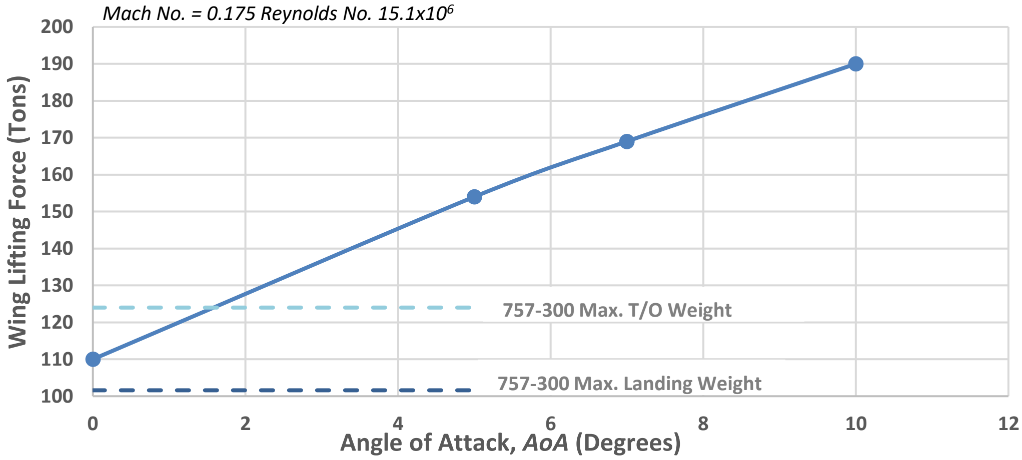

Figure 3-36: Total lift measured for both wings of the scaled DLR at 4 different AoA [101]

To conclude; the numerical method and meshing approach for the airframe were found valid and reasonably accurate, and would provide a suitable environment to develop the pylon & spoiler models.

3.4.2 Spoiler Design

Whilst the DLR F11 model features high-lift devices, it does not fully represent an aircraft configured for braking/reverse thrust operation. Upon touchdown, aerodynamic brakes, known as ‘spoilers’, ‘airbrakes’ or ‘speed-brakes’, are deployed. It was necessary therefore to develop these features for the scaled DLR F11 model, to create an accurate representation of the aircraft braking. Whilst the spoilers do not normally interact with engine aerodynamics, it is not clear whether or not a thrust reversing VPF engine, (which ingests air through the bypass nozzle) is affected by the wing/spoiler wake.

Spoilers, are devices typically fitted to the suction surface of an aircraft’s wing. Located between 25-50% of the wing chord, they are essentially flat plates, that when stowed, form the normal wing surface. When deployed, they impinge on the freestream, disrupting wing aerodynamics, which reduces the lift whilst simultaneously increasing the drag. [102]

Spoilers essentially have four fundamental purposes:[103]

- To operate as air-brakes during landing or aborted take-off, due to the increased aerodynamic drag.
- To act as lift-dumpers upon touchdown, rapidly degrading the wing’s lift coefficient. This transfers the aircraft weight from the wings to the wheels, improving wheel traction and brake effectiveness immediately upon landing.
- Act as speed-brakes during flight; preventing excessive speed being acquired during quick descent from altitude.
- Outboard spoilers are often used in conjunction with the ailerons, to increase the roll responsiveness during low-speed flight, i.e. on approach.

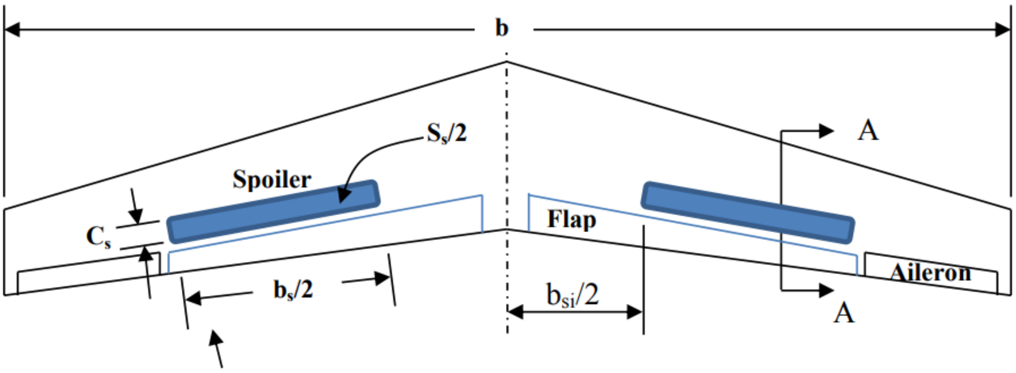

a. Top-view of the wing and spoiler

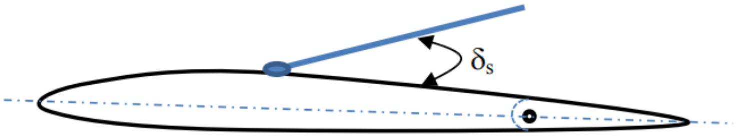

b. Side-view of the wing and spoiler (Section AA)

Figure 3-37: Definition of spoiler geometry parameters [104]

Figure 3-37 presents typical spoiler geometric parameters. *Table 3-11* provides typical values for these parameters from existing aircraft types. Most notably, the spoilers account for about 4-7% of the wing surface area. It is from this set of data that the geometry of the DLR F11 spoilers was defined.

No	**Aircraft**	**Type**	**m_{TO} (kg)**	**S_s/S**	**C_s/C**	**b_{si}/b**
1	Bombardier CRJ200	Regional jet airliner	21,523	0.041	0.07-0.15	0.13
2	Airbus 320	Twin jet airliner	73,500	0.071	0.14-0.23	0.24
3	Boeing 777	Wide-bodied jet airliner	299,575	0.054	0.11-0.14	0.12
4	Airbus A400M	Military transport	126,500	0.06	0.12-0.15	0.3
5	Embraer ERJ-145	Regional jet airliner	20,600	0.045	0.09-0.13	0.11

Table 3-11: Specifications of spoilers for several aircraft types [104]

Given the nature of the spoiler's aerodynamic purpose, the design process is relatively simple. Six identically sized flat plates, of dimensions 2000mm length, 800mm width & 5mm thickness were added to the trailing edge of the wing's suction surface (*Figure 3-38*). The design of the spoilers was undertaken as part of an MSc project in support of the doctoral study. As such, further detail on the process in the relevant thesis. [105]

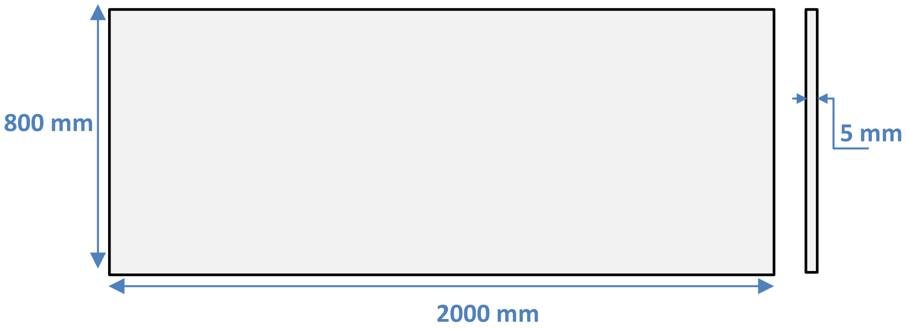

Figure 3-38: Dimensions of the spoiler plates

The distribution of the plates was such that 4 outboard, and 2 inboard spoilers were defined. This arrangement follows suit with current aircraft, such as the Boeing 787 series, Airbus A350 series, and Airbus A320 Neo. The plates when stowed occupy approximately 50% of the chord at the farthest outbound spoiler, and 25% of the outer-inboard spoiler. The resulting design corresponds with a spoiler/wing area ratio (S_s/S) of 0.0413, which sits inline typical limits specified in *Table 3-11*. Literature indicates that a typical deployment limit for the spoiler deflection angle, δ_s, lies around 35-50˚. [106] Therefore, a value of 50˚ was chosen, and applied to the spoiler plates in ICEM, shown in *Figure 3-39 & 3-40.*

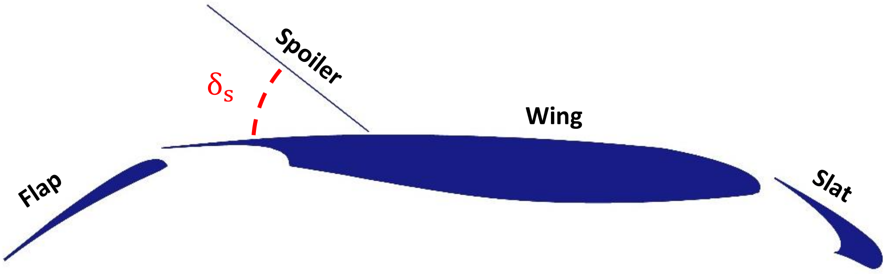

Figure 3-39: Cross-sectional view of the wing at 75% span, including outer-most spoiler

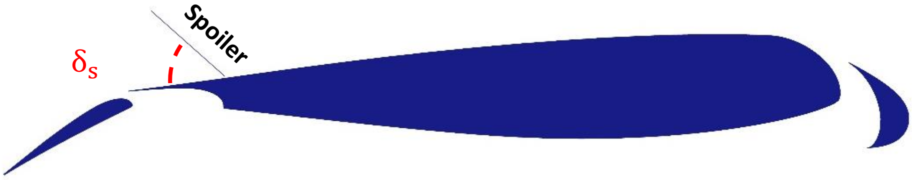

Figure 3-40: Cross-sectional view of the wing at 5% span, including inner-most spoiler

The resulting DLR F11 model is shown in *Figure 3-41*, with the inboard/outboard spoilers highlighted in red/blue respectively. The model was then meshed, tested, and performance measurements were taken to verify that the design's effectiveness fell within expected levels.

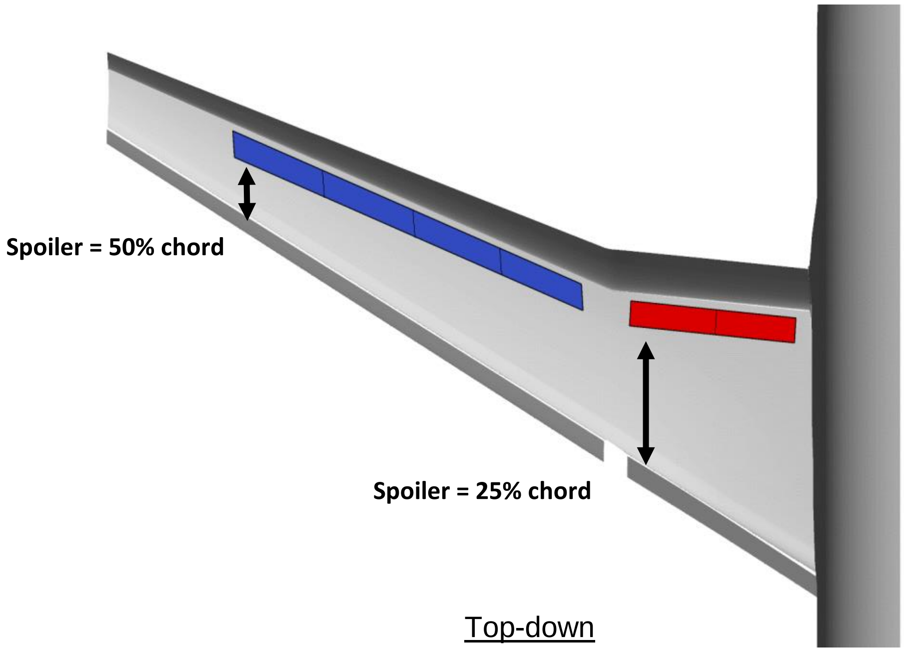

Top-down

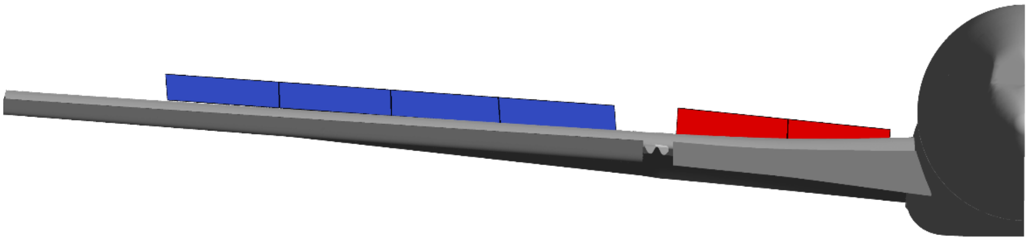

Head-on

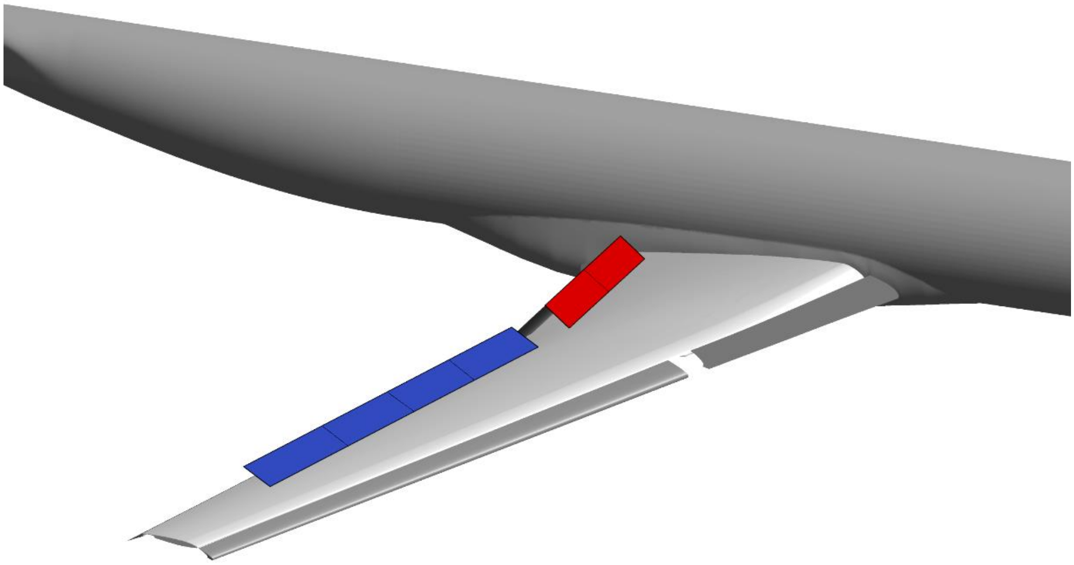

Above-front-side

Figure 3-41: Visuals of the 3D airframe model including deployed spoilers

3.4.3 Pylon Design

The final component required before final assembly could begin, was the engine pylon. The pylon has the structural function of connecting the engine to the airframe, transmitting the thrust forces, whilst damping vibration transfer between the hardware. The main element of the pylon is a central struct, which acts as the main structural member, seen in *Figure 3-42*. A hollow, aerodynamically favourable casing is then fitted to reduce drag. Additionally, the pylon contains the control, fire suppression, fuel & hydraulic system services to the engine, houses the bleed air pipework, and is also partially designed as a firewall. [107]

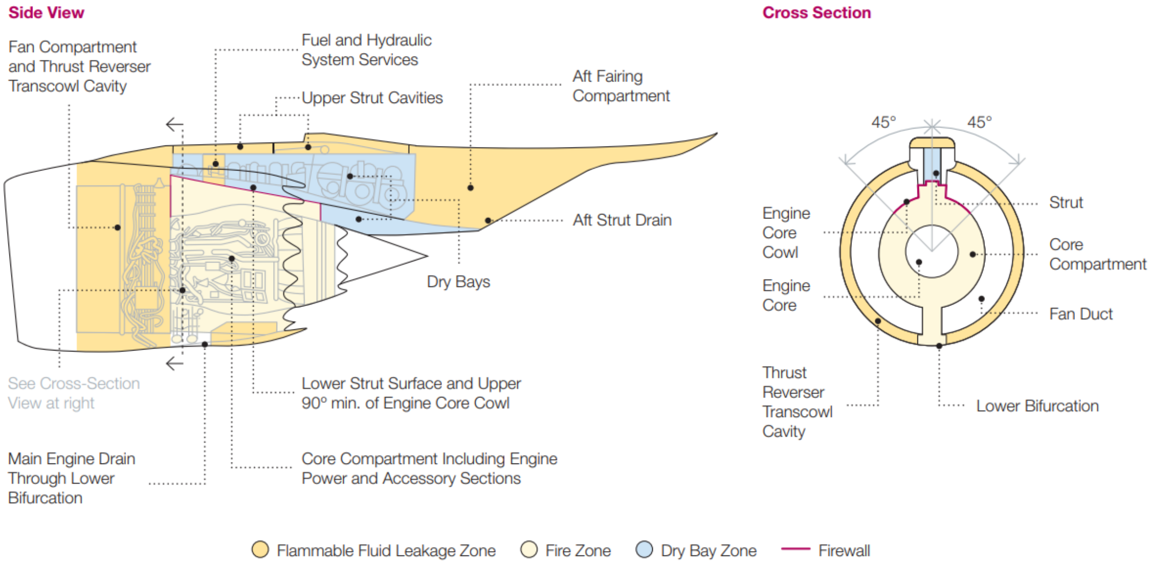

Figure 3-42: A modern pylon design as presented by Boeing [99]

The pylon design methodology was established by another supporting MSc project; alike the design of the spoilers. The method is based on the outcome of research into engine-airframe installation aerodynamics which recently published by Stankowski. [108, 109] It has been long established that the position of the engine relative to the wing can affect the cruise aerodynamic performance, such as reducing nacelle drag by up to 20% compared with an isolated engine. Furthermore, the effect on the exhaust system when exposed to the wing pressure-field can increase or decrease the gross propulsive force, from between a -0.1% to a +0.6% improvement. [108] Thankfully, the installation-aerodynamics study provided a guideline as to where best to position an under-wing mounted turbofan for optimal thrust/drag metrics. *Figures 3-43 & 3-44* summarises the engine positioning methodology established by Stankowski. [109] The two bar graphs compare the measured cruise performance for the different engine-location configurations, with regards to nacelle drag and engine thrust.

	dx/L_{nac}	dz/L_{nac}
A1	-0.453	0.0647
B1	-0.259	0.0647
C1	-0.065	0.0647
A2	-0.453	0.129
B2	-0.259	0.129
C2	-0.065	0.129
A3	-0.453	0.194
B3	-0.259	0.194
C3	-0.065	0.194

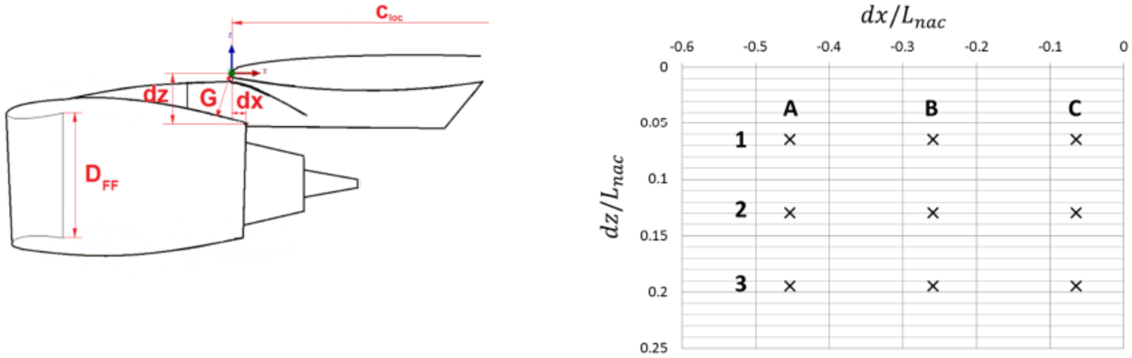

Figure 3-43: Method for measuring engine-wing location [109]

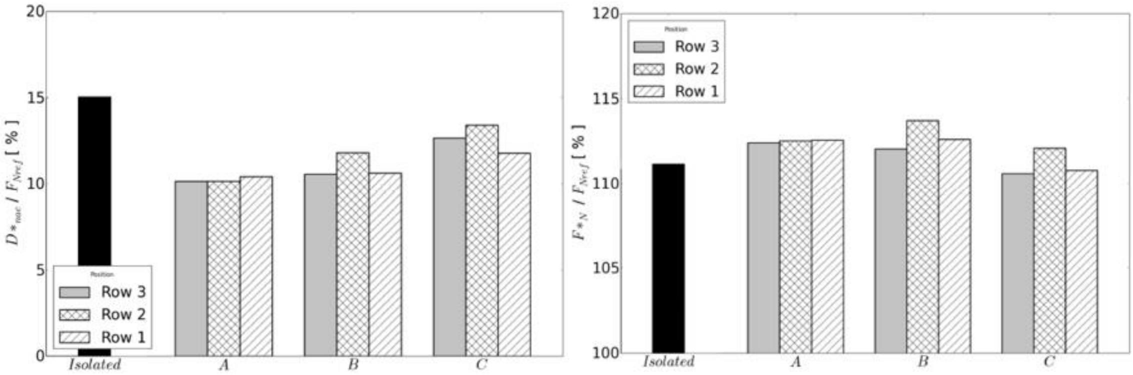

Figure 3-44: Comparison of nacelle drag & engine thrust for different engine positions [109]

The engine location is measured by the vertical and horizontal distance between the highest point of the bypass nozzle, and the leading edge of the wing. The horizontal placement has a greater potential impact on aerodynamic performance, and the most favourable approach is to position the engine closest to the wing horizontally and lowest from the wing vertically. The design generated on the MSc project, which was carried forward into the final CFD model on this project is detailed below in *Table 3-12* & visualised in *Figure 3-46*. The dimensional choices are coherent with existing modern aircraft, falling within a common design space for the Boeing 777/Trent 800, Airbus A300B/CF6-50 and A320Neo/PW1000. [110] The lateral location of the engine (along the wing-span) was based upon the current aircraft; the transition point in the wing structure, where the TE becomes swept back (*see Figure 3-45*).

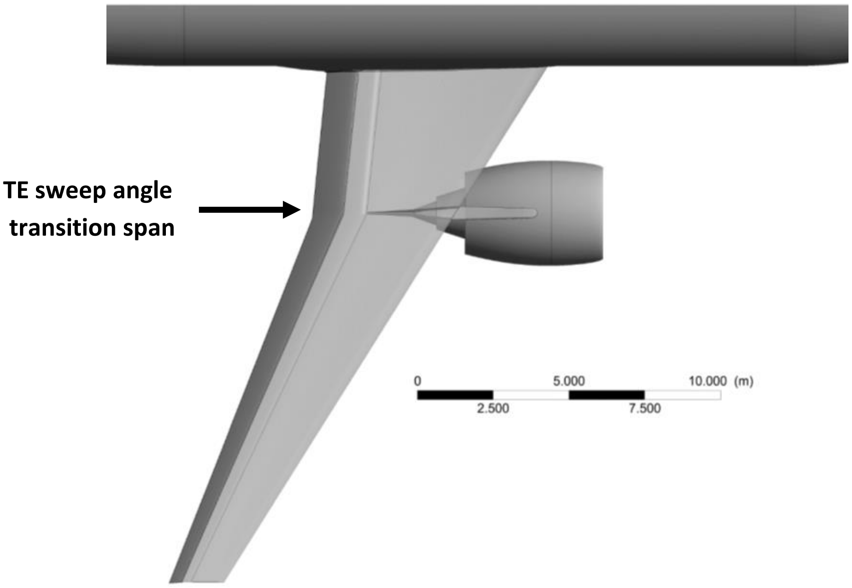

Figure 3-45: Wingspan location of pylon (with slats retracted/removed for clarity)

Dimension	Value
Vertical (dz)	405 mm
Horizontal (dx)	327 mm
Lateral (engine-fuselage distance)	3310 mm

Table 3-12: Engine position relative to wing leading edge

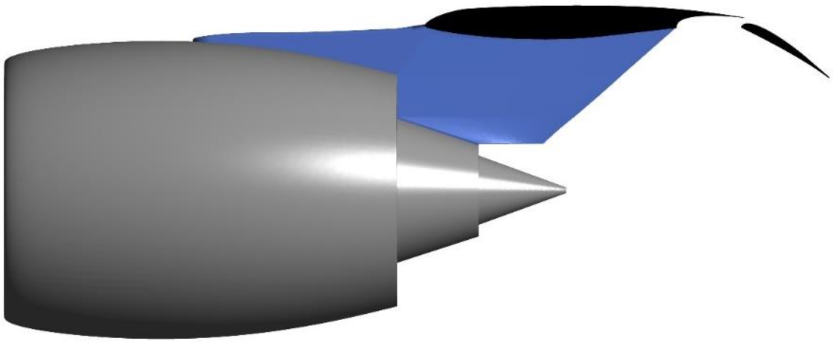

Figure 3-46: Cross-sectional view of the pylon & engine

Once the 2D dimensions were established, work on the 3D pylon model began. This was carried out in CATIA, due to the inherent flexibility & stability of the software with CAD geometries, compared with suites such as ANSYS ICEM. The pylon was assembled from stacked symmetrical NACA aerofoils (0008, 0010, 0012, 0015), placed at key-points vertically (namely the core nozzle inner diameter, internal & external bypass nozzle diameters, and the top of the nacelle). These were then scaled along the longitudinal axis, essentially stretching them to suit the geometric requirements. The profile at the top of the nacelle was also modified to extend the LE to near the midpoint of the nacelle, shown in Fig 3-47. This provides a reasonable clean aerodynamic shape to the pylon, with the appropriate boat-tail trailing edge. A small cut-off was also made to TE of the 4 NACA profiles, to give a defined thickness to the back of the pylon of 40mm, following what was seen from observing real-world examples. The fundamental geometric parameters for the pylon are presented in *Table 3-13*.

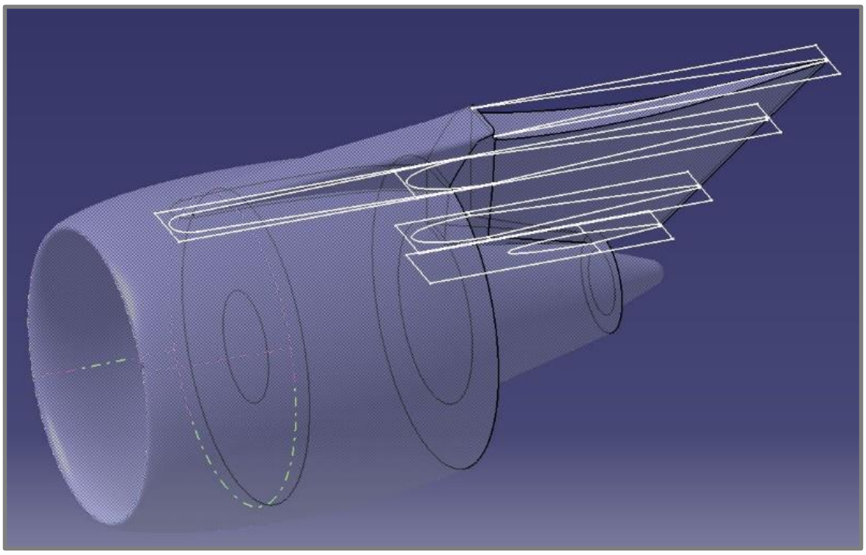

Figure 3-47: Assembly of the pylon by use of stacked NACA aerofoils

Dimension	Value
Pylon maximum lateral thickness	470 mm
Pylon base profile trailing edge angle	138˚
Pylon maximum axial length	5214 mm
Front fairing slope angle	7˚
Core nozzle to lower trailing edge	490 mm
Lower trailing edge thickness	40 mm

Table 3-13: Pylon geometry data

The final part of the pylon design was establishing the ground clearance beneath the engine when the aircraft is landed. The ground clearance is defined as the vertical separation between the lowest part of the nacelle and the ground-plane. The clearance is typically limited by two factors. Firstly, the risk of inlet distortion and/or FOD ingestion under high power at static conditions, or during thrust reversal operation. Secondly, to ensure that the engine will not strike the ground should the wing flex downwards, such as at touchdown during a hard landing. Furthermore, the ground clearance has a direct impact on the maximum fan diameter available, as the space under the wing is limited by the aircraft wing position, and landing gear height. An initial clearance of 0.6 m was selected, based on existing values available in the public domain; contained within airport planning manuals published by the airframe manufacturers. This value is close to the limit of current aircraft. A summary and comparison of the real-world values is provided in *Table 3-14*. The ground clearance varies with the aircraft weight, due to the compression in the landing gear suspension. As such, values for ground clearance with empty payload and maximum payload masses are quoted. *Figure 3-48* illustrates the ground clearance to scale.

Aircraft/Engine	Ground Clearance	
	Min	Max
Airbus A321 Neo (CFM LEAP-1A or PW1100G)	0.47 m	0.58 m
Airbus A350-900 (RR Trent XWB)	0.60 m	0.79 m
Boeing 737 MAX (CFM LEAP-1B)	0.43 m	0.56 m
Boeing 757-300 (PW2043)	0.81 m	0.99 m
Boeing 757-300 (RB211-535E4)	0.91 m	1.09 m
Boeing 777-300ER (GE90-115B)	0.73 m	0.99 m
Boeing 787-8 (GEnx-1B)	0.74 m	1.07 m
Boeing 787-8 (RR Trent 1000)	0.71 m	1.07 m

Table 3-14: Comparison between ground clearances for twin-engine transport aircraft [111, 112, 113, 114, 115, 101]

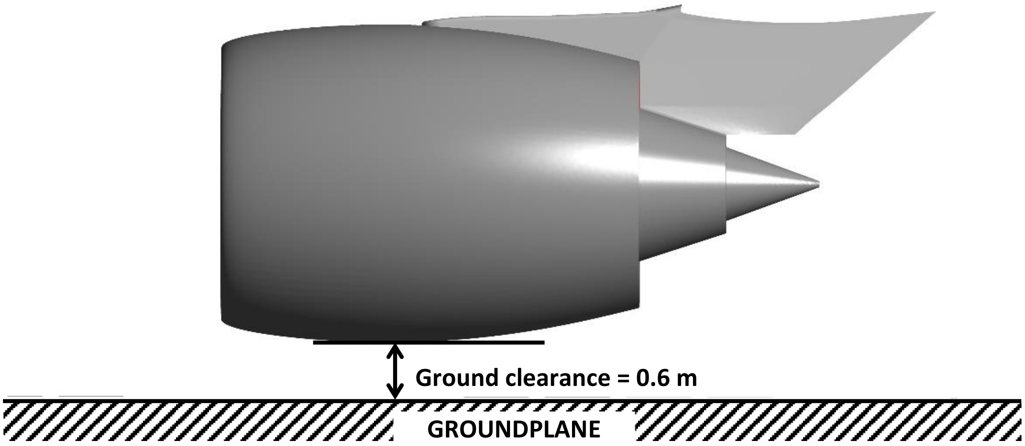

Figure 3-48: Ground clearance beneath the developed engine model

The requirement for a pylon in the VPF reverse thrust research model was to provide an approximate geometric representation of a real-world design, whilst negating unnecessary details for computational simplicity. Given the low freestream velocities, it was not required to be aerodynamically optimised. Nevertheless, an engine/pylon/airframe model was meshed in ICEM following the method established in the validation & grid independency studies. Testing was then carried out to identify any aerodynamic issues – of which none were identified, and is discussed briefly in *Ch 4.3.2*.

This defines the process for the creation of the pylon external geometry. However, the internal profile of the pylon within the bypass nozzle and duct (highlighted in *Figure 3-49*) also needed to be modelled, to allow realistic flow simulation during reverse thrust. Using the pre-established annular lines of the bypass nozzle and duct, the internal structure was created from the bypass nozzle. A user generated radial profile was then created to provide the desired blunt leading-edge shape, as shown in *Figure 3-50*. The pylon extends approximately two thirds up the bypass duct. A clearance between the OGV and internal pylon leading edge was maintained of approximately 2 OGV chord lengths, to ensure upstream interference was minimised. This also allowed a degree of separation between blades/pylon geometries, and the OGV/bypass duct interface.

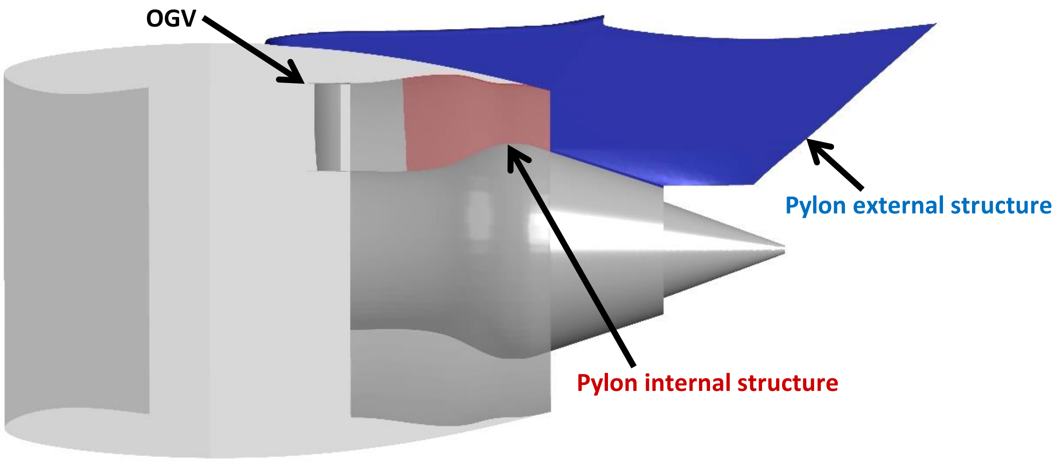

Figure 3-49: Cross-sectional view of the pylon internal & external assemblies

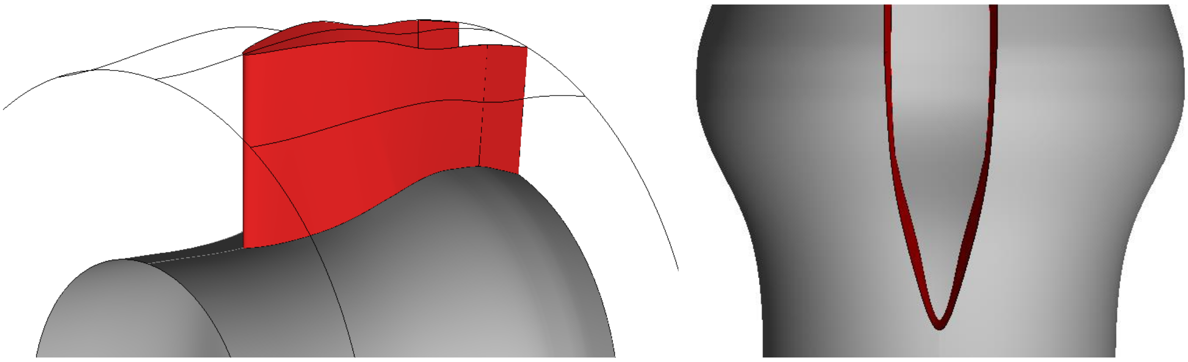

Figure 3-50: Internal pylon geometry

An initially unforeseen issue affecting both pylon & nacelle designs, was the bypass nozzle area reduction when the pylon is in attached to the engine. The nozzle's ability to ingest flow during fan-reversal is critical to achieving a manageable pressure-recovery level within the bypass duct. As the exhaust is the most constrictive part of the bypass flow path, the size of the nozzle throat will directly influence overall aerodynamic performance within the nacelle.

During design-space-exploration studies, it is common practice for engine-designers and researchers alike, to use isolated engine analysis as a baseline for design, and simplicity. The GEMINI model does not specifically account for a pylon; as the code has been developed following the aforementioned 'isolated-engine' approach. It was quickly realised during the GEMINI model development that the cold-stream exhaust design would need to take the pylon definition into account to maintain an appropriate nozzle throat-area.

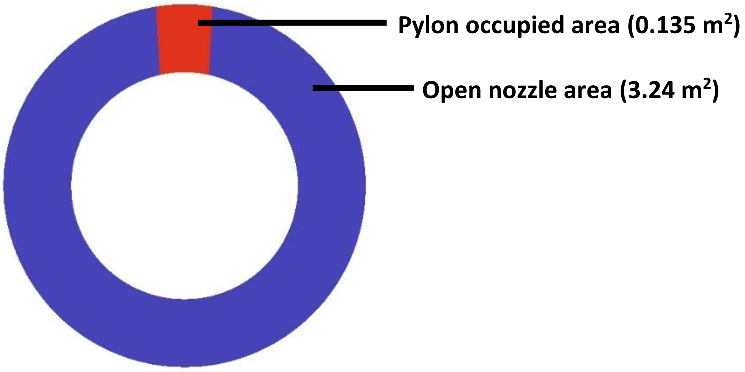

Figure 3-51: Bypass nozzle area

The final GEMINI model developed satisfies the engine design with the pylon attached. The cross-sectional area of the pylon in the BP nozzle-exit plane was estimated to be ~0.135m^2, as can be seen in *Figure 3-51*. This value was added to the BP exit-area value in the GEMINI input files. The resulting design therefore, gives the correct nozzle area with the pylon fitted. With the pylon removed (such as the isolated engine case), the increase in nozzle area was measured to be 4.16%. The bypass nozzle areas from both the TURBOMATCH engine cycle, and the GEMINI nacelle/exhaust design (with & without pylon), are presented in *Table 3-15*, as both numerical and percentile values.

Throat Area (Bypass Nozzle)	Area	% Deviation
TURBOMATCH	3.245 m^2	-
GEMINI (without pylon)	3.380 m^2	+4.16%
GEMINI (with pylon)	3.239 m^2	-0.77%

Table 3-15: Bypass nozzle throat-area data

One would expect a marginal improvement in the total pressure recovery of the bypass nozzle. However, it was decided to tolerate this variation between the isolated & integrated models, as it was deemed more important to maintain the same profile of the nacelle/BP nozzle TE lip for comparison. The effect of a larger area bypass nozzle on internal dynamics may provide some additional insight, but mainly the isolated case intentions are for external analysis.

3.5 CFD Approach & Meshing

As stated as part of the project aims & objectives, the research on this project is primarily undertaken using computational fluid dynamics (CFD) simulations. It is important therefore, to establish exactly which CFD software package was used, and the approach regarding solver settings, meshing techniques, and boundary conditions. This chapter does not intend to provide the reader with an in-depth understanding of CFD theory, which is well documented in the ANSYS user manuals and related publications. [116, 117]

3.5.1 CFD Software

The CFD software package utilised throughout this project is ANSYS 16.2. Cranfield University has long held an educational license for the ANSYS package, which is comprised of numerous programs for multiple engineering disciplines & applications. Within ANSYS are two of the most widely used CFD codes currently on offer; Fluent & CFX. Preference for CFX was quickly established for the following reasons:

- The program has been developed with a strong bias towards turbomachinery, including the semi-automatous meshing suite for blade passages; Turbogrid, and various pre-solver and post-processing options which make setting up complex models relatively simple.
- The code is flexible, offering a choice of several different inlet & outlet boundary types to be used.
- CFX by default includes several turbulence models, including the *κ-ω SST* model; which the industrial sponsor had expressed preference for at the start of the project.
- The author had some pre-existing experience using CFX, presenting a shallower learning curve for the program.

All of the fluid dynamic modelling and testing conducted as part of this research, utilised the Reynolds-averaged Navier-Stokes (RANS) equations for the fluid simulations. This provides a time-averaged solution, where the flow field values are calculated as averaged values, smearing out oscillating and fluctuating phenomena. A RANS based solver was chosen over other solver types for the following four reasons:

- The large size of the research model – with multiple systems modelled
- Limited computational resources to run the simulations
- The number of simulation cases required to capture the full landing speed spectrum
- The results in this thesis are the first generation of simulations on the assembled research model

A time-averaged solution was therefore deemed most suitable for initially quantifying the flow phenomena prescribed in the project's main aims (*ref. Ch. 1.2*), within a feasible timescale.

Additionally, the flow solutions are dependent on how well suited the turbulence models are to the type of simulation being conducted.

The *κ-ω* based SST model accounts for the transport of the turbulent shear stress and gives highly accurate predictions of the onset and the amount of flow separation under adverse pressure gradients. [116] As such, it has become one of the standard turbulence models for aerospace CFD applications, where accurate modelling of stall inception is crucial. The model is a two-equation eddy-viscosity, which combines the two well established, standalone *κ-ω & κ-ϵ* turbulence models. It has been long known that these two models both present shortcomings individually. The *κ-ϵ* model has a tendency to under-predict boundary layer separation in high-pressure-gradient scenarios, but offers accurate modelling of the freestream. The *κ-ω* on the other-hand offers good simulation of the boundary layer shearing, but is often too sensitive to inlet freestream turbulence properties. The *κ-ω SST* model utilises the *κ-ω* to capture the inner 50% of the boundary layer, whilst the *κ-ϵ* equations capture the freestream dynamics. As a result, the *κ-ω SST* model is deemed more capable of predicting accurate high-speed flow solutions than either of the two-equation models alone. However, a penalty must be accepted when adopting the model; which is an increase in the computational memory required to run the solver. Additionally, some short-comings still exist where the model has been found to overpredict turbulence in regions of large normal strain (such as regions of stagnation or strong acceleration). However, the under-prediction is significantly less than the *κ-ϵ* model, and overall the model offers an attractive compromise between processing time and solution accuracy. [116, 118]

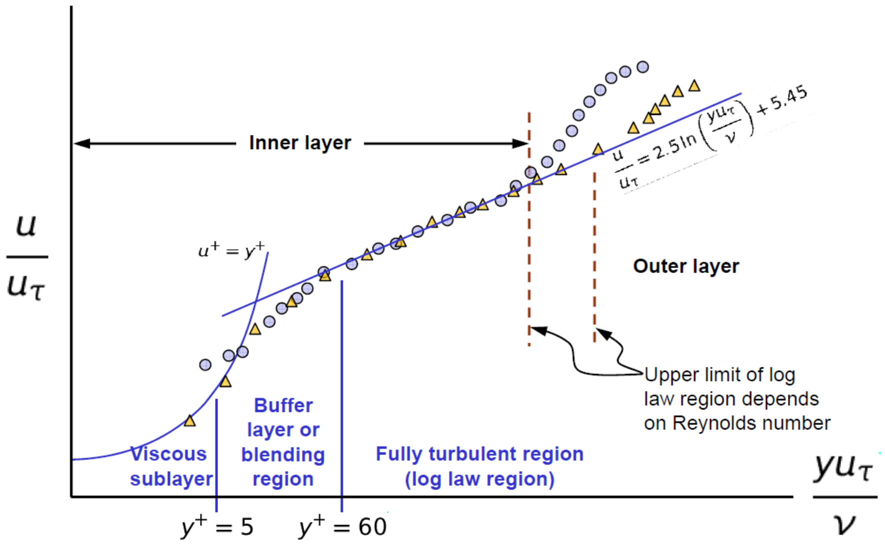

Figure 3-52: Non-dimensional velocity in boundary layer [119]

Additionally, when selecting a turbulence model, it is important to understand the relevant mesh fidelity required in the near-wall regions (shown in blue in *Figure 3-52*), to properly model the boundary layer growth and stability. This is usually expressed as a factor of the dimensionless wall distance, Y^+.

$$Y^+ \equiv \frac{u_\tau y}{v} \qquad \textbf{(3-1)}$$

Where
$\boldsymbol{u_\tau}$ = *friction velocity next to the wall*
$\boldsymbol{y}$ = *distance to the wall*
$\boldsymbol{v}$ = *kinematic viscosity of the fluid*

The Y^+ fundamentally depends on the Reynolds number & boundary layer performance, and therefore varies with freestream viscosity, density & velocity. The *κ-ω SST* model offers two approaches to the boundary layer modelling. A full-fidelity calculation of the boundary layer may be conducted with a $Y^+ \approx 1$. Alternatively, a boundary layer approximation using a near-wall treatment can be used, for lightweight lower-resolution simulations, with a Y^+= 30-300. [116] As one would expect, the solution accuracy is degraded using the near-wall treatment method, especially for instances of flow separation or stall. Therefore, the full-fidelity approach is the preferred method for turbomachinery-related domains.

3.5.2 Meshing

Apart from the solver & simulation settings, another criticality to ensuring accurate CFD solutions is the fluid representation. In computational modelling this manifests in the form of geometry meshing. Given the research models contain 6 different mesh domains (fan, splitter/middle-passage, OGV, bypass duct, external/airframe, core-exhaust duct), no single meshing approach works for all geometries. Three methods were adopted, which are summarised in the following subchapters.

3.5.2.1 Turbogrid Structured Meshing

One of the key features of ANSYS CFX is the semi-automated blade meshing suite, Turbogrid. This method was used to generate high quality structured meshes for all turbo-domains (VPF, OGV, ADP baseline fan/FEGV/CIGV). The suite has a relatively simply GUI, in which parameters can be specified for the mesh generation. An example for generating one of the meshes is provided following, to briefly explain the method.

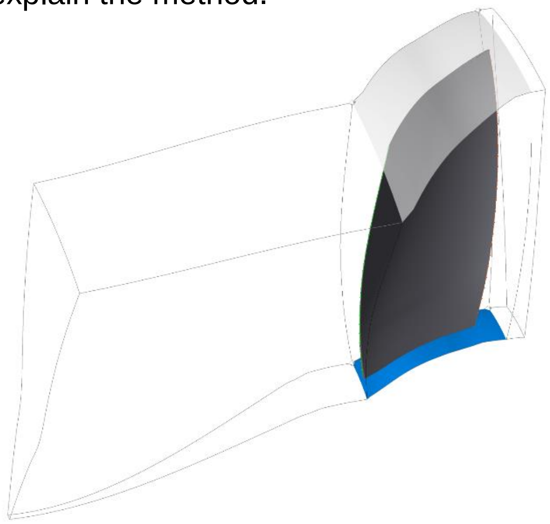

Figure 3-53: Turbogrid domain created from .curve files

The geometry was loaded into Turbogrid in its native file format. This comprises of 3 separate comma-separated-value text documents, with the suffix ‘.curve’. Two of these files represent the hub & shroud 2D annular lines respectively. The third represents a single blade, presented as a set of radially stacked profiles, expressed in cartesian point data. Once the geometry is accepted by Turbogrid as valid, a 3D representation of the domain is generated within the GUI. The meshing procedure can then begin.

The target overall element count for the domain is first input to the mesher, as well as the near-wall cell height for both the blade and hub/shroud end-walls. This value is determined by calculating the dimensionless wall distance corresponding with a $Y^+$of approximately 2. It was found that using values below 2 sometimes introduced errors around the leading/trailing edges due to tolerances between the geometric profile and the mesh topology. Given the size of simulations used for fan and OGV testing, this approach was reasonable, as the computational time required was still only a few hours per 1000 iteration.

The software then automatically generates the appropriate grid topology for a single passage, and generates the structured mesh by defining multiple span-wise layers through around the blade (shown in *Figure 3-54*).

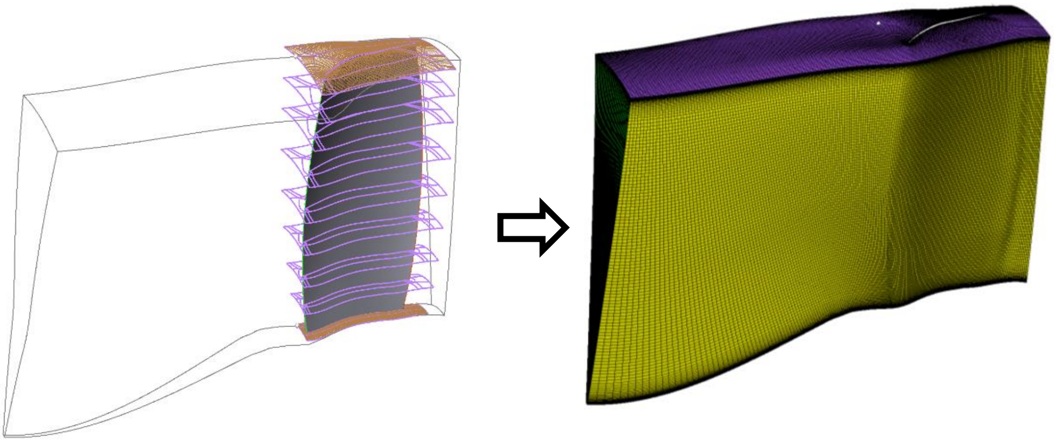

Building of topology through span-wise layers **Mesh created from automated layer procedure**

Figure 3-54: Turbogrid meshing procedure

An automated check is then conducted on the mesh, and any elements found to intrude on the quality limits, such as (skewness, aspect ratio etc), are highlighted to the user for correction or dismissal.

Further details for the Turbogrid method are well documented by an MSc thesis which contributed towards the validation of the baseline ADP geometry. [97] This applies for all turbo-domain meshes except for those used in the final assembled model, for which a separate mesh-independency study was conducted. This was in an aim to reduce the total number of nodes for the whole simulation, by using somewhat coarser meshes in the fan & OGV regions; the most densely meshed components of the whole model. A summary of the mesh parameters is provided in *Table 3-16* for all Turbogrid generated fluid domains. Additionally, the validation & verification work on the VPF & OGV models is provided in *Ch 4.2*.

3.5.2.2 ICEM Structured Meshing

For the axisymmetric ducts, a structured approach was easily adopted using ANSYS ICEM. Whilst not specifically linked to CFX like Turbogrid, ICEM offers a flexible mesh generation suite for both structured and unstructured meshing. The strategy for generating the ICEM structured meshes, required for the middle-passage, core exhaust duct, isolated nacelle, and the bypass duct (without pylon) domains started with a simple 2D mesh. For the middle-passage domain, where the fan outlet is split into either the bypass or core streams, the domain is split into blocks to correspond with the duct arrangement (*Figure 3-55*). For the bypass duct (without spoiler) and core exhaust duct, this was not necessary as the domains are single inlet/outlet ducts.

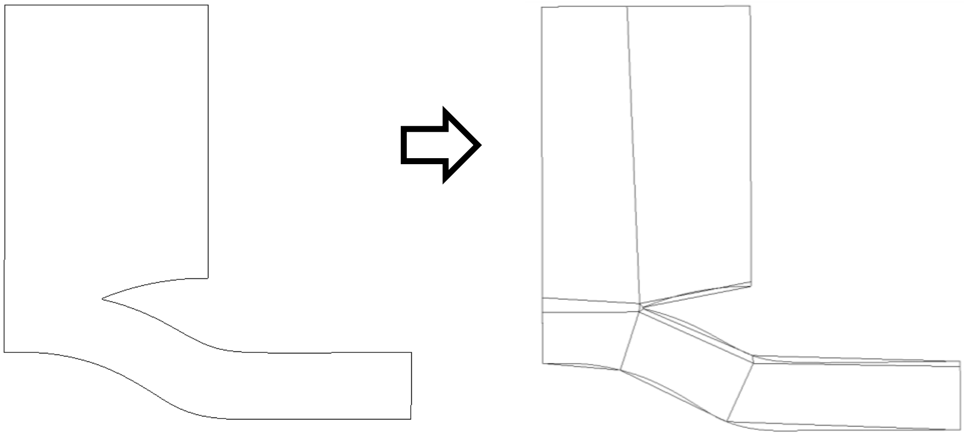

Passage 2D geometry

Blocking of the 2D geometry

Figure 3-55: 2D geometry blocking in ICEM

The next stage is to introduce the first set of elements to the 2D mesh, by setting the near-wall element height and expansion ratios again using values corresponding to $Y^+ \approx 2$. However, the freestream nodes are spaced further apart than the Turbogrid domains, due to the inherently lower resolution in an open duct, as appose to a blade passage. This reduces the computational demand required to populate and iterate a flow solution for the domain.

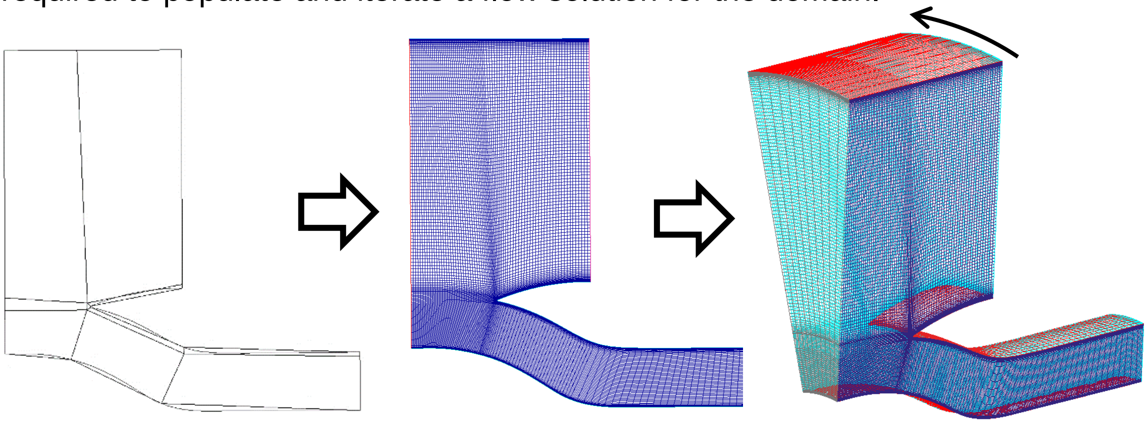

Blocked 2D geometry **2D mesh defined** **Rotational extrusion to 3D mesh**

Figure 3-56: 3D mesh generation procedure for structured ICEM domains

Refinement is conducted where necessary to smooth out any sudden transitions in element size observed in the mesh. This is done by either redistributing or changing the number of nodes in a specified block, or adjusting the blocks themselves to redistribute the elements. Once a suitable 2D mesh has been generated, quality checking algorithms built into ICEM are run to identify any areas of the mesh that need attention. Although, due to the manually structured nature of the process, and the simple domain geometries, the user should already be aware of any problematic regions during mesh creation.

Having established confidence in the 2D mesh, it can now be extruded to 3D. For an annular duct, this is done by using the mesh extrusion (by rotation) tool. This adds layers to the mesh in the 3rd dimension (cylindrical), by specifying the number of degrees per layer. For single-passage domains this is kept to a 20° slice, in-line with the fan domain (18 blades). To convert the mesh to fully-annular, more layers are added until the mesh extends through the full 360° annulus. The evolution of the mesh is illustrated in *Figure 3-56.*

The final stage is to select element faces along the boundaries of the mesh, and assign these to individual 'parts', which can later be specified as boundaries (such as walls, inlets, interfaces etc). These can be seen in *Figure 3-56*, as the boundaries are coloured differently. The mesh was then exported in .cfx5 format, a native CFX mesh file-type.

3.5.2.3 ICEM Unstructured Meshing

For the complex geometric models, namely the airframe domain, a more flexible meshing solution was required. ANSYS ICEM is also capable of producing unstructured meshes in hexahedral, tetrahedral & hybrid meshes. Unstructured meshing is generally a more challenging task to undertake compared to structured, due to the lack of control on the node distributions, and reliance on the automated meshing algorithms to control the geometry-mesh conformation. Additionally, the mesh is computationally more demanding. The lack of structure requires coordinates to be stored for every node; resulting in generally slower computational speeds, and less accurate solutions. A comparison between a structured (hexahedral) & unstructured (tetrahedral) mesh around an airfoil is provided in *Figure 3-57.*

Unlike Turbogrid, the automatic mesh-generation is not tailored to a particular geometry format (such as a blade passage). Therefore, whilst still automated, significant more user input is required to ensure the intended mesh structure is obtained, and the geometry properly represented, as there is no specified grid topology. The method which is briefly described, was developed and validated as part of the MSc project work associated with the airframe model development. Therefore, a more in-depth description of the procedure is published in the relevant Masters theses. [105, 110]

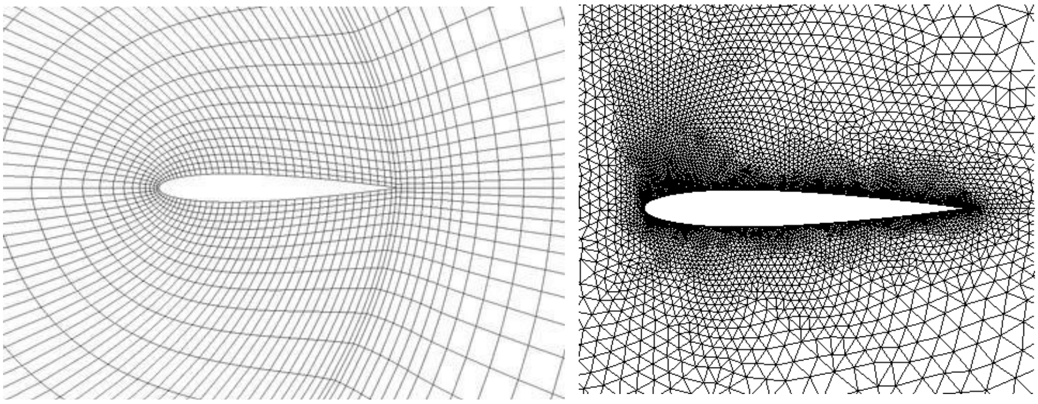

Figure 3-57: Comparison between structured & unstructured meshes around an airfoil [110]

The first stage of creating an unstructured mesh in ICEM is to ensure the geometry is properly defined, and any gaps between surfaces are below the tolerance of the smallest expected mesh elements. Once the geometry definition is of an acceptable quality, the automated part of the meshing program is setup. All unstructured meshes presented in this research used tetrahedral elements to represent the fluid. They have proven to be highly adaptable across a broad range of CFD applications, and was one of the mesh types for which CFD results were published in NASA's 2nd HLPW (DLR F11). [84] Tetrahedral-based meshes have demonstrated accurate simulation of the DLR F11 at Mach 0.175 – near the peak freestream velocity of the reverse-thrust study, given a landing speed of 140 knots (Mach 0.2).

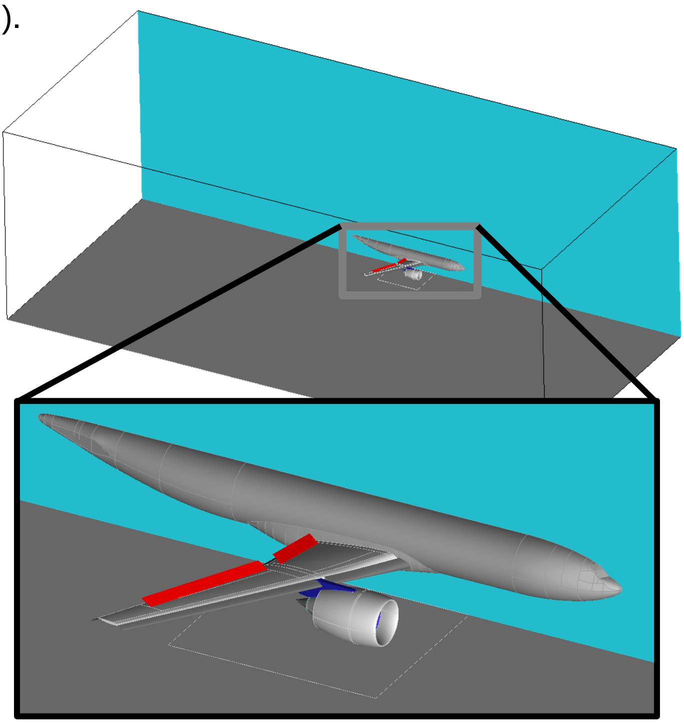

Figure 3-58: Surfaces of the airframe domain

The mesh generation procedure first computes a surface mesh around the aircraft geometry (*Figure 3-58*), and the edge of the domain, (such as the ground-plane, symmetry plane & far-field). At this point, any errors in the mesh can be identified, as problematic regions generally only appear near to surfaces. This is done using the automated checking tool available in ICEM.

Once establishing a suitable surface mesh (*Figure 3-59*), a flood-fill is then performed, which can follow one of several algorithms for populating the domain volume with mesh elements. For this study, the octree algorithm was adopted, as it is generally considered the simplest and most robust method of volume-meshing. [117] *Figure 3.60* shows a cross-section through the volumetric mesh.

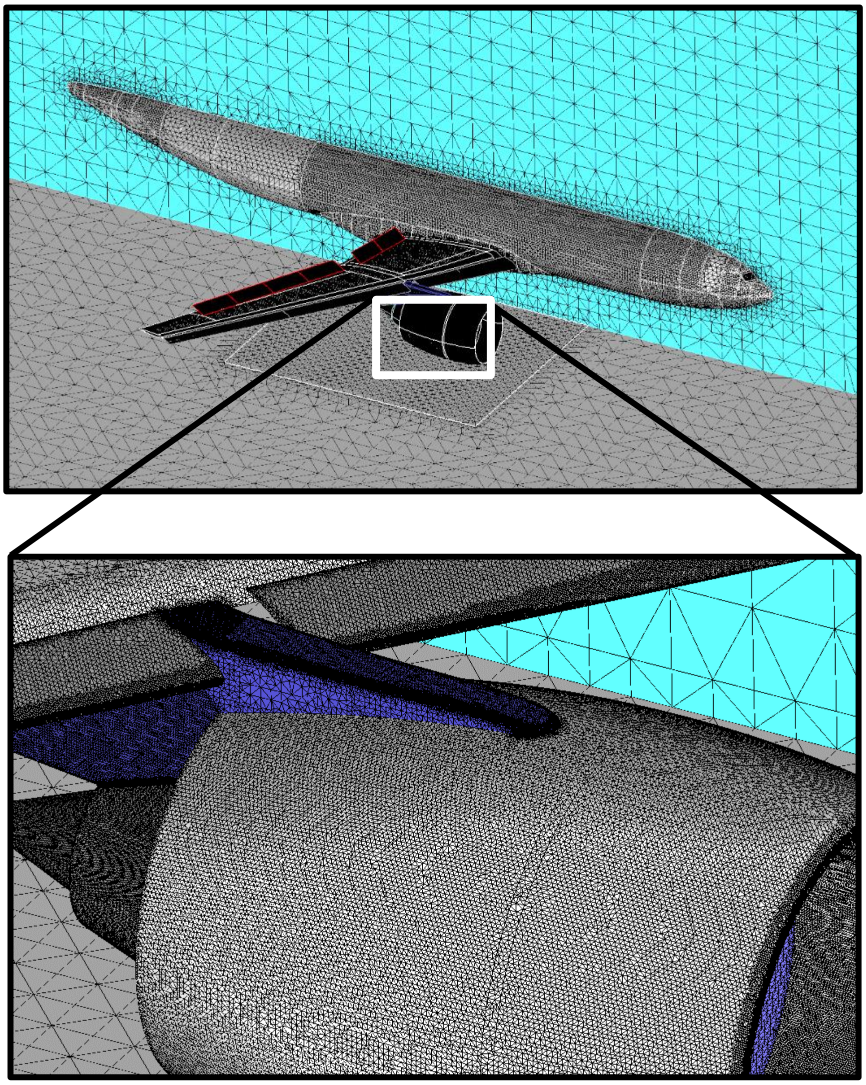

Figure 3-59: Tetrahedral surface mesh

Meshing the airframe in this manner was by far the most challenging part of all CFD modelling work undertaken on the project. However, this was mainly attributed to the ‘dirty’ CAD definition of the publicly available DLR F11 model, rather than ICEM itself. Duplicate curves and misaligned surfaces were a widespread problem, which given the complex nature of the wing & high lift devices made re-creating the geometry impractical.

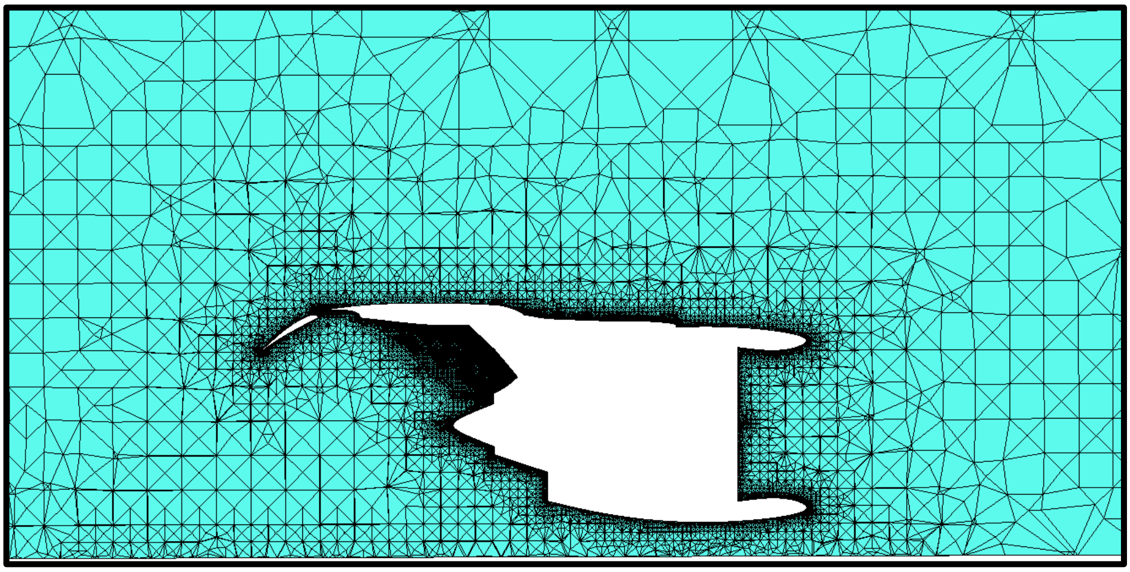

Figure 3-60: Cut-through of volumetric Octree type mesh

The final stage once the surface & volumetric meshes have been produced, was to conduct a smoothing procedure. The smoothing procedure can be automatically conducted immediately after the flood-fill process is performed, or manually through the smoothing toolbar in ICEM. The tool by default identifies the 1% worst quality elements (usually local to one or more surfaces). The nodes local to the problem area are then redistributed using an iterative process, to refine the local mesh structure, and improve the worst areas of the mesh. Assuming the resulting mesh is of suitable quality, it can be exported alike its structured counterpart, to a .cfx5 file. *Tables 3-16* to *3-18* conclude the meshing methodology, providing element numbers for all domains which contribute to the research models for reference.

Domain	#Elements	Target Wall-height
External (Isolated nacelle)	2.1 million	0.001 m
Single-passage Fan	5.8 million	0.0003 m
Splitter Duct	647k	0.0001 m
Single-passage OGV	173k	0.00013 m

Table 3-16: Elements for single-passage isolated nacelle model

Domain	#Elements	Target Wall-height
External (Airframe)	19.1 million	0.001 – 0.0005 m
Single-passage Fan	5.8 million	0.0003 m
Full Annulus Fan (per passage)	510k	0.0007 m
Splitter Duct	2.8 million	0.0001 m
Full Annulus OGV (per passage)	167k	0.0005 m
Bypass duct (with pylon)	1.9 million	0.001 m
Core exhaust nozzle	173k	0.001 m

Table 3-17: Elements for integrated model with both single-passage & full annulus fans

Model Configuration	Total #Elements
Isolated (all single-passage)	8.72 million
Integrated (single-passage fan)	36.45 million
Integrated (full annulus)	39.88 million

Table 3-18: Elements for single-passage isolated nacelle model

3.6 Arrangement of Research Models

Having established how the model geometries have been created, the overall structure and setup of the final research models for this project can now be discussed. Two variants of reverse-thrust VPF models were assembled from the developed geometries. The primary model represents the fully integrated engine scenario; with all components of the airframe, engine & pylon modelled above a ground-plane. However, an isolated engine scenario model was also created, by replacing the airframe with an axisymmetric external mesh of the nacelle only. As such, the arrangement of both integrated and isolated models (*Figure 3-61*), regarding domain interfaces, boundary conditions, and simulation 'handles', is presented following.

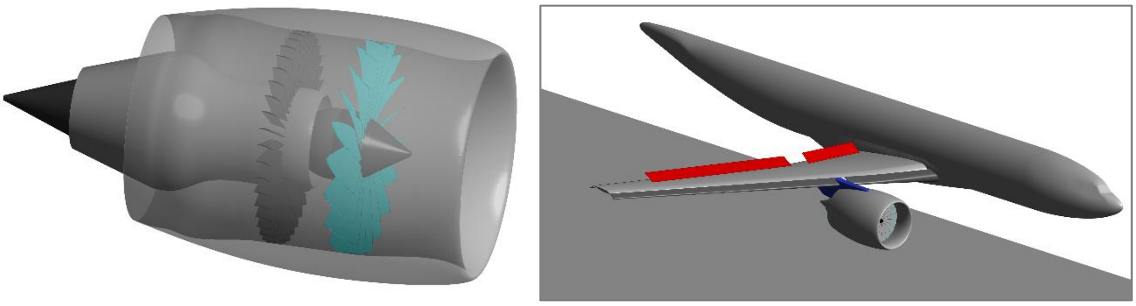

Figure 3-61: Isolated & integrated VPF reverse-thrust research models

3.6.1 Integrated Research Model

The integrated research model comprised of all the developed geometries on this project, and was established with the aim to addressing the project aim; the study of integrated reverse-thrust aerodynamics for a VPF fitted turbofan. Two versions of the integrated model were developed. The first featured a single-passage fan domain, with mixing-plane type interfaces at the either end, and a rotational periodic interface on the passage sides. The second featured a full-annulus 18-blade fan domain, with frozen rotor interfaces at either end, and no rotational periodic interfaces. All other engine-internal domains were fully annular, as this was deemed necessary to capture any circumferential distortion in the bypass duct and/or core inlet duct.

The domains which make up the integrated model include:

- **Unstructured mesh (tetrahedral)**
  - Airframe/external mesh with far-field
  - Bypass duct (with internal pylon model)
- **Structured (hexahedral)**
  - Fan (18 blades – single passage & full annulus representations)
  - Middle-passage (splitter – full annulus)
  - OGV (40 blades – full annulus)
  - Core exhaust duct

A cross-sectional schematic of the assembled model with these domains highlighted, with both single-passage and full annulus fans, in *Figures 3-62 & 3-63* respectively.

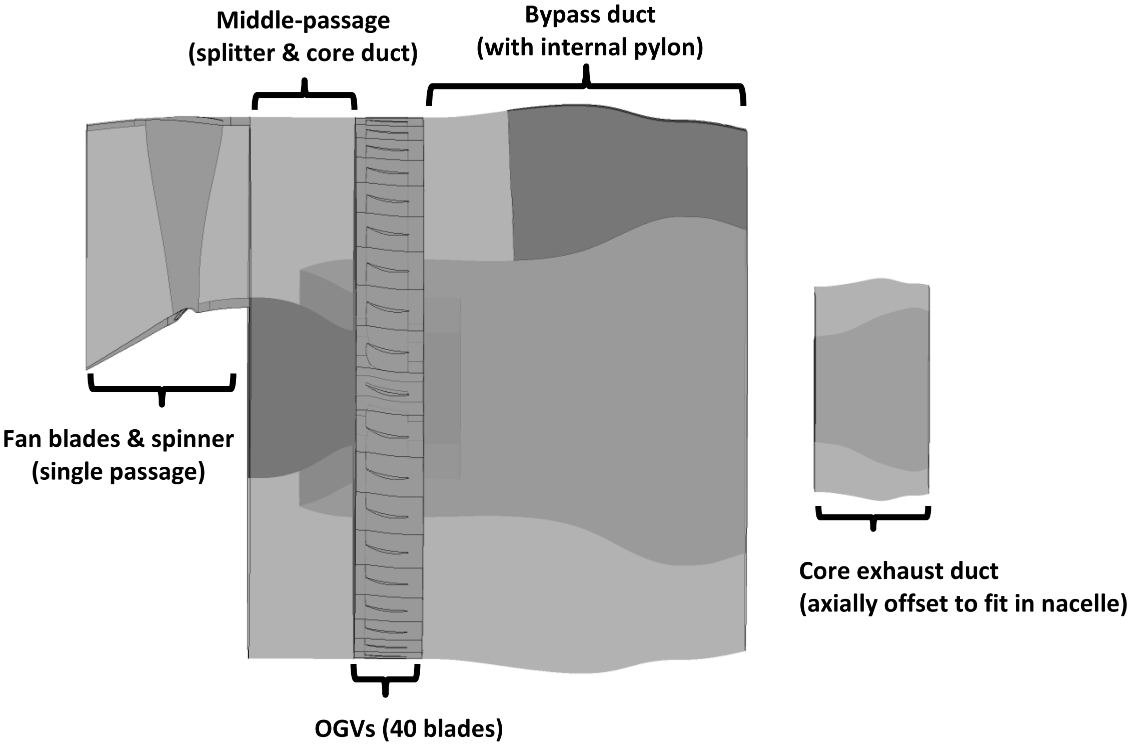

Figure 3-62: View of internal engine domains for integrated model with single-passage fan

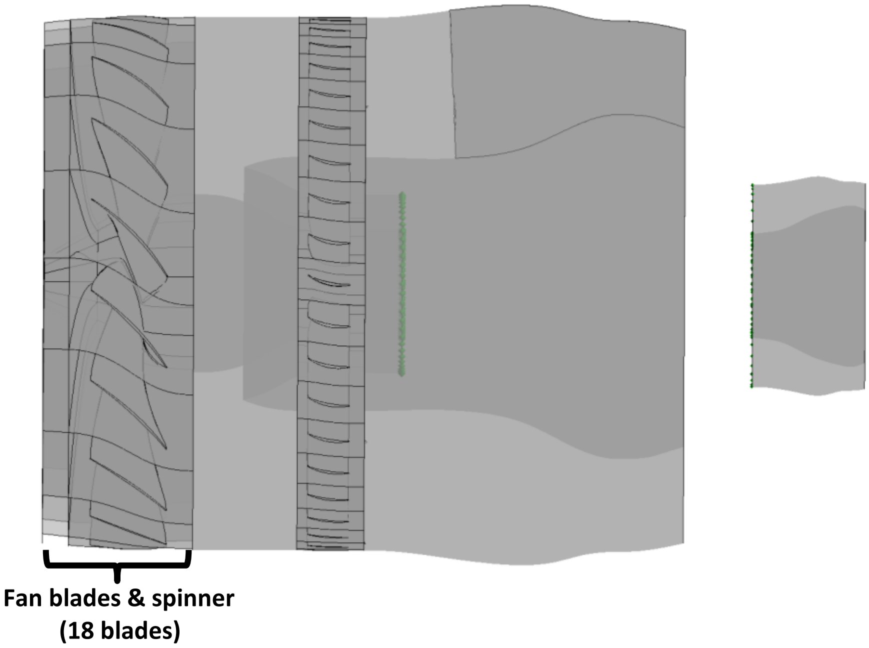

Figure 3-63: View of internal engine domains for integrated model with full-annulus fan

The full-annulus domains were created by duplicating the single-passage meshes rotationally around the principle axis, and ‘stitching’ them together. The number of copies made corresponded with the number of blades for the stage, and thus providing full 360˚ representations. By joining the single-passage meshes together, CFX-Pre treats them as one domain, simplifying solver setup. *Figure 3-64* presents the internal domains assembled within the nacelle/exhaust/pylon model.

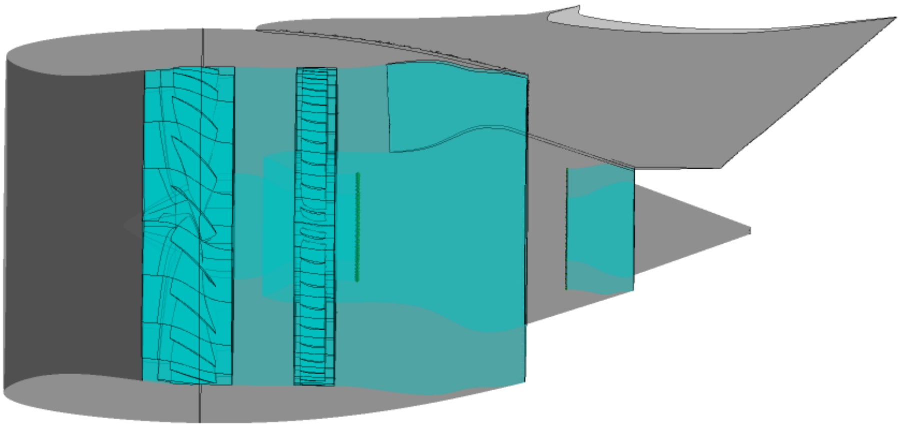

Figure 3-64: Fully annular internal domains assembled inside the airframe nacelle

3.6.2 Isolated Research Model

The isolated research model shares the same fundamental geometry and internal domains as its integrated counterpart, however, given the lack of circumferential variation, it was first developed with single-passage domains throughout, with the aim to be considerable lighter than the integrated model computationally. All domains corresponded with the single-passage fan domains' 20˚ annular segment. A replacement domain was produced for the bypass duct (which became an extension to the OGV domain outlet rather than remaining an independent domain). This did not include the pylon.

As the external mesh is now axisymmetric, a manual structured mesh was created, following the method described under *Ch 3.5.2.2*. The external mesh also included the core exhaust duct, replacing the integrated cases' separate domain. Integration of the bypass duct into the OGV domain, and core exhaust duct into the external domain, reduced the number of interfaces, improving computational speed and solution accuracy. A cross-sectional view of the assembled isolated case single-passage domains is presented in *Figure 3-65*.

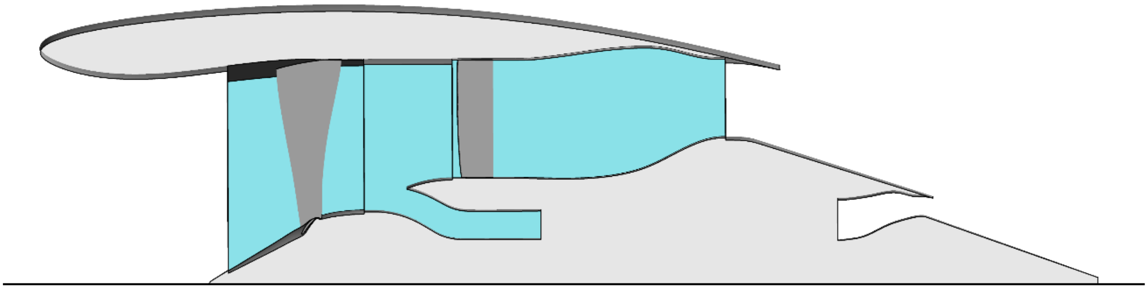

Figure 3-65: Cross-section of assembled single-passage internal domains for isolated engine

3.6.3 Interfaces Types

The 'interface' refers to the numerical connection formed within the CFD software, to allow the fluid to move between domains. As such, 6 interfaces exist in the integrated model. All domains were set in the stationary frame of reference, except for the fan passages, which were rotating. Where a change in reference frame is present, the interface requires a model to transfer the gas properties, depending on the simulation architecture. In the full annular research models, a frozen-rotor type interface was used for flow transition across both sides of the fan domain. The frozen rotor models the blade effectively 'frozen in time', allowing wake profiles and circumferential flow variations to be transferred into nearby domains.

The alternative 'mixing-plane' type interface was also used, but only for single-passage simulations; where a change in rotational segment size was present (e.g. from 18 blades to 40). Whilst more flexible in operation, this mixing-type interface functions by averaging/smearing the flow in radial bands, losing the finer details of circumferential flow variations. In return, the computational cost is much lower compared with a full annulus representation. In the context of this research, this is critical, as the scale of the model requires computational memory only obtainable with a dedicated high-performance computer (HPC) to run. Therefore, it was deemed essential to test both single-passage and full-annular versions of the integrated model's fan, to establish whether this was a necessary feature to capture the aerodynamics.

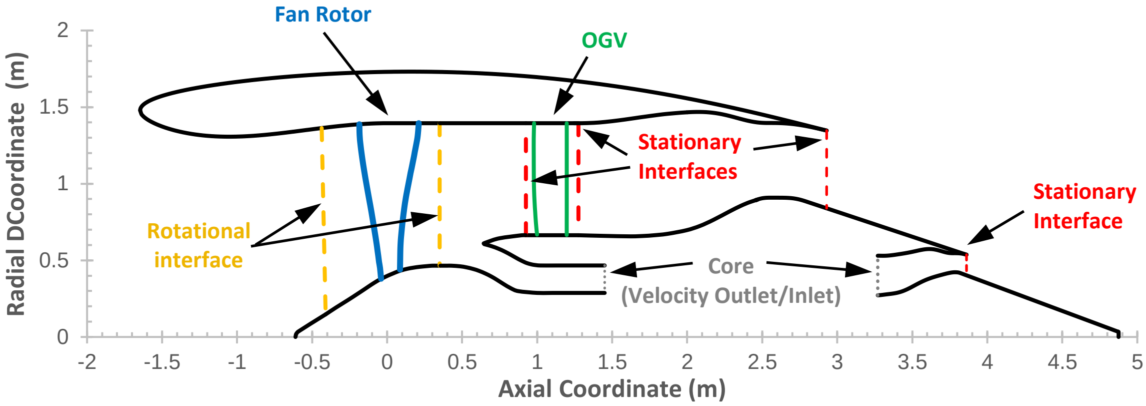

Figure 3-66: Interface & engine boundary arrangement for the research models

For all the full-annulus cases where stationary-stationary interfaces were used, no frame change/mixing model was required. Although some interpolation is still needed across the interface, where fidelity can be lost due to the inherent misalignment of the nodes on either side of the interface. This is most prevalent between unstructured and structured domains, such as the fan/external, OGV/bypass, and core-exhaust-duct/external interfaces. *Figure 3-66* provides a visual overview of the developed VPF engine internal domain interfaces.

3.6.4 Simulation Handles & Controls

The selection of several handles has already been discussed in previous sections. The reduction in airspeed throughout the landing phase, and the ability to vary engine power settings by implementing fan pitch and/or RPM changes, is expected to introduce significant variation in VPF reverse-thrust system performance. To grasp a firm understanding of the operational performance of a reversing VPF design, these variables need to be studied. Three main variables were identified which could be used to conduct the research. These are summarised in the following points.

- **Fan blade pitch** – The pitch setting when the fan is reversed. As already discussed, -92˚ pitch was used, based on the VPF study undertaken at Cambridge UTC. [120]

- **Fan RPM** – The fan RPM determines the maximum energy transfer available to the working fluid, varying both pressure ratio and mass-flow. The RPM is set directly in the fan-domain overview, and can be changed for each simulation. The reverse-thrust simulations presented in this thesis all studied the fan operating at 92% RPM. Again, this was based upon the preliminary 22” ADP results from the Cambridge UTC study.
- **Aircraft airspeed** – As the aircraft decelerates upon landing, the dynamic head onto the fan is expected to affect the reverse-thrust flow regime. Lower-speeds are expected to provide higher thrust reverser effectiveness values. Understanding this factor is vital to assessing the potential VPF reverse-thrust systems offer, and establishing better insight into its limitations. The airspeed is defined by setting the far-field inlet normal-speed. Maintaining constant total pressure & total temperature values across the far-field boundaries maintains the ambient conditions. Additionally, the ground-plane is set with a wall velocity, corresponding with the airspeed. This is to simulate the velocity difference between the aircraft and the runway. A head/tail/crosswind could be introduced by varying the velocity components between the inlet & ground-plane, however this was not undertaken in this study. Speeds between 140 to 5 knots were simulated on both models, based on the Boeing 757 quoted landing speed. [121]

3.6.5 Computational Procedure

The final part to understanding the method is the procedure with which the computational process was conducted. One of the many benefits of conducting a study of this nature at Cranfield University is the availability of the institutes private high-performance computer (HPC). This is a necessity when running the type of large-scale high fidelity CFD cases found in this study. Throughout most of the project, Cranfield’s Astral-2 HPC was the current system available to Masters & doctorate students alike. Its successive replacement; Delta, was activated in August 2017, therefore testing and results generation of the assembled research models was carried out on this platform. Both systems operate alike, but the computational speed available from Delta is notably quicker. Delta consists of a total of 118 computational nodes, each containing two Intel E5-2620 v4 (Broadwell) CPUs, giving 16 CPU cores and 128 GB shared memory. The result of which, is a total of 1888 available computational cores, with a theoretical peak processing performance of 60.0 TFlops. [114] However access is typically limited to ≤128 cores per case. This is important to appreciate when reviewing the time required to run the model, in *Table 5-1*.

3.6.6 Fluid Settings & Boundary Conditions

The fluid settings and the boundary conditions for the model will now be summarised. For those with a background in CFD, this is fundamental to understanding the configuration of the simulation solver, and a necessary reference for future studies.

All domains were set with a reference pressure value of 0. Therefore, all quotes pressure values are absolute. The fluid material used was the air-ideal-gas model, available by default in CFX. For all reverse-thrust simulations, the same ambient conditions were also used, corresponding the with International Standard Atmosphere (ISA) values for sea-level below.

Total Pressure: 101,325 Pa (1 atmosphere)
Total Temperature: 288.15 K (15˚C)

Additionally, a summary of the boundary condition settings, which are shared across both integrated and isolated cases, is provided in *Table 3-19*. Some of these boundaries are used as handles to change the simulation scenario settings, which is described in more depth in *Ch 3.6.5*. The exact settings used for each configuration of the research simulations is provided in *Table 5-1* & *5-2*.

Location	Boundary Type	Settings
Core Duct Outlet	Normal velocity outlet	Set by estimated IPC inlet velocity
Core Exhaust Inlet	Normal velocity outlet	Set by ATLAS/TM model output
Far-field (Sides & Rear)	Opening (entrainment)	Zero turbulence gradient
Far-field (Inlet)	Normal velocity inlet	Velocity set by airspeed handle
Fan Blade(s)	Smooth no-slip wall	Rotating – set by fan RPM handle
Fan Hub & Spinner	Smooth no-slip wall	Rotating – set by fan RPM handle
Fan Shroud	Smooth no-slip wall	Counter-rotating (stationary)
All Other Internal Walls	Smooth no-slip wall	None
Airframe Walls	Smooth no-slip wall	None
Ground-plane	Smooth no-slip wall	Wall velocity – set by airspeed handle
Periodic (for single-passage)	Periodic Interface	Rotational periodic
Symmetry	Symmetry	None

Table 3-19: Boundary conditions for the research models

The method presented effectively simulates the aircraft stationary, with the ground-plane and far-field inlet air travelling identical relative speeds directly towards the aircraft. This approach is required when using a fixed mesh to simulate a vehicle moving through fluid nearby a stationary runway. The far-field sides and outlet were set as opening boundaries, with the entrainment model (which allows it to operate robustly regardless of flow exit angle). [116] This requires a zero-gradient turbulence intensity setting, as well as the relative pressure (which is set at atmospheric; 101325 Pa). The far-field dimensions for both the isolated and integrated models are presented in *Figures 3-67 & 3-68* respectively.

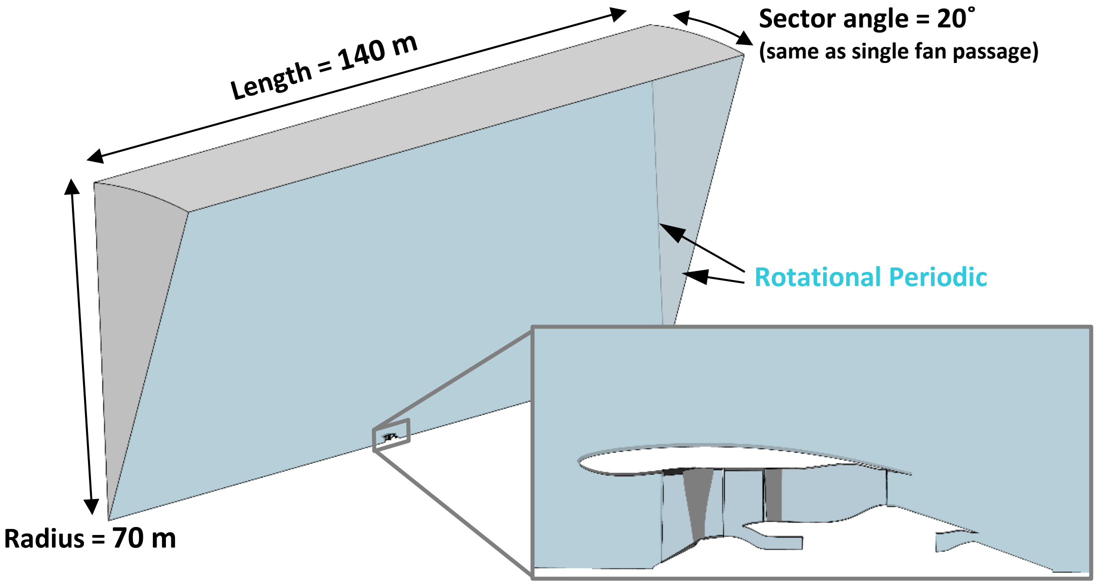

Figure 3-67: Far-field of the isolated research model

The far-field dimensions for both cases were determined and measured non-dimensionally from a reference length; the fan diameter. For the isolated case, featuring a cylindrical far-field, the radial distance was set as 25 fan diameters. The longitudinal distance was set at 50 fan diameters upstream and downstream (this equates to 20 engine/nacelle lengths).

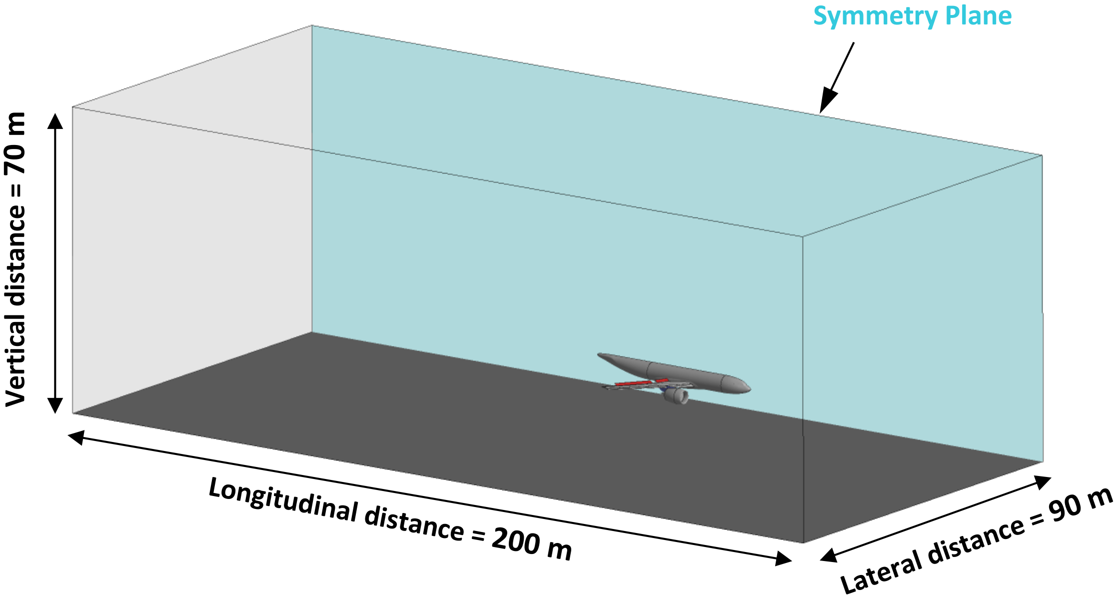

Figure 3-68: Far-field dimensions of the integrated research model

The final research models far-field dimensions are 50 fan diameters longitudinally, and 25 fan diameters for both vertical and lateral distances

For the integrated model, a symmetry plane is used on the vertical boundary along fuselage centreline, such that only half of the whole aircraft is modelled. This is a technique commonly used for engine-aircraft studies, which halves the computational requirements of the model. Whilst this can distort the flow-field locally under certain conditions near the symmetry plane, given the lack of proximity to the nacelle; it is not considered to be an influence on engine related aerodynamics.

Regarding the engine core, the IPC inlet (which is an outlet with respect to the fluid domain), was represented as a normal-velocity outlet boundary. Whilst decoupled via a gearbox, the IPC is still mechanically connected to the fan, and its RPM is directly proportional. Therefore, N1 applies to both fan & IPC, which needs to be taken into account when changing the fan speed in the model.

Knowing this, the IPC inlet axial velocity was estimated at approximately 185 m/s for a fan speed of 92%, and this was used as the initial setting for the core duct outlet boundary. This could be adjusted after the first set of simulation runs, to refine the boundary if necessary.

As for the core-exhaust, the fluid boundary upstream of the exhaust duct was represented as a velocity-inlet. This boundary inlets the high temperature core exhaust out of the LPT system. Lacking in the development of a reverse thrust 0D model (due to the absence of predictable fan performance), the settings for this boundary were based upon the values from the EoR TURBOMATCH result. A temperature of 822K, with an inlet velocity of 120 m/s was used, and maintained throughout the reverse-thrust configurations. Whilst refining this boundary to better match the different cases is not in itself challenging, the required time for additional simulations to run meant that is was unfeasible within the project timescale, once the final research models had been developed.

Furthermore, variations in the core exhaust flow conditions were deemed unlikely to independently cause exhaust-gas re-ingestion. It was deemed more likely that this would be a result of the bypass/core nozzle architecture, resulting in the bypass nozzle’s inlet stream-tube shearing with the hot stream. Small variations on the exhaust gas properties were not expected have a significant impact on whether or not this took place.

3.6.7 Summary of Assumptions/Simplifications

Concluding the methodology, a summary of the simplifications or assumptions made during the development and setup of the research model, is provided following.

- **Axisymmetric nacelle** -The nacelle is axisymmetric, which is a simplification on real designs, but should have marginal effect on system-level aerodynamic performance.
- **Modified fan** – The fan is a modified version of NASA’s ADP. With a reduced hub/tip ratio, the geometry is now notably different from the

original design, achieving approximately 87.5% isentropic efficiency at cruise (compared with the ADP's 94.5%). As such, it can no longer be deemed an optimised design, but it does still perform comparably with the original ADP with respect to the FPR and FTR radial profiles at forward thrust. This also leads to a discontinuity between the 3D fan model and the 0D engine performance model, where the fan was assumed to reach efficiency levels more in line with the ADP. However, for the purposes of investigating reverse-thrust aerodynamics the model was still deemed adequate, with potential to improve of replace the 3D fan model under future studies if necessary.

- **Non-optimised nozzles –** Whilst the nacelle forebody is based off the 22" ADP nacelle, the nozzles on the developed engine model were created from scratch using Cranfield's GEMINI code. Due to time constraints, no additional work to refine the design was carried out, once a satisfactory geometry had been created. This will likely have a small impact on the bypass nozzle performance during reverse thrust. However, the design is considered a good representation of a modern high BPR turbofan, and is ideal for establishing a foundation of knowledge bypass nozzle operating regime, using a conventional design.
- **Additional Engine Simplifications –** No additional struts were added within the bypass duct or core nozzle duct apart from the pylon. No ESS, or nearby turbomachinery was included. The core engine inlet duct was left empty. This simplification was justified by concerns regarding the numerical model stability if they ESS blades were featured, given the nearby fluid-outlet boundary. Additionally, time was not available to conduct an ESS design study under the project.
- **Ground Clearance –** The vertical clearance between the lowest point of the nacelle & the ground plane was determined based upon quoted data from airframe manufacturer technical documents. The distance was set at 0.6 m, which lies in the typical range for the most modern aircraft in service.
- **Engine Technology –** Assumptions were made regarding the engine core technology capabilities; namely the T30, T40, & OPR limits. As the engine

model was developed with an expected entry into service between 2025-2030 (to represent an UltraFan™), these limits exceed those found in current production engines of comparable size. Whilst the T30 & T40 limits remain confidential, they were chosen after consultation with the UltraFan™ team at Rolls-Royce, and were in-line with the latest estimated limits for the ‘middle-of-the-market’ UltraFan™, at the time the TURBOMATCH work was conducted. Furthermore, the 0D model did not feature VPF performance maps, but modelled the engine fitted with a fixed-pitch fan, with identical cruise operating characteristics.

- **Airframe Simplifications –** No actuation linkages for the wing flaps or slats were included, or the corresponding aerodynamic housings under the wing. The airframe does not include landing gear, or tail-plane surfaces (horizontal/vertical stabilizers).
- **Symmetry Plane –**The integrated research model features only half of the full aircraft, using a vertical symmetry plane down the fuselage centreline as previously discussed.
- **Symmetrical Pylon** – The pylon model created for the project is of simple design, using symmetrical NACA profiles to provide an aerodynamically suitable profile. However real-world pylons are typically not symmetrical, due to the variation in exhaust pressure-fields between the inboard and outboard sides of the pylon.

4 Model Validation & Verification

Having established the methodology for the development of the research models, this chapter aims to provide a summary of the validation and verification procedures which were undertaken on the individual components. Whilst this is not essential to understand the results or conclusions of this research, it is a vital part in establishing confidence and accuracy of any CFD based study. More-so for the topic of VPF thrust-reversal, as no comparable CFD or experimental data had been published on reverse-thrust fan performance at the time of this work, other than that provided from Cambridge UTC. It should be noted that all CFD validation/verification work (forward flow) achieved convergence levels of 10e-5 for the mass & momentum residuals, using RANS equations. The convergence of flow residuals for the primary components validation is provided in *Appendix B.*

4.1 Annular Models

4.1.1 TURBOMATCH 0D Cycle Model

Whilst the TURBOMATCH model does not have a direct implication to the results of the simulation, it does affect the design and sizing of the engine, due to the predicted future technology limits for an engine entering service between 2025-2030. The 0D model block arrangement, which represents the thermodynamic stages of the engine, as previously mentioned, was taken directly from a previous UTC doctoral study, and represents a potential UltraFan™ engine architecture. [16] The thermodynamic model & optimiser were both tested and validated extensively under previous work. Therefore, other than a sanity check of the engine model which was selected, no further verification or validation work was deemed necessary for the purpose of this project. It should also be noted that the 0D design was undertaken with the assistance of the previous work's author.

4.1.2 ATLAS 2D Annular Model

The 2D ATLAS model, which was used to estimate the component annular size and arrangement, was also developed according to previous UltraFan™ studies conducted with Cranfield UTC. [16, 88] The engine model was refined until the number of compressor/turbine stages was aligned with the UltraFan™ concept, and the gas-path was deemed aerodynamically feasible, compared to existing designs. The final design was reviewed by the same doctoral author who developed the TURBOMATCH model, as that study also involved extensive use of ATLAS.

Additionally, conclusions from the weight estimation analysis did not highlight anything untoward about the design, and it is difficult to determine the overall engine weight, without conducting additional research. It was no possible from existing literature to determine approximate weight values for VPF modules, their secondary systems (such as actuator controls), and the benefits from removal of conventional TRUs. The weight estimation lies outside of the project scope, given the timescale for the project. Therefore, the model was deemed adequate for the study, given that it only provides limited input to the CFD engine design; namely the engine length and core inlet/outlet positions.

4.1.3 GEMINI Nacelle & Bypass/Core Nozzle

The GEMINI annular nacelle & nozzle design is the only part of the annular design module which contributes directly to the CFD geometry. A lightweight analysis of the design's aerodynamic performance at cruise was therefore required. A model was setup at cruise (Mach 0.8) consisting of only the isolated nacelle domain. The boundaries were set to match the TURBOMATCH result file, regarding total pressure and temperature. These were then refined to ensure the correct mass-flow was obtained.

The verification was conducted in two parts. The first part focussed on the nacelle performance and drag. A common metric described by Walsh & Fletcher to assess nacelle performance is the pod drag (*ref. Eq 4-1*). [74] The pod drag was extracted from CFX by determining the sum of the forces acting on the exposed walls of the nacelle (namely, nacelle lip & outer surface, aft-body core casing, and external plug).

$$Pod\ Drag = 0.5 \cdot \rho \cdot {V_\infty}^2 \cdot C_{DF} \cdot A \qquad \textbf{(4-1)}$$

Where
$\boldsymbol{C_{DF}}$ *= drag factor, usually varying between 0.002 and 0.003*
A *= nacelle surface area*

The calculated drag factor value for the CFD prediction was 0.002778. Furthermore, examining contours of Mach number and turbulent kinetic energy indicate no immediate issues with the aerodynamics.

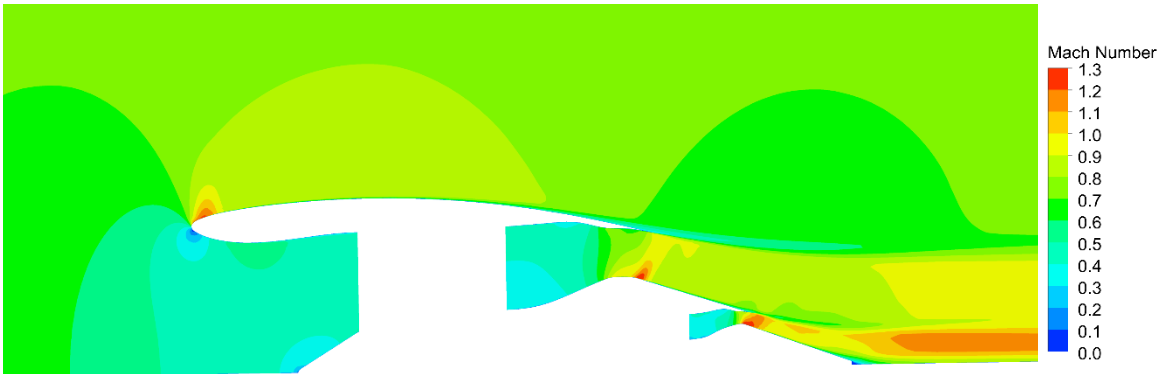

Figure 4-1: Cruise Mach contours for the GEMINI created nacelle/nozzles model

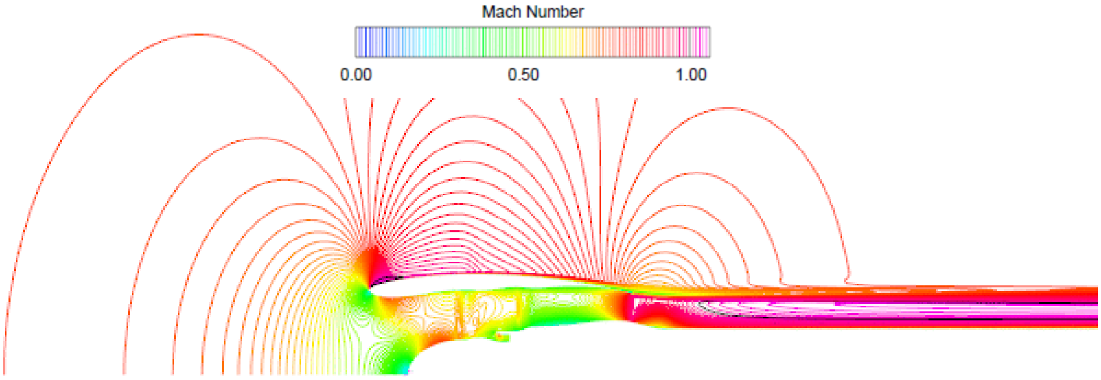

Figure 4-2: Cruise Mach contours from a CFD based NASA publication [96]

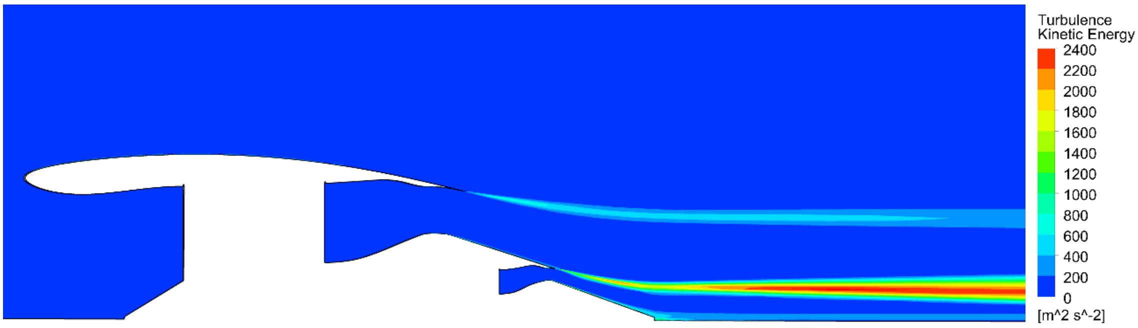

Figure 4-3: Turbulence kinetic energy contours for the GEMINI created nacelle/nozzles model

Validating the GEMINI model against the published ADP nacelle only extends as far as the nacelle lip & main body. The exhaust systems are not directly comparable, due to the lower specific-thrust design of the GEMINI engine. Comparing Mach contour plots for the GEMINI & ADP nacelles (*ref. Figure 4-1 & 4-2*), the two designs form similar flow-fields. The stagnation point on the nacelle leading edge is approximately the same location in both cases, indicating similar inlet stream tube geometry. The turbulence kinetic energy contours shown in *Figure 4-3* do not indicate significant drag from the nacelle; identifying only the shearing layers between the core, bypass and freestreams, with no premature separation on the nacelle trailing edge.

The more important aspect of the GEMINI model verification was the performance assessment of the exhaust systems, particularly the bypass nozzle. It is particularly important to ensure this is designed correctly, as it acts as the main engine intake during reverse thrust, particularly at lower speeds where the dynamic head onto the fan is relatively low, allowing potentially a greater amount of mass-flow to be reversed. Two parameters found widely used in literature for gas turbine nozzle performance measurements are the nozzle velocity coefficient, C_v, and nozzle discharge coefficient $C_{D.noz}$. [86, 93] C_v accounts for reduction in exhaust velocity due to skin friction losses in the exhaust duct. $C_{D.noz}$ determines the blockage factor at the nozzle exit plane, induced by the boundary layer, or any flow separation present. Both these parameters are formulated below: -

$$C_v = \frac{V_{noz\ exit}}{V_{ideal}} \tag{4-2}$$

Where
$\boldsymbol{V_{ideal}}$ *= ideal exit velocity of the nozzle*
$\boldsymbol{V_{noz\ exit}}$ *= actual exit velocity of the nozzle, which can be determined from Eq. 4-3*

$$\frac{V}{\sqrt{T}} = \frac{M \cdot \sqrt{(\gamma \cdot R)}}{\sqrt{\frac{T}{t}}} \tag{4-3}$$

Where
$\boldsymbol{M}$ *= Mach number*
$\boldsymbol{\gamma}$ *= ratio of specific heat (1.4 for bypass, $1.3\dot{3}$ for core)*
$\boldsymbol{R}$ *= ideal gas constant (287.05 J/kgK)*
$\boldsymbol{T}$ *= total temperature*
t *= static temperature*

$$C_{D.noz} = \frac{A_{effective}}{A_{geometric}} \tag{4-4}$$

The calculated values for these two parameters, for the bypass and core exhaust systems, are presented in *Table 4-1* & *4-2* respectively.

BYPASS EXHAUST SYSTEM	
Parameter	**Value**
$V_{noz\ exit}$	293.4 m/s
V_{ideal}	301.5 m/s
C_v	0.973
$A_{effective}$	3.174 m^2
$A_{geometric}$	3.246 m^2
$C_{D.noz}$	0.978

Table 4-1: Bypass exhaust system cruise measured performance

CORE EXHAUST SYSTEM	
Parameter	**Value**
$V_{noz\ exit}$	464.1 m/s
V_{ideal}	477.8 m/s
C_v	0.971
$A_{effective}$	0.257 m^2
$A_{geometric}$	0.271 m^2
$C_{D.noz}$	0.949

Table 4-2: Core exhaust system cruise measured performance

The measured values lie within typical values for turbofan engines. [86, 93] To conclude, whilst no design space exploration was conducted for the nacelle/nozzle 2D annular design, the preliminary verification indicates adequate performance at cruise. The model was therefore deemed to provide an accurate representation of a potential near-future turbofan, with no compromising features for the improvement of reverse thrust.

4.2 Turbomachinery

4.2.1 Baseline ADP Validation

In order to verify the final scaled variable-pitch fan model, the process begins with validation of the baseline ADP. By first ensuring the mesh and solver are able to accurate predict flow through the ADP according to experimental data, confidence can be established in the CFD method when testing the modified fan if the same approach is adopted. A mesh independency and validation study was therefore conducted on the baseline ADP geometry, to ensure that mesh resolution, solver controls, and the geometric definition itself were fit for purpose.

The mesh independency study consisted of 4 different mesh-cases, between 0.5 million and 6 million elements in total for all domains (fan, middle-passage, CIGVs & FEGVs). The fan operating configuration tested was cruise. Mesh dependency was identified below 1 million elements total, as shown in *Figure 4-4*. The Y^+ corresponding with the coarsest mesh is between 5 & 10; outside of the recommended value for the *κ-ω SST* turbulence model's high-resolution boundary layer mode. Therefore, a median mesh density of ~3 million elements was chosen, corresponding with a $Y^{+} \approx 2 - 4$.

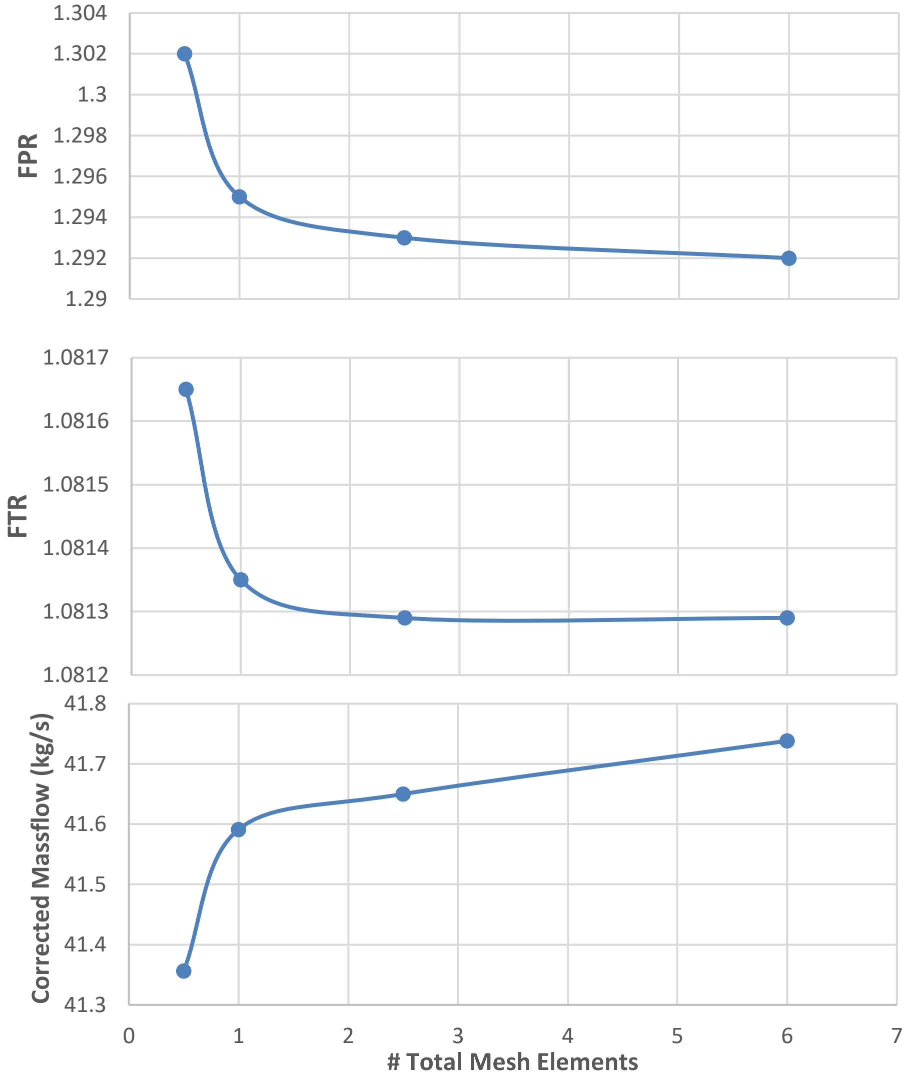

Figure 4-4: Comparison of fan performance for mesh dependency analysis

The mesh-independent CFD results were then validated against experimental and computed data, published by NASA. [45, 47] This was done essentially by comparing span-wise profiles for FPR, FTR, and/or isentropic fan efficiency, depending on the available data for the operating point in question. Four operating points were simulated; approach, cutback, sea-level take-off (SLTO) and cruise. The results were found to have high solution accuracy when compared with the published data, with marginal variations at the end-walls. This was expected, as there are were minor differences between the NASA and

Cranfield simulations; the Cranfield model lacks tip/hub clearance modelling, and has an extended duct inlet.

A summary of the validation results is presented following. The data presented in *Figures 4-5 & 4-6* were calculated using measuring stations within the engine, as described in the appropriate NASA report. As such, the span-wise profiles for approach, cutback & SLTO are measuring the bypass stream only. This is not the case for the cruise results, taken from a different report, where the engine model did not feature a splitter or core duct. The cruise results represent the full span-wise performance of the fan, not just the bypass stream.

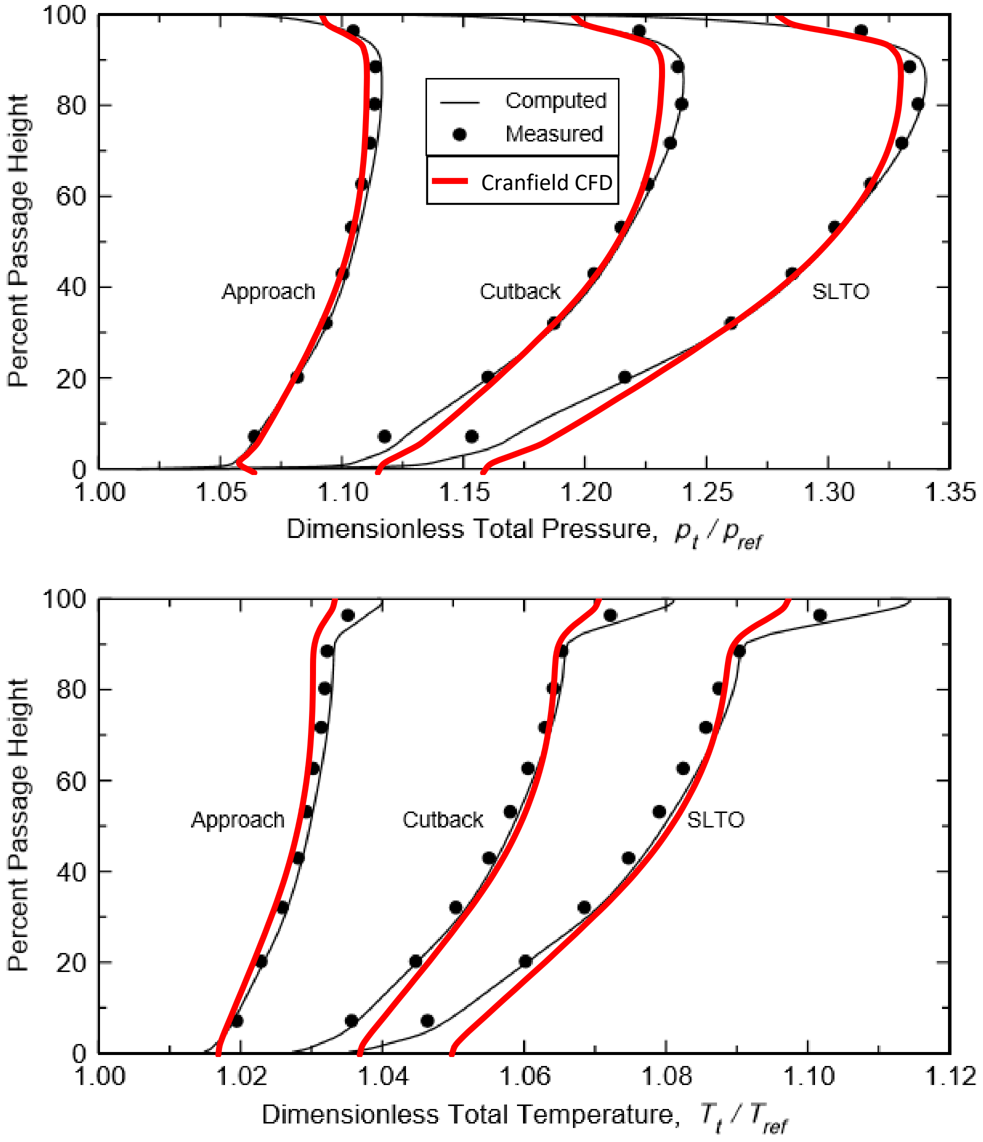

Figure 4-5: Comparison of span-wise FPR & FTR for ADP rotor at +9˚ pitch [47]

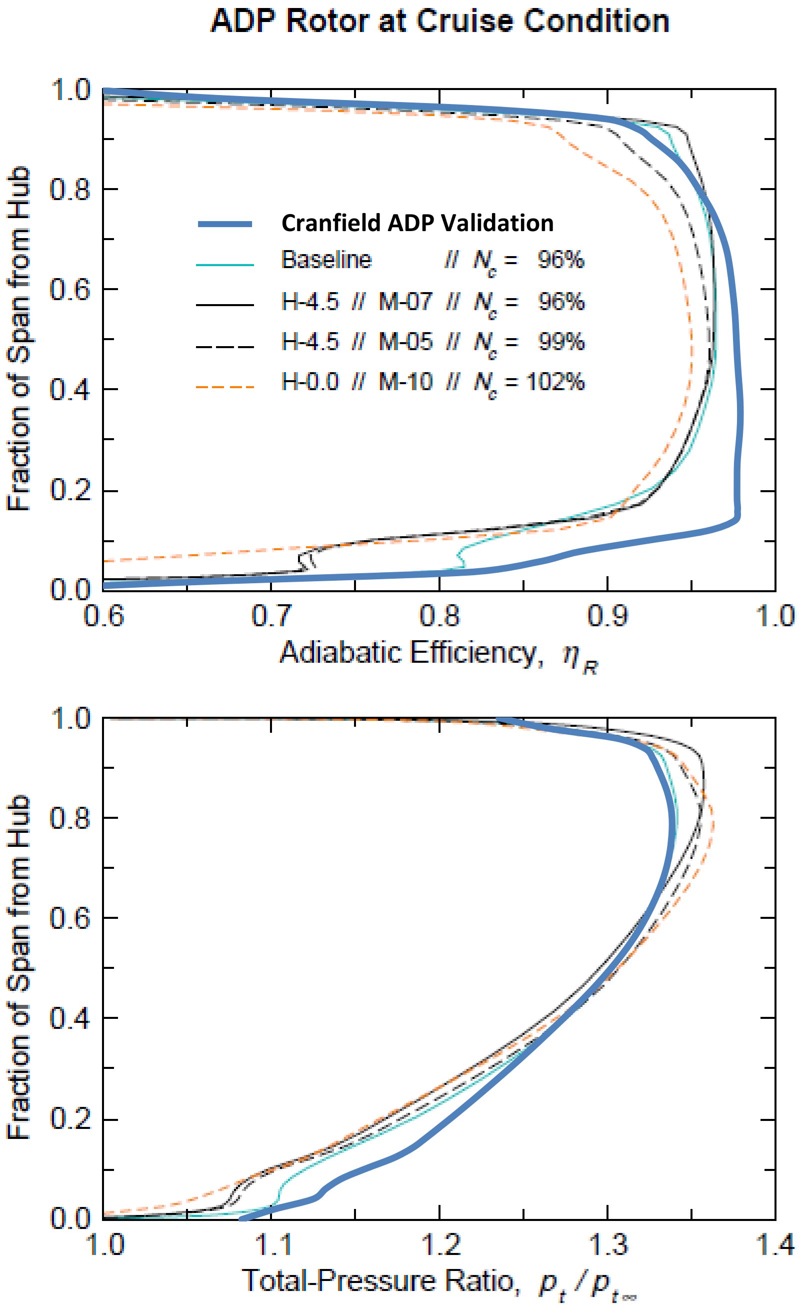

Figure 4-6: Comparison of span-wise FPR & adiabatic efficiency for the ADP rotor [96]

The matching was reasonable for the ADP at cruise; the most notable variation was in hub efficiency, and a slightly change in the gradient of the FPR profile. However, these can be attributed most or entirely to the small difference in measuring stations behind the fan between the NASA and Cranfield work, and the different annulus of the splitter-less ADP. A comparison between the computed & published ADP mass-flows is also provided in *Table 4-3*.

	NASA Published [45, 46, 47]		**Cranfield CFD**	
	Massflow (kg/s)	**BPR**	**Massflow (kg/s)**	**BPR**
Cruise*	41.65	13.3	41.86	13.2
SLTO	36.16	10.5	36.66	10.7
Cutback	31.23	10.7	30.99	10.4
Approach	22.73	9.9	22.42	10.1

Table 4-3: Mass-flow & BPR comparison for ADP baseline CFD validation

The ADP OGV was also validated, as it would later form the geometric input for the full-sized engine's OGV. Comparisons of Mach number profile for both the baseline ADP fan & OGV are provided in *Appendix C*. These contributed to the overall conclusion that the model had successfully captured the aerodynamic characteristics according to the published data. Additionally, *Appendix D* contains the simulation results from the baseline ADP, using the SOCRATES through-flow code, although this was a secondary validation study.

4.2.2 Scaled Fan Verification

The scaled fan verification was a key part of the model development, and significant work was undertaken to establish a geometry that provided a reasonable level of design point (cruise) performance. The validation study follows the same approach as the baseline ADP; comparing profiles of span-wise efficiency and FPR. The FPR span-wise profile is comparable in *Figure 3-22*, and the efficiency profile is provided in *Figure 4-7*. The profile shows the same slight improvement in efficiency at the outer 50% span of the blade, but degrades further at the hub, as already mentioned in the methodology.

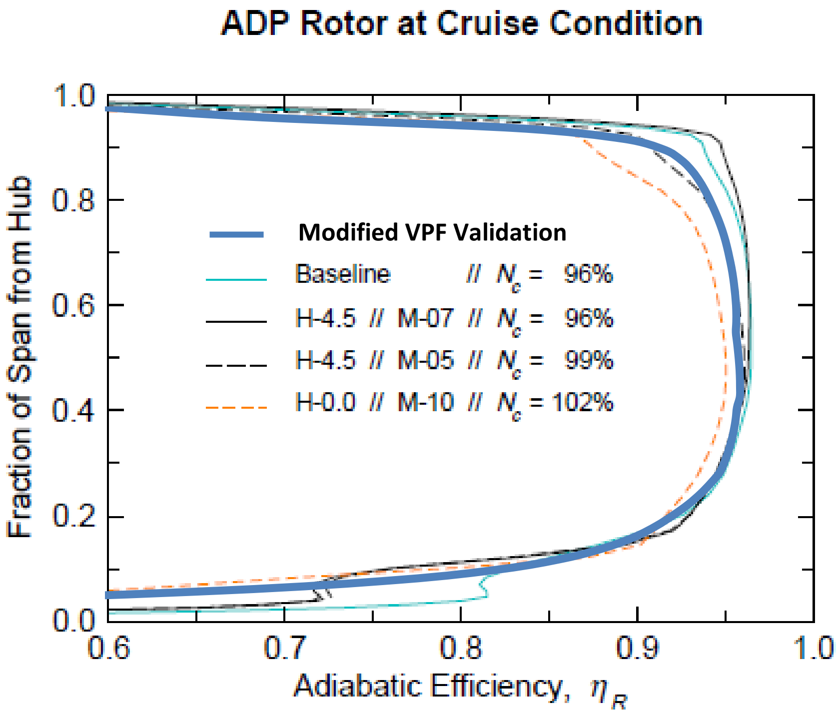

Figure 4-7: Span-wise adiabatic efficiency for the modified VPF & NASA ADP rotors [96]

It was important to understand the reduction in hub performance, and an investigation was conducted by assessing Mach number contours (*Figure 4-8*), shockwave formations, and pressure-fields around the simulated rotor.

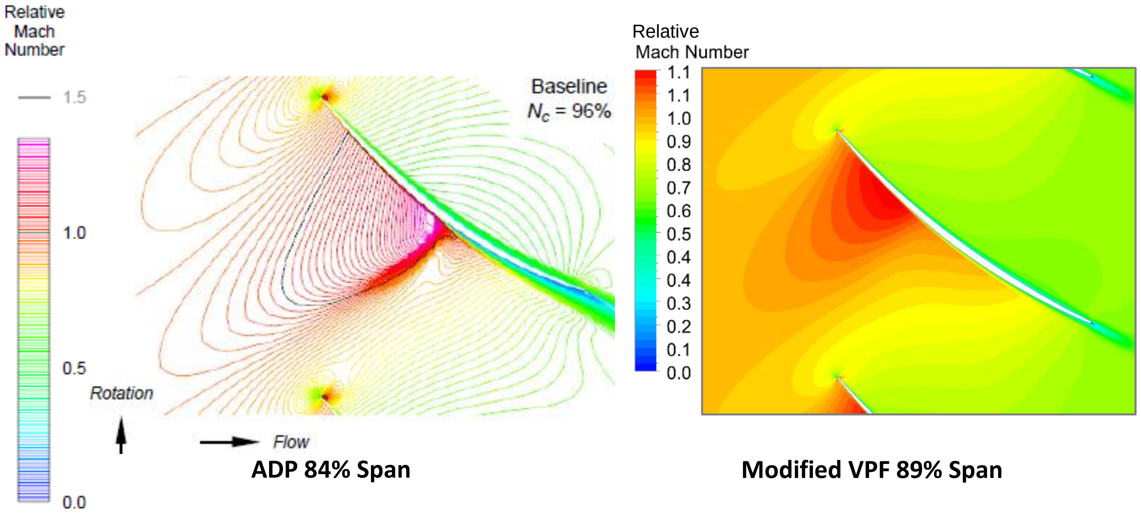

ADP 84% Span

Modified VPF 89% Span

Figure 4-8: Relative Mach number contours for ADP & modified VPF rotor at cruise *[39]*

The two directly comparable contour plots were taken at differing spans, but represent the same normalised radial position, and thus the same blade speed. Additionally, midspan and hub sections are also presented. However, due to the lack of published cruise Mach contours at these span-wise positions, they are compared against SLTO results, which in terms of RPM and FPR are very similar, even with the slight difference in blade pitch.

Efficiency was comparable overall with the ADP, although the hub efficiency dropped to below 60% towards the end-walls, falling more in-line with the 102% RPM case reported by NASA. The reduction in hub/tip ratio had reduced the passage area between the blades towards the root, as previously described during the fan modification process. The result is that the fan blade hub operates closer to the choking point, regarding the formation of shockwaves in the passage, seen in *Figure 4-9*. Therefore, observing the efficiency curve the fan hub region bearing closer resemblance to the 102% RPM NASA seems logical.

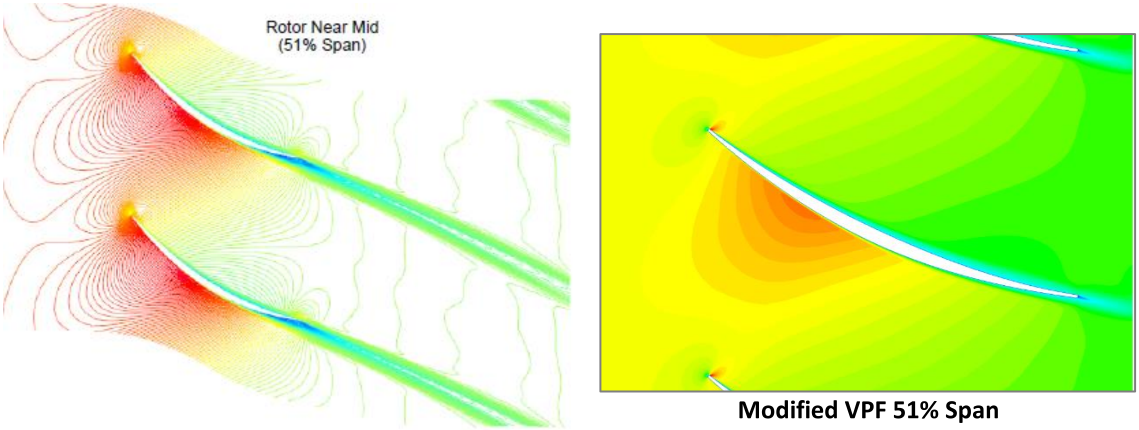

Modified VPF 51% Span

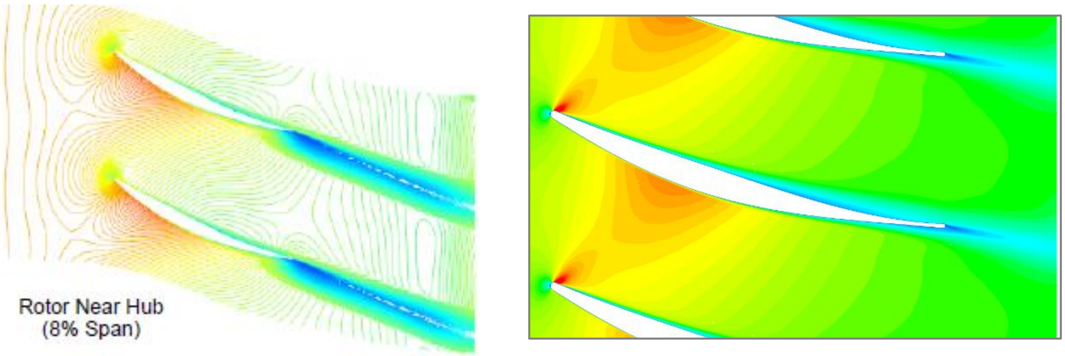

Modified VPF 8% Span

Figure 4-9: Relative Mach number contours for ADP & modified VPF at SLTO/cruise respectively [47]

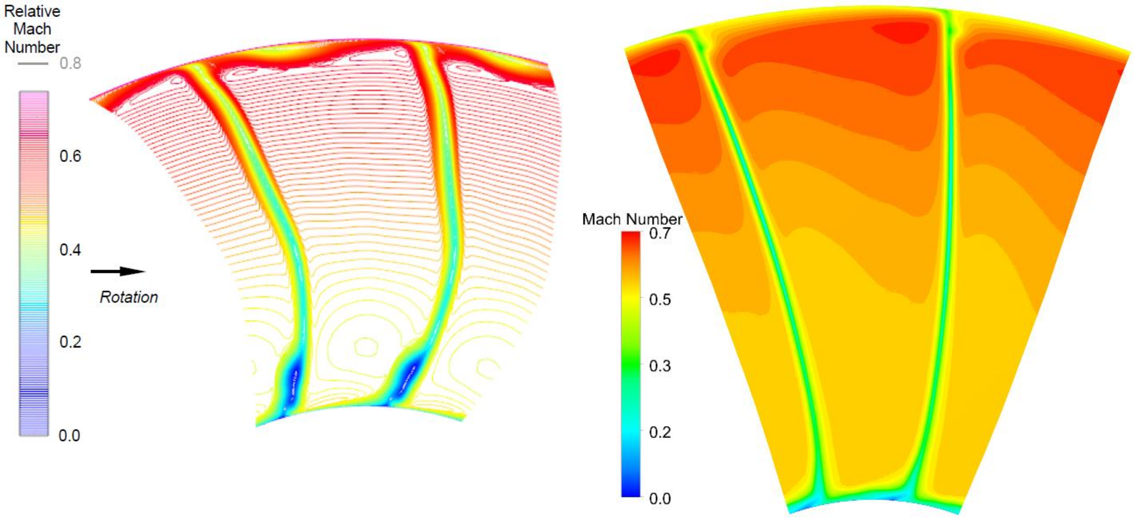

Figure 4-10: Relative Mach number contours downstream of the ADP & modified VPF rotors at SLTO/cruise respectively [47]

Weak normal shocks at the hub due to the reduced passage-width, and therefore throat, resulted in delamination across the aft section of the pressure surface. The outcome was an exit flow deviation much higher than anticipated. Whilst this area is clearly not ideal, the flow dynamics are not unlike those of the original ADP, as seen in *Figure 4-10*. The difficulty in achieved satisfactorily resolved hub aerodynamic performance can be attributed to three fundamental reasons. Firstly, the hub section cannot achieve a high-pressure ratio given the inherently higher stage loading at lower spans. This means that any additional losses, (such as those attributed to boundary layer delamination or shockwave formation) have a disproportionate effect on the local compression efficiency. Secondly, as the span decreases, the blades physically become closer together. This increases the diffusion characteristic of the blade passages; reducing flow capacity by narrowing the throat. In response, the flow accelerates to a higher velocity, moving closer to choking. Thirdly, these losses are difficult to avoid, given the mechanical requirement for thicker profiles towards the rotor hub.

A final summation of the fan-stage operating characteristics at cruise are presented in *Table 4-4*.

Parameter	Design Value	CFD Value
BP Outlet PR	1.294	1.272
Core Delivery PR	1.10	1.02
Peak FPR	1.35	1.33
BPR	13.5	13.8
Inlet Mass-flow	1,160 kg/s	1,181 kg/s
Overall η_{isen}	0.945	0.875

Table 4-4: Operating aerodynamic characteristics for the modified VPF fan at cruise

Having assessed the fan's aerodynamic performance, it was clear that some improvement was available by further refinement, which should allow an efficiency closer to 95% to be possible. However, overall it was still considered to be a good representation of a VPF, providing appropriate outlet characteristics not unlike the original ADP, and fulfils its requirement of researching VPF reverse thrust. Additionally, this work remains relevant to the original ADP, including the Cambridge UTC study.

4.2.3 Splitter Verification

Regarding the splitter verification, the geometry was based off the Trent 1000 production engine, and was marginally displaced radially when integrating to the developed engine model. The main verification requirement for this component is that the splitter LE is properly situated radially in the fan-outlet stream for the desired bypass ratio at cruise. Furthermore, no spillage or flow delamination around the splitter is tolerable. The duct and splitter geometry streamlines were also compared with published CFD streamlines from NASA. *Figure 4-11* shows ADP splitter streamlines published by NASA, whilst *Figure 4-12* features the scaled VPF's splitter streamlines.

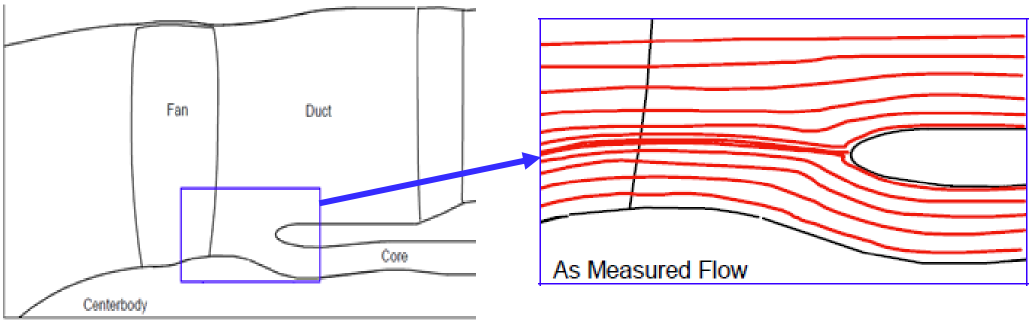

Figure 4-11: ADP reported splitter streamlines at cruise [123]

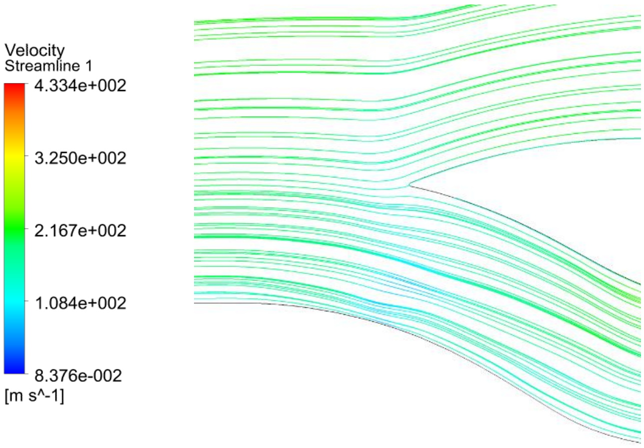

Figure 4-12: Velocity streamlines at cruise for the scaled VPF's splitter

Nothing untoward was found with the splitter or the core duct; the mass flow requirements were satisfied for the engine core, without aerodynamic concern. Data on the splitter aerodynamics is provided in *Table 4-3* below.

Parameter	CFD Value
BPR	13.8
Core Cruise Corrected Mass-flow	79.8 kg/s
Compressor Inlet Delivery PR	1.02
Compressor Inlet Axial Velocity	190 m/s

Table 4-5: Splitter & core inlet duct performance

4.2.4 Scaled OGV Verification

With regards to verifying flow performance, the OGVs (or FEGVs as referred to on the ADP) were required to fulfil one main requirement; intercept the swirling bypass flow downstream of the fan, and correct it such that the exiting flow direction is completely aft, with minimal aerodynamic losses. This maximises the forward thrust, as the nozzle exit axial velocity is increased. Following refinement of the modified OGV model, satisfactory aerodynamic performance was achieved. This was verified by assessing the extent of boundary layer delamination, and measuring the averaged exit flow angle downstream of the OGV stage (*see Figure 4-13*). Regarding the exit flow angles, the maximum deviation was less than 5˚, and the measured mass-flow-averaged angle at the OGV outlet was 88˚ degrees (with 90˚ being ideal).

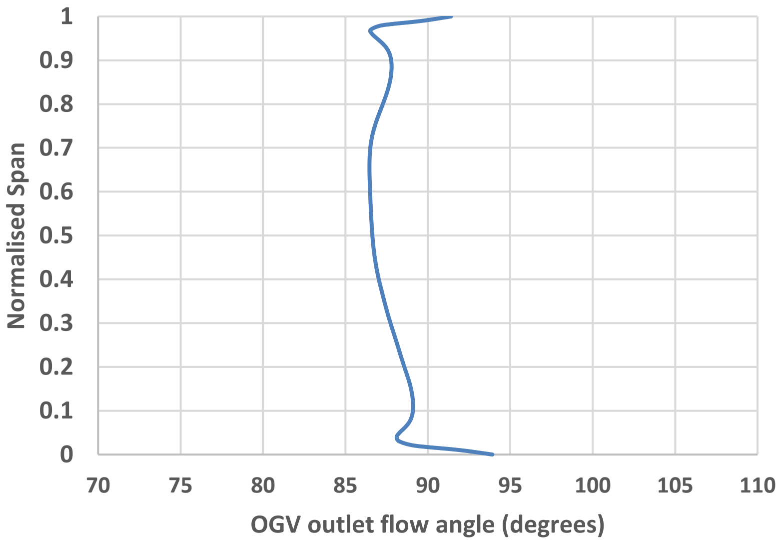

Figure 4-13: Span-wise distribution of modified OGV outlet flow angle

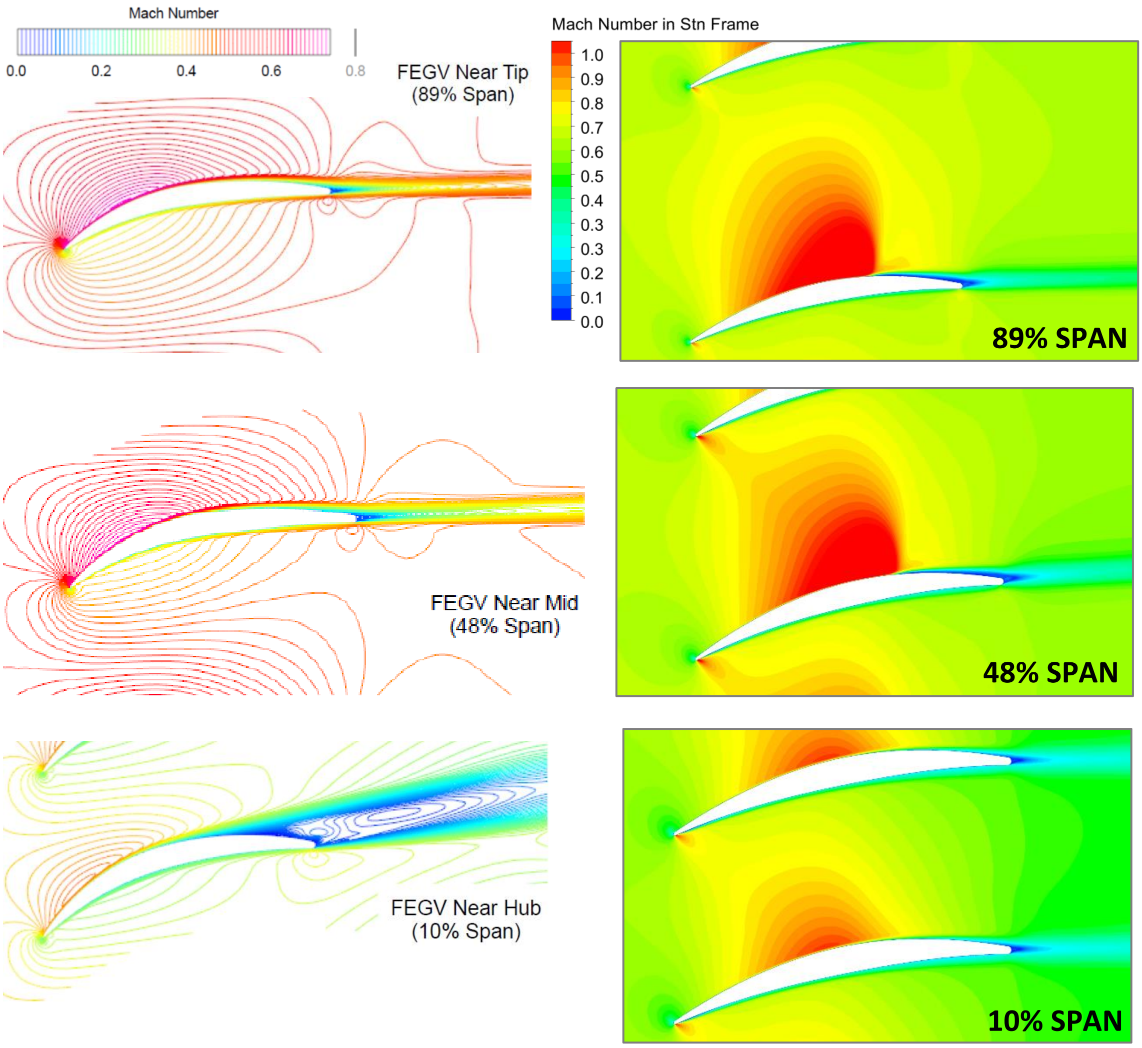

NASA's ADP OGV at SLTO ***Cranfield's modified OGV at cruise***

Figure 4-14: Comparison between ADP & modified OGV span-wise Mach number contours [47]

The final OGVs which were integrated into the research model performed comparably with the original ADP, with marginally less flow separation observed towards the hub region. However, due to the absence of published data for the OGV performance at cruise, the verification was conducted again against the SLTO performance, shown in *Figure 4-14*. Since the SLTO configuration requires the fan pitch changed by 9 degrees from cruise, there is some disruption to the velocity triangles and exit angle of the fan blades. Therefore, an incidence is induced onto the OGVs not experienced at cruise, which could account for earlier onset of boundary layer separation in the baseline ADP results. Additionally, the

OGV camber angle is somewhat reduced on the modified version, making it inherently less susceptible to flow separation. This can also be observed on the span-wise outlet contours of Mach number shown in *Figure 4-15*. The main observable difference in the outlet profiles is the modified VPF version seems to generate narrower more uniform wakes towards the hub. It is unclear whether this is due to the changes made during OGV scaling & modification, or whether this is attributed to the incidence caused by the off-design fan pitch angle at SLTO. This could also explain the slightly higher Mach number regime between the downstream wakes of the modified OGVs. At cruise pitch the fan operates with a higher axial velocity for a given blade speed, due to the opening of the fan blades. Thus, a slightly higher velocity through the OGV passages would also be expected.

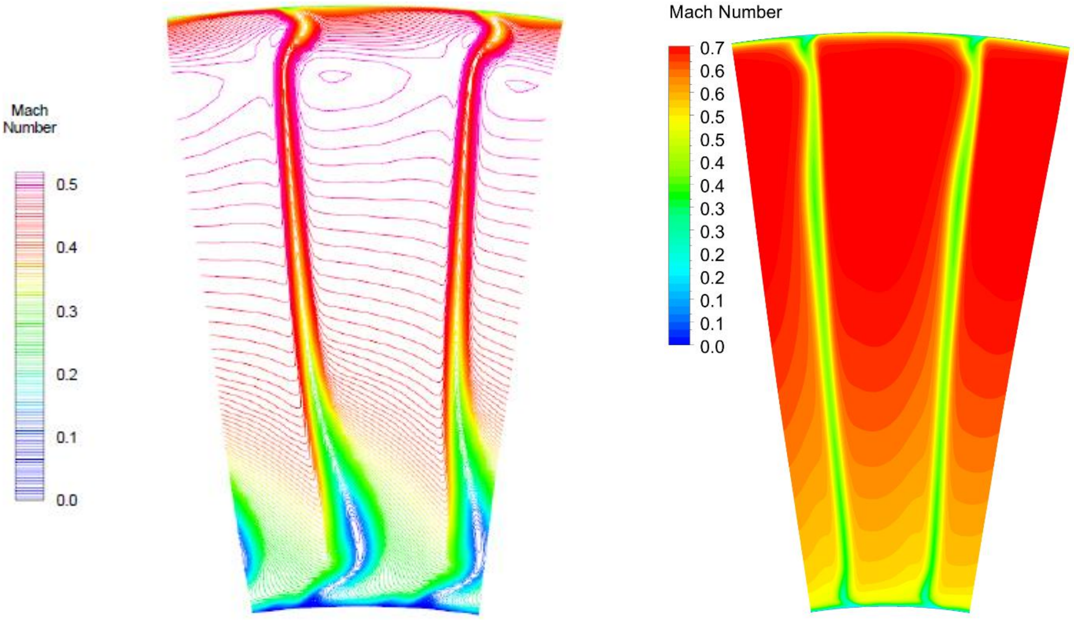

Figure 4-15: Span-wise Mach contours on the outlet of the ADP & modified OGVs [47]

Overall the guide vanes performed as intended, and were deemed adequate for the purpose of researching reverse-thrust. However, having undertaken hub/tip and stagger/camber angle changes, the model was notably different from the ADP baseline OGV/FEGV. Whilst the Mach number in the OGV passage was higher than that published in the ADP literature, this should not be of concern to reverse-thrust studies, as the expected mass-flow through the bypass duct under these conditions is significantly lower than nominal, according to the VPF work done at Cambridge UTC. [117] Furthermore, the OGV test simulations delivered the expected mass-flow to the bypass outlet, without significant pressure loss.

4.2.5 Full-Annular Mesh Independency

The final integrated research model with single-passage internal domains featured in excess of 30 million elements. With the transition to full-annulus modelling, there were concerns regarding the computational time required to run the model. This was no more relevant than in the case of the fan domain, where the default mesh contained 6 million elements per passage. With 18 blades, the increase in mesh size was unacceptable, and a brief mesh independency study was conducted to quantify the minimum resolution required to simulate the reversed-fan's performance characteristics. The fan's reverse-pitch operating regime is complex in nature, and is explained in some depth in *Chapter 5*. However, for the purpose of understanding the validation, its operation is not comparable with a conventional fan. With this in mind, a less compressor-orientated approach to assessing the fan's performance was conducted, by measuring circumferentially-averaged flow angles up and downstream of the stage, as well as Mach number distributions. Several meshes of varying resolution were generated, using the mesh parametric scaling functions in Turbogrid. These ranged from 230,000 elements to 6 million. *Figures 4-16* to *4-18* present some of these span-wise plots.

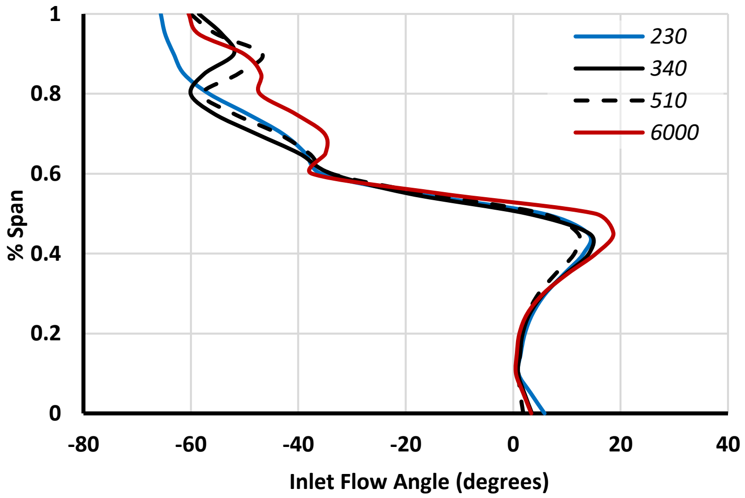

Figure 4-16: Inlet flow angle of the reversed fan stage at -92˚ pitch, 92% RPM

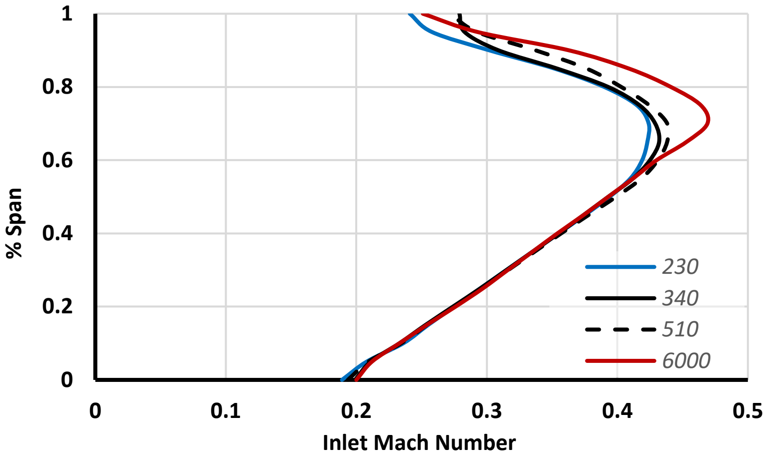

Figure 4-17: Inlet Mach number for fan stage at -92˚ pitch, 92% RPM

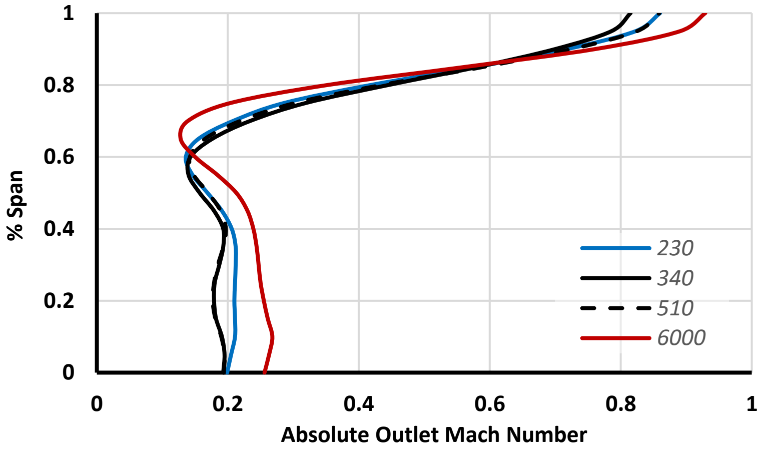

Figure 4-18: Outlet absolute Mach number for fan stage at -92˚ pitch, 92% RPM

Findings from the mesh independency study indicated that the reduced density grids could adequately capture the reversed rotor aerodynamics below 60% span. Beyond this span; in the fan’s most effective aerodynamic region when reversed, some variation in flow dynamics can be observed. This has been attributed to the extremely challenging flow conditions to resolve in the numerical model during flow reversal, including large separations transmitted across the rotational periodic boundary. A grid convergence index (GCI) comparison was also conducted (*Appendix F*), from which it was determined the 500k mesh performed most efficiently/accurately. This was used for the creation of the full annular model. Mesh refinement work on the OGV and middle-passage domain was also undertaken, although these yielded marginal reductions in element count; as they were already deemed relatively lightweight. This did not therefore warrant another dependency study for these domains.

4.3 Airframe Models

4.3.1 Scaled DLR F11 Validation

Selecting the DLR F11 as the aircraft model for the study provided a wealth of publicly available data, against which to validate to CFD method. The airframe contributes significantly to the assembled research model, providing not only the largest geometry definition (the airframe itself), but also simulates the flow-field surrounding the engine, defining the ambient inlet/outlet conditions to the whole simulation. It is therefore essential to ensure that the approach developed to meshing the airframe is properly validated. A summary of this work is presented following. The first part required another mesh independency study; assessing the lift coefficient across 5 different density meshes, provided in *Figure 4-19*. The lift coefficient represents the lift generated per-unit area of the wing reference surface area, and is calculated according to Equation 4-5.

$$C_L = \frac{L}{A \cdot 0.5 \cdot \rho_\infty \cdot {V_\infty}^2} \qquad \textbf{(4-5)}$$

Where
$\boldsymbol{L}$ *= lift force*
$\boldsymbol{A}$ *= reference wing surface-area*

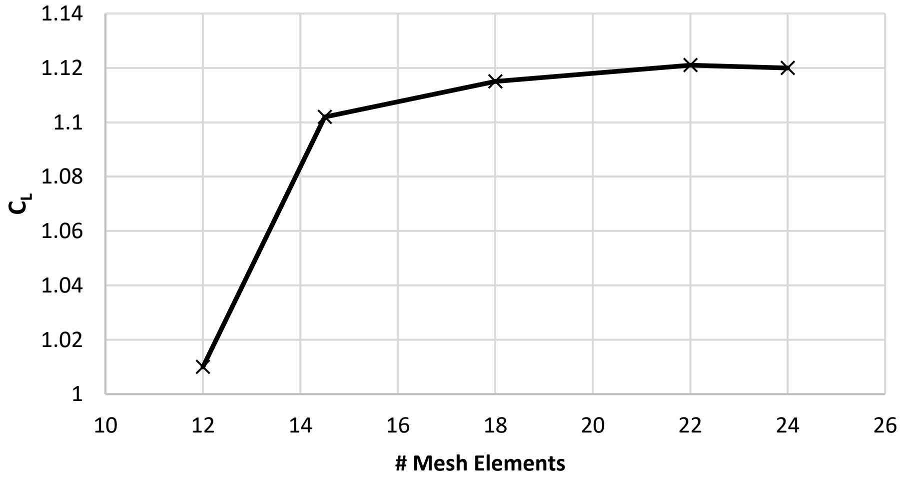

Figure 4-19: Scaled DLR F11 mesh independency study

Having established guidelines for the airframe mesh density, a study of the wing & high-lift device aerodynamic accuracy was carried out, studying surface pressure distributions, and lift-coefficient (across several angles-of-attack; 0˚, 5˚, 7˚ & 10˚). Public domain data encompasses both experimental (wind tunnel) performance data, and CFD derived results. The CFD results, as mentioned in the methodology chapter, were conducted by numerous parties involved in NASA/AIAA's HLPW 2, and include both structured and unstructured meshing approaches. *Figure 4-20* presents only unstructured CFD & experimental results for comparison. The verification cases were conducted in sync with the flow conditions specified by the DLR F11 workshop (Mach 0.175, T_{total} = 114 K, P_{ref} = 295 kPa). [77]

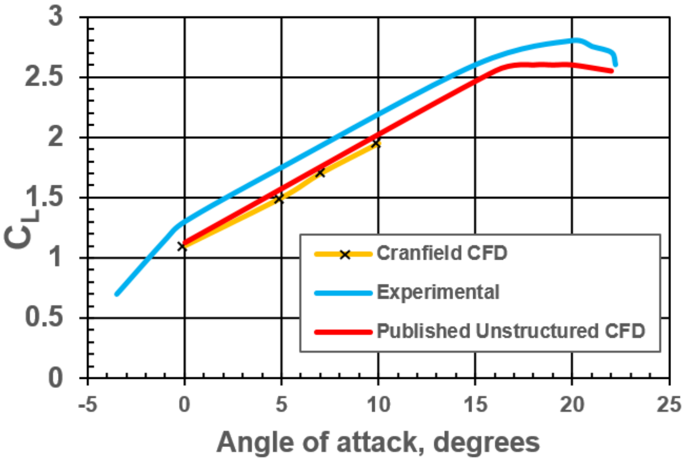

Figure 4-20: Lift coefficient validation plot for scaled DLR F11 [84]

The values of C_L calculated from the Cranfield scaled DLR F11 simulations matched the published data for other unstructured CFD results. [84] The model presents a slight under-prediction of the C_L by approximately 0.2, however this appears to be an inherent feature across both Cranfield's and HLPW2 unstructured mesh simulations. The final stage of the baseline airframe validation was to compare the static pressure coefficient (C_P) distributions across the lifting hardware (wing, slat & flap). *Figure 4-21* presents these distributions at 68% span with reference to published results. Distributions for 29% & 89% are also provided in *Appendix E* for reference.

$$C_P = \frac{P - P_\infty}{0.5 \cdot \rho \cdot {V_\infty}^2} \tag{4-6}$$

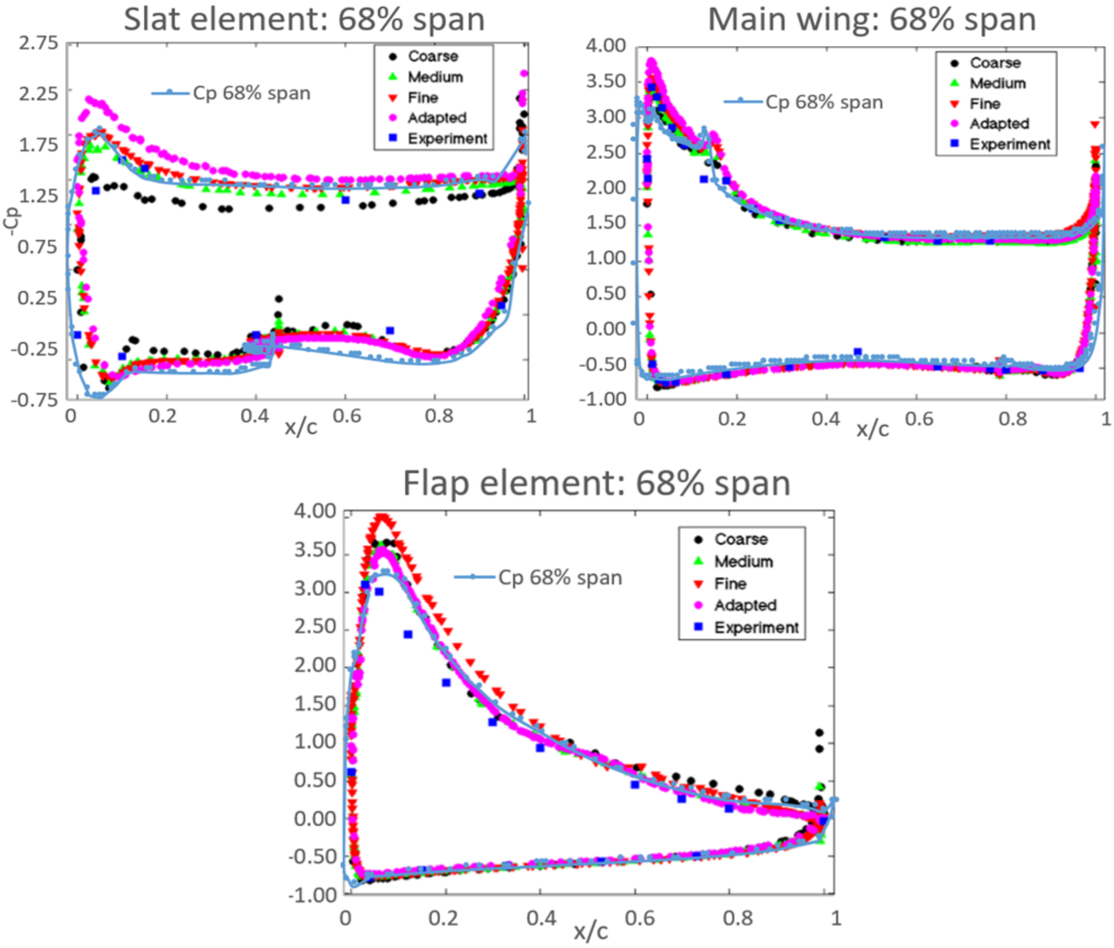

Figure 4-21: Stream-wise distributions of pressure on scaled DLR F11 wing, flap & slat at 68% span [124]

4.3.2 Spoiler Verification

The spoiler verification procedure involved measuring the drag force directly associated with the spoiler surfaces and mapping the variation with speed. The trendline should follow a square-law, due to the rise in kinetic energy associated with higher velocities. Three speeds were studied; (140, 100 & 60 knots respectively), with the corresponding measured spoiler drag forces presented in *Figure 4-22*.

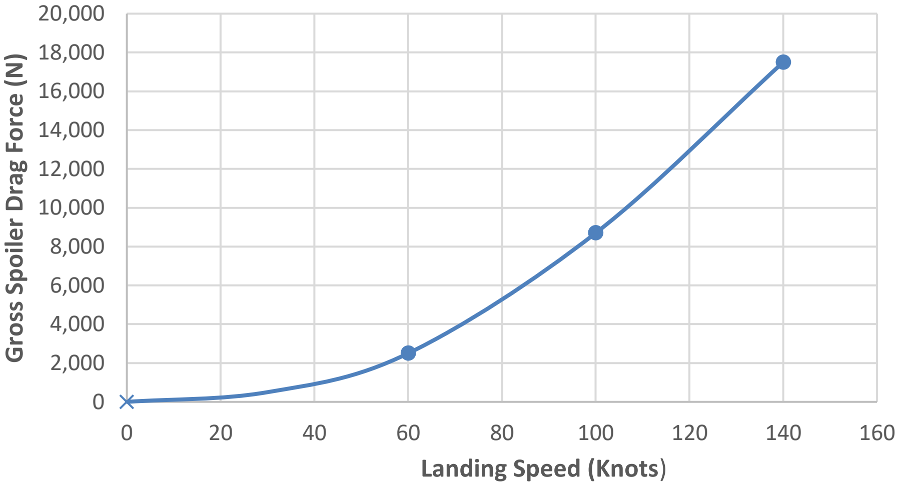

Figure 4-22: Measured Spoiler Drag for both wings during landing

A sanity check was also conducted on the spoiler drag, to ensure that it was of the correct magnitude, by determining the drag coefficient according to Equation 4-7. This was then compared against experimental data for an inclined flat plate.

$$C_D = \frac{Drag}{A.q} \tag{4-7}$$

Where
$\boldsymbol{C_D}$ *= Drag coeffcicient*
$\boldsymbol{A}$ *= reference area*
$\boldsymbol{q}$ *= Dynamic pressure*

The C_D calculated for the spoilers was approximately 0.59, with a tolerance of 5%. This correlates with the published drag (*Figure 4.23)* for an inclined flat plate with similar characteristics as the spoilers developed for the DLR F11 (AoA = 50˚ & with close proximity to the wind-tunnel floor), where C_D ≈ 0.5 – 0.65 for high aspect-ratio plates.

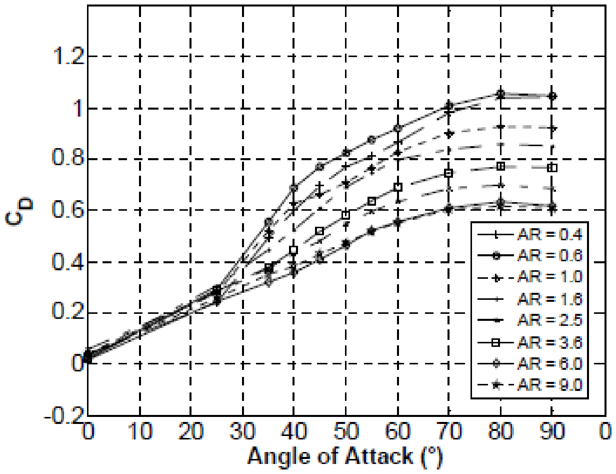

Figure 4-23: Experimentally derived drag coefficient for an angled flat plate [125]

Additionally, a visual inspection of the CFD solutions was undertaken to verify the spoilers were performing as intended, presented in *Figure 4-23*. Mach number distributions, static pressure fields & velocity vectors of the flow around the plates were studied, and nothing untoward was identified in the results.

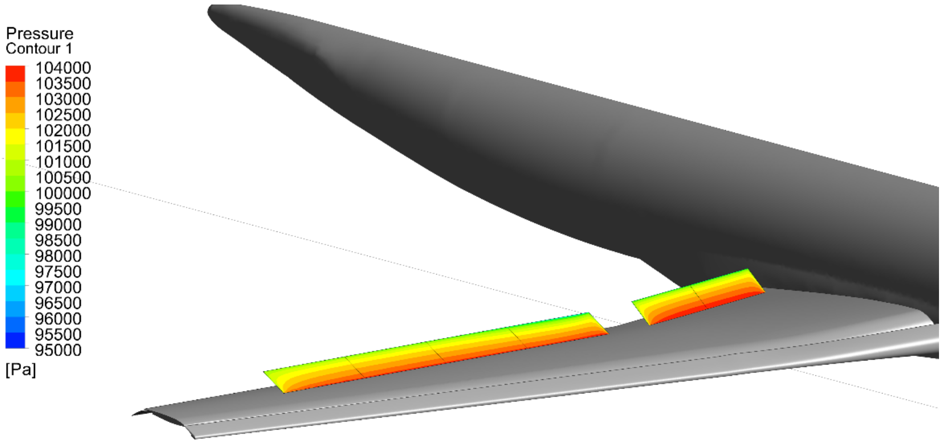

Figure 4-24: Spoiler surface static-pressure contours at 140 knots airspeed

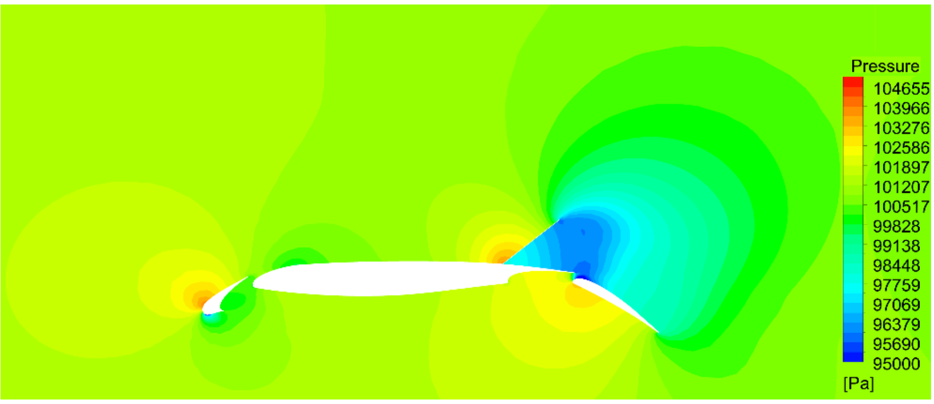

Figure 4-25: Static pressure contours around the inner outboard spoiler at 140 knots airspeed

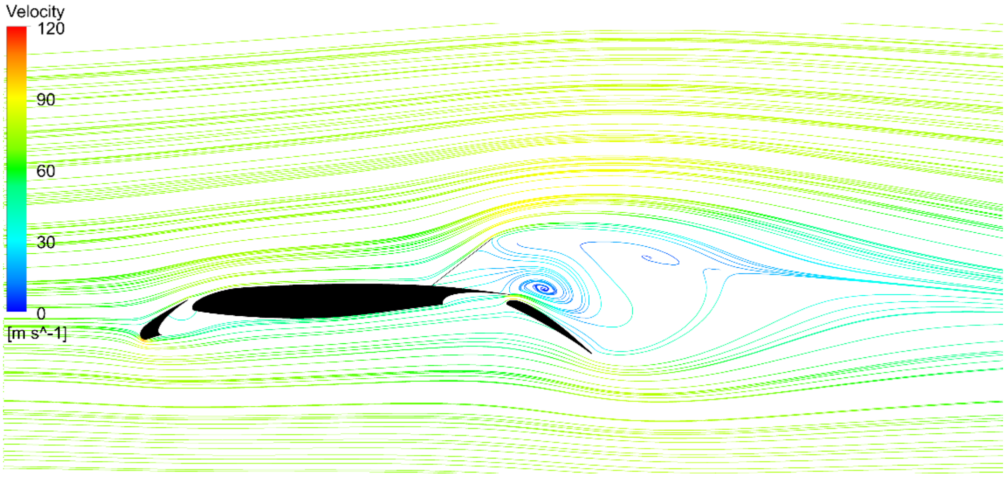

Figure 4-26: Velocity streamlines around the inner outboard spoiler at 140 knots airspeed

The spoilers generated a significant increase in the wing momentum drag, with large recirculating low-pressure fields behind the plates, which are shown in *Figures 4-24* & *4-25*. The lift was also degraded, as the flow deflection from wing the flap was mitigated by the low- pressure field behind the wing. As such, the spoilers were considered to work accordingly, and were suitable for the requirements of this study.

4.3.3 Pylon Verification

To assess the performance and adequacy of the pylon model, several test cases varying landing speed were run in CFX; much alike the spoilers. The pylon analysis involved assessing the pylon flow interactions, via assessing Mach number & pressure fields. The design proved satisfactory, with the only mentionable feature being a region of separating low-velocity flow on the inboard side of the pylon boat-tail. This can be seen in *Figures 4-26* to *4-28*, where the pylon's lower side in the images is nearest the fuselage. This is a well-documented phenomenon, occurring due to pylon/wing interference and the high-pressure field under the wing. [126, 127] To account for this, pylons are generally design laterally non-symmetrical. [128] This shouldn't present a significant issue during reverse-thrust simulations however, and the complexities of improving the pylon design further were not deemed a wise investment in time. Having identified no other unusual characteristics of the pylon, it was deemed verified for the purposes of this study.

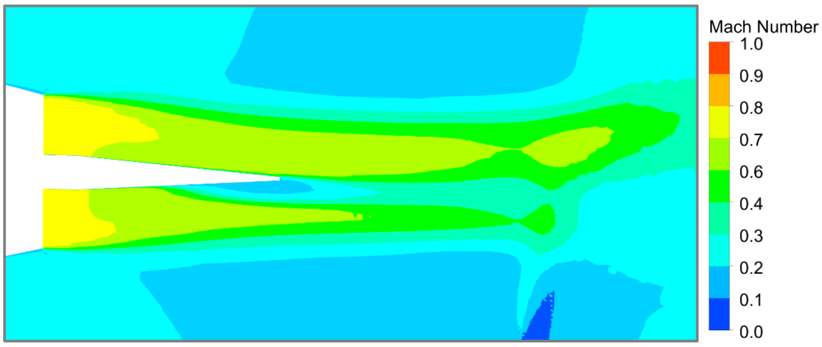

Figure 4-27: Mach Number contours at mid-bypass height around the nacelle

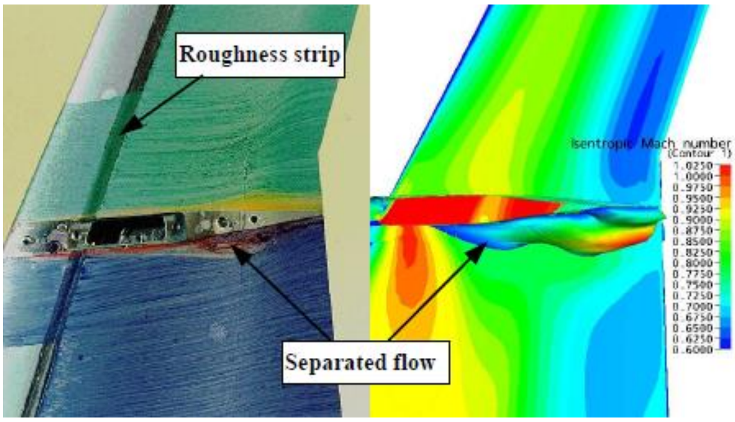

Figure 4-28: Pylon separation from interference flow dynamics observed on the DLR F6 [126]

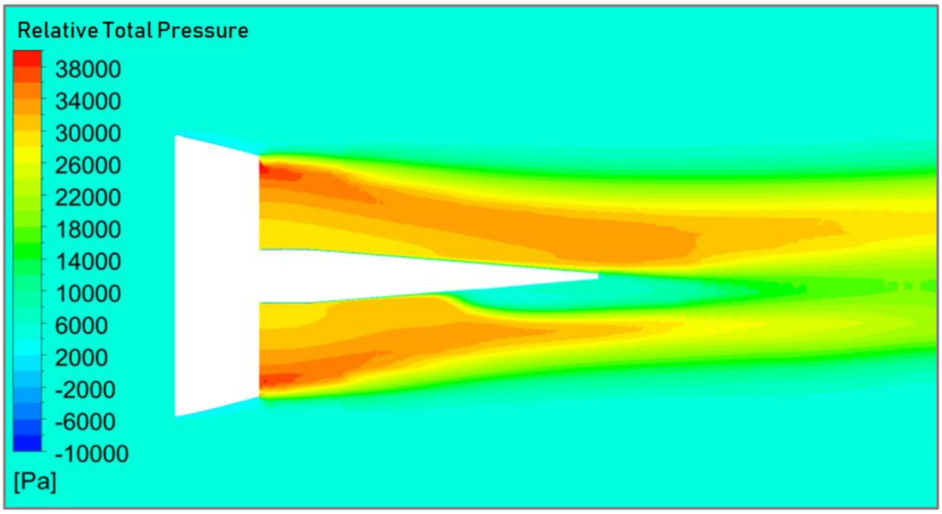

Figure 4-29: Relative total pressure contours at mid-bypass height around the nacelle

5 Results

This chapter presents the main findings from the developed VPF reverse-thrust research model results. After a summary of the analysis metrics (*Ch. 5.1*), discussion of the results is presented from three aspects.

The first discussion (*Ch 5.2*) focusses on the solver/numerical model performance. This includes both a description of the solution convergence, and a summary of identified discrepancies in the fan flow predictions between full-annulus and single-passage versions.

In the following section (*Ch 5.3*) the insight gained into VPF reverse-thrust aerodynamics is presented and discussed. The results are reviewed from several perspectives, each focussing on a different aspect of the aerodynamic operation of the engine.

The final section presents the calculated thrust reverser effectiveness from the CFD predictions, by measuring net momentum change at the engine inlets/outlets. The limitations of this method are also discussed.

5.1 Analysis Metrics

An overview of the metrics derived and/or utilised for flow analysis of the reverse-thrust research model is presented below:

- Velocity streamlines for bulk flow analysis, studying mainly fan passage & external engine aerodynamics.
- Mach number and total pressure contours for visual identification of pressure gradients, and stagnating flow associated with separation.
- Distortion metrics DC_{60}, RDI, & CDI for quantifying the extent of distortion onto the ESS/IPC face (*ref. Eq 2-6 to 2-9*).
- Thrust reverser effectiveness, η_{rev}, for estimating the engine braking performance characteristics (*ref. Eq 2-3*). The exact method for calculating this from the CFD results is also presented.

5.2 Solver Performance

Before discussing the aerodynamic simulation results, the performance of the numerical method needs to first be established. Fundamentally, the solver uses three timescales between iterations, which mimic the fluid's transition through the domains. The timescales are determined by the average residency time for the fluid within the simulation domain. The external/far-field domain, engine internal domains, and the rotating fan domain each operate with timescales an order of magnitude apart. The external/far-field domain mean residency time is inversely proportional to the freestream/airspeed velocity; for 100 knots landing speed the timescale is approximately 4 seconds. The internal engine (stationary) domains operate under a shared timescale of approximately 0.04 seconds, whilst the fan domain (rotating) operates with a timescale of 0.0012 seconds.

As a result, the model tends not to reach high levels of convergence, with three residual oscillation frequencies observed in the convergence graph (*Figure 5-1*); corresponding with the three timescales.

The solver was run for 2000 iterations per case, using 128 cores of Cranfield's central high-performance computer (HPC); Delta (*ref. Ch 3.6.6*). It was found that after the first 500 or so iterations (with auto-timescales), the velocity residuals stabilised with a convergence level between $1e^{-3}$ & $1e^{-4}$, whilst the mass-flow residual reach convergence closer to $1e^{-5}$. *Figure 5-1* presents a solver residual convergence plot for a single case. Further examples of the convergence graphs for the initial simulations are provided in *Appendix G*. The computational time required for 2000 iterations varied between the different versions of the model; proportional to the total element/node count of the domains used. The time required for simulation runs on Cranfield's Delta are also included in *Table 5-1*.

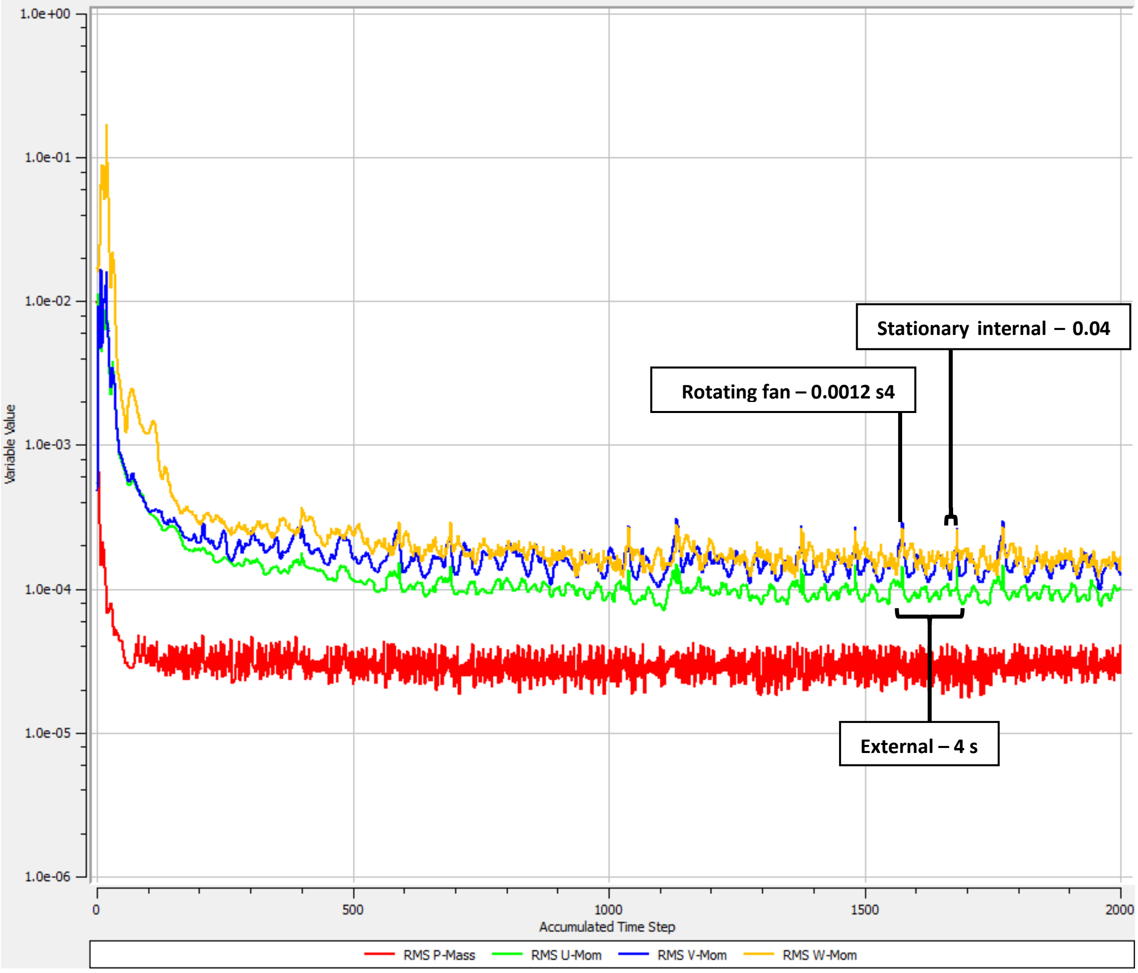

Figure 5-1: Convergence of main residuals for integrated single-passage model @ 110 knots

Whilst taking results from the 2000th iteration may not yield the most accurate results, it was deemed the most practical given the early stages of the research model's development. Time constraints towards the end of the project prevented additional investigation into the solver's numerical performance being conducted.

Configuration	Fan	Fan	Landing speed (knots)	Time*
Integrated w/single-passage	*-92˚*	*92%*	*130, 110, 60*	*24 hours*
Isolated all single-passage	*-92˚*	*92%*	*130, 110, 60*	*11 hours*
Integrated full-annulus	*-92˚*	*92%*	130, 110, 60	*15 hours*

Time for 2000 iterations

Table 5-1: Initial research model configurations tested

The results from these initial runs were considered test cases; to assess the CFD code's capability in predicting the flow, and to identify any variations or errors in the solver calculations which could not be sensibly accounted for. This is discussed in more depth in the following section.

5.2.1 VPF Modelling: Single-Passage vs Full Annulus

Having returned the first set of results from the cases presented in *Table 5-1*, it was determined that the fan performance varied between the single-passage and full-annulus representations. The results were analysed to determine the cause and physical manifestation of the variations. *Figures 5-2* & *5-3* present comparisons between velocity streamlines for the single-passage and full-annular integrated cases, at the same landing speeds (60 & 110 knots respectively). There exists a large recirculation zone within the blade passage, which traverses the rotational periodic boundary in the single-passage fan. The fan operation during reverse pitch (covered in more depth in *Ch 5.3.1*), experiences aerodynamic blockage and high radial flow migration due to the axial stagnation of flow in the fan passage. This becomes more noticeable at higher landing speed, due to the rising dynamic head and momentum drag imposed on the fan stage. This hypothesis is supported when observing the highly circumferential streamlines of relative velocity, both up & downstream of the fan stage in *Figures 5-2* & *5-3*.

The highly three-dimensional flow regime, coupled with the proximity of the rotational periodic interface to the blade surfaces due to the chosen pitch-setting, impose high demands on the periodic interface. Not only is data transferred across the boundary, but in at least two regions under the tested fan pitch/RPM setting, recirculation across the boundary takes place. These regions can be seen in *Figure 5-4*, which plots streamlines on the surface of the periodic interface. The result is a degradation in numerical solver stability, and it is considered 'bad practice' in CFD modelling to allow disturbed flow to interact with the numerical boundaries.

Comparing the convergence graphs between the two fan representations (*ref. Appendix G*), the full-annulus model achieved a slightly better degree of convergence and stability versus the single-passage. This has been attributed directly to the removal of the periodic interfaces, as there is otherwise no difference between the numerical models.

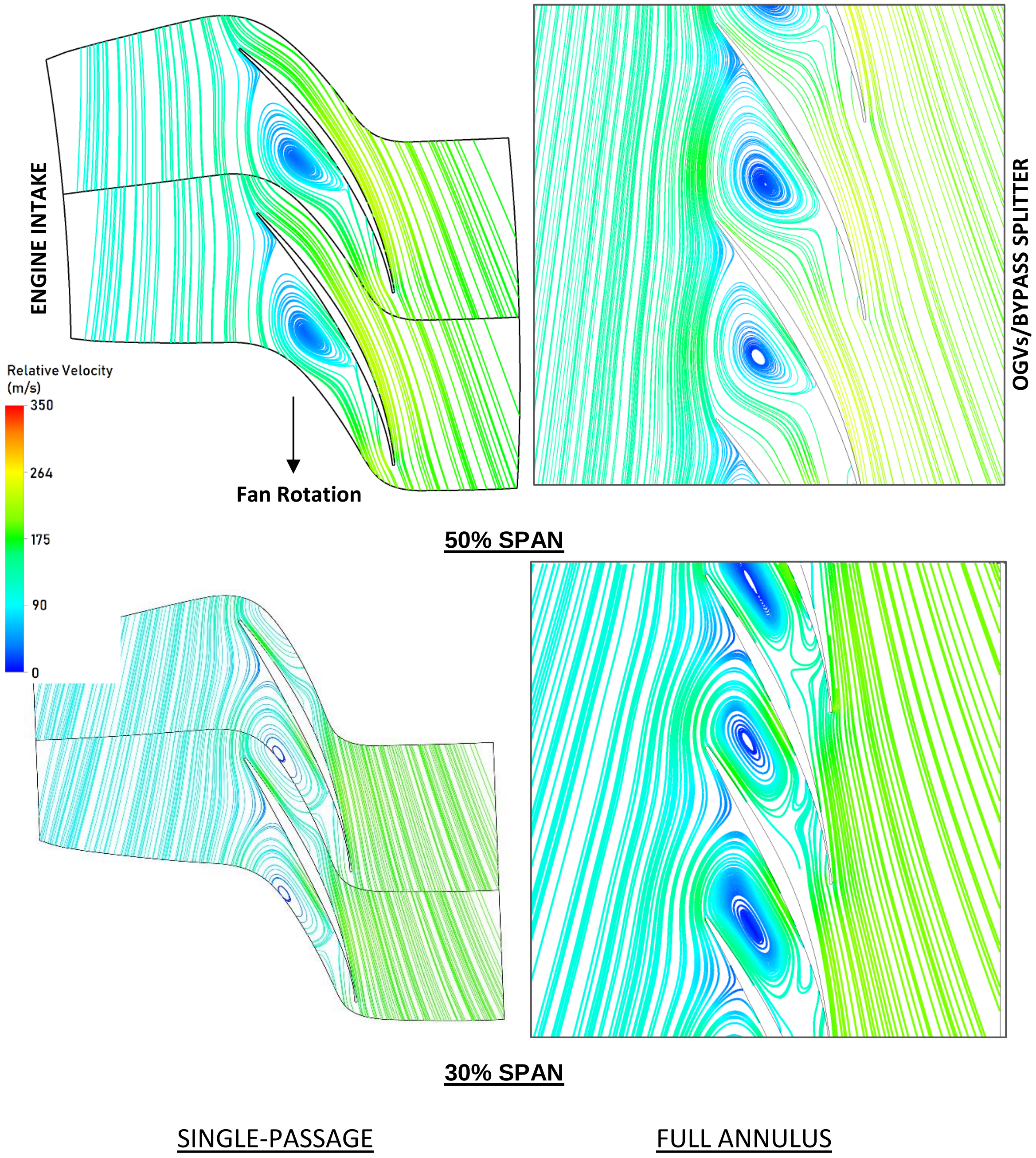

Figure 5-2: Blade-to-blade velocity streamlines at 60 knots landing speed

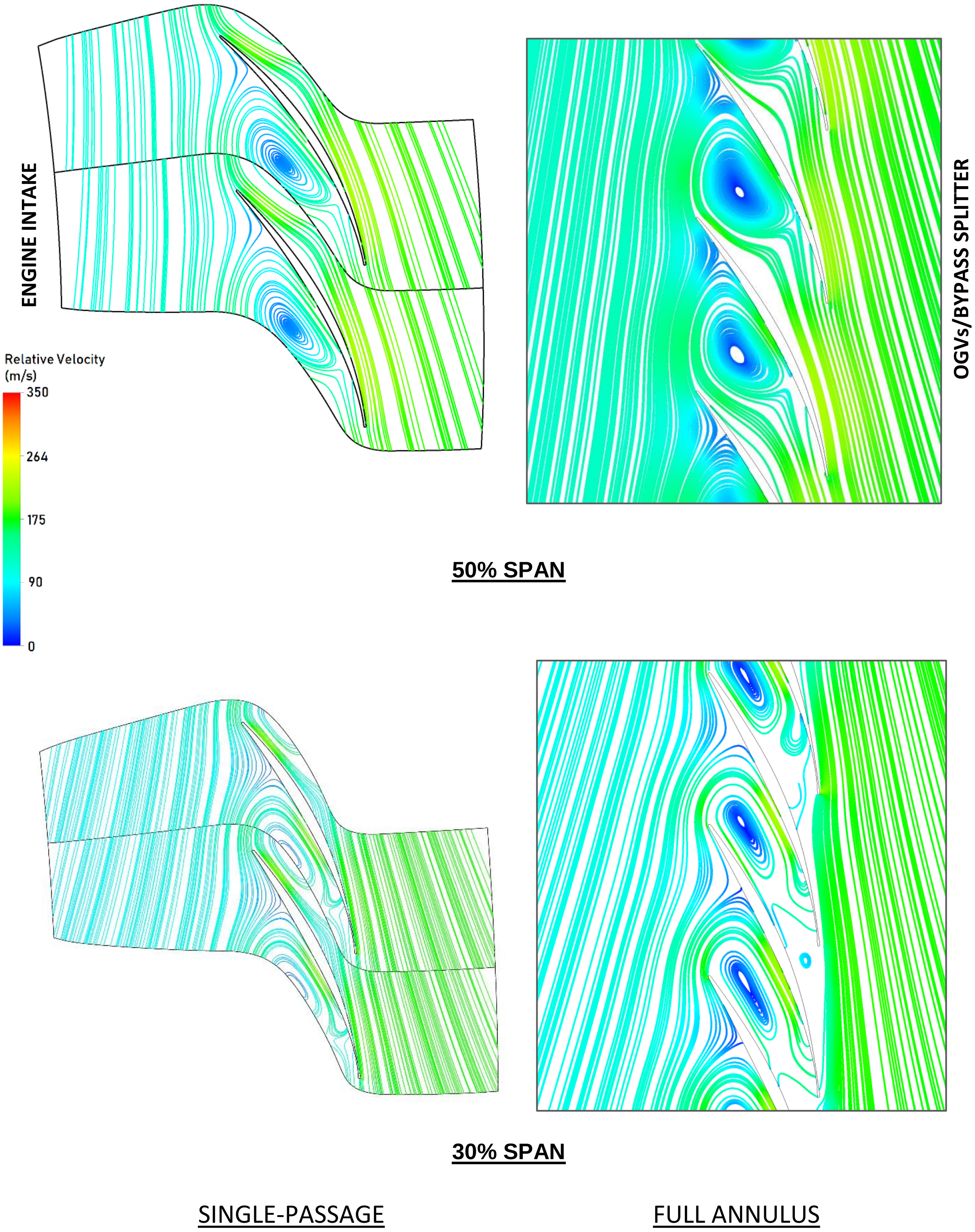

Figure 5-3: Blade-to-blade velocity streamlines at 110 knots landing speed

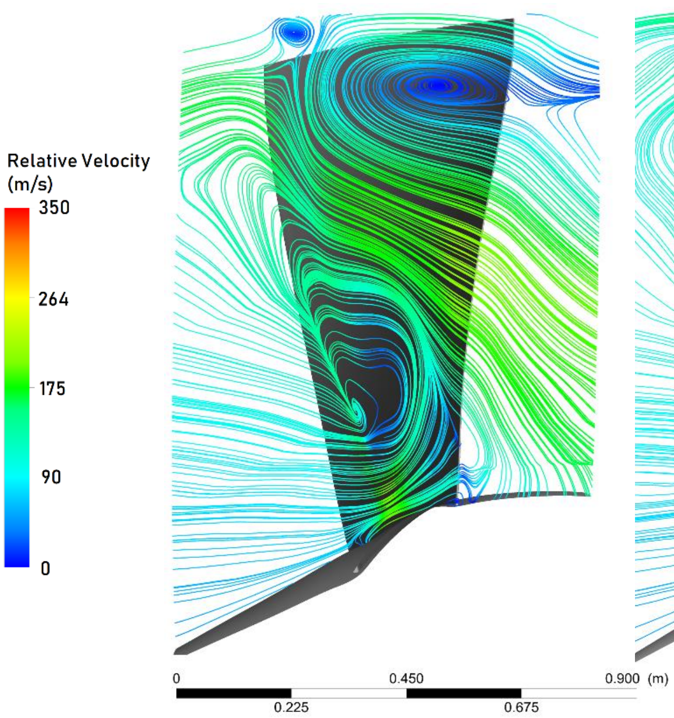

Figure 5-4: Surface streamlines on the single-passage fan periodic at 60 & 110 knots

Furthermore, the variation in the results due to the fan periodic interface also manifests in a change in some of the reverse-thrust performance metrics. It was found that the fan's operating mass-flow was notably reduced in the single passage variants, resulting in a deviation in the span-wise location of where reverse-flow is observed. This can be seen in *Figure 5-5*, where the deviation is most prominent between the 60 knots cases.

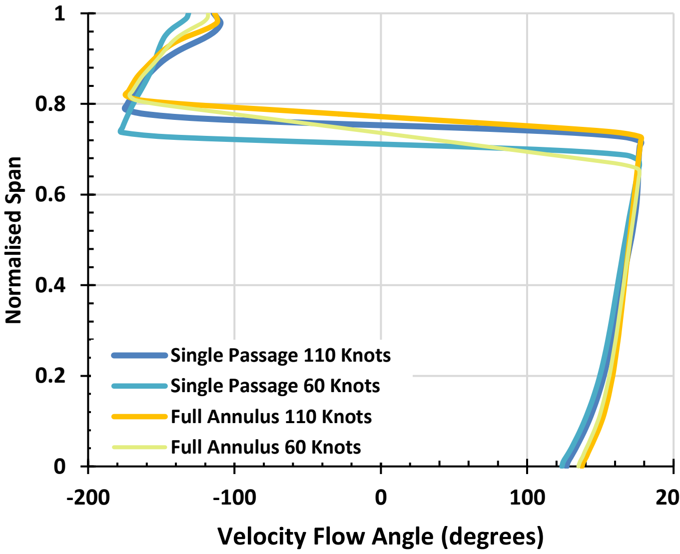

Figure 5-5: Comparison of circum. averaged velocity flow angle on the fan inlet interface

A similar issue is also present in the single-passage OGV of the isolated nacelle model. Whilst the OGV blades are stationary and fixed geometry, the flow-field behind the fan – which is largely circumferential (from the fan's swirling effect) caused similar regions of turbulence & eddy swirling in the OGV passages due to the high negative incidence onto the blades, which cross directly over the periodic interface. Velocity streamlines through the OGV passage are presented below in *Figure 5-6*.

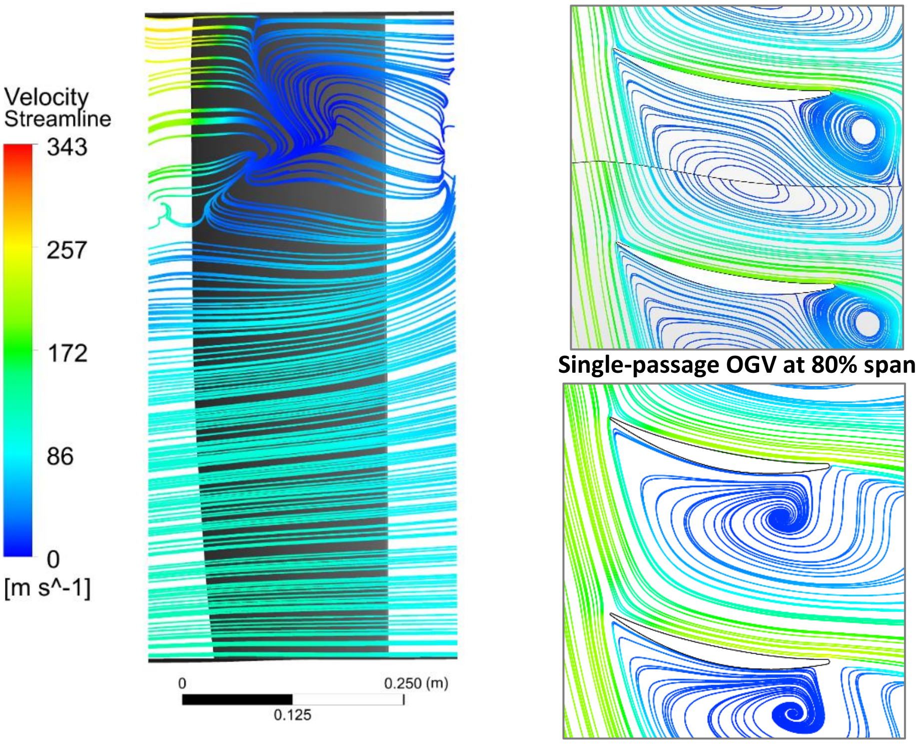

Single-passage OGV at 80% span

Surface Streamlines on Periodic Interface

Full-annulus OGV at 80% span

Figure 5-6: Velocity streamlines through OGV stage of integrated models

In response to these findings, the single-passage models were discarded in favour of full 360˚ annulus versions. As the isolated nacelle model was only developed in single-passage, a full annulus version was developed. This was done following the pre-established method of 2D-to-3D mesh extrusion for the empty ducts and far-field domains, and for the 3D turbo-domains rotational duplicates were created (*ref. Ch 3.5.2*). The dimensions of the cylindrical far-field remain the same as before (radius = 70 m, longitudinal = 140 m). However, due to time-constraints towards the end of the project, priority was given to running a full landing speed set of the integrated full annulus model. The model has however been made available for the use on future studies within the UTC, and is considered on par with the full annulus integrated model with respect to solution credibility/performance. *Figure 5-7* shows the assembled isolated nacelle model.

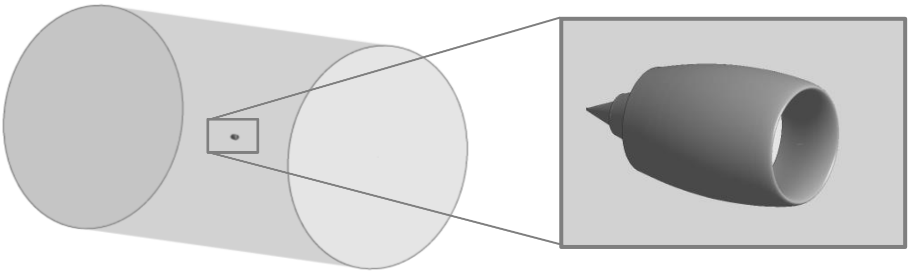

Figure 5-7: Far-field domain of the full annulus isolated nacelle

To conclude then, rotational periodic interfaces are typically suitable for use in turbomachinery where the aerodynamics are relatively ordered, and flow is pumped axially. However, when attempting to simulate flow conditions of a reverse-thrust VPF with blades in close proximity to each other, the conventional approach of single-passage modelling does not suffice. This finding is particularly important to any future studies into VPF reverse thrust, with the recommendation to adopt only full annulus turbomachinery models.

5.3 Integrated Engine Aerodynamics

Having established that a full annulus representation of all engine internal domains is required, a new set of simulations were setup and run on Delta, using only full annulus models. However, given the limited time remaining on the project, full annulus simulations of the isolated nacelle were considered secondary priority, and no further simulations were achieved. Additionally, only one full set landing speed cases were returned for the integrated full annulus model. Subsequent discussion therefore focusses on this integrated case alone. Due to the heavy computational nature of the full annulus models, A summary of the simulation case configuration is provided in *Table 5-2*.

Configuration	Fan Pitch	Fan RPM	Landing Speeds (knots)
Integrated full-annulus	*-92˚*	*92%*	*140, 130 to 20 (in increments of 10)* & 5

Table 5-2: Research model full annular case configurations tested

5.3.1 Fan Performance

The first assessment of integrated research model results focusses on the fan aerodynamic performance and operation. *Figures 5-12* to *5-14* present velocity streamlines through the fan passage at three key landing speeds, 140 knots, 60 knots and 5 knots (approximately static). Immediately identifiable is the large regions or recirculating flow between the blades at 50% and 25% spans. The hub region of the blade experiences total aerodynamic blockage, due to the shallow inlet angle and narrow blade-to-blade distance at the fan inlet (normally the outlet side). Moving up the span, as the blade spacing increases, some flow is ingested from the splitter-duct side of the fan, but the extent of which is determined by the landing speed. At 140 knots the static backpressure imposed from the freestream dynamic head pushes the recirculating bubble further into the passage, until it extends almost the entire region of blade overlap. At mid-speed (60 knots) the recirculation has partially diminished and migrated to the front of the fan, allowing flow to be pulled into the passage from the rear at 50% span. This flow is then ejected radially outwards towards the tip, whilst adopting a whirl velocity equivalent to the fan's rotational speed. Therefore, the fan operates more like a centrifugal pump than an axial compressor. Some of this high-pressure gas is discharged out of the nacelle inlet as the swirling reverse-stream discussed in *Ch 5.3.2*.

The resulting shear between the fan and the flow behind the stage (in the splitter-duct) results in a similar region of high pressure swirling air at the other radius, which accounts for the blockage on the OGV shroud (*Figure 5-6*) and the large flow circulation pattern observed in the bypass duct. This shears against the incoming air through the bypass nozzle feeding the IPC, and is eventually completely reversed to head back towards the fan.

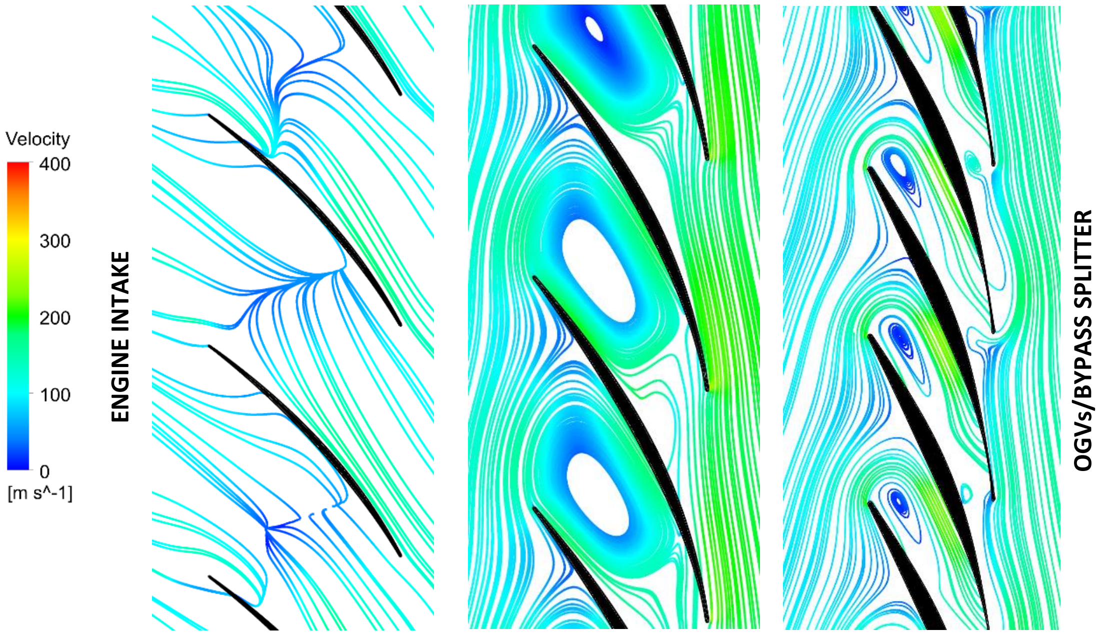

95% Span 50% Span 25% Span

Figure 5-8: VPF blade-to-blade relative Mach number contours at 140 knots

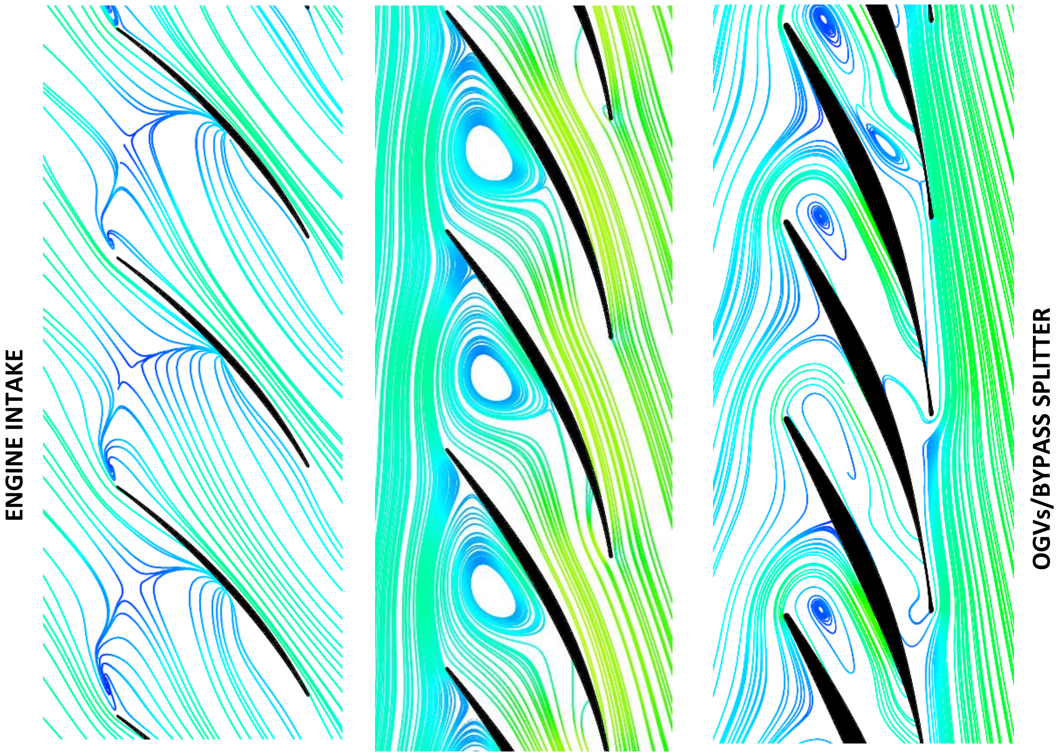

95% Span 50% Span 25% Span

Figure 5-9: VPF blade-to-blade relative Mach number contours at 60 knots

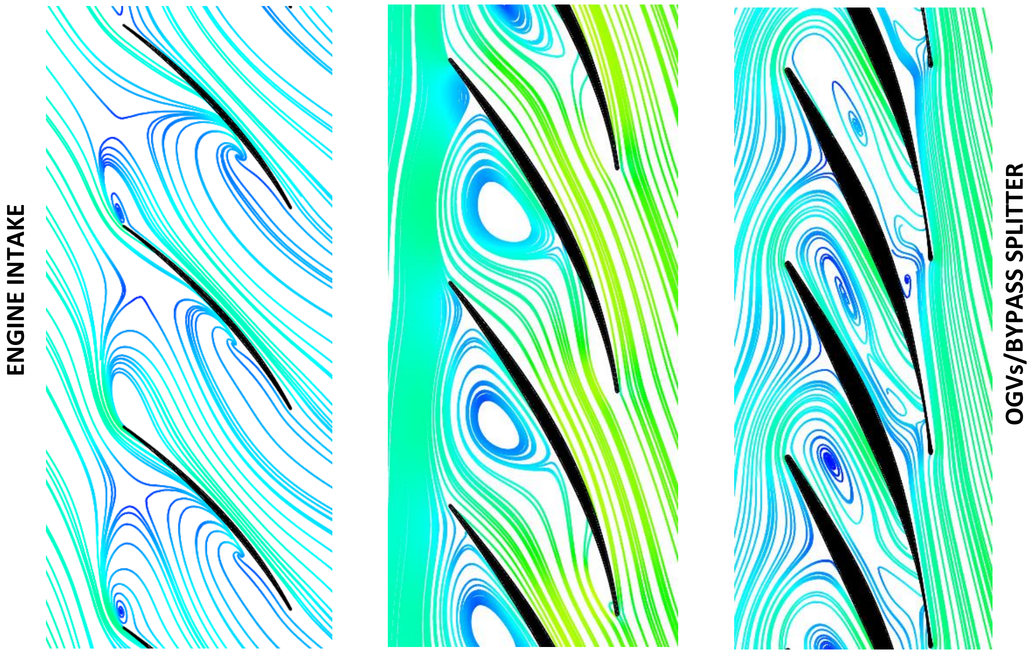

95% Span 50% Span 25% Span

Figure 5-10: VPF blade-to-blade relative Mach number contours at 5 knots

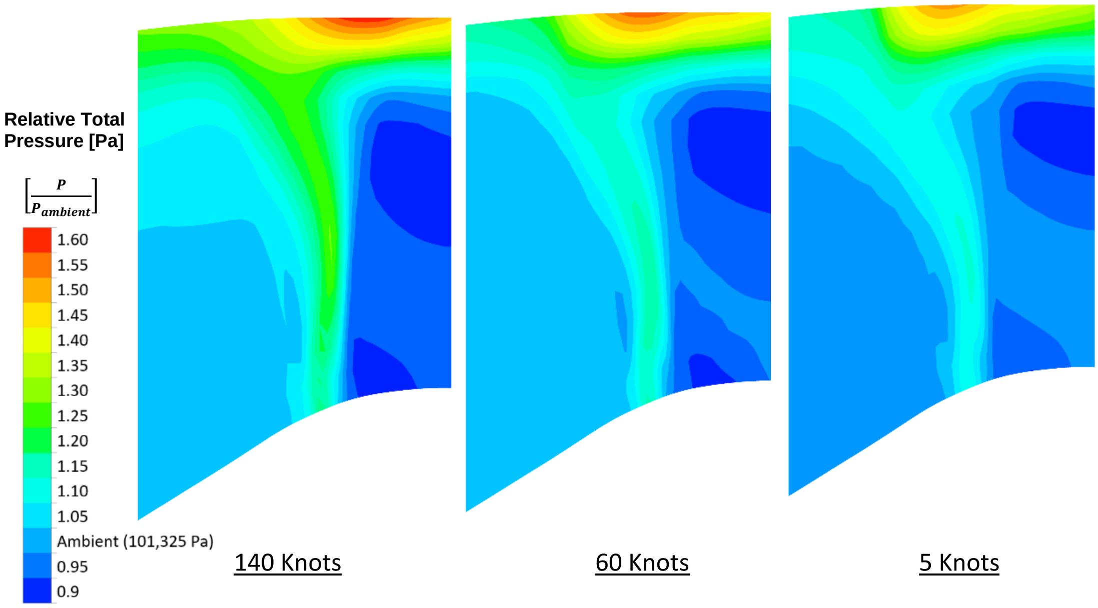

140 Knots 60 Knots 5 Knots

Figure 5-11: Meridional relative pressure contours (circumferentially averaged) in the fan

Figure 5-15 shows the circumferentially averaged meridional relative pressure contours through the fan domain. The most prominent variation is the change in pressure gradient intensity between the two sides of the fan stage. This is largely due to the change in dynamic pressure with landing speed. Also seen is the high-pressure band of gas expelled from the fan tip, due to the radial flow operating regime of the fan. This radial migration of flow can be seen when ignoring the circumferential velocity components, such as shown in the meridional streamlines onto the fan in *Figure 5-16*. No flow managed to pass through the fan stage axially rearwards at any of the tested speeds (140 – 5 knots).

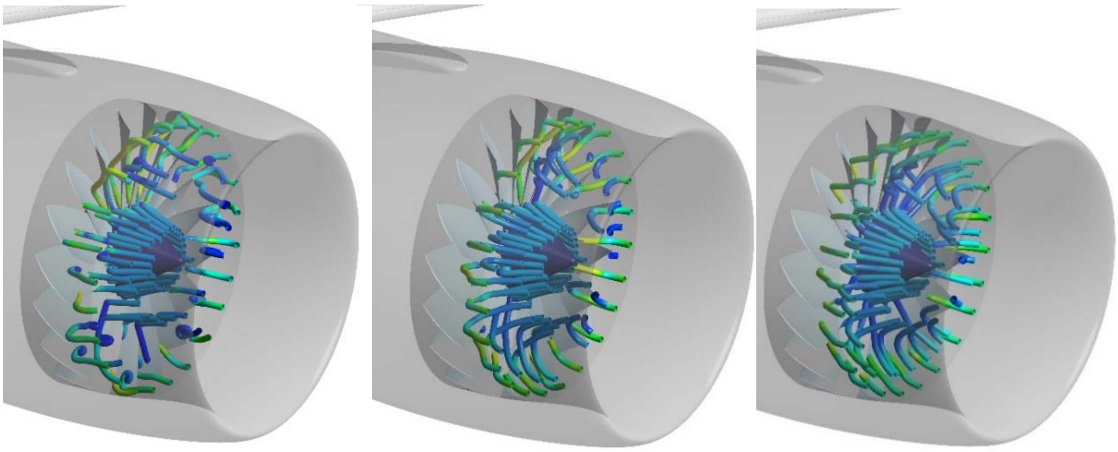

140 knots **60 knots** **5 knots**

Figure 5-12: Meridional streamlines of flow into the fan face at various landing speeds

To conclude, the fan produces an effective band of high pressure air at the outer radial region of the stage, by working mainly the freestream air imposed onto it. This is pressurised to a sufficient level to discharge out of the nacelle inlet at all speeds, but remains attached to the nacelle surface rather than forming a reverse-flow stream-tube extending upstream of the engine. The whole stage is aerodynamically blocked, requiring air to be drawn in through the bypass duct to supply the engine core. This is contrary to what was expected, as all previous VPF publications indicate that the aerodynamics are somewhat comparable to a normal axial fan stage, only pumping the fluid against the conventional direction of flow. The operating regime appears stable across all landing speeds, although it is unclear to what extent the fan flow is unsteady or fluctuating, due to the large regions of turbulent & disordered flow between blades.

It is not expected that the time-averaged solutions provide full insight into the fan aerodynamic operation, especially given the complex aerodynamics occurring within the blade passages. However, as this is one of the first known studies of its type (CFD modelling of VPF reverse thrust), the simulation results still yield valuable insight into quantifying the magnitude of possible aerodynamic concerns from an engine designer’s perspective.

5.3.2 Bypass Duct/Nozzle Aerodynamics

The bypass aerodynamics are a crucial factor to assessing the fan & core compressor’s ability to ingest flow from the rear of the engine, and to understand the sources of circumferential distortion generated throughout the integrated model. The flow patterns observed in and around the bypass duct are generally consistent across the whole landing speed spectrum. The high-pressure swirling flow exiting the fan tip on the aft-side expands into the outer region of the bypass duct. The first breakdown of this stream occurs when the flow contacts the OGVs with a high negative incidence. Most of the fluid is blocked, and the high-pressure field is retained in the splitter duct. This results in a pressure ‘void’ behind the OGVs, where only a fraction of the fluid managed to traverse the stage into the bypass duct at the outer radial region. The fluid that does make it to this region shears against the incoming stream on the inner of the bypass duct. The incoming stream feeds both the engine core, and to some extent the fan. Additionally, the bypass ingested flow consists almost exclusively of fluid already worked and expelled (in reverse) by the fan. This re-cycling of gas only ceases when the landing speed reduces to below 30 knots. This may have a negative effect on core performance and operability, due to the rise in entropy of the working fluid before entering the first stage IPC.

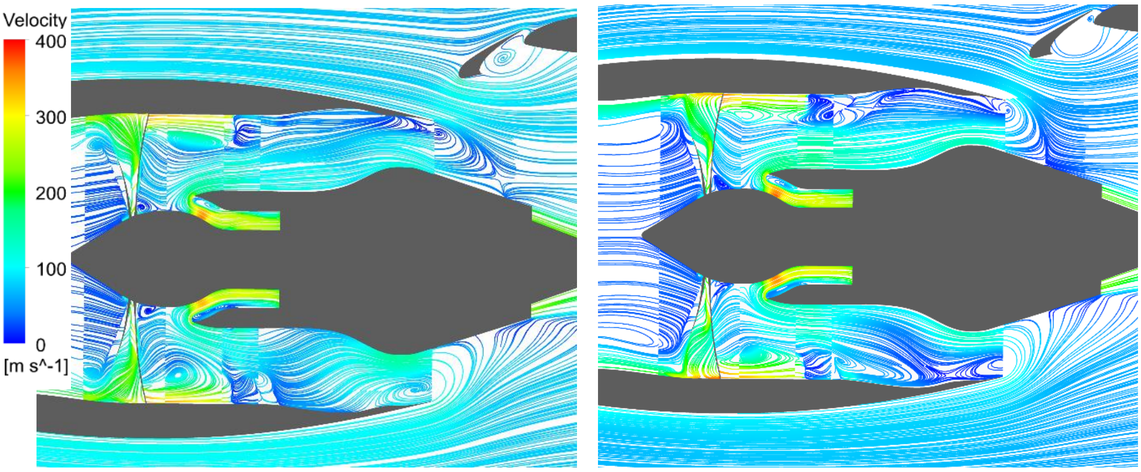

140 knots **100 knots**

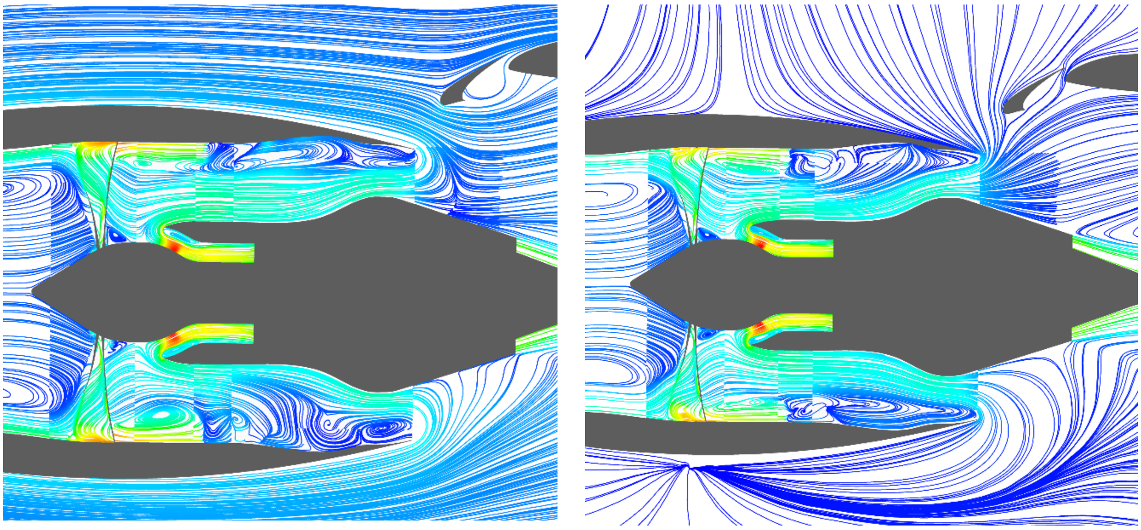

60 knots **5 knots**

Figure 5-13: Velocity streamlines into the bypass duct

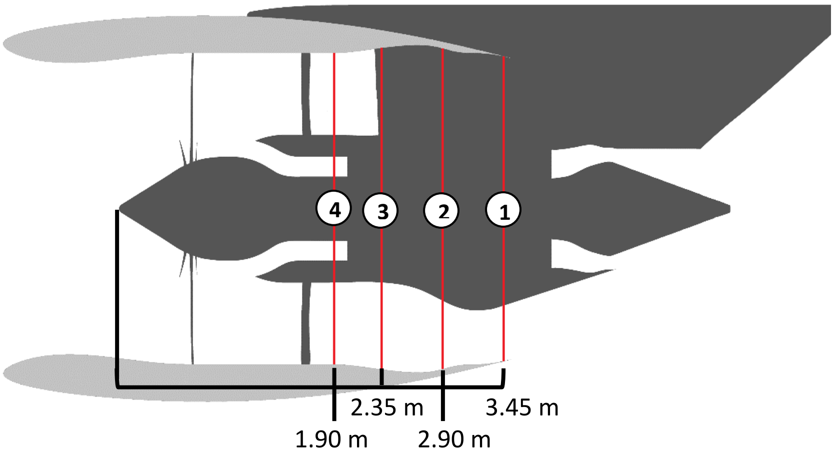

Figure 5-14: Locations of total pressure observation planes in the bypass duct

Having reviewed the meridional streamlines in and near the bypass duct (presented in *Figure 5-13*), four vertical planes were created, upon which contours of total pressure were plotted. The location of these measuring planes is shown in *Figure 5-14*. The most forward sitting plane is located just downstream of the OGV stage, whilst the most rearward plane is located on the bypass nozzle vertical plane.

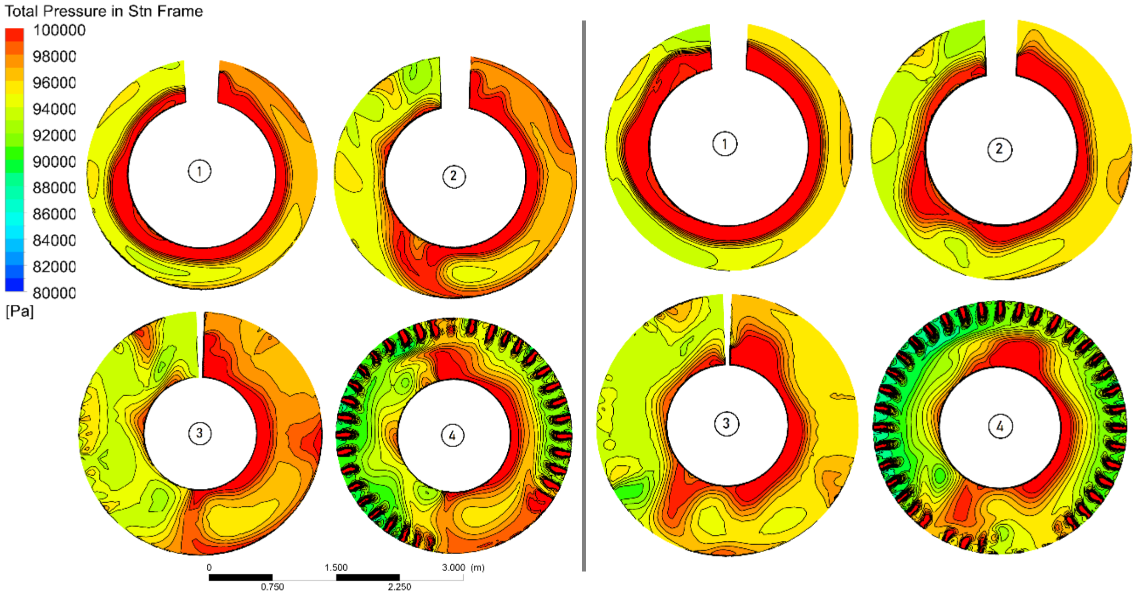

140 knots **100 knots**

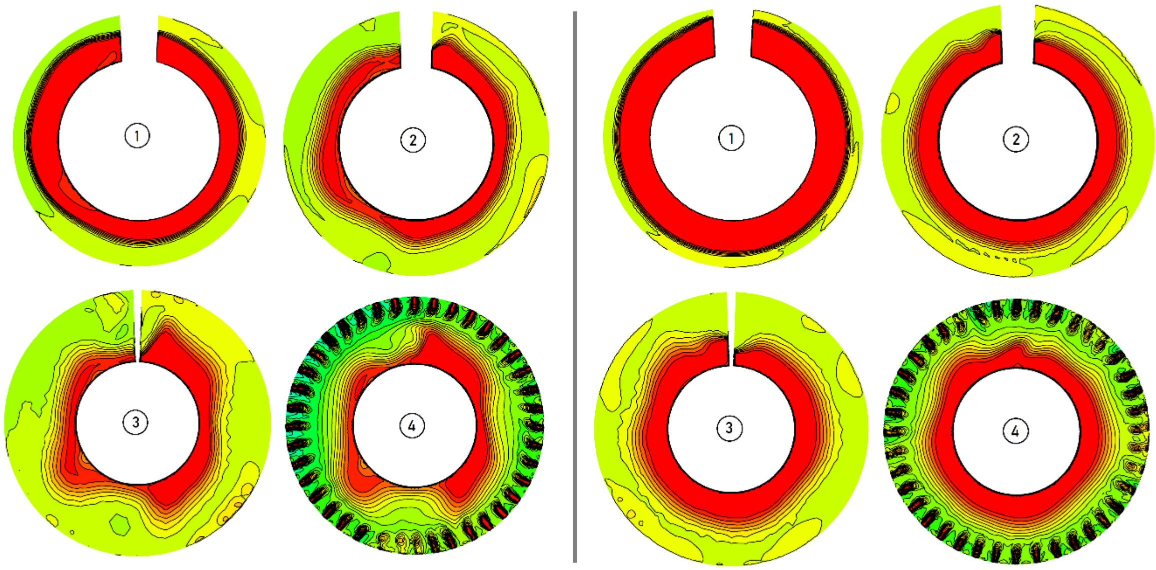

60 knots **5 knots**

Figure 5-15: Bypass duct annular total pressure fields (viewed from behind)

Figure 5-15 highlights the extent of circumferential total pressure variation through the bypass duct on the 4 vertical planes. The images are viewed from the rear of the engine, where the right side is outboard (towards the aircraft wing tip). The inner bypass duct stream (which feeds the IPC/fan) is largely recovered with minimal pressure loss (approximately 100 kPa compared to 101.3 kPa ambient). The outer stream is considerably lower, with a total pressure of approximately 88-94 kPa depending on where the observations are taken. Mixing/shearing takes place between the two streams, resulting in the shallower pressure gradients seen in planes 3 & 4. As such, the two streams can be easily identified due to the difference in colour on the contours maps. Additionally, the outer stream can be identified easily on plane 4, where the OGV wakes are clearly visible, showing the region of flow with a mean rearward axial velocity. It can also be seen that at 140 & 100 knots, this does not occur in the lowest sector of the annulus, where no OGV wakes are present. Additionally, a circumferential pressure gradient extending clockwise from the pylon is observed, which is most notable in planes 1-3 for the 140 knots case. Both this, and the variation in OGV wakes on plane 4 are the result of a single aerodynamic factor; the blockage due to the pylon. This will now be explained in more detail.

As already mentioned, the bypass flow is sourced almost exclusively from the fan's reversed flow, which carries a significant degree of swirl. This swirl migrates around the nacelle until reaching the bypass nozzle, upon which a section becomes laterally blocked by the pylon. This can be seen in *Figure 5-16*, where only streamlines leading into the bypass nozzle are drawn. A region of exposed nacelle surface is seen, most prominent in the 140 knots case. The direction of the pressure gradient (clockwise/anti-clockwise) is dependent on the fan's rotational direction. It is hypothesised therefore that there may be some aerodynamic variation depending on which direction the fan is rotating, coupled with which side of the fuselage the engine is mounted. This could lead to different levels of core inlet distortion and fan reverse thrust generation for each engine, and is another important finding that should be considered on future VPF work.

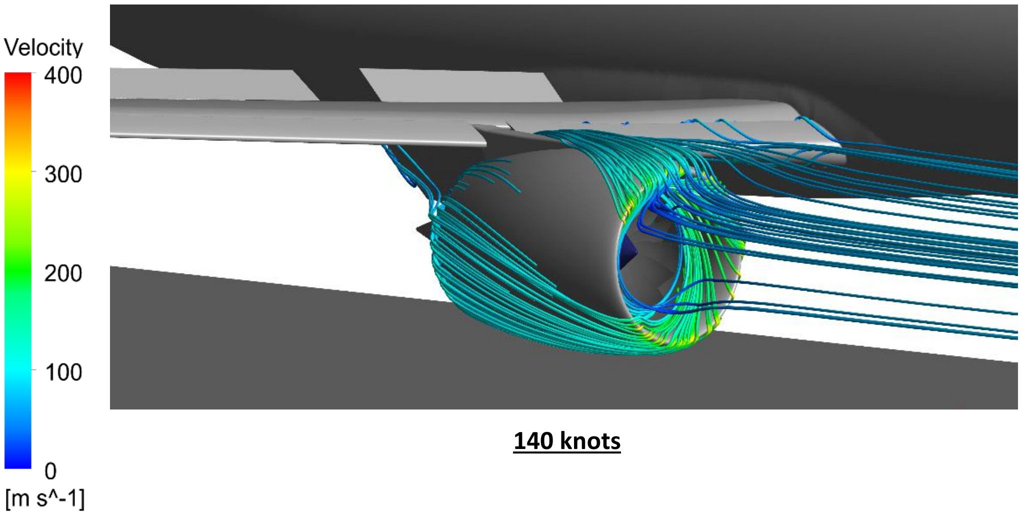

140 knots

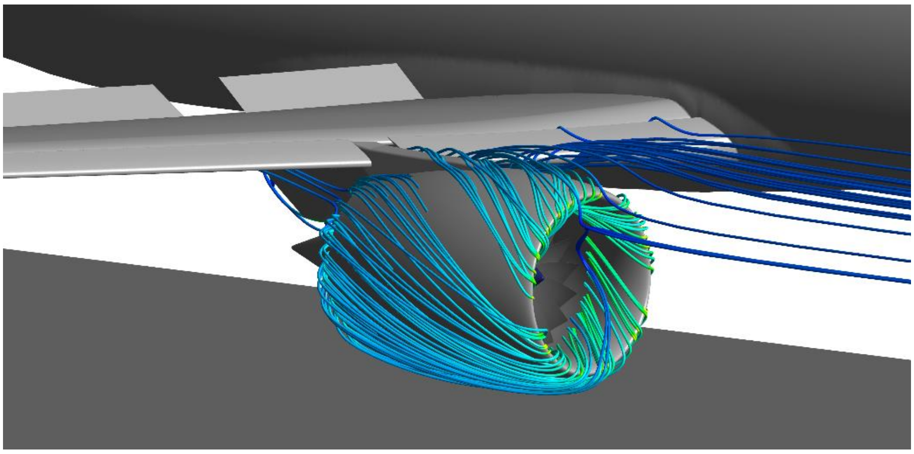

60 knots

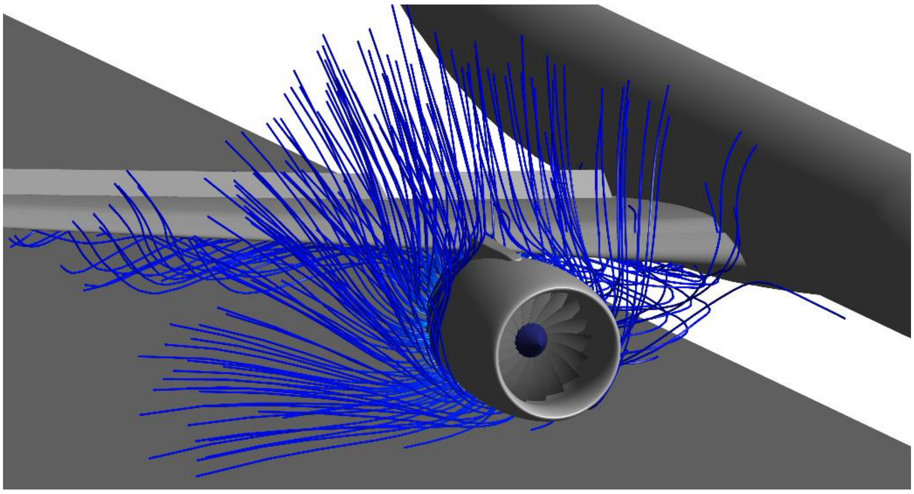

5 knots

Figure 5-16: Velocity streamlines passing through the bypass interface

5.3.3 Core Inlet Distortion

Perhaps the most important insight the integrated research model provides is the prediction of aerodynamic distortion feeding the engine core, including installation effects from the presence of the nearby wing/fuselage/pylon. This analysis is broken down into two parts; visual inspection of the aerodynamics (viewed on the meridional and circumferential planes), and distortion analysis at the estimated IPC inlet using the metrics established in *Ch 2.8*.

The meridional flow dynamics in and around the core inlet duct/splitter are presented in *Figure 5-17*, in the form of Mach number contours. It can be seen that the splitter boundary layer flow delaminates at the splitter leading edge, due to the small turning radius required to navigate into the core. This results in a band of low-pressure stagnant air around the outer radius of the inlet duct, immediately downstream of the splitter. The result is a significant amount of blockage to the duct, accelerating the undisturbed inner flow stream, until a shockwave forms where the ESS would typically be located. This separated flow can be seen in more clarity through the streamlines presented in *Figure 5-18*. This occurs across the entire landing speed range, with the shock strengthening at lower landing speeds, due to the lack of circumferential flow velocity; resulting in a slight increase in the average thickness of the separated region around the splitter.

Furthermore, there is significant variation between the upper and lower annulus contours/streamlines for the high-speed cases, where the lower delamination bubble is notably thicker, extends further downstream the duct, and is of lower internal velocity. This is not observed on the 5 knots case however, and it should be noted that the flow characteristics are changed dramatically when the engine is static versus at speed. As previously shown, at all but static conditions, the bypass re-ingests the reverse stream ejected from the fan, which carries with it a large swirl/vortex effect around the nacelle. This swirling momentum is maintained, even as far as the core inlet. However, at static, the bypass ingested air is sourced from the far-field, resulting in more ordered & axially orientated flow – thus a reduction in circumferential distortion. The circumferential distortion is visually presented in *Figures 5-20* to *5-23*, with *Figure 5-19* providing specifications as to where the observation planes were located in the core inlet duct.

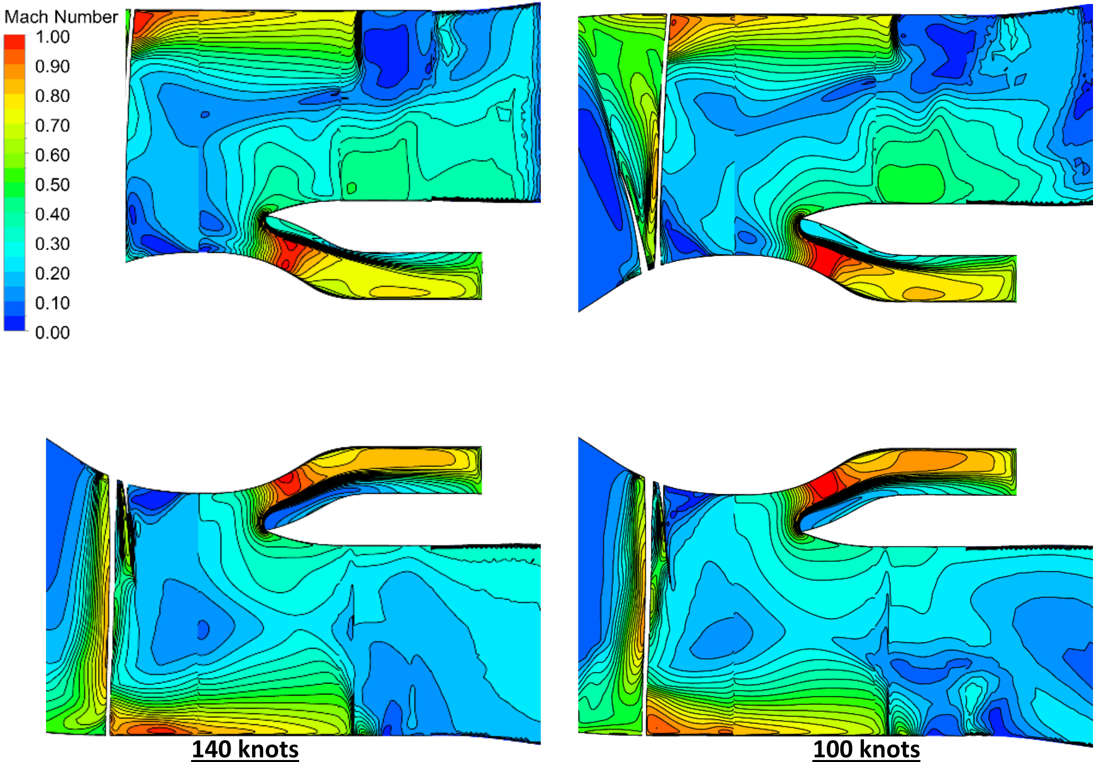

140 knots **100 knots**

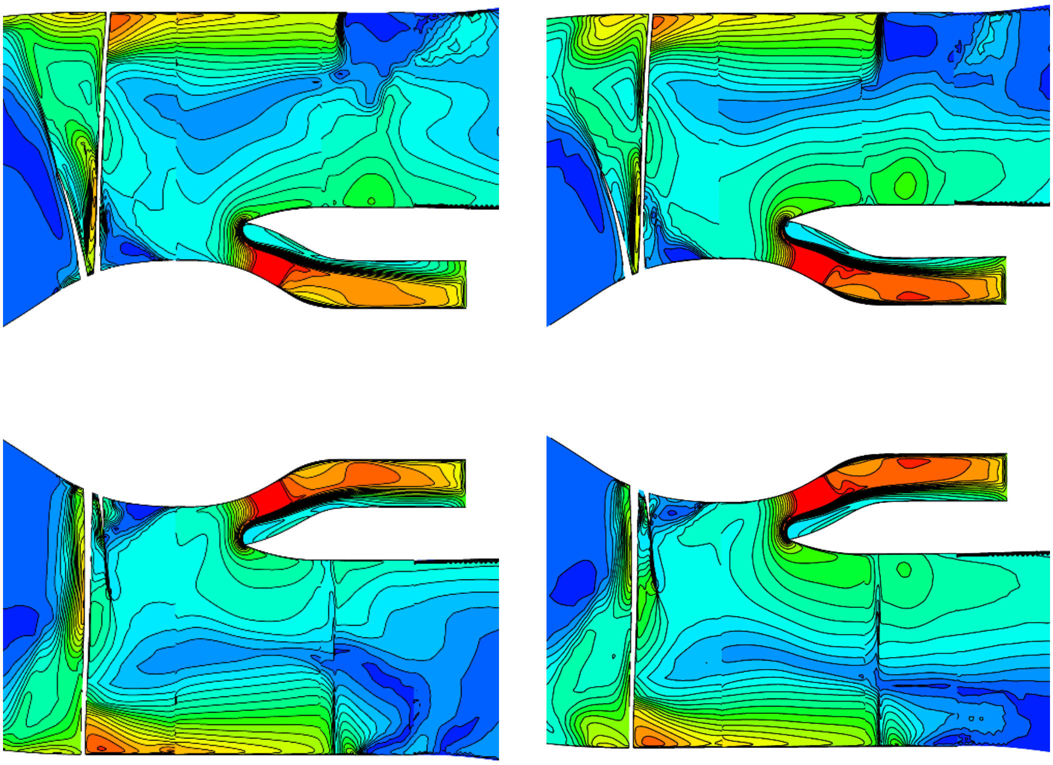

60 knots **5 knots**

Figure 5-17: Meridional Mach number contours focussed around the splitter/core inlet

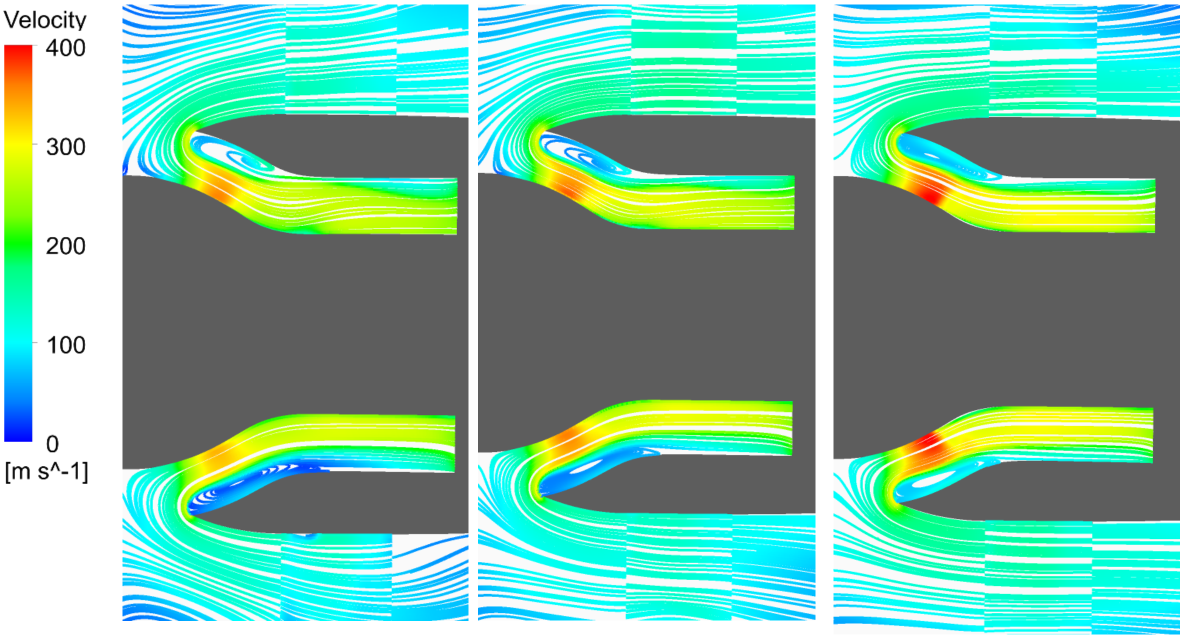

140 knots **100 knots** **5 knots**

Figure 5-18: Meridional Mach number contours focussed around the splitter/core inlet

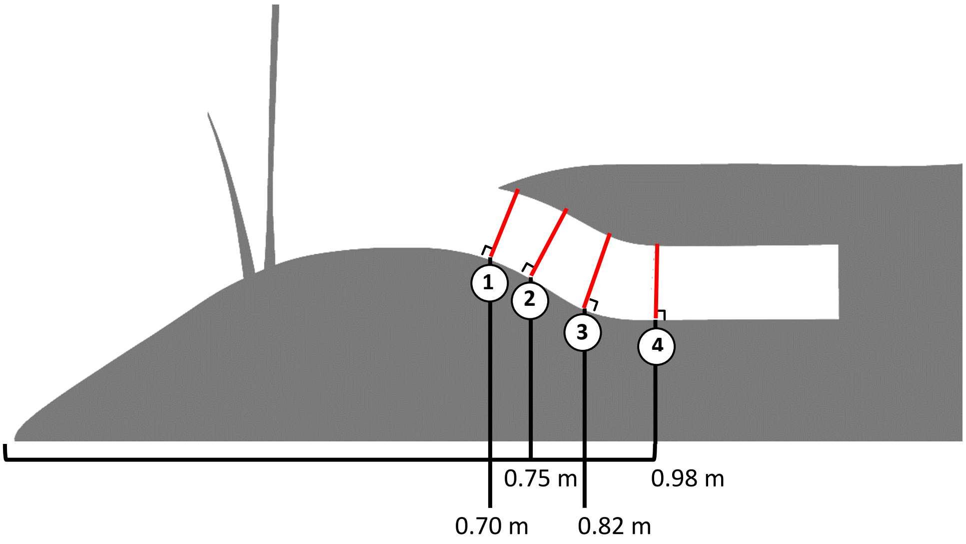

Figure 5-19: Locations of total pressure observation planes in the core inlet duct

For visualising the circumferential distortion, 4 planes were created in the core inlet duct, upon which total pressure contours could be mapped. These planes were set perpendicular to the lower end-wall of the duct, and are positioned where the ESS and IGV stages would approximately be located.

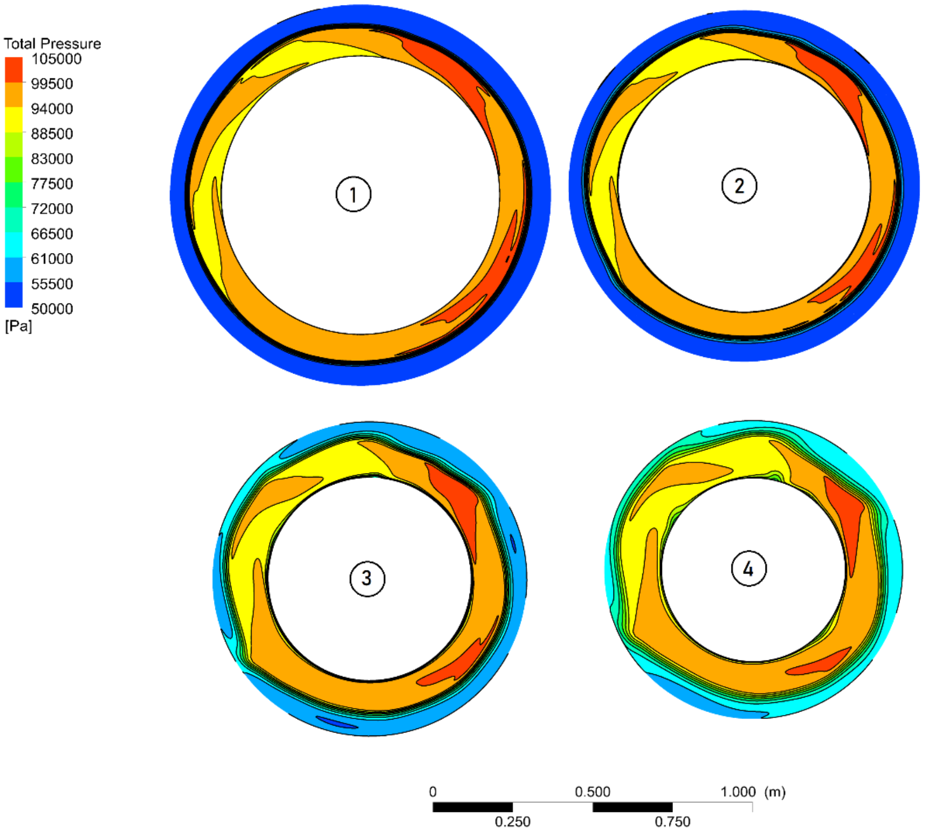

Figure 5-20: Core duct annular total pressure fields at 140 knots landing speed

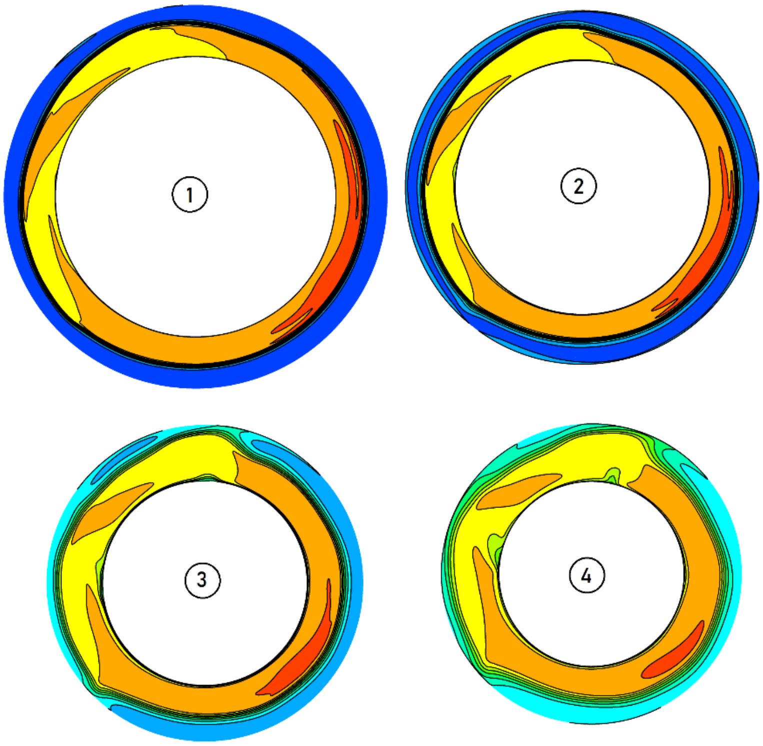

Figure 5-21: Core duct annular total pressure fields at 100 knots landing speed

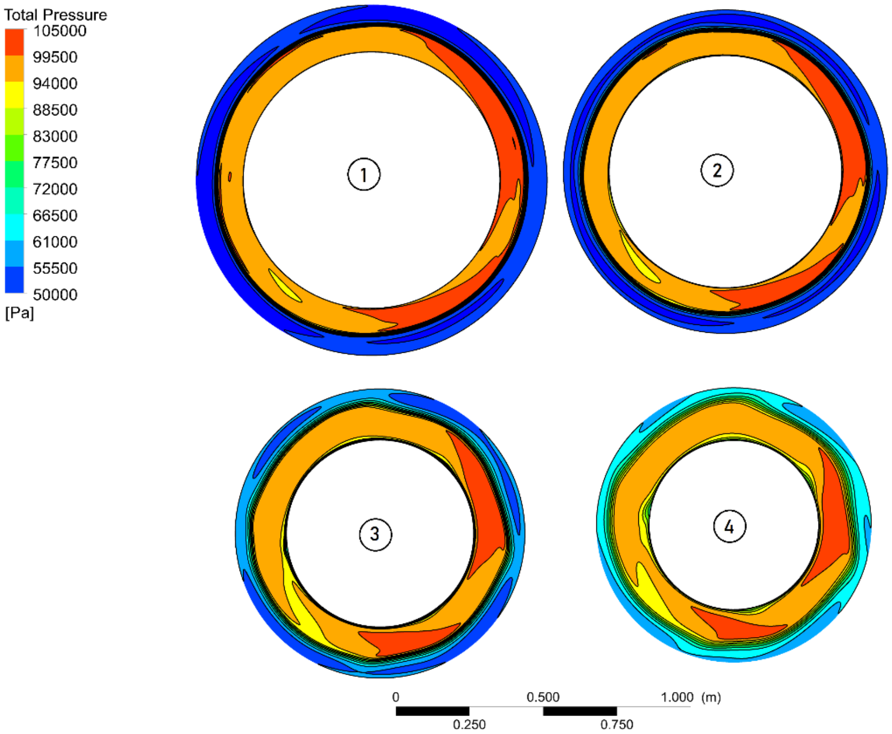

Figure 5-22: Core duct annular total pressure fields at 60 knots landing speed

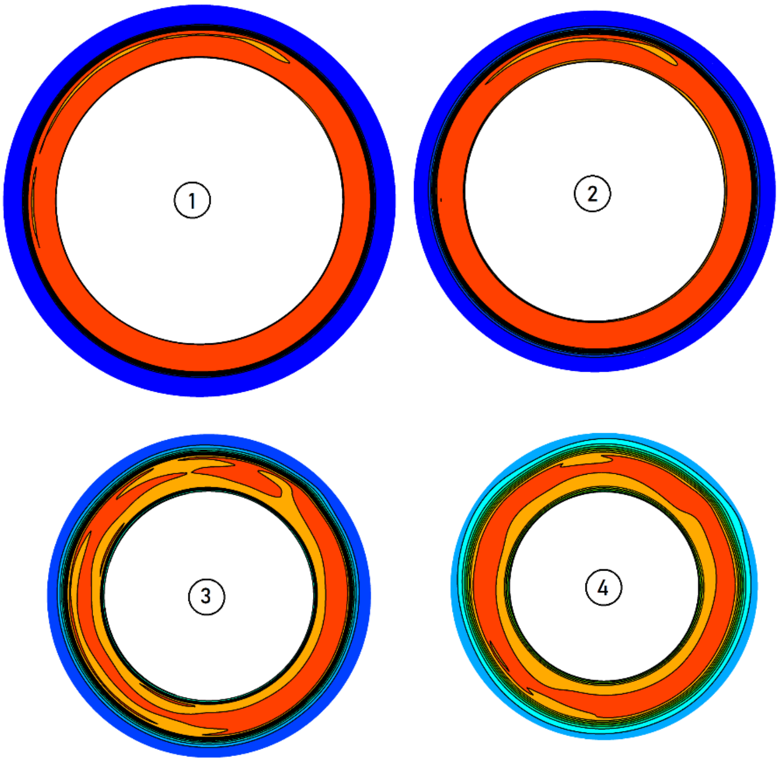

Figure 5-23: Core duct annular total pressure fields at 5 knots landing speed

The core duct total pressure planes in *Figures 5-20* to *5-23* indicate that the low-pressure band on the outer radius of the duct exists across the whole annulus, and is consistent across the first two measuring planes at all speeds. This is significant, with an internal total pressure in the separation region of ≤50 kPa, indicating a 50% recovery from ambient. Downstream of these two planes the two pressure regions have begun mixing, reducing the radial pressure gradient.

Additionally, some circumferential distortion was witnessed, most prominently on the high-speed cases. This is attributed to both the swirl induced by the fan, and blockage of the pylon. The fan induced swirl can clearly be seen by the spiralling regions of low total pressure at 140 & 100 knots, in the non-separated (inner) region. As the flow migrates down the duct, the circumferential distortion grows in cross-sectional area by mixing with the outer radial band in localised sectors. The worst affected region is the lower-inboard side of the engine, and is attributed in part to the blockage of the pylon. Additionally, the pressure-field underneath the wing, between the engine, fuselage & the ground-plane may also contribute to this.

The extent of both circumferential and radial distortion was measured using the DC_{60}, RDI, & CDI metrics from *Ch 2.8*. The results of the calculations are presented as numerical values in *Table 5-3*, and visually in *Figure 5-24*. These were calculated at plane 4, shown in *Figure 5-19*.

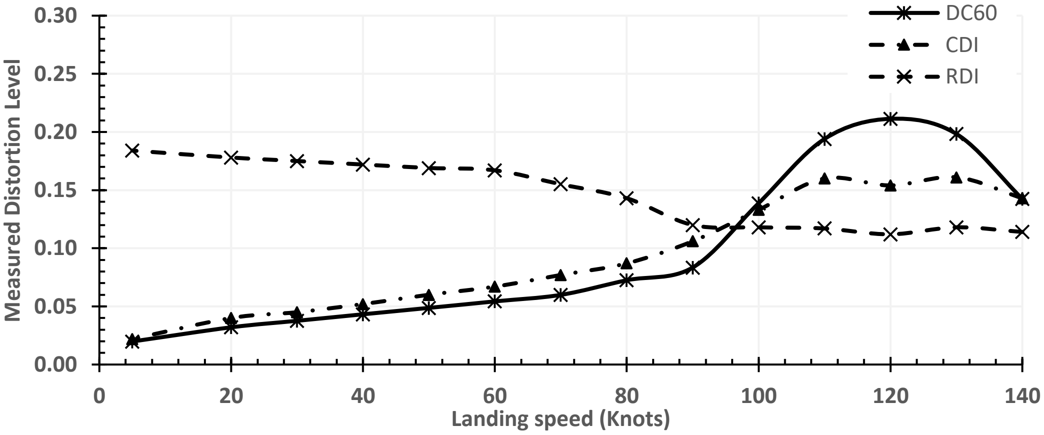

Figure 5-24: Calculated distortion metrics against landing speed for the integrated case

The results indicate that the extent of both radial & circumferential distortion is dependent on the freestream velocity. It has already been established that the circumferential distortion increases with landing speed, as shown in the total pressure contours in *Figures 5-20* to *5-23*. The calculated values for DC_{60} and CDI both correlate with this conclusion, as does the sector in which the worst total pressure distortion occurs. This is primarily because as the landing speed decreases, the interaction between the fan ejected reverse-flow and core-inlet flow weakens. However, the calculated values of DC_{60} peak at 120 knots, and slightly subdue at 140 knots. This is due mainly to the thickening of the separated flow region within the duct from 120 to 140 knots. As a result, the average total pressure on the measuring plane is lower, skewing the values calculated for DC_{60}.

Speed (knots)	*DC_{60}*	Min 60˚ sector (degrees)*	*CDI*	*RDI*
140	0.1424	90˚ to 150˚	0.143	0.114
130	0.1983	90˚ to 150˚	0.161	0.118
120	0.2113	90˚ to 150˚	0.154	0.112
110	0.1940	90˚ to 150˚	0.160	0.117
100	0.1387	90˚ to 150˚	0.133	0.118
90	0.0834	90˚ to 150˚	0.106	0.120
80	0.0725	90˚ to 150˚	0.087	0.143
70	0.0599	90˚ to 150˚	0.077	0.155
60	0.0543	90˚ to 150˚	0.067	0.167
50	0.0487	90˚ to 150˚	0.060	0.169
40	0.0432	90˚ to 150˚	0.052	0.172
30	0.0376	90˚ to 150˚	0.045	0.175
20	0.0320	90˚ to 150˚	0.040	0.178
5	0.0198	90˚ to 150˚	0.022	0.184

As viewed from the front of the engine

Table 5-3: Calculated distortion metrics for the core-inlet duct

In contrast, the radial distortion decreases with landing speed as the fan is less able to ingest flow from the bypass duct side. As previously mentioned, this is due to the high static back-pressure imposed on the fan by the freestream dynamic head. This pushes the recirculation region further into the fan blade passages; preventing flow from being ingested from the bypass side. Additionally, it is understood that the high degree of swirl associated with the bypass ingested flow at high landing speed mitigates the extent of radial distortion observed due to flow turning around the splitter.

Whilst the distortion levels are concerning, particularly regarding some of the circumferential distortion witnessed in the high-speed cases, it should be appreciated that no ESS or (V)IGV geometries was modelled. It is expected that the presence of turbomachinery in the duct would act (to some extent) to mitigate distortion and unwanted swirl of the ingested flow. The measured Mach number of flow local to the splitter inlet is no higher than 0.6, and typically closer to 0.4 (*ref. Figures 5-17 & 5-18*). As such, there should be sufficient upwind effect on the flow dynamics for the presence of a static blade passage to ‘straighten’ the flow into a more favourable order. Additionally, the radial distortion, whilst problematic to the extent of passage choking and pressure loss, is not to be considered detrimental or decisive with regards to VPF thrust reversal. The splitter geometry was deliberately chosen to represent what is found on current turbofan engines, to assess the extent that redesign to accommodate reverse-thrust operability needs to be considered. A less aggressively shaped splitter, with a rounder or blunt nose would no doubt reduce the severity and size of the outer-radial low-pressure zone, without necessarily compromising on normal aerodynamic performance. Therefore, these results indicate the potential for distortion to develop within the engine, but it is not clear whether this applies in reality. The CFD solutions obtained are also of the steady-state time-averaged nature. Therefore, unsteady core inlet distortion may be present which has not been observed, contributing additional operability concerns for the core compressors.

5.3.4 External Engine Aerodynamics

The final section of the in-depth integrated results addresses the two concerns raised in the project scope. The first is the occurrence of hot gas re-ingestion from the core exhaust into the bypass duct during reverse thrust. The second is the identification of engine-ground interactions which could result in FOD ingestion. This is done in two parts; by reviewing the flow-path of the core exhaust streams, and by plotting axial streamlines which pass directly underneath the nacelle and into the bypass duct. *Figure 5-25* shows the paths taken by the simulated flow from the core exhaust. Three features have been identified within the core flow which vary with landing speed. At high speed the suction of flow into the bypass duct, and lack of coinciding bypass exhaust stream-tube results in upward deflection of the core exhaust plume such that it passes directly under the deployed flap at the high landing speeds. This is further exasperated by the low-pressure field behind the spoiler. Potentially this could be concerning if it results in thermal cyclic stress on the flap structure, although similar flow dynamics are experienced during conventional cascade TRU deployment.

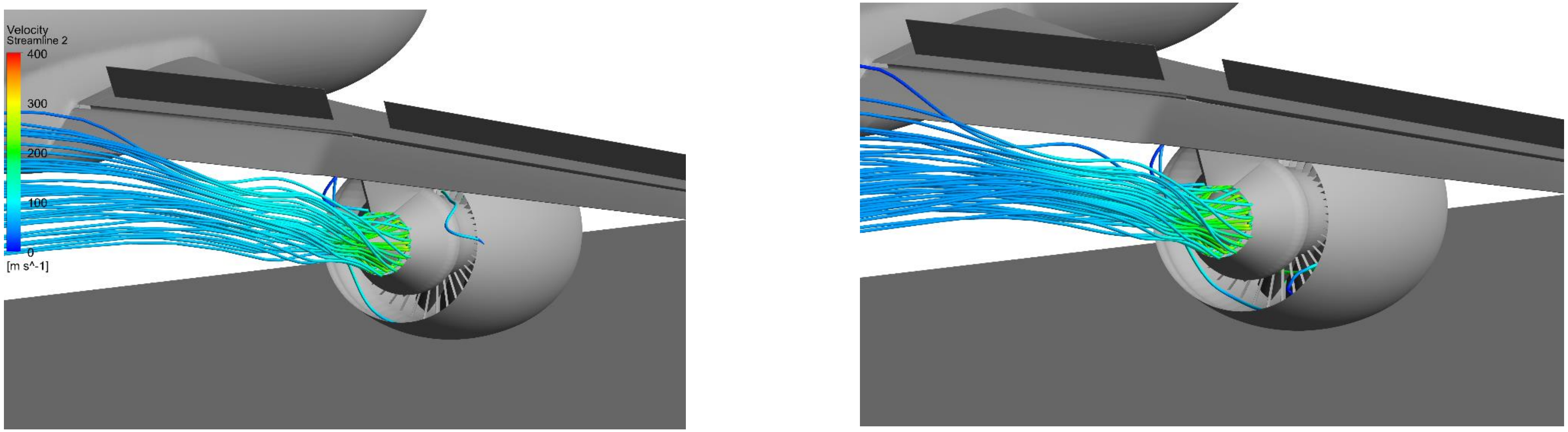

140 knots

100 knots

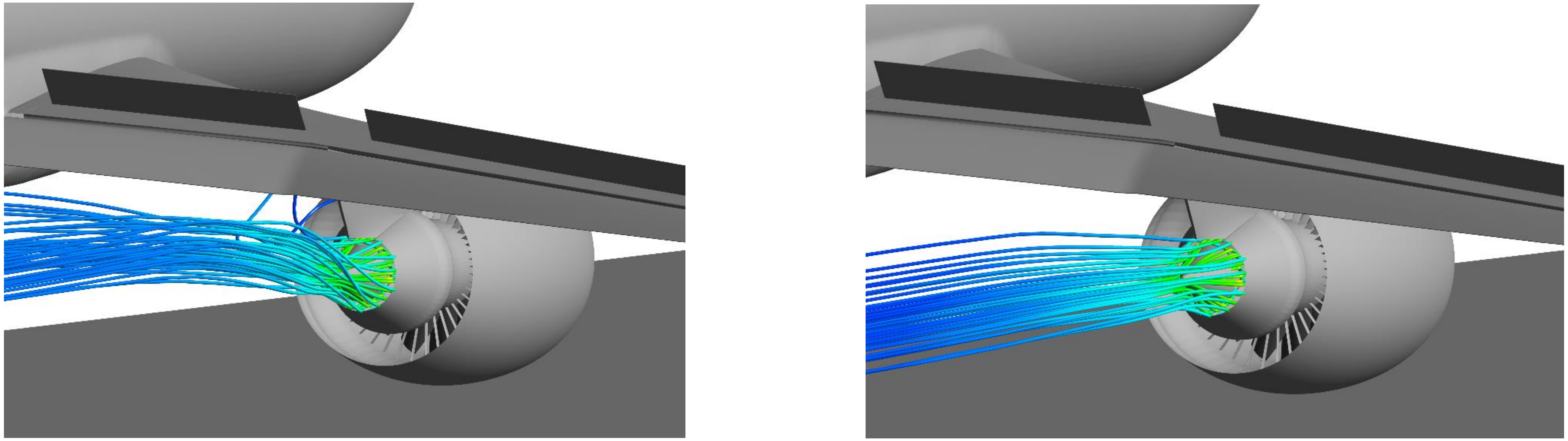

60 knots

5 knots

Figure 5-25: Core exhaust streamlines at different landing speeds

Additionally, it appears that a vortex is being induced onto the exhaust stream at above static speeds, which it is speculated to be due to the swirling of the flow around the nacelle and into the bypass duct. Furthermore, apart from at static, a small amount of the exhaust which exits the core nozzle directly under the pylon lower surface, finds its way back into the bypass duct and internal aerodynamics. However, the localised and minimal extent to which this is observed likely means that a more refined pylon; producing a lesser wake profile near the core exhaust stream tube would resolve this.

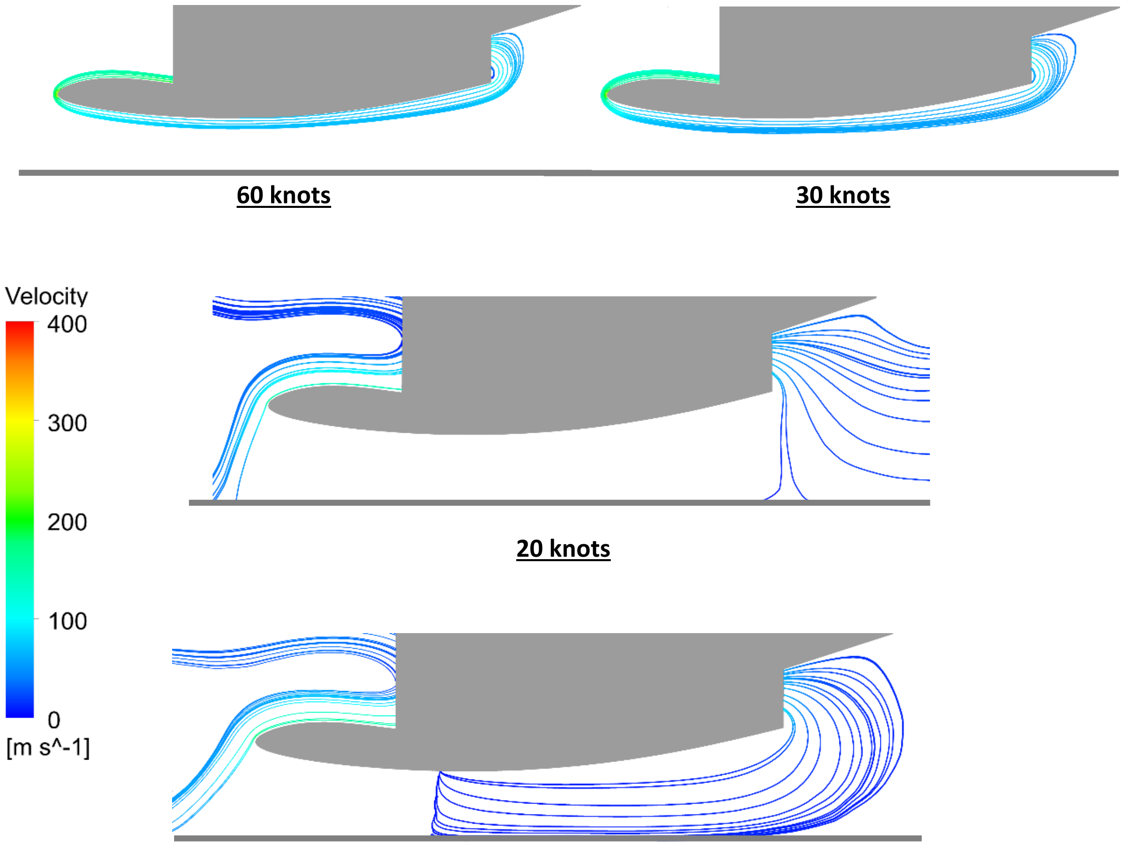

60 knots **30 knots**

20 knots

5 knots

Figure 5-26: Bypass ingested streamlines in the meridional plane, under the nacelle

Regarding the ground-plane interactions, the VPF simulation demonstrated promising results. The controversial flow-pattern induced around the nacelle from the expelled swirling fan air provides a degree of stability to the flow underneath the nacelle, presented in *Figure 5-26*. The results indicate that the engine remains self-contained, feeding the bypass exclusively from the fan’s reverse-jet, down to at least 30 knots landing speed. By 20 knots, the flow is sourced downstream from the bypass nozzle, and begins to interact with the ground, although it is unclear to what extent FOD ingestion poses a risk to the engine, as external engine flow-field is radically different compared to conventional TRU operation.

At approximately static conditions, the flow into the bypass nozzle is sourced directly under the engine nacelle, and entirely from the freestream. This subdues by 20 knots, where fan ejected flow begins to supply the bypass nozzle. However, a large scrolling flow pattern is observed around the engine, as the freestream velocity is low enough that the reverse stream boundary layer has detached from the nacelle lip surface (*ref. Figure 5-27*). Whilst this presents the greatest aerodynamic interaction between the engine and ground, the sharp turning required to re-enter through the bypass duct would no doubt have a FOD filtering effect, alike centrifugal scroll intakes found on some helicopter engines. Additionally, when the landing speed reduces such that the fan exit stream detaches from the nacelle, the stream projects upstream of the engine, acting like a blower.

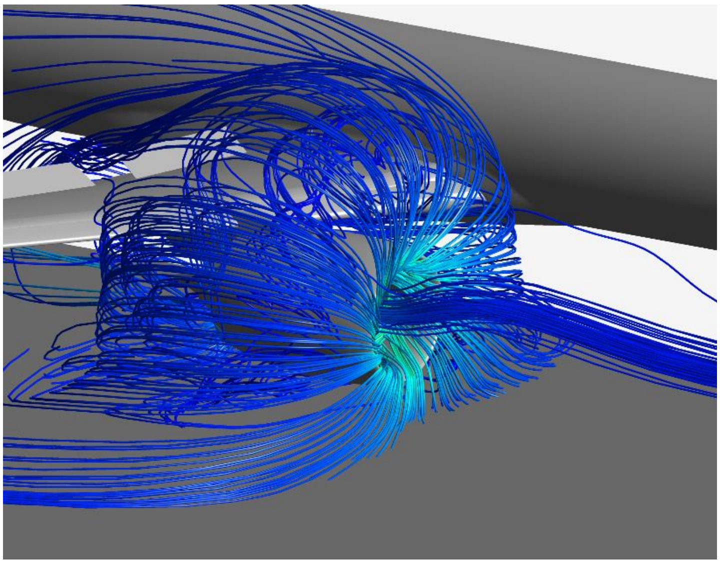

Figure 5-27: Fan exit streamlines at 20 knots landing speed

This may in-fact reduce FOD risk by removing debris from the runway as the aircraft approaches. Regardless of whether this is the case, it can be determined that the FOD risks associated with VPF thrust reversal cannot be compared with conventional TRUs, due to the considerable difference in aerodynamic operation.

Additional work is therefore needed on this area to establish a method for estimating FOD risk to the engine, should the interest in VPFs persist.

5.3.5 Effects on Spoiler Aero-Braking

Whilst spoiler performance was not a primary area of interest in this study, a lightweight assessment was conducted to identify whether the reverse-thrusting VPF had an impact on the spoiler aero-braking effectiveness. This took the form of a gross drag force assessment of the spoilers, and comparison against ‘clean airframe’ results (*ref. Figure 4-22),* obtained during the spoiler verification procedure, shown in Figure 5-28.

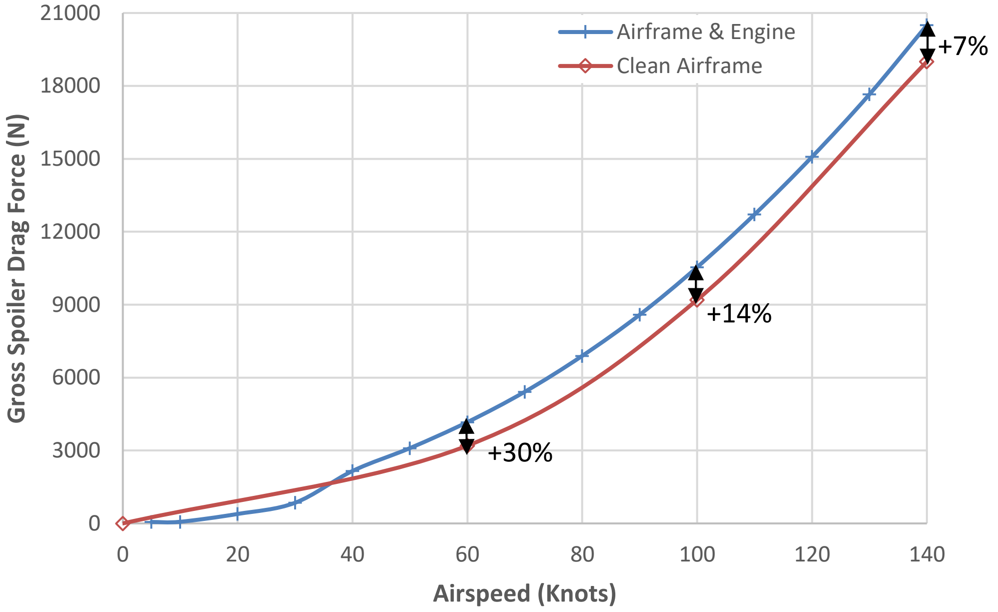

Figure 5-28: Spoiler gross drag force comparison with landing speed

As can be seen, there is a notable improvement in the braking effectiveness of the spoilers when the reverse-thrusting VPF engine is fitted. This is due to the low-pressure field behind the bypass nozzle, as flow is being re-ingested through it. The low-pressure field behind the nacelle exasperates the intensity of the nearby low-pressure field behind the spoiler plates, resulting in the increased gross drag force. This results in a 7-30% improvement in spoiler effectiveness, depending on the landing speed in question. Whilst considerable, this is not considered an exclusive phenomenon of the thrust-reversing VPF. Conventional

TRUs operate in a similar manner – blocking the bypass nozzle and redirecting the flow. This is not therefore considered to be a notable improvement over conventional systems. The second observation from *Figure 5-28* is below 30 Knots landing speed, where the airframe & engine drag suddenly diminishes. This is due to the change in engine-related flow field. When the reverse-flow jet detaches from the nacelle below 30 Knots, the engine flow field extends over the wing upper surface (*shown in Figure 5-27*). This disrupts the airflow over the wing, reducing the pressure gradient between the front/back of the spoiler plates. However, by 30 Knots most of the kinetic energy of the landing aircraft has been dissipated, so aero-braking at this speed is largely irrelevant.

5.4 Thrust Reverser Effectiveness

Given the complex flow patterns witnessed around the engine inlet whilst the aircraft is carrying any degree of speed, the conventional approach of estimating drag/thrust using a control volume was put into question. Where exactly to draw the control volume needs careful deliberation & research. The method also needs to be robust enough to handle more varied flow-fields, as may be encountered under different fan operating conditions (RPM, pitch-setting). This also requires further simulations to be conducted, to map out a wider range of the VPF's reverse thrust performance characteristics. As such, a low-fidelity method of assessing the fundamental thrust component generated by the engine was undertaken.

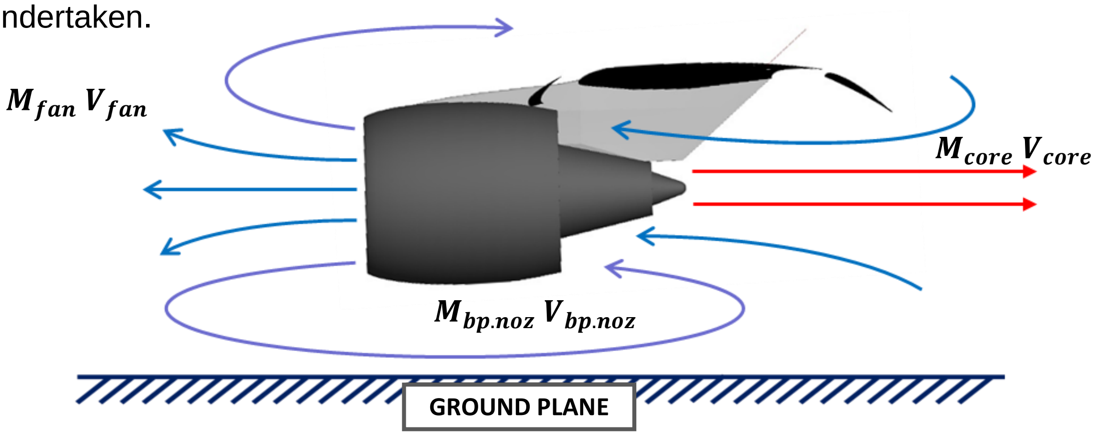

Figure 5-29: Calculating method for reverse-thrust

The method estimates reverse-thrust by measuring net-momentum change (net mass-flow & velocity transitioning across the bypass nozzle, core nozzle, and nacelle inlet interfaces), as shown in *Figure 5-29*. The thrust reverser effectiveness is then determined by normalising the measured net-thrust against nominal static forward thrust, to give thrust reverser effectiveness, η_{rev}. The value for nominal forward thrust of the engine model is 40,000 lbf/178 kN, in accordance with the project objectives (*ref. Ch 1.2*).

The thrust reverser effectiveness against landing speed is presented in *Figure 5-30*. It should be appreciated that this method does not account for additional aerodynamic forces, such as added skin-friction drag caused by the swirling flow around the nacelle during mid- to high-speed operation. The flow dynamics are fundamentally different using the VPF reverser, as opposed to conventional TRUs. With this in mind, the calculated values provide an insight into the tested VPF thrust reverser effectiveness across the speed range, but do not represent the total braking force on the aircraft model. The total values are therefore expected to be significantly higher.

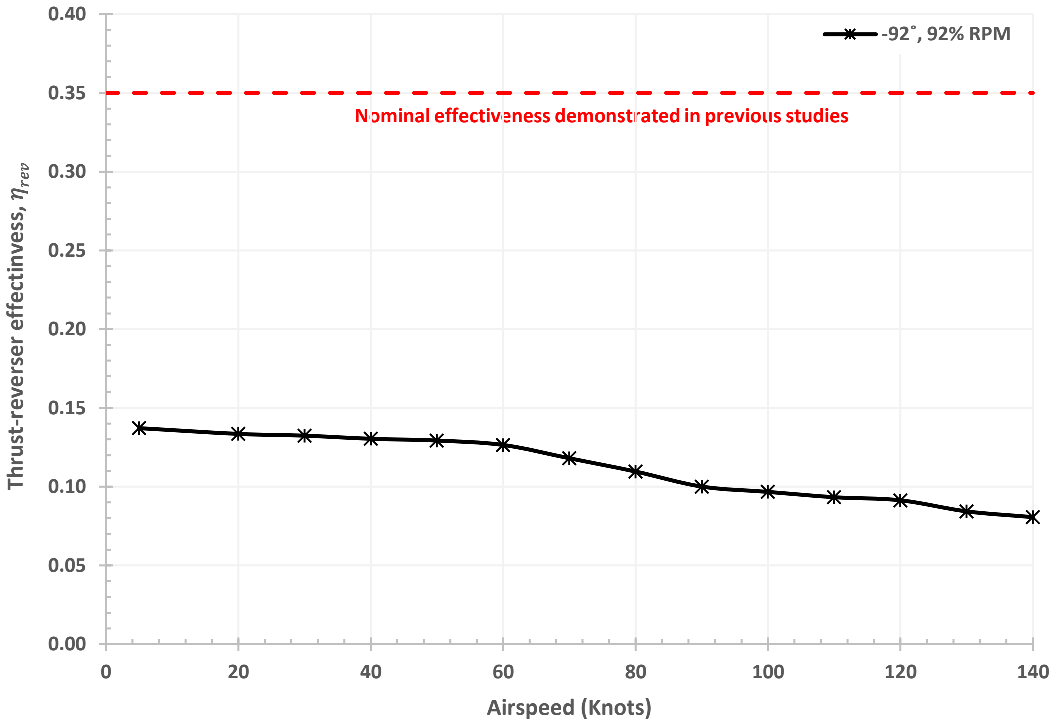

Figure 5-30: Thrust reverser effectiveness calculated from CFD solution

The calculated thrust reverser effectiveness for the tested fan configuration was found to be in the region of 8-14%, with the peak value achieved at the lowest landing speed. This appears much lower than what has been described in static tests from the QCSEE and Kutzenov NK-92 studies, where nominal effectiveness was quoted in the region of 30-35% (comparable to conventional TRUs). [10, 56] It is not possible to ascertain whether the modified VPF model can achieve performance on par with the pre-existing test cases; the -92˚ pitch setting that the fan was tested at was selected as a conservative starting point. Further exploration of the fan performance at alternative pitch/RPM configurations is needed.

However, even achieving only 8-14% effectiveness, the drag induced component of pushing the nacelle through the freestream with an aerodynamically blocked fan, will no doubt contribute a significant component to the total braking force. Furthermore, the -92˚ pitch setting that the fan was tested at was selected as a conservative starting point. It is unlikely that the first fan configuration tested is the optimal setting, especially having reviewed the initial ADP reverse-thrust performance map from the study at Cambridge, where a more open pitch setting (such as -86˚) may result in higher FPR and mass-flow.

Additionally, should thrust-reversing VPF technology be implemented in future turbofan engines, it may be possible to achieve greater thrust reverser effectiveness by varying the fan pitch/RPM depending on the relative airspeed. This requires considerable investment in time & effort to map out the full reverse-thrust fan characteristics. However, to some extent it should be considered necessary to fully appreciating the potential offered by the system. It should also be noted that from the ground-plane interaction assessment, the engine seems to be capable of operating down to at least 30 knots before engine-ground interaction became apparent. Whilst this may present only a marginal reduction in landing distance for normal weather operation, in wet or icy surface conditions where thrust reversers are the dominant braking system (*ref. Figure 2-9*), the VPF may offer a substantial improvement.

6 Conclusions

The main aim of the project was to establish an engine-airframe research model adequate for predicting & assessing reverse thrust aerodynamics for turbofan engines. This study was the first undertaken into VPF thrust-reversal within the Cranfield Rolls-Royce UTC. Given the scale of the work required to develop and assemble the research model, the knowledge gained on the project only relates to a single tested fan pitch & RPM configuration. However, given the inherent lack of publications on the subject, this first set of results still provide a significant contribution to aerodynamic understanding of VPF reverse thrust. This chapter therefore presents a summary of the concluded outcomes from this thesis, followed by contributions to knowledge, and recommendations for future work.

6.1 Major Outcomes

The major outcomes from the doctoral project are broken down into several segments, each summarising the findings of a different aspect of the study. These are presented below:

1. A robust research model for the prediction and investigation into reverse-thrust aerodynamics of variable pitch fans has been developed and tested, satisfying the main aim of this project (*ref. Ch 1.2*). The model has delivered an initial set of results, and is considered a practical tool for conducting further aerodynamic research. This has already begun under a successive doctoral study into VPF reverse thrust within the Cranfield Rolls-Royce UTC.
2. The methodology which was established to assemble the engine-airframe geometry provides guidelines for the development of similar models under future studies. Several simplifications and non-ideal characteristics of the model were identified & tolerated, such as the non-optimal performance of the fan, and pylon aft-section separation during cruise (*ref. Ch 4.2.2 & 4.3.3*). With adequate foresight, these issues could be mitigated on future studies, or at the very least pre-emptively assessed to determine if additional time should be allocated to improve the method in these areas.

3. During initial testing of the research model after first assembly of the components, discrepancies were identified between variants using single-passage and full-annulus representations of the turbomachinery. This was deemed a result of the fan's unconventional aerodynamic operating mode. Due to the pitch setting, normal axial flow through the fan stage was not established at any of the tested landing speeds. Instead, the fluid between the blades is ejected radially towards the shroud casing. The result of this is the formation of large circulating flow regions located directly over the periodic interface of the single-passage models. This distorted the numerical boundary, reducing the predicted reverse-stream mass-flow exiting the front of the engine. The same problem persisted in the OGV duct, where towards the tip, high negative incidence caused similar regions of axially stagnant flow. As such, it has been determined that single-passage modelling, whilst perfectly adequate for predicting generally well-aligned flow in turbomachinery, breaks down under the radically different aerodynamics of a reverse-thrust VPF. This a fundamental discovery, and future modelling should therefore consist exclusively of full-annulus turbomachinery representations. This applies to both integrated & isolated engine scenarios.
4. Whilst only a single fan configuration was tested in the full annulus integrated case (*-92˚ from cruise pitch, 92% RPM*), significant insight was gained into the engine's external & internal aerodynamics. Some concerns were raised regarding the lack of convergence achieved in the numerical solver. However, the model is deemed sufficient to provide preliminary insight into the complex three-dimensional flow patterns associated with VPF reverse thrust.
5. Thrust reverser effectiveness was calculated, ranging from 8% at 140 knots landing speed, to 14% at 5 knots. The values were determined only from the momentum change measured at the nacelle/nozzle boundaries. As such, the drag component of the total braking force, which is expected to be considerable, has not been accounted for. The unique external engine aerodynamics during thrust reversal; specifically, the ingestion and then immediate expulsion of fluid through the nacelle intake, before being re-ingested through the bypass nozzle (*at 30 knots and above*), raised concerns

regarding use of a control volume method for drag estimation. Therefore, the thrust reverser effectiveness measured is still considered promising, but further work is needed on the subject.

6. The fan operated consistently, producing an outer radial band of reversed-flow from the nacelle intake at all tested landing speeds. The blade passages were aerodynamically blocked, due to the pitch setting being too closed. Reverse thrust was still generated, as the blockage and fan's high RPM forced flow to accelerate radially in the stage. During this radial migration, the flow adopts the fan's rotational speed, becoming highly swirled. This occurred on both sides of the fan. On the front, the radial pressure gradient continued to ingest the freestream at the hub, regardless of the misalignment of the fan blades to the flow direction. On the rear, normal flow interception was observed at mid-span, but this subsided as the landing speed increased to approximately 100 knots, where the radial flow streams between the blades were displaced aft; blocking the entire blade passage from the rear except the tip. Shearing still occurred between the fan and the flow residing in the splitter-duct, which largely maintained the radial pressure gradient along the fan stage's rear face.
7. Distortion within the bypass & core inlet duct was measured, and several significant flow phenomena were observed, previously unrecorded in the public domain. These are summarised in the following points:
    - At almost all speed cases the reverse flow stream was observed to exit the fan at the outer radius, before turning around the nacelle lip, to travel rearwards toward the bypass duct. This flow carried a significant swirl velocity corresponding with the fan's rotational speed. As such the presence of the pylon acts to block a significant section of the bypass nozzle, creating a circumferential gradient of total pressure. This is considered the primary contributor towards circumferential distortion into the core inlet. The calculated values of DC_{60} and CDI were high, but not exceeding what was quoted as typical limits for turbofan compressors. Overall, circumferential distortion increased with landing speed.

- Radial distortion was persistent across all CFD results processed. Large regions of low total pressure were identified in the outer radius of the core inlet. This was initiated by boundary layer delamination of the flow turning around the splitter's sharp leading edge. This observation was concerning, but it is also expected that the losses could be easily addressed by using an alternative, 'blunter' splitter design. The radial distortion was highest during low landing speed operation, as the swirling bypass stream at high speeds was found to reduce the severity of the distortion.
- The OGVs do not seem to impinge on the flow travelling up the bypass duct towards the core, however significant blockage is found at the OGV outer radius, which encounters the highly swirled flow energised by the fan.
- A very small amount of the core exhaust stream was pulled back into the bypass duct during mid & high landing speed simulations. The re-ingested exhaust gas consistently originated from where the core nozzle & pylon lower surfaces intersect, but entered the bypass duct at mid-span, avoiding direct ingestion into the core. As the pylon is a simplified representation, and the results are only numerical flow predictions, it is not known whether this is an issue for real-world engines.

8. Regarding the extent of ground-plane interaction observed, the results indicated that VPF thrust reversal can potentially be operated below the threshold of 60-80 knots which conventional TRUs are restricted by. The ingested flow into the bypass duct was sourced exclusively from flow adjacent to the nacelle wall. Only when the landing speed reduced to below 30 knots did the flow-field fundamentally change; where the reverse-thrust stream was projected upstream of the engine, rather than following the curvature of the nacelle lip. This may not be the case if the fan aerodynamics are radically different under alternative pitch settings.
9. The core exhaust stream was diverted upwards, which was most noticeable at high freestream speeds. The lack of a bypass exit stream, coupled with the

low-pressure region directly behind the wing (induced by the spoilers), pulls the core exhaust stream tube towards the wing flap. This could present some concerns regarding thermal cyclic stress on the flap structure, should core exhaust be close enough to transfer significant thermal energy. This is not unique however, and conventional cold-stream TRUs experience similar issues. Therefore, this may be an area of interest for future work.

6.2 Contributions to Knowledge

From the work conducted & presented in this thesis, the following areas can be considered contributions to knowledge:

1. The methodology described in *Chapter 3* documents the work undertaken to develop the novel CFD-based VPF research model. The method covers development of new components, and adaptation of existing geometries. Once assembled these components represent a conventional twin-engine aircraft during landing, with low-specific thrust turbofan engines. The methodology therefore provides a reference for future studies of a similar nature.
2. From the initial test cases run on the research model following assembly, it was discovered that single-passage turbomachinery domains are not sufficient to model reverse-pitch VPFs. The highly radial flow regime within the stage exceeds the tolerable capabilities of periodic-type interfaces in the numerical solver. This resulted in a significant degradation in measured reverse-thrust mass-flow, and thus braking effectiveness. It is recommended that full annulus representations of turbomachinery are adopted for future CFD studies into VPF reverse thrust.
3. Demonstration of the capacity to predict time-averaged flow solutions within a novel large-scale CFD research model. This includes the computational performance requirements needed to undertake a CFD study of this nature, in terms of run-time & processing power (*ref. Table 5-1 & Ch 3.6.6*).
4. The groundwork to quantifying the complex three-dimensional flow associated with VPF thrust reversal has been laid. The results presented are believed to

be the first of their kind to be published in the public domain. Whilst there is some limited data freely available from historic VPF studies, none have assessed in depth either the effects of landing speed on engine aerodynamics, or the potential issues introduced when the engine is installed beneath the wing of a landing/decelerating aircraft.

6.3 Recommendations for Future Work

The main recommendations for future work are listed below: -

- **Continue to utilise the research model to achieving a better understanding of the VPF system's potential & operation:**
  - Further map out the fan operating regime by testing further blade pitch setting & RPM configurations. To achieve maximum effectiveness, it is likely the fan's pitch angle would be marginally varied as the landing speed reduces during landing. By populating the effectiveness map with more pitch/RPM configurations, a more accurate indication of the systems nominal braking performance should be obtained.
  - Develop a robust control volume method, or suitable alternative for the determination of total braking force on the aircraft during landing. Results presented in this thesis on the VPF's reverse-thrust performance only accounts for momentum change, and not aerodynamic drag.
  - Determine the fan work energy during thrust reversal, and input to the TURBOMATCH model to allow core simulations to be undertaken. This should provide insight into the power-state of the core, and whether or not the current system is capable of operating within thermal limits given the undesirable IPC conditions.
  - Investigate the effects of cross-wind on the flow distortion identified in the previous chapter. Additionally, this may lead to a reduction in the fan effectiveness if the bypass nozzles ability to ingest flow is impinged by fuselage interference/blockage of the freestream.

  - Conduct a study into the risks of foreign object debris (FOD) ingestion. Current TRUs are typically disengaged between 80-60 knots; it would be an important factor to consider when reviewing the systems potential of VPF thrust reversers, if they could be operated below this speed.
  - Introduce an ESS stage to the research model, located in the core inlet duct. The implications of the turbomachinery within the area of distortion may have a dampening effect. Conversely, the flow swirl from the OGVs may result in aerodynamic blockage at the ESS, due to the high positive incidence (*ref. Figure 3-28*).
  - Conduct a transient simulation on the model, to better understand the fan's performance. Insight into the unsteady aerodynamics may highlight concerns within the time-averaged solutions which brings into question their validity.

- **Investigate the use of a short slim-line type nacelle:**

  Whilst providing potential improvements to normal operation through drag & weight reduction, the use of a slim-line type nacelle will likely affect the thrust reverser effectiveness due to changes in the external flow-field. This requires significant redevelopment of the nacelle, pylon & bypass duct geometries. However, this may present a more realistic representation of a future VPF fitted UHBR turbofan.

- **Address total pressure recovery in the bypass duct by considering introducing the following features:**
  - Auxiliary intakes on the nacelle, alike those mentioned on the Rolls-Royce/SNECMA M45H/RB.401 engine (*ref. Figure 2-28*). This could manifest in one of several forms:
    - Blow-in doors, similar to those found on some military aircraft.
    - A two-part nacelle, whereby the aft-body translates rearwards, alike a conventional cascade reverser. This would increase the bypass

    nozzle area both at the rear, and through the new opening in the middle of the nacelle.
    - Deployable scoop intakes likened to those found on the ‘crocodile multi-door reverse’ concept studied by NASA. [28] These would operate alike the blow-in doors, but increase the drag whilst providing ram air.
  - Variable bypass nozzle geometry, including ‘exlets’ and similar systems (such as the SNECMA patent mentioned in *Ch 2.7.1*). [60] The potential benefits of these systems to VPF thrust reversal have been clearly documented under the QCSEE studies by NASA. [56] However, more research is required to ascertain the exchange rate between additional weight & drag, and improvements in reverse thrust performance.

- **Address radial distortion identified within the core intake**
  - Develop an alternative splitter geometry with a round or ‘blunt’ leading edge profile, rather than the sharp Trent 1000 based one. It is expected this would reduce (although probably not eliminate) the extent of radial distortion/separation at the core inlet duct/ESS stage entry. Changes to the splitter may also be feasible without introducing performance losses during normal operation.
  - Core auxiliary intakes may offer another solution to address the splitter flow separation. Providing a secondary flow path, either upstream or downstream of the ESS/VIGV stage(s) may offset the losses and radial distortion observed, independently of the splitter design.
  - Active flow control for the splitter boundary layer. The use of an active flow control system may be a less intrusive option than auxiliary intakes to addressing the bypass nozzle pressure recovery, delaying boundary layer breakdown on the splitter surface. This would add a bleed air requirement during operation however, which would push the core to work slightly harder.
  - Investigate the effects of relocating the OGVs upstream of the splitter. This would reduce the swirl observed within the core inlet duct. Similar concepts

were patented by NASA during the QCSEE study. [62] Additionally, several production engines have featured pre-splitter OGVs, such as Honeywell's HTF7000 & GE/Honda's HF120 (*shown in Figure 6-1*). [53, 129] However, these are both small thrust class, medium/low BPR engines, and there maybe structural reasons why this is not feasible for large UHBR turbofans.

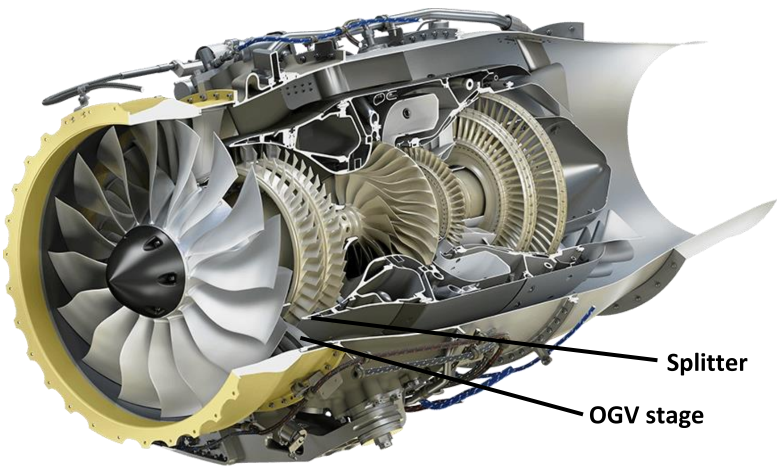

Figure 6-1: GE/Honda HF120 engine with OGVs upstream of splitter [129]

7 References

[1] Aviation Benefits Beyond Borders, “Aviation Benefits - Economic Growth,” [Online]. Available: https://aviationbenefits.org/economic-growth. [Accessed 2018].

[2] Boeing, Current Market Outlook 2017-2036, Sourced from Boeing.com, 2017.

[3] ACARE, “Strategic Research & Innovation Agenda - FlightPath2050 Goals,” Sourced from acare4europe.org, 2018.

[4] Rolls-Royce, “Trent 1000 engine data,” Sourced from Rolls-Royce.com, 2018.

[5] J. Whurr, “Future Civil Aeroengine Architectures & Technologies,” in *10th European Turbomachinery Conference*, Lappenranta, Finland, 2013.

[6] P. Giannakikis, Design Space Exploration and Performance Modelling of Advanced Turbofan and Open-Rotor Engines, EngD Thesis, School of Engineering, Cranfield University , 2013.

[7] C. P. D. M. G. Krishnan, “An Assessment of Relative Technology Benefits of a Variable Pitch Fan and Varaible Area Nozzle,” *AIAA Joint Propulsion Conference,* Vols. AIAA 2013-3604, 2013.

[8] L. S. Langston, “Turbine Fuel Efficieny: Fitting Pitch,” ASME, 2011. [Online]. Available: https://www.asme.org/engineering-topics/articles/turbines/turbine-fuel-efficiency-fitting-a-pitch.

[9] M. Winter and R. B. Hanson, “Thrust vectorable fan variable area nozzle for a gas turbine engine fan nacelle”. European Patent Application Patent EP 1 916 405 A3, 11 01 2012.

[10] N. D. Kuznetsov, “Propfan Engines,” in *AIAA/SAE/ASME/ASEE 29th Joing Propulsion Conference and Exhibit*, Monterey, California, USA, 1993.

[11] D. C. Reemsnyder and D. A. Sagerser, “Effect of Forward Velocity and Crosswind on the Reverse-Thrust Performance of a Variable-Pitch Fan Engine,” NASA Technical Memorandum TM-79059, Lewis Research Center, 1979.

[12] Z. T. Applin, K. M. Jones, B. E. Gile and P. F. Quinto, “Subsonic Aerodynamic Charactersitics of Semispan Commercial Transport Model with Wing-Mounted Advanced Ducted Propellor Operating in Reverse Thrust,” NASA Technical Paper 3427, Langley Research Center, Virginia, USA, 1994.

[13] A. McKenzie, “Axial Flow Fans and Compressors: Aerodynamic Design and Performance,” in *Cranfield Series on Turbomachinery Technology*, Ashgate Publishing, 1997.

[14] W. G. R. Calvert, “Transonic Fan and Compressor Design,” in *Proceedings of the Institute of Mechanical Engineers Vol 23 Part C*, 1999.

[15] A. Jackson, “Optimsation of Aero and Industrial Gas Turbine Design for the Environment,” PhD Thesis, School of Engineering, Cranfield University, 2009.

[16] C. Mourouzidis, “Cycle Optimisation & Preliminary Design of Very Low Specific Thrust Turbofan Engines,” UTC PhD Thesis, School of Aerospace, Transport & Manufacturing, Cranfield University, 2016.

[17] P. &. Whitney, “Pratt & Whitney PW1000G website,” http://www.pw.utc.com/PurePowerPW1000G_Engine, 2018.

[18] Rolls-Royce, “Rolls-Royce to build new facility in Dahlewitz, Germany, to test components for next generation aero engines,” https://www.rolls-royce.com/media/press-releases/yr-2014/070314-generation-aero-engines.aspx, 2014.

[19] P. &. Whitney, “Image sourced from purepowerengines.com/photos.htm,” 2018.

[20] G. Norris, “Rolls-Royce Details Advance and UltraFan™ Test Plan,” Aviation Week & Space Technology , http://aviationweek.com/commercial-aviation/rolls-royce-details-advance-and-ultrafan-test-plan, 2014.

[21] K. V.E., Thermodynamic Preliminary Design of Civil Turbofans and Variable Geometry Implementation, PhD Thesis, School of Engineering, Cranfield University, 2006.

[22] SkyBrary, “SkyBrary - Thrust Reversers: Flight Crew Guidance,” [Online]. Available: https://www.skybrary.aero/index.php/Thrust_Reversers:_Flight_Crew_Guidance#Accidents_and_Incidents. [Accessed 2018].

[23] J. Yetter, Why Do Airlines Want and Use Thrust Reversers?, Langley Research Center: NASA Technical Memorandum 109158, 1995.

[24] J. Y. S.C. Asbury, Static Performance of Six Innovative Thrust Reverser Concepts for Subsonic Transport Applications, NASA/TM-2000-210300, 2000.

[25] G. O. L.G. Trapp, “Aircraft Thrust Reverser Cascade Configuration Evaluation Through CFD,” *AIAA 41st Aerospace Science Meeting and Exhibit,* no. AIAA-2003-0723, 2003.

[26] F. S. Foundation, “ALAR Tool Kit,” *FSF ALAR Briefing Note 8.3 - Landing Distances,* vol. Flight Safety Digest. Flight Safety Foundation, 2000.

[27] A. J. S. R. P. P. M. S. V. S. T. Mahmood, “Thrust Reverser for a Mixed Exhaust High Bypass Ratio Turbofan Engine and its Effect on Aircraft and Engine Performance,” Proceedings of ASME Turbo Expo 2012, Copenhagen, Denmark, 2012.

[28] E. B. G.J. Noel, “Thrust Reverser Analysis for Implementation in the Aviation Environmental Design Tool (AEDT),” U.S. Department of Transportation, PB2007-111124, 2007.

[29] A. J. V. S. P. P. T. Mahmood, “Thrust Reverser for a Seperate Exhaust High Bypass Ratio Turbofan Engine and its Effect on Aircraft and Engine Performance,” *Proceedings of ASME Turbo Expo,* no. GT2011-36297, 2011.

[30] Rolls-Royce, “Rolls-Royce - The Jet Engine 5th Edition,” Rolls Royce Technical Publications Department, Derby, England, 1996.

[31] A. Linke-Diesinger, “Systems of Commercial Turbofan Engines: An Introduction to Systems Fuctions,” Springer, New York, U.S.A, 2008.

[32] Google.com, “Sourced from Google Images 2018,” https://www.flickr.com/photos/48018541@N04/galleries/72157623570087434/.

[33] W. Commons, “Image sourced from Wikimedia Commons 2018,” https://commons.wikimedia.org/wiki/File:Reverse.thrust.klm.fokker70.arp.jpg.

[34] T. H. Z. S. P.N. Shah, “Full-Scale Turbofan Demonstration of a Deployable Engine Air-Brake for Drag Management Applications,” *Proceedings of ASME Turbo Expo 2016,* Vols. GT2016-56708, 2016.

[35] S. A. J. Yetter, “Static Performance of a Wing-Mounted Thrust Reveser Concept,” *34th AIAA/ASME/SAE/ASEE Joint Propulsion Conference & Exhibit,* no. AIAA 98-3256, 1998.

[36] SNECMA, “By-pass Turbojet including a Thrust Reverser,” no. Patent # US12100603 Granted 10-4-2008, 2007.

[37] K. J. I. Halliwell, “Fuel Burn Benefits of a Variable-Pitch Geared Fan Engine,” no. AIAA 2012-3912, 2012.

[38] M. I. A. S. M.J. Wilson, “The Effect of Stagger Variability in Gas Turbine Fan Assemblies,” *ASME Journel of Turbomachinery,* vol. 129, p. 404, 2007.

[39] R. Mazzawy, “Performance Study for Benefits of Variable Pitch Composite Fan,” in *Proceedings of ASME Turbo Expo 2010*, Glasgow, UK, 2010.

[40] W. O. R.D. Moore, “Aerodynamic Performance of 1.38-Pressure-Ratio Variable-Pitch Fan Stage,” NASA Technical Paper 1502, Lewis Research Center, 1979.

[41] A. C. A. S. S. Bianchi, “Stall Control and Recovery in a Low-Speed Axial Fan through the use of Variable-Pitch in Motion Blades,” in *Proceedings of ASME Turbo Expo 2012*, Copenhagen, Denmark, 2012.

[42] E. L. J.A. Violette, “Mechanical Design of a Variable Pitch Fan for Turbofan Engines,” in *Proceedings of ASME Turbo Expo 2016*, Glasgow, UK, 2010.

[43] A. B.G. McKay, “The UltraFan Engine and Aircraft Based Thrust Reversing,” in *48th AIAA/ASME/SAE/ASEE Joint Propulsion Conference & Exhibit*, Atlanta, Georgia, USA, 2012.

[44] R. N. E. M. D. P. D. S. D.E. Hobbs, “Low Noise Research Fan Stage Design,” NASA Contractor Report 195382 , United Technologies Corporation, Pratt & Whitney, East Hartford, Connecticut, 1995.

[45] R. Jeracki, “Comprehensive Report of Fan Performance from Duct Rake Instrumentation on 1.294 Pressure Ratio, 806 ft/sec Tip Speed Turbofan Simulator Models,” NASA Technical Memorandum TM-2006-213863, Glenn Research Center, Cleveland, Ohio, 2006.

[46] V. Holcombe, “Aero Propulsion Technology (APT) Task V - Low Noise ADP Engine Definition Study,” NASA Contractor Report CR-2003-212521, United Technologies Corporation, Pratt & Whitney, East Hartford, Connecticut, 2003.

[47] D. Tweedt, “Computation Aerodynamic Simulations of an 840ft/sec Tip Speed Advanced Ducted Propulsor Fan System Model for Acoustic Methods Assessment and Development,” NASA Contractor Report CR-2014-218129, AP Solutions Inc, Cleveland, Ohio, 2014.

[48] W. Willis, “Quiet Clean Short-haul Experimental Engine (QCSEE) Final Report,” NASA Contractor Report CR-159473, General Electric Company, 1979.

[49] F. International, “SuperFan-powered A340 a possibility,” Flight International, 6 December 1986.

[50] R. G. O'Lone, “McDonnell executives question target date of SuperFan engine,” *Aviation Week & Space Technology,* no. February, pp. 30-31, 1987.

[51] F. International, “Variable-Pitch Fans: Progress In Britain,” Flight International, 19th April 1973, p. 615.

[52] R. Denning, “Variable Pitch Ducted Fans for STOL Transport Aircraft,” in *ASME Gas Turbine and Fluids Engineering Conference & Products Show 72-GT-61*, San Francisco, California, USA , 1972.

[53] B. G. M. Daly, Jane's Aero Engines 28th Edition, Jane's Information Group Inc, 2010.

[54] J. Stevens, “Turbomeca's Astafan,” *Flight International,* pp. 553-555, 20th April 1972.

[55] N. E. Samanich, D. C. Reemsnyder and H. E. Bloomer, “Reverse Thrust Performance of the QCSEE Variable Pitch Turbofan Engine,” NASA Technical Memorandum TM-81558, Lewis Research Center, 1980.

[56] J. W. Schaefer, D. A. Sagerser and E. G. Stakolich, “Dynamics of High-Bypass-Engine Thrust Reversal Using Variable-Pitch Fans,” NASA Technical Memorandum X-3524, Lewis Research Center, 1977.

[57] W. J. Demers, D. J. Nelson and H. S. Wainauski, “Hamilton Standard Q-Fan Demonstrator Dynamic Pitch Change Test Program - Final Report,” NASA Contractor Report CR-134861, 1975.

[58] W. F. Vier, “Quiet Clean Short-Haul Experimental Engine (QCSEE) Test Results from a 14 cm Inlet for a Variable Pitch Fan Thrust Reverser,” NASA Contractor Report-134867, 1975.

[59] D. A. Dietrich, T. G. Keith and G. G. Kelm, “Aerodynamic Performance of Flared Fan Nozzles Used as Inlets,” NASA Technical Memorandum TM X-3367, Lewis Research Center, 1976.

[60] SNECMA, “Inversion De Poussee Dans Une Turbomachine Avec Soufflante A Calage Variable”. European Patent Office Patent FR3052191 (A1), 08 12 2017.

[61] P. Middleton, “STOL Fans from Dowty,” *Flight International,* pp. 89-91, 21 January 1971.

[62] L. H. Smith, “Reverse Pitch Fan with Divided Splitter”. USA Patent US4005574, 1 Feburary 1977.

[63] R. D. Moore and G. Kovich, “Aerodynamic Performance of Two Variable-Pitch Fan Stages,” NASA Technical Memorandum TM X-73416, Lewis Research Center, 1976.

[64] R. M. B. B. R.G. Giffin, “Quiet Clean Short-Haul Experimental Engine (QCSEE) Aerodynamic and Aeromechanical Performance of a 50.8 cm (20 in.) Diameter 1.34 PR Variable Pitch Fan with Core Flow,” NASA CR-135017, Lewis Research Center, 1977.

[65] M. Carnevale, F. Wang and L. di Mare, “Low Frequency Distortion in Civil Aero-Engine Intake,” *Proceedings of ASME Turbo Expo 2016,* no. GT2016-56203, 2016.

[66] K. Lee, B. Lee, S. Kang, S. Yang and D. Lee, “Inlet Distortion Test with Gas Turbine Engine in the Altitude Engine Test Facility,” *27th AIAA Aerodynamic Measurement Technology and Ground Testing Conference,* no. AIAA 2010-4337, 2010.

[67] J. Murphy, “Intake Ground Vortex Aerodynamics,” PhD Thesis, Department of Aerospace Sciences, Cranfield University, 2008.

[68] M. Frascella, P. K. Zachos, D. G. MacManus and D. Gil Prieto, “Pressure Flow Field and Inlet Flow Distortion Metrics Reconstruction from Velocity data,” *34th AIAA Applies Aerodynamics Conference,* 2016.

[69] C. Reid, “The Response of Axial Flow COmpressors to Intake Flow Distortion,” *ASME Publication,* no. 69-GT-29, 1969.

[70] A. Mehdi, “Effect of Swirl Distortion on Gas Turbine Operability,” PhD Thesis, Power & Propulsion Department, School of Engineering, Cranfield University, 2014.

[71] J. Castaneda, A. Mehdi, D. di Cugno and V. Pachidis, “A Preliminary Numerical CFD Analysis of Transonic Compressor Rotors when Subjected to Inlet Swirl Distortion,” in *Proceedings of ASME Turbo Expo 2011*, Vancouver, British Colombia, Cananda, 2011.

[72] W. T. Cousins and M. W. Davis, “Evaluating Complex Inlet Distortion with a Parallel Compressor Model: Part 1 - Concepts, Theory, Extensions, and Limitations,” in *Proceedings of ASME Turbo Expo 2011*, Vancouver, British Columbia, Canada, 2011.

[73] M. W. Davis and W. T. Cousins, “Evaluating Complex Inlet Distortion with a Parallel Compressor Model: Part 2 - Applications to Complex Patterns,” in *Proceedings of ASME Turbo Expo 2011*, Vancouver, British Columbia, Canada, 2011.

[74] P. P. Walsh and P. Fletcher, Gas Turbine Performance 2nd Edition, Blackwell Publishing, 2004.

[75] H. Hoheisel and H. F. Geyr, “The Influence of Engine Thrust Behaviour on the Aerodynamics of Engine Airframe Integration,” *CEAS Aeronautical Journal,* vol. 3, pp. 79-92, 2012.

[76] T. P. Stankowski, “Aerodynamics of Propulsion System Integration for Modern Aero-Engines,” PhD Thesis, School of Aerospace, Transport and Manufacturing, Propulsion Engineering Centre, Cranfield University, 2016.

[77] G. M. Gatlin, S. M. Rivers, S. L. Goodliff, R. Rudnik and M. Sitzmann, “Investigation of the DLR-F6 Transport in the National Transonic Facility (Invited),” *26th AIAA Applies Aerodynamics Conference,* pp. AIAA-2008-6917, 2008.

[78] K. R. Laflin, S. M. Klausmeyer, T. Zickuhr and et al., “Data Summary from Second AIAA Computational Fluid Dynamics Drag Prediction Workshop,” *Journal of Aircraft,* vol. 42, no. 5, pp. 1165-1178, 2005.

[79] J. C. Vassberg, E. N. Tinoco, M. Mani and et al., “Summary of the Third AIAA CFD Drag Prediction Workshop,” in *AIAA Paper 2007-0260*, Reno, Nevada, USA, 2007.

[80] J. C. Vassberg, M. A. DeHaan, S. M. Rivers and R. A. Wahls, “Development of a Common Research Model for Applied CFD Validation Studies,” in *26thg AIAA Applied Aerodynamics Conference*, Honolulu, Hawaii, USA, 2008.

[81] J. C. Vassberg, E. N. Tinoco, M. Mani, B. Rider and et al., “Summary of the Fourth AIAA Computational Fluid Dynamics Drag Prediction Workshop,” *Journal of Aircraft,* vol. 51, no. 4, pp. 1070-1089, 2014.

[82] D. W. Levy, K. R. Laflin and et al., “Summary of Data from the Fifth AIAA,” *Journal of Aircraft,* vol. 51, no. 4, pp. 1094-1213, 2014.

[83] E. N. Tinoco, O. P. Brodersen and S. Keye, “Summary of Data from the Sixth AIAA CFD Drag Prediction Workshop: CRM Cases 2 to 5,” *55th AIAA Aerospace Sciences Meeting, AIAA SciTech Forum,* no. AIAA 2017-1208, 2017.

[84] C. L. Rumsey and J. P. Slotnick, “Overview and Summary of the Second AIAA High-Lift Prediction Workshop,” *Journal of Aircraft,* vol. 52, no. 4, pp. 1006-1025, 2015.

[85] AIAA/NASA, “The 2nd AIAA CFD High Lift Prediction Workshop (HiLiftPW-2),” NASA, 2013. [Online]. Available: https://hiliftpw.larc.nasa.gov/index-workshop2.html. [Accessed March 2018].

[86] W. J. Walsh, F. S. Lamar and R. T. Kawai, “The High-Bypass-Ratio Variable-Pitch Turbofan for Transport Aircraft Propulsion,” in *AIAA Aircraft Systems and Technology Meeting*, Dallas, Texas, USA, 1976.

[87] R. T. Kawai, “Aircraft Installation Requirements and Considerations for Variable Pitch Fan Engines,” in *AIAA 5th Aircraft Design, Flight Test and Operations Meeting*, St Louis, Missouri, USA, 1973.

[88] B. L. Cleton, “Variable Geometry Exhaust System for Low Specific Thrust Turbofans,” PhD Thesis, School of Aerospace, Transport and Manufacturing, Cranfield University, 2017.

[89] K. W. Ramsden and P. K. Zachos, “Compressors Preliminary Design,” Thermal Power MSc course notes, Cranfield University, 2012.

[90] D. G. MacManus, “Turbine Preliminary Design,” Thermal Power MSc course notes, Cranfield University, 2012.

[91] UEC Aviadvigatel , “UEC Aviadvigatel engines website,” [Online]. Available: http://www.avid.ru/en. [Accessed 2018].

[92] I. Goulos, G. Giangaspero and D. MacManus, “GEMINI v2.0 User-Guide,” Cranfield UTC in Performance Engeering confidential document, 2017.

[93] I. Goulos, D. MacManus, T. Stankowski, P. Woodrow and C. Sheaf, “Civil Turbofan Engine Exhaust Aerodynamics: Impact of Bypass Nozzle After-body Design,” *Aerospace Science and Technology,* vol. 73, pp. 85-95, 2018.

[94] D. E. Hobbs, R. J. Neubert, E. W. Malmborg, D. H. Philbrick and D. A. Spear, “Low Noise Research Fan Stage,” NASA Contractor Report CR-195382, Lewis Research Center, 1995.

[95] C. Iek and D. R. Boldman, “Three-Dimensional Viscous Flow Analysis of an Advanced Ducted Propeller Subsonic Inlet,” *Journal of Aircraft Propulsion and Power,* vol. 11, no. 2 NASA-TM-106240, 1995.

[96] D. L. Tweedt, “Preliminary Aerodynamic Investigation of Fan Rotor Blade Morphing,” NASA Contractor Report CR-2012-217815, AP Solutions Inc, Cleveland, Ohio, 2012.

[97] M. Moretti, “CFD Modelling and Performance Analysis of Variable Pitch Fan,” UTC (Thermal Power) MSc Thesis, School of Aerospace, Transport and Manufacturing, Cranfield University, 2016.

[98] C. A. Hall and T. S. Williams, “Reverse Thrust Aerodynamics of Variable Pitch Fans,” in *ASME Conference Publication 2018 (Draft paper) GT2018-75739*, 2018.

[99] FAA Regulations & Policies, “120-42B - Extended Operations (ETOPS and Polar Operations),” FAA, Department of Transportation, USA, 2008. [Online]. Available: https://www.faa.gov/documentLibrary/media/Advisory_Circular/120-42B.pdf. [Accessed 2017].

[100] L. R. Jenkinson, P. Simpkin and D. Rhodes, “Civil Jet Aircraft Design,” Butterworth-Heinemann, 1999.

[101] Boeing Commercial Airplanes, “757-200/300 Airplane Characteristics for Airport Planning,” D6-58327, Sourced from Boeing.com, 2002.

[102] D. P. Raymer, “Aircraft Design: A Conceptual Approach,” AIAA, Washington DC, 1992.

[103] D. Howe, “Aircraft Conceptual Design Synthesis,” Professional Engineering Publishing Limited, London & Bury St Edmunds, UK, 2000.

[104] M. Sadraey, “Spoiler Design,” Daniel Webster University, [Online]. Available: https://pdfs.semanticscholar.org/bd1b/6abeea3cd9ae9022324c55c58556ce8f631e.pdf. [Accessed 2016].

[105] D. Cuenca Blasco, “3D-CFD Model Design and Intergration of a Variable Pitch Fan Engine,” UTC (Thermal Power) MSc Thesis, School of Aerospace, Transport and Manufacturing, Cranfield University, 2017.

[106] P. Jackson, “Jane's All the World's Aircraft,” Jane's Information Group Inc., 2006-2007.

[107] Boeing, “AERO QTR_04 10 - A Quarterly Publication,” Boeing Commercial Airplanes, 2010. [Online]. Available: https://www.boeing.com/commercial/aeromagazine/articles/2010_q4/3/.

[108] T. P. Stankowski, D. G. MacManus, C. T. Sheaf and N. Grech, “Aerodynamics of Aero-Engine Installations,” in *54th AIAA Aerospace Sciences Meeting*, San Diego, California, USA, 2016.

[109] T. P. Stankowski, D. G. MacManus, C. T. Sheaf and N. Grech, “Aerodnamic Interference for Aero-Engine Installations,” in *54th AIAA Aerospace Sciences Meeting*, San Diego, California, USA, 2016.

[110] F. S. Mastropierro, 3D-CFD Modelling and Simulation of a Modern Medium-Size Civil Aircraft in Landing Conditions, UTC (Thermal Power) MSc Thesis, School of Aerospace, Transport and Manufacturing, Cranfield University, 2017.

[111] Airbus, A321 Aircraft Characteristics Airport and Maintenance Planning, AIRBUS S.A.S., 31707 Blagnac Cedex, France: Sourced from Airbus.com, 2018.

[112] Airbus, A350 Aircraft Characteristics Airport and Maintenance Planning, AIRBUS S.A.S. 31707 Blagnac Cedex, France, 2017.

[113] BOEING, 737 Max Airplane Characteristics for Airport Planning, D6-38A004: Boeing Commercial Airplanes , 2017.

[114] Boeing Commercial Airplanes, 777-9 Airplane Characteristics for Airport Planning, D6-86073: Boeing Commercial Airplanes, 2018.

[115] Boeing, 787 Airplane Characteristics for Airport Planning, D6-58333: Boeing Commercial Airplanes, 2014.

[116] ANSYS, “ANSYS CFX Documentation,” [Online]. Available: Available online from https://www.sharcnet.ca/Software/Ansys/17.0/en-us/help/ai_sinfo/cfx_intro.html.

[117] ANSYS, “ICEM User Guide,” [Online]. Available: Avialable from https://www.sharcnet.ca/Software/Ansys/16.2.3/en-us/help/icm_user/icem_usermanual.html.

[118] J. E. Bardina, P. G. Huang and T. J. Coakley, “Turbulence Modeling Validation Testing and Development,” NASA Technical Momorandum TM-110446 , 1997.

[119] ANSYS, “Introduction to ANSYS FLUENT - Lecture 6 - Turbulence Modelling,” Customer Training Manual, 2010. [Online]. Available: http://imechanica.org/files/fluent_13.0_lecture06-turbulence.pdf.

[120] *Collaboration with Tim Williams (PhD) at Cambridge University UTC.*

[121] Boeing, “FAA Reference Code and Approach Speeds for Boeing Aircraft,” Boeing Commercial Airplanes, 2016. [Online]. Available: http://www.boeing.com/assets/pdf/commercial/airports/faqs/arcandapproachspeeds.pdf.

[122] R. Stanworth, Cranfield University Delta HPC Cluster User Guide Issue 1.0, Information Services, Cranfield University, 2017.

[123] D. A. Topol, C. L. Ingram, M. J. Larkin, C. H. Roche and R. D. Thulin, Advanced Subsonic Technology (AST) 22-Inch Low Noise Research Fan Rig Preliminary Design of ADP-Type Fan 3, NASA Contractor Report CR-2004-212718, 2004.

[124] K. C. Chitale, M. Rasquin, J. Martin and K. E. Jansen, “Finite Element Flow Simulations of the EUROLIFT DLR-F11 High Lift Configuration,” in *AIAA 2014-0749*, 52nd Aerospace Sciences Meeting, National Harbor, Maryland, USA, 2014.

[125] X. Oritz, D. Rival and D. Wood, “Forces and Moments on Flat Plates of Small Aspect Ratio with Application to PV Wind Loads and Small Wind Turbine Blades,” *energies,* pp. 2438-2453, 2015.

[126] R. B. Langtry, M. Kuntz and F. R. Menter, “Drag Prediction of Engine-Airframe Interference Effects with CFX 5,” in *42nd Aerospace Science Meeting & Exhibit*, Reno, Nevada, USA, 2004.

[127] A. Ko, W. H. Mason and B. Grossman, “Transonic Aerodynamics of a Wing/Pylon/Strut Juncture,” in *21st AIAA Applied Aerodynamic Conference*, Orlando, Florida, USA, 2003.

[128] R. Devine, K. Cooper, R. Gault and J. K. Watterson, “Comparison of Conventional and Compression Pylon Designs for an Underwing Nacelle,” *Journal of Aircraft,* vol. 46, no. 1, pp. 325-328, 2009.

[129] GE Honda Aero Engines, “GE Honda,” [Online]. Available: http://www.gehonda.com/engine/explore.html. [Accessed 2018].

Appendix A – GEMINI Geometric Parameters

General Design

Fan_R_out_1	1.395
L_eng	3.5
M_int_throat	0.72
f_en	0.7
f_nac	2.473
f_nac_te	0
f_max	0.4
r_max_ratio	1.22
f_nac_nose	0.013
int_contr_ratio	1.6
f_thr	0.22
f_int	1.4
f_infl	0
f_sp	0.05
f_ar	2.9
f_bp	3.0
f_turb	0.45
f_noz	1.0
f_pl_base	0.05
alpha_sp	35
alpha_hade	5
alpha_nac	14
alpha_nac_min	5
alpha_noz	18
alpha_noz_min	5
alpha_pl	19
BP_Hade_angle_in	0.0
BP_Hade_angle_out	0.0
CR_Hade_angle_in	0.0
CR_Hade_angle_out	0.0
Fan_OGV_angle	0
BP_nozzle_curvature_ratio_in	5.0
BP_nozzle_curvature_ratio_out	3.0
BP_nozzle_length_ratio	1.0
BP_nozzle_area_ratio	1.12
BP_CP_radial_offset_ratio	1.0
BP_CP_outer_line_slope	-7
BP_in_duct_linear_design	No
BP_out_duct_linear_design	No
CR_nozzle_use_BM	No
CR_nozzle_curvature_ratio_in	2.0
CR_nozzle_curvature_ratio_out	3.0
CR_nozzle_length_ratio	0.6
CR_nozzle_area_ratio	1.04
CR_CP_radial_offset_ratio	1.0
CR_CP_outer_line_slope	-4
CR_in_duct_linear_design	No
CR_out_duct_linear_design	No

Spinner

Spinner angle	32
Nose curvature	0.03

Nacelle

l_nac_ratio	3.28
r_hi_ratio	1.0599
r_if_ratio	0.024
r_max_ratio	1.235
f_max	0.395
beta_nac	13.0
beta_nac_min	6.0
f_throat	0.36
CR	1.28
f_infl	0.0

Exhausts

Fan_R_out_1	1.395			
Fan_R_out_2	1.025			
LPT_R_out	0.38			
r_max_ratio	1.235			
BP_nozzle_R_out	0.965			
BP_nozzle_L_out	2.1			
L_CR_cowl	0.8			
L_fan_OGV	1.05			
L_LPT_OGV	2.3441			
BP_BT_angle	18			
CR_BT_angle	20			
BP_Hade_angle_in	5.0			
BP_Hade_angle_out	3.83			
CR_Hade_angle_in	0			
CR_Hade_angle_out	2.0			
Fan_OGV_angle	0			
Nacelle_aft_min_thickness	0.01			
Core_cowl_min_thickness	0.01			
BP_nozzle_curvature_ratio_in	4.75			
BP_nozzle_curvature_ratio_out	6.0			
BP_nozzle_length_ratio	0.50			
BP_nozzle_area_ratio	1.05			
BP_CP_radial_offset_ratio	0.72			
BP_CP_outer_line_slope	0			
P_in_control_point_1	0.15	0.01	3.0	-5000
BP_in_control_point_2	0.52	0.024	20	-5000
BP_out_control_point_1	0.1575	0.013	4.5	-5000
BP_out_control_point_2	0.52	0.035	2.0	-5000
BP_in_duct_linear_design	No			
BP_out_duct_linear_design	Yes			
Design_curved_CC	No			
CR_nozzle_use_BM	No			
CR_nozzle_curvature_ratio_in	2.0			
CR_nozzle_curvature_ratio_out	1.5			
CR_nozzle_length_ratio	0.5			
CR_nozzle_area_ratio	1.1			

CR_CP_radial_offset	0.9
CR_CP_outer_line_slope	0
CR_in_duct_linear_design	No
CR_out_duct_linear_design	No
CR_nozzle_use_BM	No
CR_nozzle_curvature_ratio_in	1.0
CR_nozzle_curvature_ratio_out	3.0
CR_nozzle_length_ratio	0.3
CR_nozzle_area_ratio	1.1
CR_CP_radial_offset_ratio	0.9
CR_CP_outer_line_slope	0
CR_plug_radial_thickness	0.025
CR_cowl_TE_min_angle	2.0
Design_Z3_vent	No

Appendix B – Development Model CFD Residuals

CONVERGENCE OF MOMENTUM & MASS RESIDUALS FOR CFD OF MAIN DEVELOPMENT MODELS

Baseline ADP Validation

(Fan, splitter, CIGV, FEGV at cruise)

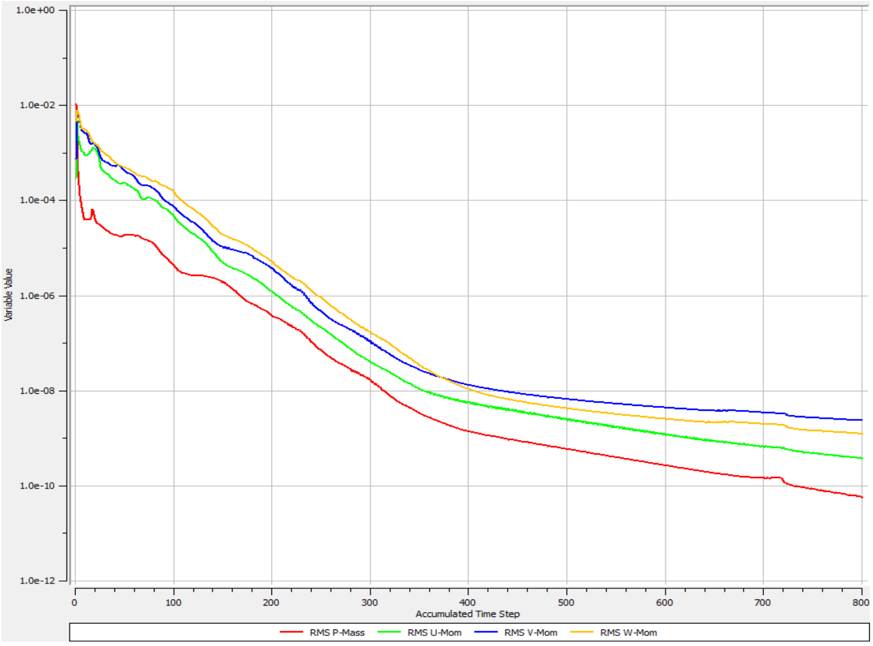

GEMINI Verification

(Nacelle & exhausts at cruise, Mach 0.8, 35,000 ft)

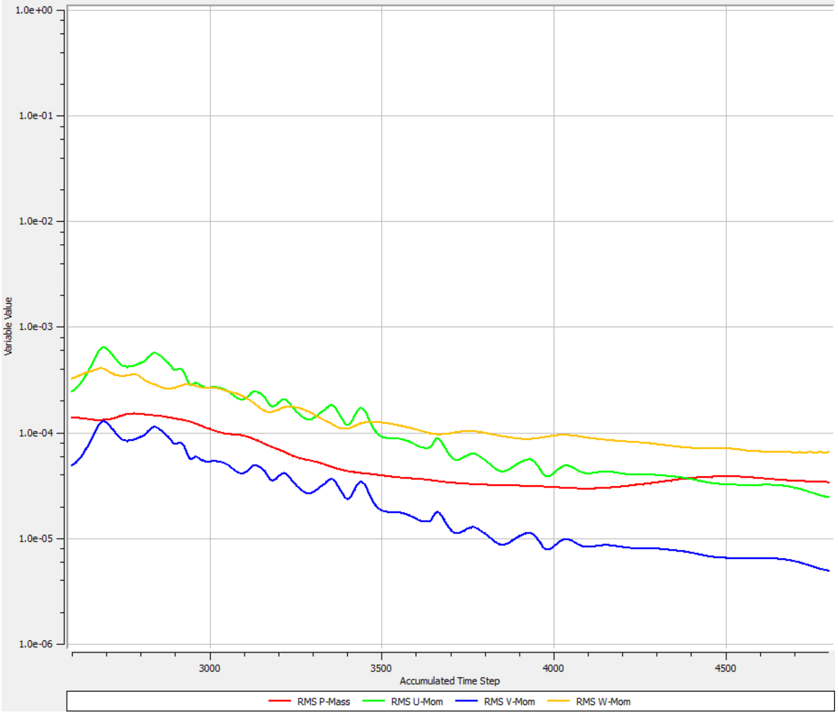

Scaled VPF Validation

(Fan, splitter, OGV at cruise)

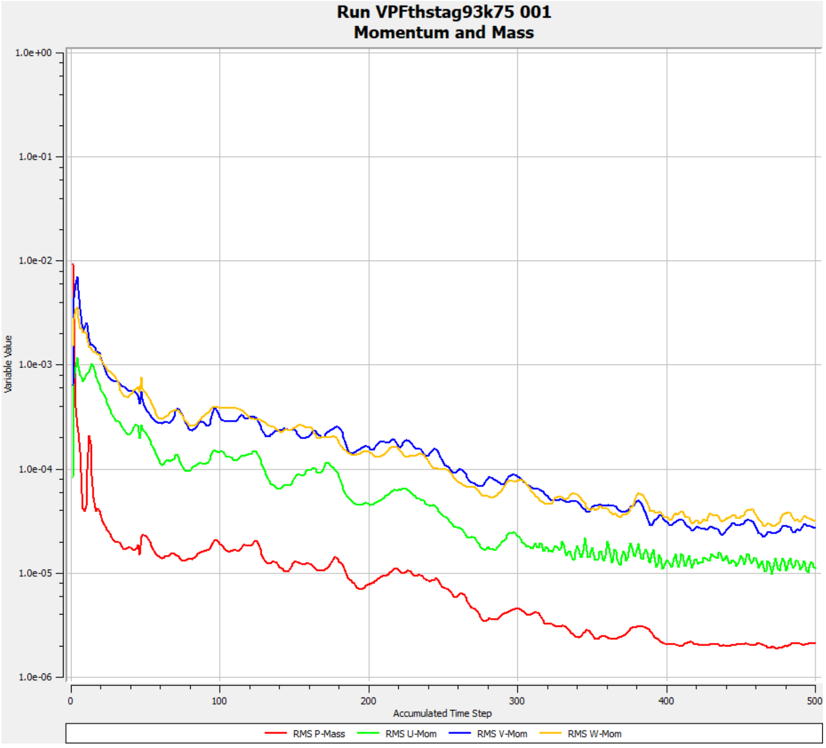

Airframe Validation

(DLR F11 clean-wing, Mach 0.175)

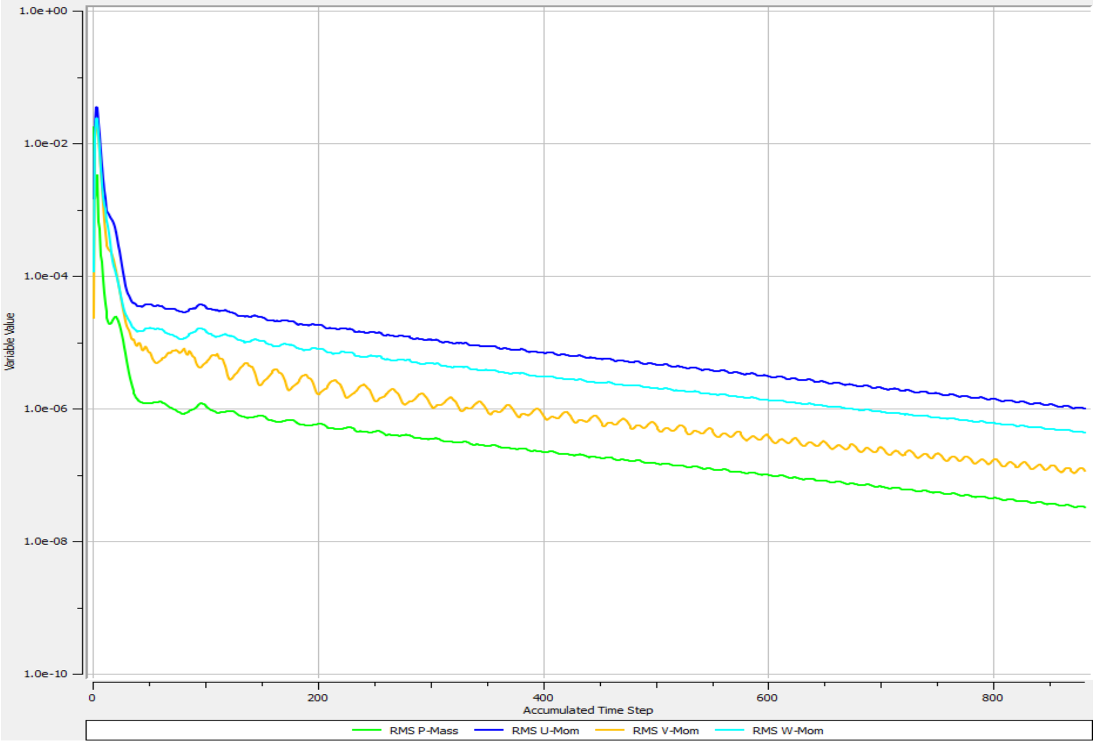

Spoiler Verification

(DLR F11, clean wing with spoiler deployed, 140 knots)

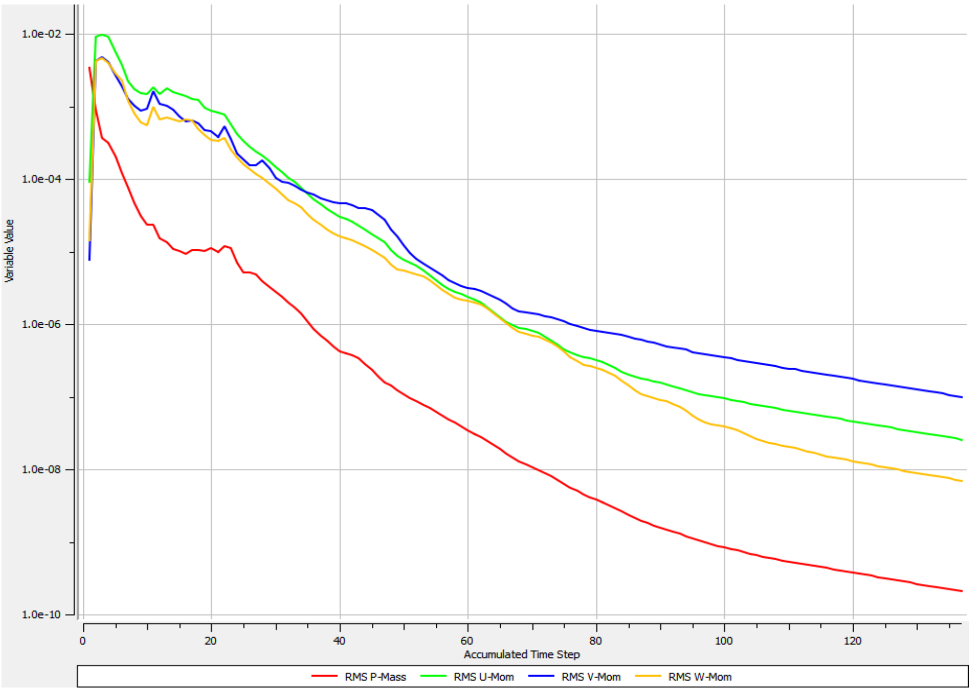

Pylon Verification

(DLR F11, with pylon and engine, 140 knots)

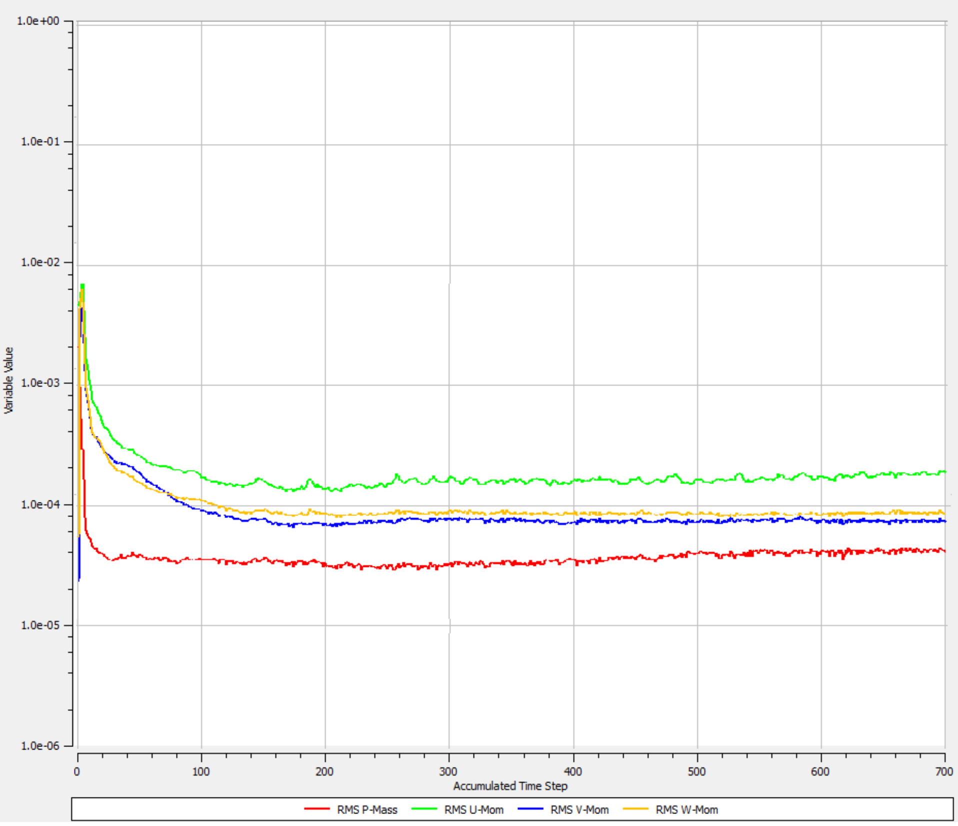

Appendix C – Mach Number Contours for Baseline ADP

ROTOR - SLTO [40]

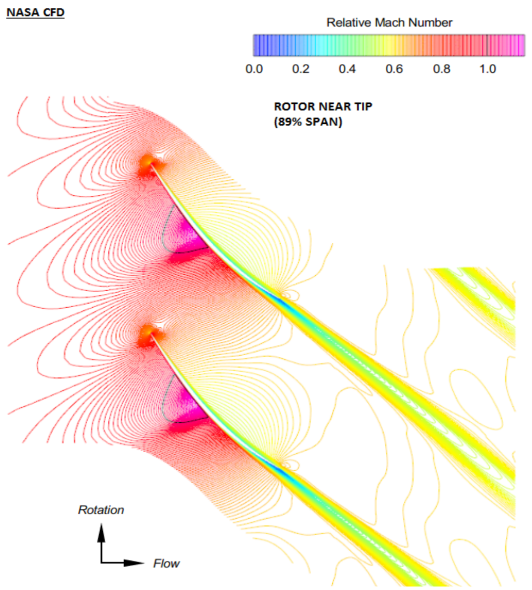

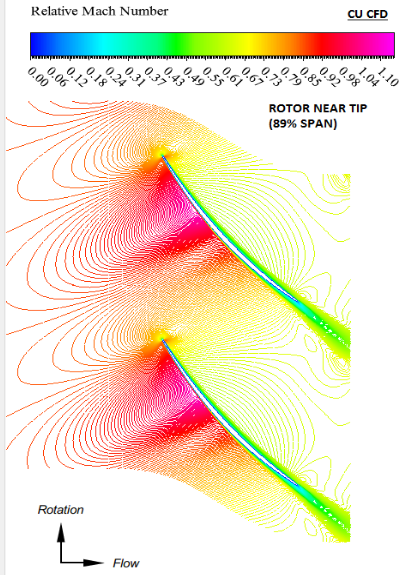

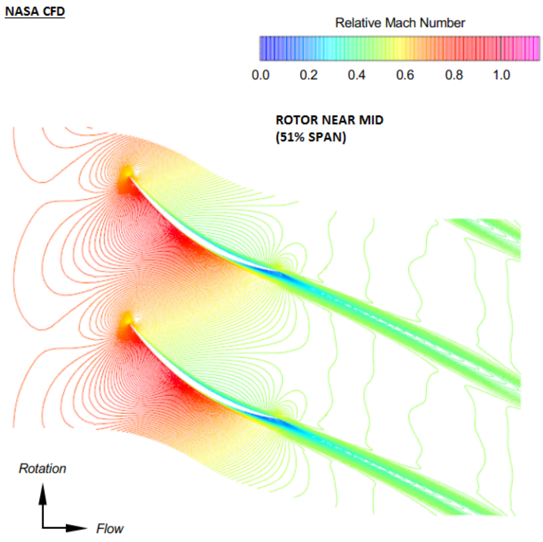

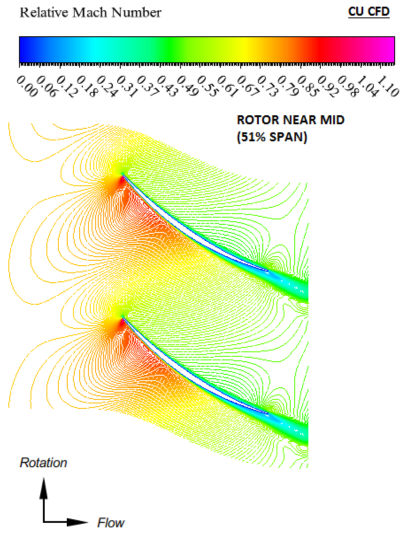

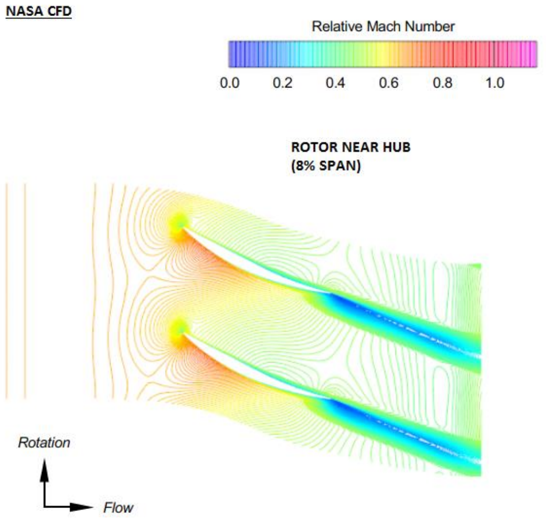

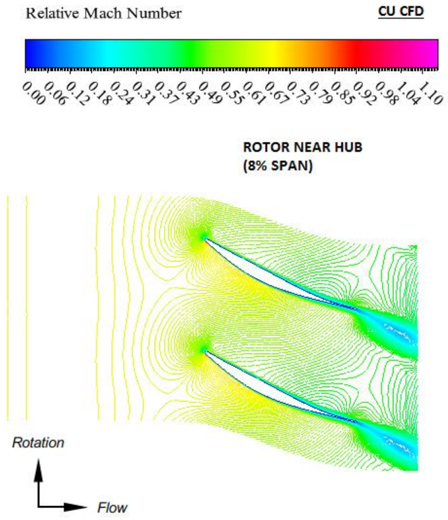

OGV - SLTO [40]

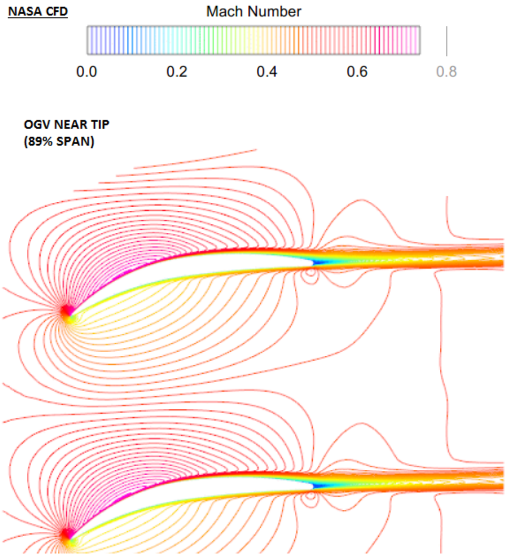
NASA CFD
Mach Number
0.0
0.2
0.4
0.6
0.8
OGV NEAR TIP
(89% SPAN)

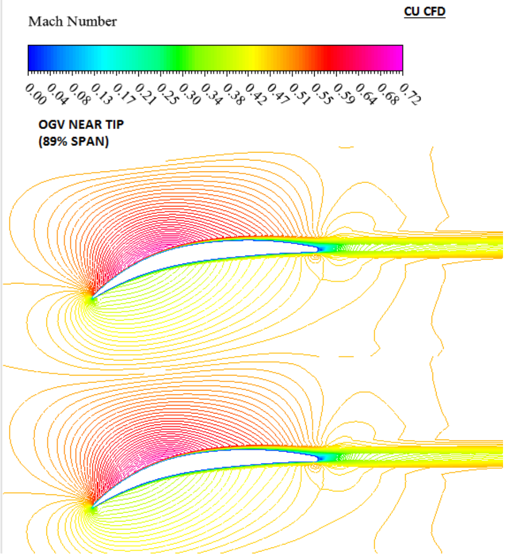
Mach Number
CU CFD
0.00 0.04 0.08 0.13 0.17 0.21 0.25 0.30 0.34 0.38 0.42 0.47 0.51 0.55 0.59 0.64 0.68 0.72
OGV NEAR TIP
(89% SPAN)

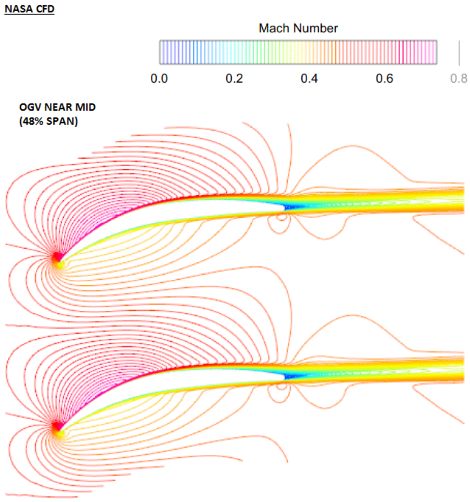
NASA CFD
Mach Number
0.0
0.2
0.4
0.6
0.8
OGV NEAR MID
(48% SPAN)

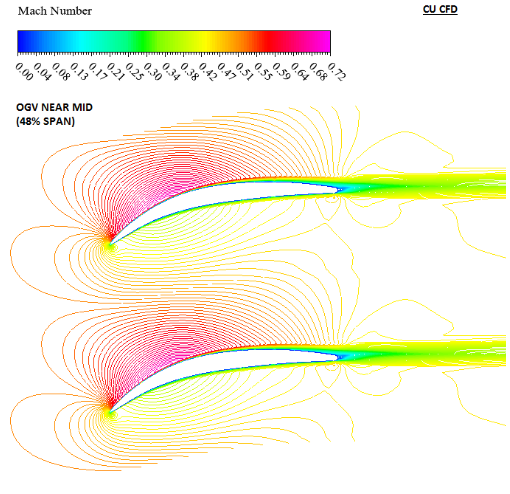
Mach Number
CU CFD
0.00 0.04 0.08 0.13 0.17 0.21 0.25 0.30 0.34 0.38 0.42 0.47 0.51 0.55 0.59 0.64 0.68 0.72
OGV NEAR MID
(48% SPAN)

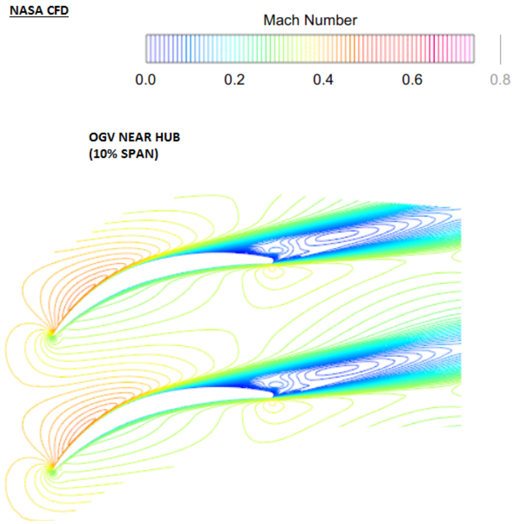
NASA CFD
Mach Number
0.0
0.2
0.4
0.6
0.8
OGV NEAR HUB
(10% SPAN)

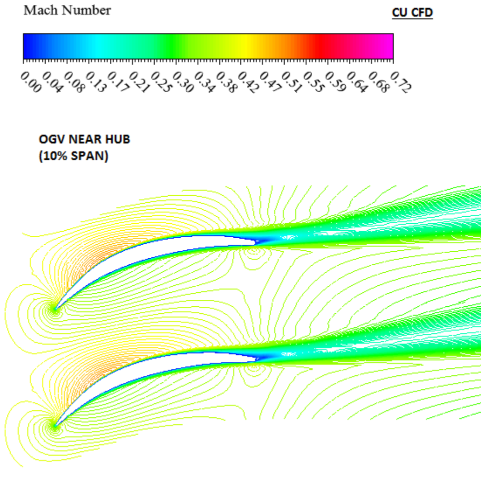
Mach Number
CU CFD
0.00 0.04 0.08 0.13 0.17 0.21 0.25 0.30 0.34 0.38 0.42 0.47 0.51 0.55 0.59 0.64 0.68 0.72
OGV NEAR HUB
(10% SPAN)

Appendix D – ADP Baseline – SOCRATES Validation [38]

ADP Fan 0 degree setting Design Point (8396.5 RPM)

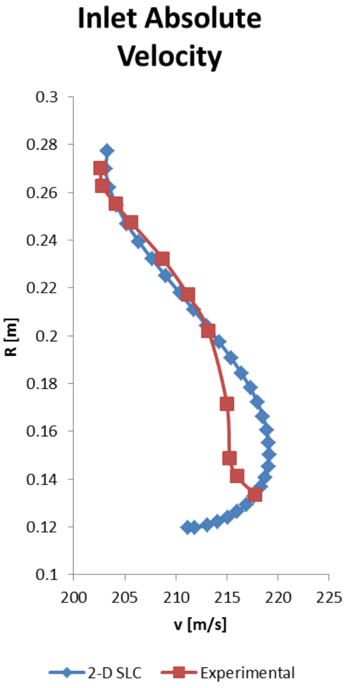
Inlet Absolute Velocity

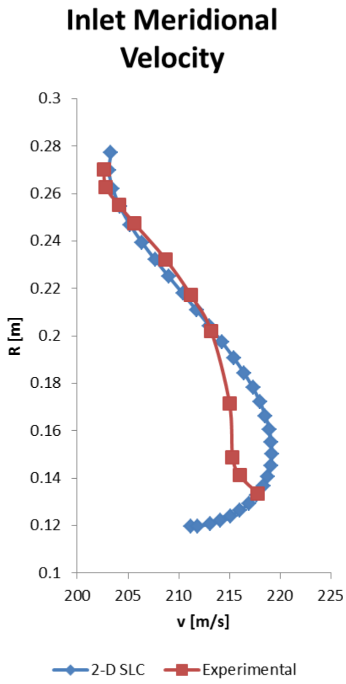
Inlet Meridional Velocity

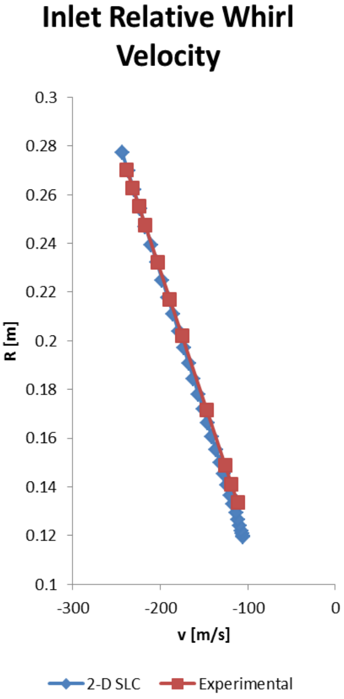
Inlet Relative Whirl Velocity

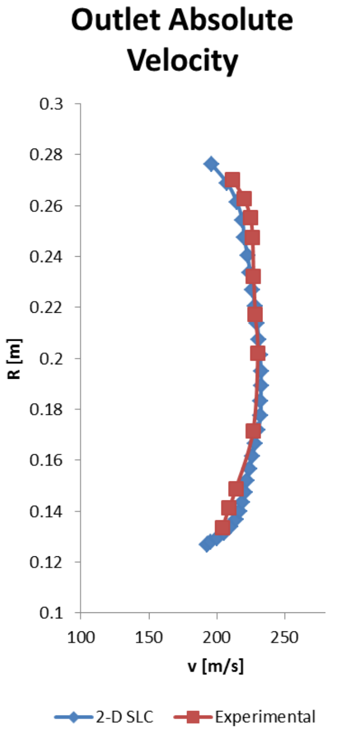
Outlet Absolute Velocity

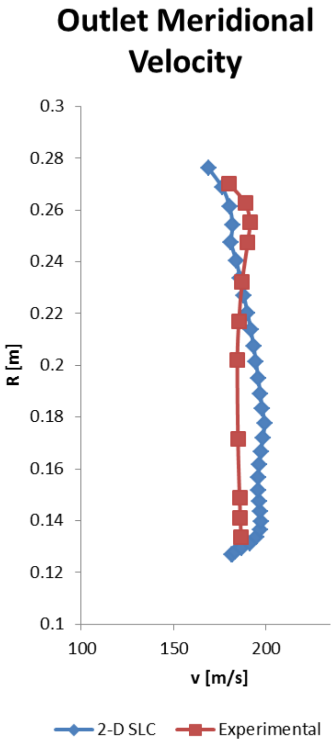
Outlet Meridional Velocity

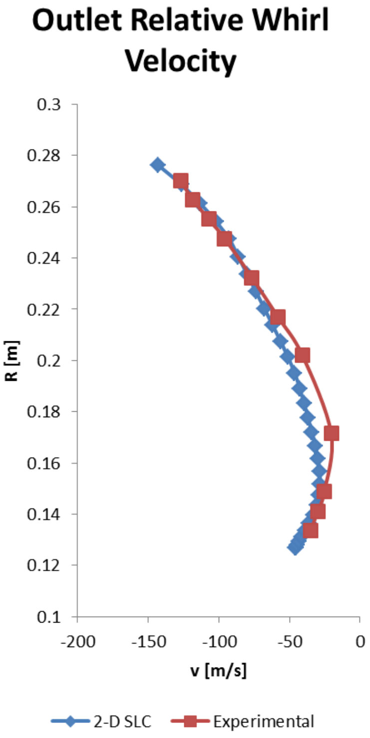
Outlet Relative Whirl Velocity

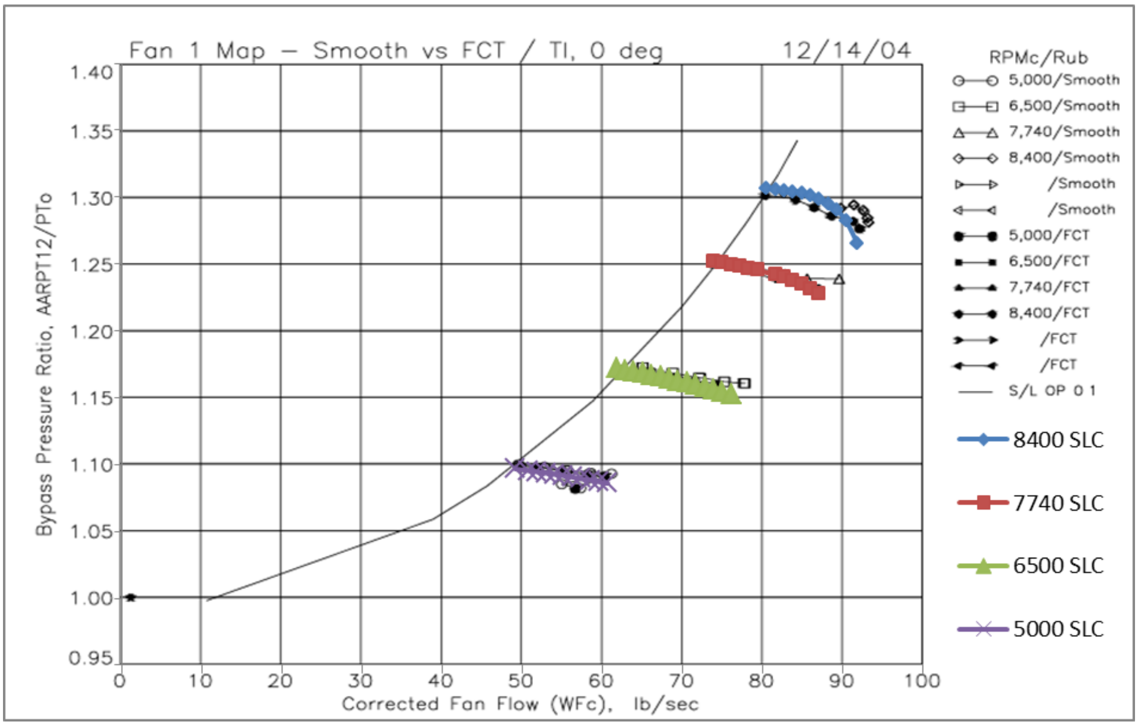
Fan 1 Map — Smooth vs FCT / TI, 0 deg
12/14/04
Bypass Pressure Ratio, AARPT12/PTo
1.40
1.35
1.30
1.25
1.20
1.15
1.10
1.05
1.00
0.95
0
10
20
30
40
50
60
70
80
90
100
Corrected Fan Flow (WFc), lb/sec
RPMc/Rub
5,000/Smooth
6,500/Smooth
7,740/Smooth
8,400/Smooth
/Smooth
/Smooth
5,000/FCT
6,500/FCT
7,740/FCT
8,400/FCT
/FCT
/FCT
S/L OP 0 1
8400 SLC
7740 SLC
6500 SLC
5000 SLC

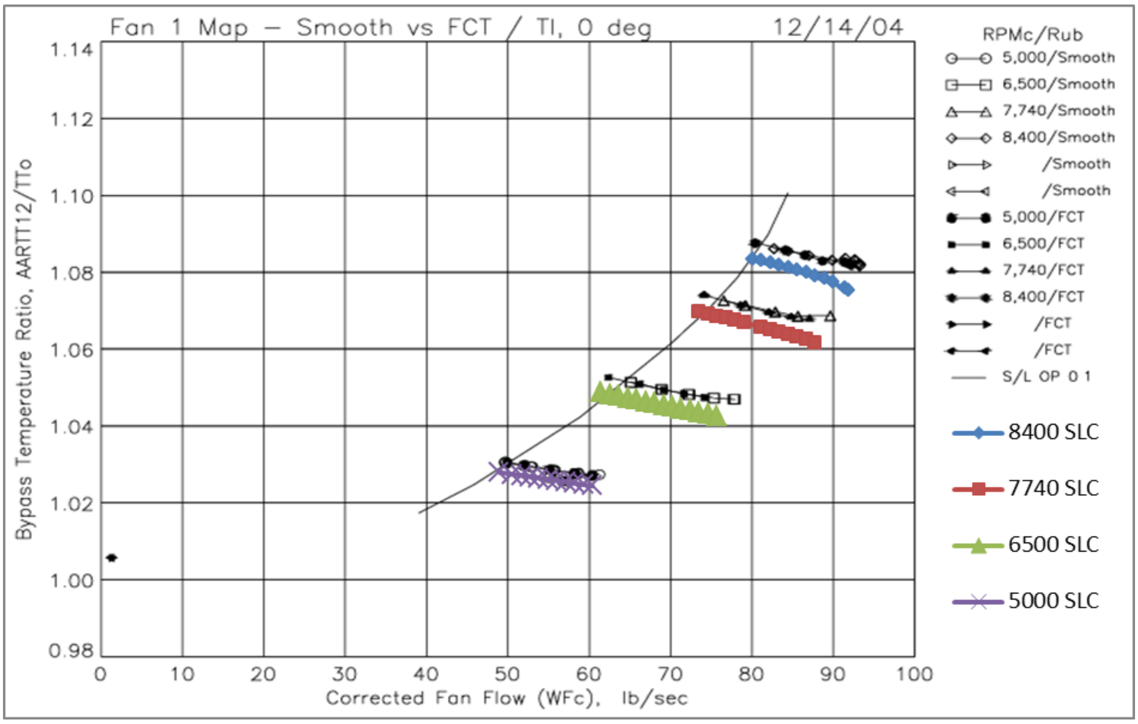
Fan 1 Map — Smooth vs FCT / TI, 0 deg
12/14/04
Bypass Temperature Ratio, AARTT12/TTo
1.14
1.12
1.10
1.08
1.06
1.04
1.02
1.00
0.98
0
10
20
30
40
50
60
70
80
90
100
Corrected Fan Flow (WFc), lb/sec
RPMc/Rub
5,000/Smooth
6,500/Smooth
7,740/Smooth
8,400/Smooth
/Smooth
/Smooth
5,000/FCT
6,500/FCT
7,740/FCT
8,400/FCT
/FCT
/FCT
S/L OP 0 1
8400 SLC
7740 SLC
6500 SLC
5000 SLC

Appendix E – DLR F11 Wing C_P Distributions [119]

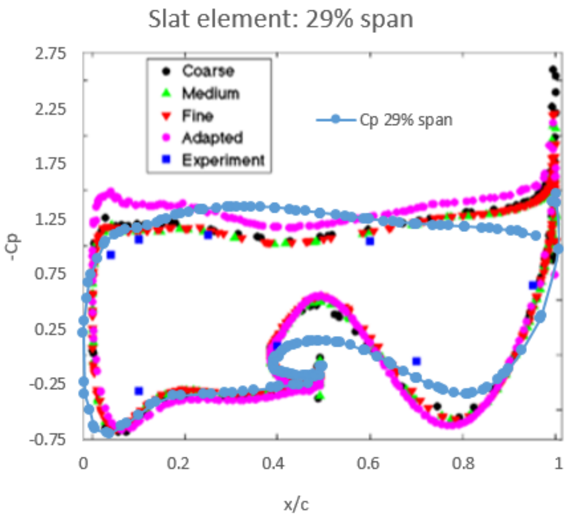
Slat element: 29% span

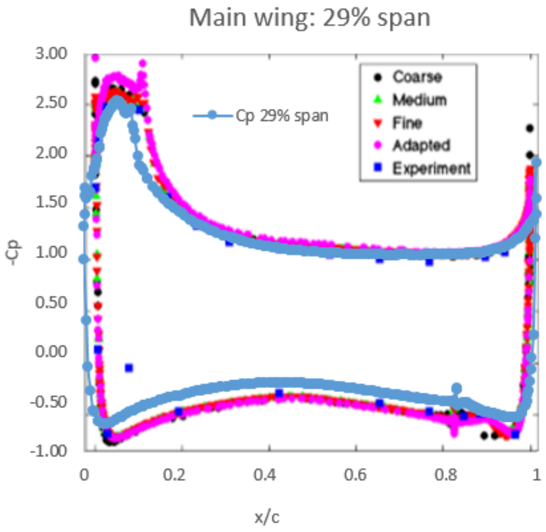
Main wing: 29% span

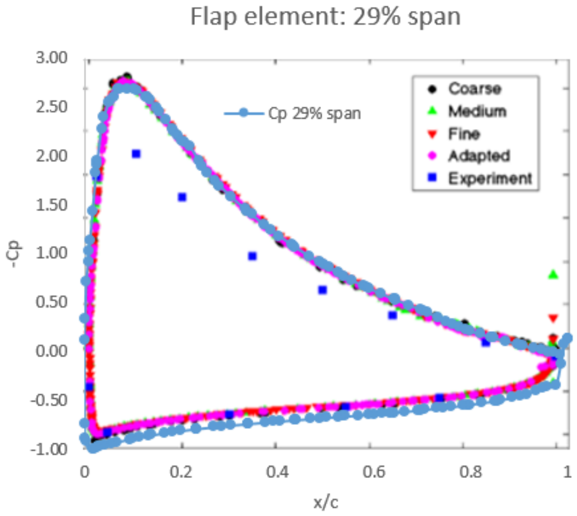
Flap element: 29% span

Slat element: 89% span

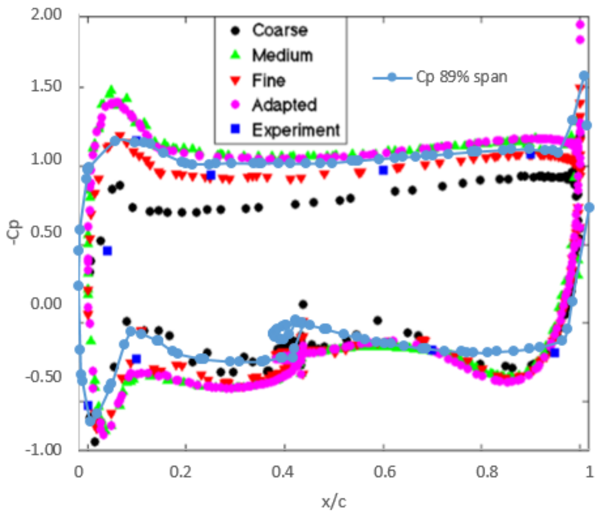

Main wing: 89% span

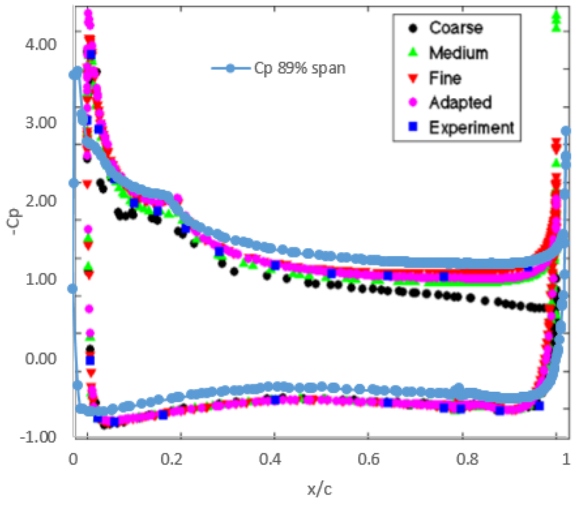

Flap element: 89% span

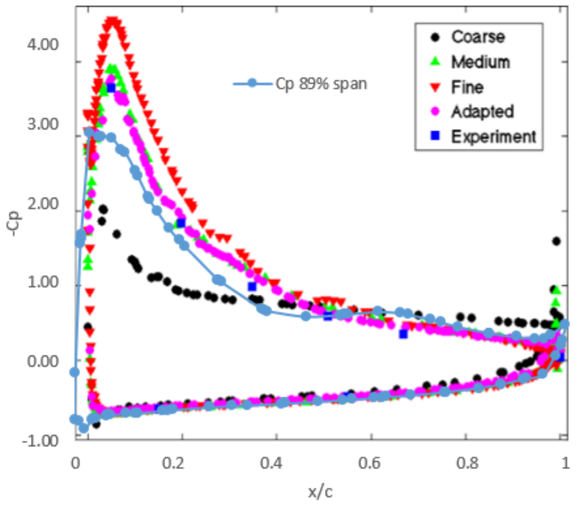

Appendix F – GCI Study for Reversed Fan

Taken from result using same # of iterations

Characteristic Parameters

GCI	PR	Effy	MFF	RMS(GCI)
340k	0.019	0.76	0.29	0.21
510k	0.019	1.49	0.05	0.04
760k	0.010	1.35	0.12	0.08

Flow Parameters 0 to 60%

GCI	Inlet Alpha	Outlet Alpha	Inlet Beta	Outlet Beta	Inlet Mach	Outlet Mach	Inlet Mach abs	Outlet Mach abs	RMS(GCI)
340k	0.31	0.18	0.06	0.04	0.01	0.09	0.39	0.24	0.19
510k	0.80	0.15	0.07	0.00	0.01	0.05	0.19	0.03	0.10
760k	0.25	0.53	1.19	0.07	0.01	0.08	0.06	0.02	0.49

Flow Parameters 60 to 100%

GCI	Inlet Alpha	Outlet Alpha	Inlet Beta	Outlet Beta	Inlet Mach	Outlet Mach	Inlet Mach abs	Outlet Mach abs	RMS(GCI)
340k	0.11	0.60	0.08	0.13	0.09	0.34	0.02	0.01	0.26
510k	0.12	0.11	0.04	0.06	0.08	0.31	0.03	0.04	0.13
760k	0.05	0.17	0.01	0.11	0.01	0.27	0.03	0.15	0.13

Gross GCI

Gross GCI	RMS GCI Characteristic	RMS GCI Flow 0 to 60	RMS GCI Flow 60 to 100	RMS(RMS(GCIs))
340k	0.21	0.19	0.26	**0.22**
510k	0.04	0.10	0.13	**0.10**
760k	0.09	0.49	0.13	**0.30**

Appendix G – Convergence for Initial Rev. Thrust Simulations

(Isolated nacelle with single-passage fan at 110 knots landing speed)

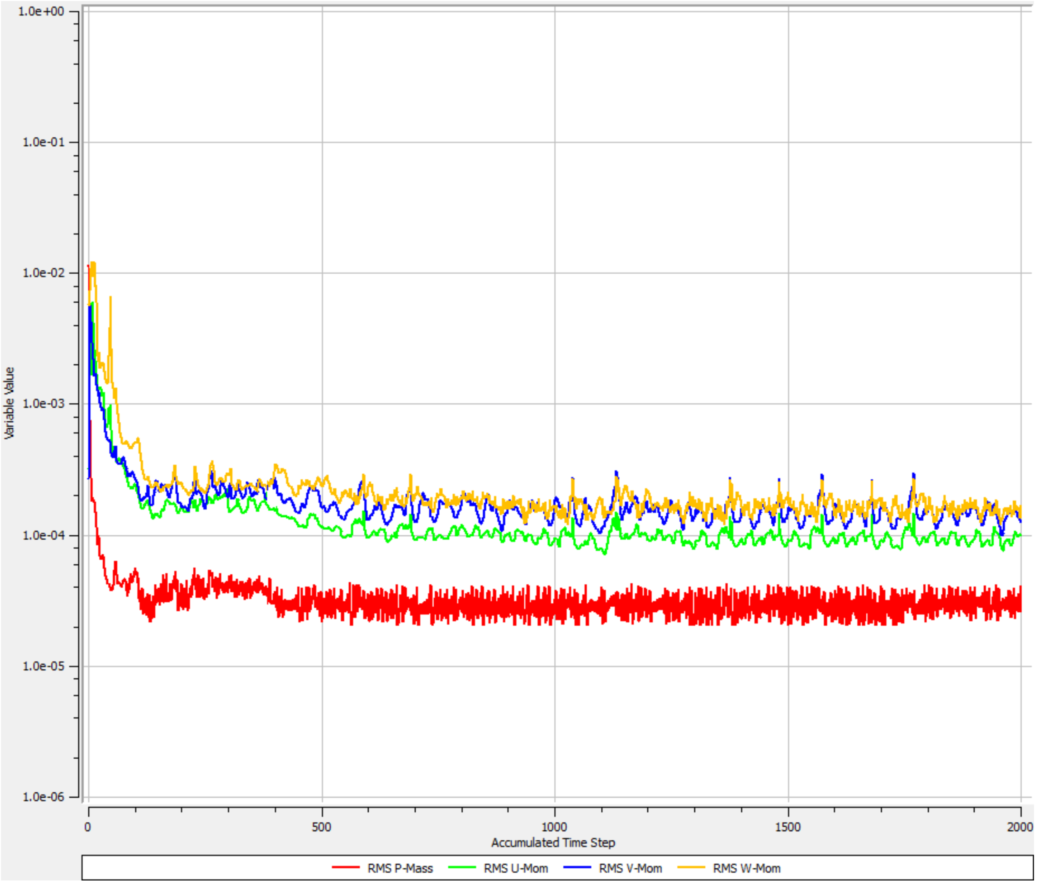

(Integrated nacelle with full annulus fan at 110 knots landing speed)

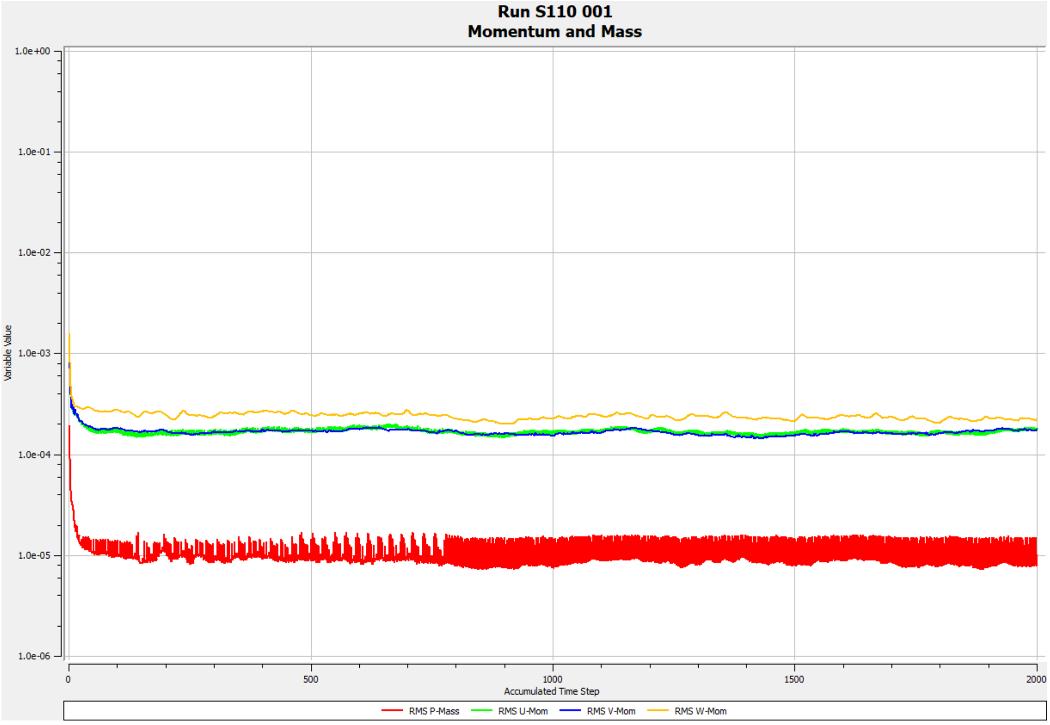

(Integrated nacelle with full annulus fan at 110 knots landing speed)

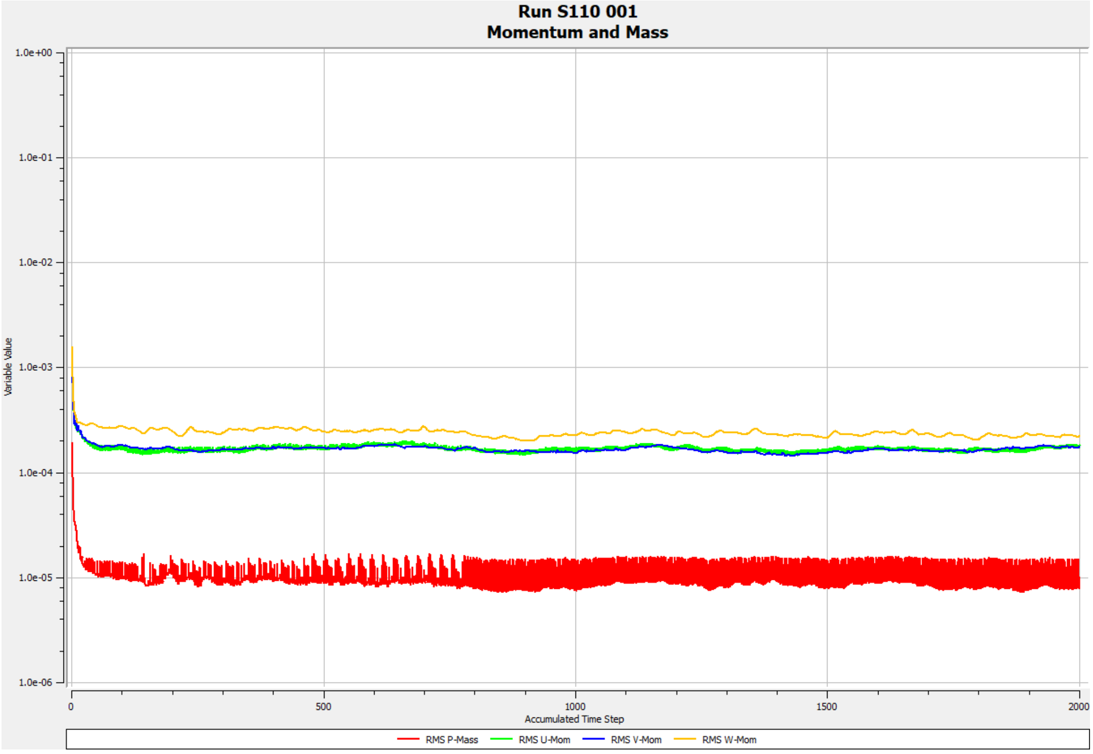

Comparison of flow angle and axial velocity for single passage & full annulus integrated cases at 110 & 60 knots. Measurements taken on the fan-face interface, using circumferentially-area-averaged values.